Design, construction and in situ testing of a muon camera for Earth science and civil engineering applications.

Ignacio Lázaro Roche

UNIVERSITÉ CÔTE D'AZUR

ÉCOLE DOCTORALE
SCIENCES FONDAMENTALES ET APPLIQUÉES

THÈSE DE DOCTORAT

Design, réalisation et test in situ d'une caméra muon pour des applications en sciences de la Terre et en génie civil

Ignacio LÁZARO ROCHE

IRIS Instruments
Géoazur UMR 7329, UCA/CNRS/OCA/IRD
Laboratoire Souterrain à Bas Bruit UMS 3538, UNS/UAPV/CNRS

Présentée en vue de l'obtention du grade de docteur en Sciences de la Planète et de l'Univers **d'**Université Côte d'Azur
Dirigée par : Stéphane Gaffet
Soutenue le : 8 Octobre 2018

Devant le jury, composé de :
José Busto, Professeur, Aix-Marseille U.
Olivier Coutant, Physicien, CNAP
Andrea Giammanco, Professeur, U. of Louvain
Stéphane Gaffet, DR, CNRS
Adnand Bitri, Ph.D., BRGM
Hans Müller, Chercheur émérite, CERN
Simon Bouteille, Ph.D., IRIS Instruments
Catherine Truffert, PDG IRIS Instruments

IRIS INSTRUMENTS

anrt association nationale recherche technologie
Cifre Conventions

UNION EUROPÉENNE
Fonds Européen de Développement Régional

Design, réalisation et test in situ d'une caméra muon pour des applications en sciences de la Terre et en génie civil.

Jury :

Président du jury

Andrea Giammanco, Professeur, Université catholique de Louvain

Rapporteurs

José Busto, Professeur, Aix-Marseille Université

Olivier Coutant, Professeur, Université Grenoble-Alpes

Examinateurs

Adnand Bitri, PhD, Bureau de Recherches Géologiques et Minières (BRGM)

Simon Bouteille, PhD, IRIS Instruments.

Hans Müller, PhD, Org. Européenne pour la Recherche Nucléaire (CERN)

Invitée

Catherine Truffert, PhD, IRIS Instruments.

«Hijos míos, si os pareciese largo el tiempo que invirtáis en leer lo que para vosotros escribo, tened presente que mucho más largo ha sido el que he invertido yo en escribirlo».

Fernán Caballero.
La mitología contada a los niños.

Résumé

Titre de la thèse : Design, réalisation et test in situ d'une caméra muon pour des applications en sciences de la Terre et en génie civil

Mots-clés : muon cosmique, tomographie, Micromegas, chambre projection temporelle, rayonnement cosmique, muographie

Cette thèse est dédiée à la création d'un nouvel outil pour la mesure directionnelle du flux muonique basé sur une chambre de projection temporelle fine avec un plan de lecture Micromegas, afin d'obtenir un détecteur compact avec une résolution angulaire compatible avec les applications d'imagerie ou de monitoring en génie civil et géophysique. La principale motivation est de développer un détecteur capable de combler le vide technologique pour les applications ayant des contraintes d'encombrement et de transportabilité.

Cette thèse fournit une revue des différentes technologies de détection de muons existantes et de leurs divers domaines d'application. Deux techniques de mesure de muons sont présentées : la muographie par transmission ou par diffusion. La muographie par transmission, mieux adaptée aux grandes cibles, est basée sur l'atténuation du flux naturel de muons cosmiques due à l'opacité des matériaux traversés. Cette technique passive et non-destructive fournit des informations originales qui pourront être intégrées dans une démarche d'imagerie.

Le manuscrit présente la méthodologie utilisée pour la caractérisation du flux incident de muons à la fois en surface et dans des conditions souterraines. Une description détaillée des processus physiques déclenchés par le passage d'un muon à travers le détecteur est fournie. Les résultats des simulations des processus de formation du signal sont présentés et commentés pour justifier les choix du design des composants clés afin de répondre aux exigences de performance quant à résolutions temporelle, spatiale et angulaire. L'influence des paramètres opérationnels ou externes tels que le gain, la température ou la présence de contaminants est également traitée.

La thèse étudieen détail les principales phases de conception et d'assemblage du détecteur MUST2, incluant (i) le design du plan de lecture Micromegas, (ii) le choix du gaz, (iii) le design d'un élément homogénéisateur de champ électrique (iv) le choix de l'instrumentation électronique et du signal de déclenchement associé au passage du muon, et (v) la création d'un système auxiliaire de gestion du gaz.

La polyvalence du détecteur MUST2 a été prouvée avec l'utilisation réussie de différentes options de déclenchement et d'acquisition. Les données sont obtenues au travers d'un logiciel développé pour le système d'acquisition modulaire du CERN SRS, puis analysées avec un algorithme de reconstruction de la trajectoire, qui récupère le temps de passage, la position 2D, les angles zénith et azimut des muons qui traversent le détecteur. Les caractéristiques, les performances et les limites de la chaîne d'acquisition de données sont présentées et évaluées. Une série de directives visant à améliorer l'efficacité de la chaîne d'acquisition est proposée.

Une série de tests de caractérisation a été effectuée dans différents environnements : faisceau contrôlé de muons, ciel ouvert, au fond d'une vallée et dans des conditions souterraines. Ces tests ont contribué à une meilleure compréhension des performances du détecteur et ont permis de régler ses paramètres opérationnels. Malgré les faibles statistiques des tests, les flux mesurés montrent une bonne corrélation avec les environnements ciblés. Une campagne de mesures en conditions réelles a été menée sur le barrage de Saint-Saturnin-les-Apt (Vaucluse). Les résultats expérimentaux obtenus, sont conformes aux valeurs anticipées par le modèle numérique, la transportabilité sur le terrain et la capacité à effectuer des mesures hors laboratoire à long terme ont été démontrées. En revanche, l'impact de la température externe sur

l'acquisition des données devra être compensée pour obtenir une acquisition stable permettant de surveiller l'évolution temporelle du flux de muons.
En conclusion, les bons résultats obtenus lors de ces tests permettent de valider la caméra MUST^2 à des fins de muographie en transmission.

Abstract

Thesis title: Design, construction and in situ testing of a muon camera for Earth science and civil engineering applications.
Keywords: cosmic muon, tomography, Micromegas, time projection chamber, cosmic rays, muography

This thesis is dedicated towards the creation of a new direction-sensitive tool for muon flux measurement based on a thin time projection chamber with a Micromegas readout, to achieve a compact detector with an angular resolution compatible with civil engineering and geophysics imagery and monitoring applications. The main motivation is to develop a detector capable to fill the technological gap for applications with compactness and transportability constraints.

The dissertation provides a review of the different existing muon detection technologies and their diverse fields of application. Two muon imaging techniques are introduced: transmission and scattering muography. Transmission muography, more suitable for big targets, is based on the attenuation of the natural-occurring cosmic-muon flux due to the opacity of the material they traverse. This non-destructive, passive technique provides original information that can be used for imaging purposes.

The work covers the methodology used towards the characterization of the incidental muon flux both on the surface and in underground conditions. A detailed description of the physical processes triggered by the passage of a muon through the detector is provided. Results of the simulations of the signal formation processes are presented and discussed to justify the design choices of the key components so as to meet performance requirements in term of temporal, spatial and angular resolution. The influence of operational or external parameters such as the gain, temperature or presence of contaminants is covered as well.

The thesis describes in detail the principal phases of design and assembly of the MUST^2 detector, including: (i) the design of the Micromegas readout layout, (ii) the choice of gas, (iii) the conception of an electric field homogenizer, (iv) the choice of the electronics instrumentation and its trigger signal, and (v) the creation of an auxiliary system to manage the gas.

The versatility of MUST^2 has been proved with the successful use of different trigger options and electronics. The data is acquired by means of software developed for the CERN's Scalable Readout System electronics and subsequently analyzed with a muon trajectory reconstruction algorithm, which retrieves the: time of passage, 2D position, zenith and azimuth angles of the muons traversing the detector. The characteristics, performance and limitations of the data acquisition chain are presented and evaluated, a series of guidelines towards the improvement of its efficiency of are provided.

A series of characterization tests has been carried out in different environments: controlled muon beam, open sky, at the bottom of a valley and in underground conditions. These tests have enabled a better understanding of the performance of the detector and allowed to tune up its operational parameters. Despite the weak statistics of the test runs, the measured muon flux has shown a good correlation with the surrounding target volumes. A campaign of measurements in real field conditions has been carried out at the Saint-Saturnin-les-Apt (Vaucluse, France) dam. The experimental results obtained are in consonance with the values anticipated by the digital model, the field transportability and the capability to perform long-term out-of-lab measurements have been demonstrated. On the downside, the impact of the external temperature on the data acquisition should be balanced out to get a steady acquisition and monitor the temporal evolution of the muon flux.

In conclusion, the successful proof-of-concept trial allows to validate the MUST^2 camera for transmission muography purposes.

Acknowledgments

The current work is the result of countless hours of dedication, not only mine but also from several people from different fields and backgrounds.

I would like to thank in the first place to my thesis supervisor, Stéphane Gaffet. Founding member of the project, his remarkable commitment, steady guidance and leadership has played a major role in every stage. I cannot express my gratitude enough, especially given all the adverse circumstances during the thesis, for devoting his time and energy to guide me during all these years.

I am particularly grateful to IRIS Instruments as well. For me it has been a privilege to join a company with such intense R&D spirit. This period has enormously broadened my knowledge in instrumentation thanks to the large spectrum expertise of its employees. It would have been impossible for me to accomplish this work without their advice.

I wish to thank the staff of the LSBB: Alain, Daniel and Jean-Baptiste (but also Michel, Claire, Naïs and Sébastien). You have been privileged witnesses of my professional development during the last lustrum. Thanks for your daily dose of encouragement and constant support. I would also extend my thanks to the BRGM and Géoazur, institutions that made possible my participation on the project.

A very special gratitude goes to the members of my thesis committee Elisabeth Pozzo di Borgo and Gilles Micolau. Thanks for kindly watching over me and for all the assistance provided.

Thanks as well to the jury members, with special mention for the reviewers, for the effort put in assessing this work and contribute to enhance its quality.

I want to thank Tom Girard for his altruism reviewing this work.

The author thanks as well the priceless assistance of the CERN's PCB workshop and the RD51 collaboration for the development of micro-pattern gas detectors technologies for allowing us to work in their facilities with their equipment. Special thanks to R. de Oliveira, O. Pizziruso, and E. Oliveri for their commitment and dedication.

I shall not forget how the outstanding contributions made by my predecessor Fanny Hivert, the passionate muographer Kevin Jourde and my "partner in crime" Thomas Serre have helped the project to move forward.

I would like to acknowledge the *Mairie* of Saint-Saturnin-les-Apt for the generous response to our project. It gave me access to the city archives and to the dam valve house with full autonomy. Its contribution not only allowed the access to a very interesting study site, but also helped improving the experimental conditions.

Me gustaría dedicar también el presente trabajo a mis padres. Su enorme sacrificio ha servido para darme la educación que me ha traído hasta aquí.

Finalement, la dédicace la plus personnelle est pour toi ; Aurélie. La thèse a été un trou noir de temps et d'énergie auquel j'ai survécu en partie grâce à tes soins, ta patience et ta gentillesse. Il n'y a pas de mots pour exprimer ma gratitude pour avoir mis de côté autant de projets de vie pendant ces trois ans et m'avoir soutenu inconditionnellement.

This research was performed within the framework of a CIFRE grant (ANRT contract #2015/0325) and supported by the European Fund for Regional Development (FEDER). Part of the materials used during the present work have been financed by the MAIF foundation.

Last but not least, **this work is dedicated to you**: the reader. Because without you, this would be meaningless. I hope that you find in here what you are looking for.

Index

List of acronyms

Acronym	Description
AGN	Active Galactic Nucleus
AMU	Aix-Marseille University
ASIC	Application-Specific Integrated Circuit
BNC	Bayonet Neill–Concelman connector
BRGM	Frech Geological Survey
CEA	French Alternative Energies and Atomic Energy Commission
CERN	European Organization for Nuclear Research
CIFRE	Industrial Convention of Formation trough Research
CNRS	French National Center for Scientific Research
CORSIKA	COsmic Ray SImulations for KAscade
CPPM	Center for Particle Physics of Marseille
CSA	Charge Sensitive Amplifier
DEM	Digital Elevation Model
Dream	Dead-time less REadout ASIC for Micromegas
ERI	University of Tokyo's Earthquake Research Institute
FEU	Front End Unit
GC	Gas Conditioner
GEM	Gas Electron Multiplier
HIP	Heritage Innovation Preservation institute
InGrid	Integrated grid
INSU	French National Institute of Universe Science
Irfu	Institute of Research into the Fundamental laws of Universe

LCTPC	Time Projection Chamber for a future Linear Collider
LEM	Large Electron Multiplier
LSBB	Low Background Noise Laboratory of Rustrel
masl	Meters Above Sea Level
MC	Monte Carlo
MHSP	Micro Hole and Strip Plate
Micromegas	MICRO MEsh GAseous Structure
MIP	Minimum Ionising Particle
MPGD	Micro-Pattern Gas Detectors
MSGC	Microstrip Gas Counter
MTRA	Muon Trajectory Reconstruction Algorithm
MUSIC	MUon SImulation Code
MUST²	MUon Survey Tomography based on Micromegas detectors for Unreachable Sites Technology
mwe	Meters Water Equivalent
MWPC	Multi Wire Proportional Chamber
NIM	Nuclear Instrumentation Module
NTP	Normal Temperature and Pressure (20ºC, 1 atm)
PCB	Printed Circuit Board
PMT	Photomultiplier
QS	Quantum satis, Latin term meaning the amount which is enough
RD51	CERN's collaboration for the development of MPGD technologies
RETGEM	Resistive Thick GEM
RMS	Root Mean Square

RPC	Resistive Plate Chambers
SATT	Society for the Acceleration of the Technology Transfer
SHV	Safe high voltage connector
SPS	Super Proton Synchrotron
SRS	Scalable Readout System
T2DM2	Temporal Tomography of Density by the Measurement of Muons
THGEM	Thick GEM
TPC	Time Projection Chambers
TTL	Transistor-Transistor logic
UAPV	Univerty of Avignon and Pays of Vaucluse
UMS	Mixed Unity of Sercive
UNS	Nice Sophia-Antipolis University
µ-pic	Micro Pixel Chamber

Notation

Symbol	Units	Description
A	$\in \mathbb{N}$	Atomic mass number or nucleon number.
AN	Unitless	Atmospheric nuclei.
c	$^{m}/_{s}$	The speed of light in vacuum (299792458 $^{m}/_{s}$).
E	GeV	Incident particle kinetic energy.
$\boldsymbol{E_{\mu}}$	GeV	Muon rest energy (0.106GeV)
$\boldsymbol{E_{\mu c}}$	GeV	Critical energy of muons in a medium.
$\boldsymbol{E_{\mu m}}$	GeV	Minimum energy required for a muon to cross a certain opacity.
m_e	$^{MeV}/_{c^2}$	Electron rest mass, (~0,511 $^{MeV}/_{c^2}$).
$\boldsymbol{W(E,\theta)}$	$\in \mathbb{R} : 0 \leq W \leq 1$	Survival probability
Z	$\in \mathbb{N}$	Atomic number or proton number.
$\boldsymbol{\gamma}$	$\in \mathbb{R}$	Energy spectrum power index.
$\boldsymbol{\gamma_{muon}}$	$\in \mathbb{R}$	Lorentz factor to calculate the time dilatation of a muon.
$\boldsymbol{\epsilon}$	GeV	Critical energy, energy at which the collision loss rate equals the bremsstrahlung rate.
$\boldsymbol{\theta}$	rad or deg	Zenithal angle, where 0 rad represents the zenith and $^{\pi}/_{2}$ rad represents the horizontal muons.
$\boldsymbol{\theta^*}$	rad or deg	Corrected zenithal angle, which considers the Earth's curvature.
$\boldsymbol{\rho}$	$^{g}/_{cm^3}$	The density, a.k.a. volumetric mass density of a substance is its mass per unit of volume.

$\boldsymbol{\varrho}$	mwe or $^{g}/_{cm^2}$	Matter opacity, defined as the matter's density times the path's length of the particle inside the medium.
$\boldsymbol{\varphi}$	rad or deg	Azimuthal angle, $\{\varphi \in \mathbb{R} : -\pi \leq \varphi \leq \pi\}$ where 0 rad represents the direction of positive Y tracks.
$\boldsymbol{\Phi_P}$	$\frac{1}{cm^2 \cdot sr \cdot s}$	Flux of primary cosmic-ray particles.
$\boldsymbol{\Phi_\mu(E_\mu, \theta)}$	$\frac{muons}{cm^2 \cdot s \cdot sr \cdot GeV}$	Differential muon flux for a given particle energy and incidental angle.
$\boldsymbol{\phi(\theta)}$	$\frac{muons}{cm^2 \cdot sr \cdot s}$	Integrated flux over energy.
Ω	sr	Solid angle visible for the detector.

List of tables

List of figures

Chapter 1. Objectives and project introduction.

1.1. Objectives

The main objective of the current doctoral thesis is to develop a new non-destructive system using muons for in-situ imaging and monitoring the density of large volumes of matter. This new geophysical tool is meant to monitor civil engineering works or geological and hydrogeological volumes.

The present work aims at enabling the market release of a new high-technology instrument in the framework of natural hazard and risk management. To do so, it is necessary to take care of the following scientific and technical issues:

- Ensure the academic/industrial know-how transfer.
- The realization of a sturdy, reliable, portable and ergonomic detector for ground and underground operation.
- The fine characterization of the detector, (for instance: spatial and temporal resolution, efficiency, gain, etc.) and calibration protocol.
- Develop of a user interface and data analysis package.
- The detector's deployment and tune-up in the case study sites to monitor: tunnel, mine, cliff or landslide instable zones.

The multidisciplinary nature of the present work, that combines particle physics, geophysics, instrumentation and industrial design among others, makes impossible to address exhaustively all the topics covered. The author aims at providing a document that allows a skilled person to understand:

- The origin and interest of cosmic muons for tomographic purposes.
- The physical processes that enable the muon detection with the presented technology.
- The considerations and design choices towards the manufacture and industrialization of the technology.
- The techniques and software developed to analyze the data acquired with the aim of characterize the muon flux trough the detector.
- The characterization process of the technology's performance.
- The results of a real case field test to validate the detector's transportability, long time data acquisition capability and dynamic imaging potential.

1.2. Project introduction

1.2.1 Context of the project

The project T2DM2 (acronym for Temporal Tomography of Density by the Measurement of Muons) was born in 2008, when Stéphane Gaffet and Pierre Salin developed the idea of using a muon detector to help to elucidate the dynamics of the water transfer process though the non-saturated zone of the Albion plateau (South–East of France). The entire massif is characterized by an important hydrogeological system, with several karstic structures within a thick unsaturated area overlying a saturated zone linked to the 1.100 km^2 broad water reservoir of Fontaine de Vaucluse, France.

The privileged position of the Low Background Noise Underground Research Laboratory (LSBB URL), as seen in Figure 1.1, allows access to the non-saturated zone of the aquifer at different depths, enabling the deployment of muon cameras to image the spatial and temporal dynamics fluid flow across the unsaturated zone of the reservoir.

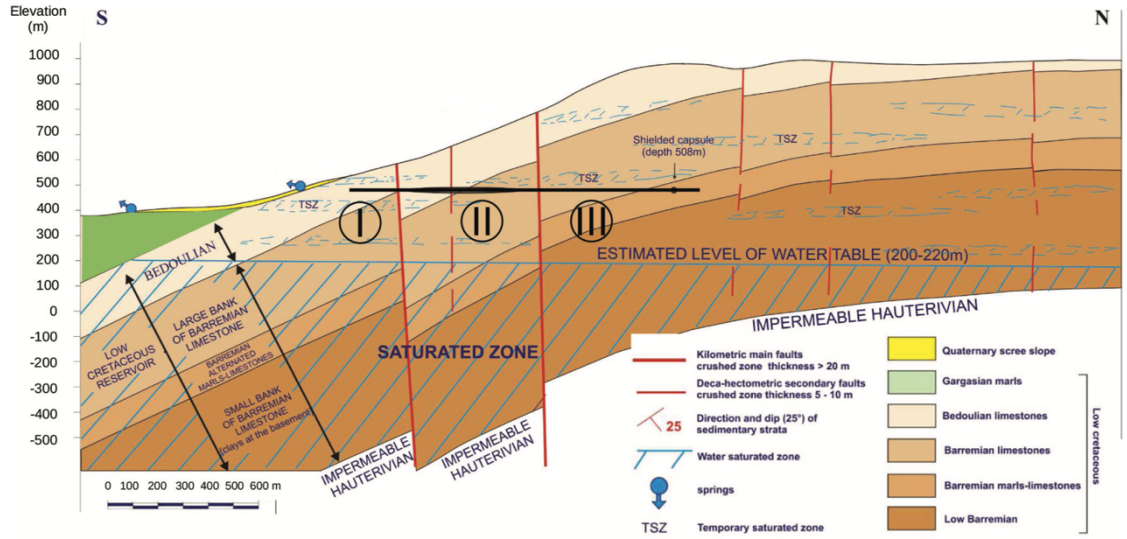

Figure 1. 1 Conceptual south-north cross-section of the southern flank of Albion plateau. The black horizontal line represents the vertical plane projection layout of the LSBB's galleries [Sénéchal, 2013][i] .

During the period of 2008-2013 the project was focused on verifying the feasibility of the concept by testing several prototypes based on combinations of different Time Projection Chambers (TPC) read by Micro-Pattern Gaseous Detectors (MPGD). Ever since, the project members have actively participated in CERN[1]'s RD51 Collaboration, whose objective is the development and out-of-CERN valorization of MPGD technologies. The mission of the RD51 is to facilitate the development of advanced gas-avalanche detector technologies and associated electronic-readout systems, for applications in basic and applied research. Because of this collaboration the project has access to the Micromegas (MICRO MEsh GAseous Structure) detector and the Scalable Readout System (SRS) to instrument it.

[1] European Organization for Nuclear Research

In parallel, the incorporation in 2012 of Fanny Hivert was the result of a collaboration between the CNRS[2] and the MAIF foundation. Her thesis, entitled: "Characterization of the rock density and its spatial and temporal variations using muons: application to the Low Noise Underground Laboratory (LSBB)" was defended in 2015. In it, she used numerical simulations of muon flux to estimate the acquisition conditions required to detect a certain density variation for a given depth, with a special interest to the scattering of muons in relation to the density of material. The combination between her model and field measurements performed with liquid scintillators provided by the CPPM[3] (ANTARES project), led to an estimation of the average density of the rocks located above the LSBB in good agreement with the expected value.

In 2013 the particle physicist co-leader of the project, Pierre Salin, retired and Stephan Gaffet, geophysicist assumed leadership of T2DM2. The LSBB hired under its own resources the author with the aim to construct a new detector based on the prototypes and capable of withstanding the field measurements in order to validate the proof of concept. This innovative muon camera, named MUST[2] (MUon Survey Tomography based on Micromegas detectors for Unreachable Sites Technology), is based on a thin TPC read by a resistive bulk-Micromegas. The resources necessary to construct 5 additional detectors were provided by a combination of LSBB's own resources and European Regional Development Fund (ERDF).

Later in 2014, Thomas Serre started a 1-year post-doctoral fellow to develop the necessary software for the particle trajectory reconstruction. His participation was possible thanks to the LSBB and INSU[4] funds.

At this point and given the potential industrial interest of the technology, the LSBB, after consultation with the Society for the Acceleration of the Technology Transfer South-East(SATT), decided to start a patent process.

In 2015, the French Geological Survey (BRGM) and IRIS Instruments joined the project and the partnership resulted in the current doctoral work. The author obtained a CIFRE[5] fellowship[6] hosted by IRIS Instruments and with the support of the French National Association of Technologic Research (ANRT). The academic institution in charge of the thesis is the *École Doctorale Sciences Fondamentales et Apliquées* of the *Université Nice-Sophia Antipolis*.

The T2DM2 project interacts periodically with the worldwide muon tomography network and participates in the annual meetings of the Muographers community. The partners of the collaboration are among the promoters of the Marie Skłodowska-Curie Innovative Training Network proposals to create a European Muography Network submitted in 2016 and in 2017 for a second round.

---

[2] French National Center for Scientific Research
[3] Particle Physique Center of Marseille
[4] French National Institute of Universe Science
[5] French acronym for Industrial Convention of Formation trough Research
[6] Reference CIFRE 2015/0325

1.2.2 The members of the collaboration

-BRGM

The BRGM (Bureau de Recherches Géologiques et Minières) is France's reference public institution for Earth Sciences applications in the management of surface and subsurface resources and risks. This organization was created in 1959 and operates as a public industrial and commercial institution, reporting to the Ministry of Higher Education, Research and Innovation, the Ministry for the Ecological and Inclusive Transition, and the Ministry of Economy and Finance.

Figure 1.2 highlights the foundational objectives of the BRGM.

Figure 1. 2 Key roles of the BRGM.

During the year 2017 a memorandum of understanding was signed between the BRGM and the University of Tokyo's Earthquake Research Institute (ERI) to enhance their scientific cooperation towards the reduction and manage disaster risks through the muography imaging technique.

The tasks of the BRGM within the collaboration are:

- To suggest and provide access to suitable study sites in order to address specific challenges for the development of the technology due to its knowledge of the geological environment and the mining sites.

- To consult during the development of a new tool for muon tomography, due to its vocation of developing new techniques and methodologies for better understanding the subsurface.

- To offer guidance on natural risk, since one of its main goals it's to "deliver the necessary tools for the management of soils, subsoils and their resources, risk prevention and policy responses to climate change".

-IRIS Instruments

IRIS Instruments, established in 1990 in Orléans (France), is a private company jointly owned by BRGM (51% holding) and the Japanese geotechnology group OYO (49%). It specializes in geophysical instrumentation for subsurface explorations and monitoring and designs. It produces and markets throughout the world geophysics equipment for environmental applications, water prospecting, geotechnologies and mineral prospecting (see Figure 1.3).

IRIS Instruments R&D's department represents more than 30% of the company activity. This department is dedicated not only to improving their exiting catalogue, but also to help provide new tools for geophysicist.

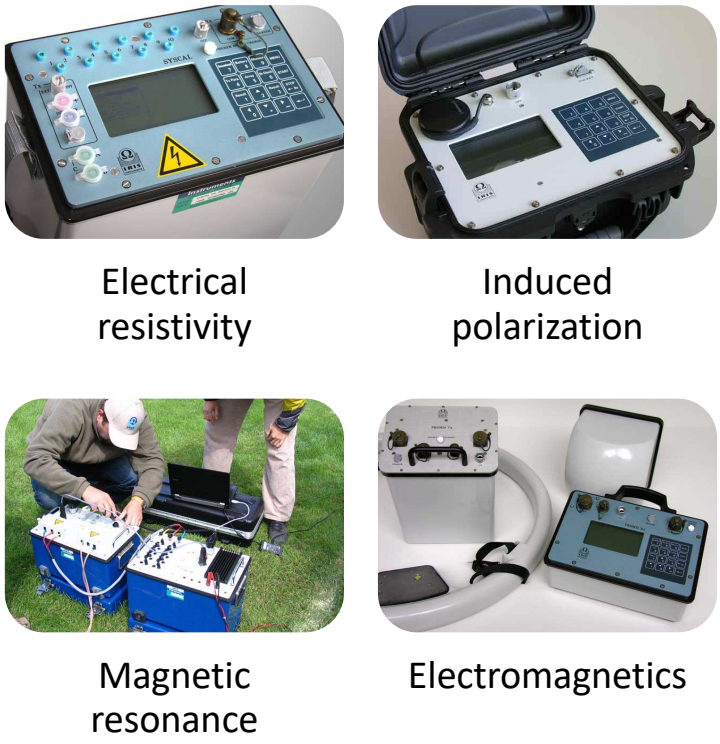

Figure 1. 3 Most well-known technologies commercialized by IRIS Instruments.

The role of IRIS Instruments as a partner is:

-To build bridges between the different actors working in the muon tomography field in order to accelerate the progress towards a reliable muography tool for geophysics.

-To advise during the process of converting a laboratory operational prototype into a sturdy product, capable of being transported and operated under harsh field conditions in a non-controlled environment.

-To lead the industrialization process of the technology given its experience in the development of geophysical tools from their conception to their commercialization worldwide.

-LSBB

The Low Background Noise Underground Research Laboratory (LSBB) of Rustrel (France) is a ground- and underground-based facility for interdisciplinary research, development and innovation. From an administrative stand point, since 2012 the LSBB is a *Unité Mixte de Service*, UMS3538, funded and led by four scientific trusteeships: (i) Aix-Marseille University, (ii) CNRS, (iii) University of Avignon and (iv) University of Nice. The trusteeship council agreed to delegate the management of the LSBB Underground Research Laboratory to the CNRS Institution represented by Younis Hermes until March 2018, and Ghislaine Gibello since April 2018, CNRS Regional Delegates for the Provence and Corsica district, acting on their behalf.

This unique laboratory is the outcome of the decommissioning in 1997 of a former launch control system of nuclear missiles. Its exceptionally low seismic and electromagnetic background noise makes it possible to carry out highly sensitive activities in a landscape far away from major sources of anthropogenic disturbances.

The LSBB URL fosters the cross-fertilization between solid Earth, Earth-atmosphere, astrophysics, particle physics, geology, geo-mechanics, electromagnetic environment, physics, rock engineering, metrology, electronics, the Cold War contemporary history and life sciences at European and international scales, and boosts the know-how transfer in diverse areas of metrology. The LSBB is based on the strength and diversity of scientific and industrial expertises available in Provence-Alpes-Côte-d'Azur, and on the openness of the LSBB platform to regional, European and international programs, taking advantages of:

• A fully equipped underground access (ranging up to 500 m depth along ~4.000 m of galleries) below ~500.000 m^2 of land within a low anthropogenic background area and within the very thick and sensitive unsaturated zone of the main European geological underground water reservoir solely filled by rainwater. It allows basic and applied researches linked notably with regard to the development of new high-sensitive instrumentation in the frame of geophysics, astrophysics, particle physics and life science.

• The presence of multi-physics experiments and instrumentations still running at LSBB that allows the emergence of new skills for metrology, instrumentation and methodology for the observation and experimentation.

The assets of the LSBB with regard to the project are the following:

- As the original promoter of the project, it is the institution that values the knowledge acquired during the former years.

- Its multidisciplinary ambience fosters the exchange with diverse disciplines, leading to original approaches to overcome the technological challenges and development of innovative applications.

- The multiple experiences carried out during over 20 years provide an exceptionally well-known operational framework in terms of geology and hydrogeology.

- It gives access to the necessary facilities for the construction of the detectors; including a clean room for the detector assembly.

- The layout of the LSBB galleries offers an easy access to an underground environment with low background noise conditions. In addition, electricity and a network connection are available in most of the facilities, easing the material deployment and enabling remote operation.

- Its surface facilities are extremely helpful for the open-sky measurements necessary for the technology validation.

1.3. References

[i] Sénéchal, G., Rousset, D. and Gaffet, S. (2013) Ground-penetrating radar investigation inside a karstified limestone reservoir. Near Surface Geophysics. Vol 11, No 3, 283 - 291

Chapter 2. Muons.

Chapter 2 abstract

Muon tomography (or muography) covers a set of techniques based on the measurement of cosmic ray muons to generate images of the material they traverse based on the material's physical properties. Primary cosmic rays from outer space hit the upper atmosphere and naturally produce a shower of secondary particles, including muons.

Cosmic muons, as a result of their high energy and lack of strong interaction, are able to penetrate up to several hundreds of meters underground. The muon flux decreases progressively according to the medium opacity, setting the basis for transmission muography (detailed in Chapter 3).

To quantify the flux decrease for imaging purposes, it is necessary to get a precise muon flux characterization at ground level as a reference input. The described empirical model allows analysis of the muon flux transmitted across the matter.

On the other hand, matter behaves as an energy filter for muons. The muons' energy spectrum evolves according to the opacity of the medium. The survival probability permits estimation of the muon flux received by the detector for and compare to the muon flux measure (e.g. critical zone survey, dam monitoring, etc.).

2.1. Introduction

What are muons? Where do they come from? What makes muons particularly suitable for imaging purposes? These are often the first questions that outsiders address when facing muography.

This chapter provides an essential introduction with a walk through the discovery of cosmic rays and the evolution of awareness about this phenomenon.

Thanks to the contribution of a large number of scientists, the behavior and components of cosmic rays have been progressively unraveled during the last 150 years. This chapter delves into the different factors that influence the development of air showers and sheds some light on how they can be modeled. Then, it will focus more specifically on the properties of muons and what makes them suitable for imaging large volumes of matter.

The chapter also addresses the characterization of the muon flux both at the surface and underground as a vector of information for muon tomography.

2.2. Cosmic Rays

2.2.1 Discovery of radiation and cosmic rays

The first sign of the existence of cosmic rays was observed in the end of the 18th century after the French physicist Charles Augustin de Coulomb made three reports on electricity and magnetism to France's Royal Academy of Sciences. In the third report, he described an experiment with a torsion balance designed by himself (see Figure 2.1), which showed that the device would spontaneously discharge due to the action of the air instead of defective insulation [Coulomb, 1785][i].

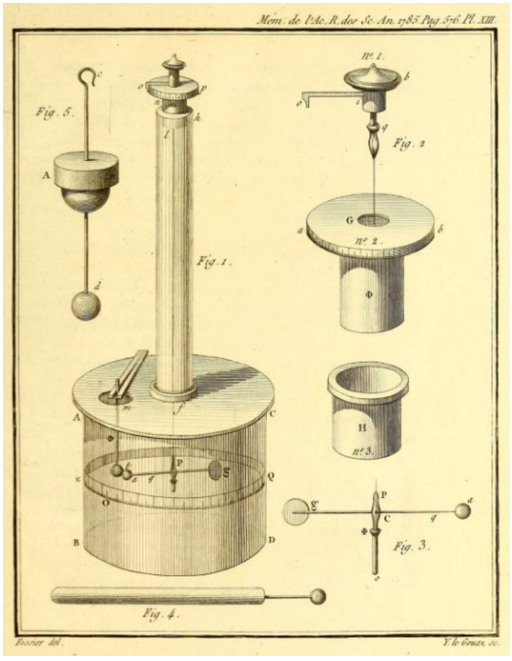

Figure 2. 1 Torsion balance electrometer. Figure from [Coulomb, 1785].

In 1850, Carlo Matteucci and later, in 1879, William Crookes showed that the rate of spontaneous discharge decreased at lower pressures. The search for an explanation for the nature of this spontaneous discharge opened the door to the discovery of radiation and subsequently cosmic rays.

The late 19th century was a fruitful period for a better understanding of subatomic physics. Wilhem Röntgen discovered X-rays in 1895 while investigating cathode rays. He realized that they could have medical applications and took an image of his wife's hand, as seen in Figure 2.2 (Left) [Röntgen, 1895] [ii]. A year later, Henri Becquerel discovered radioactivity when he placed uranium salts on top of a photographic plate enveloped in black paper. The salts caused a blackening of the plate despite the paper in between (see Figure 2.2 (Right) [Becquerel 1903] [iii]). Becquerel concluded that invisible radiation that could pass through paper was causing the plate to react.

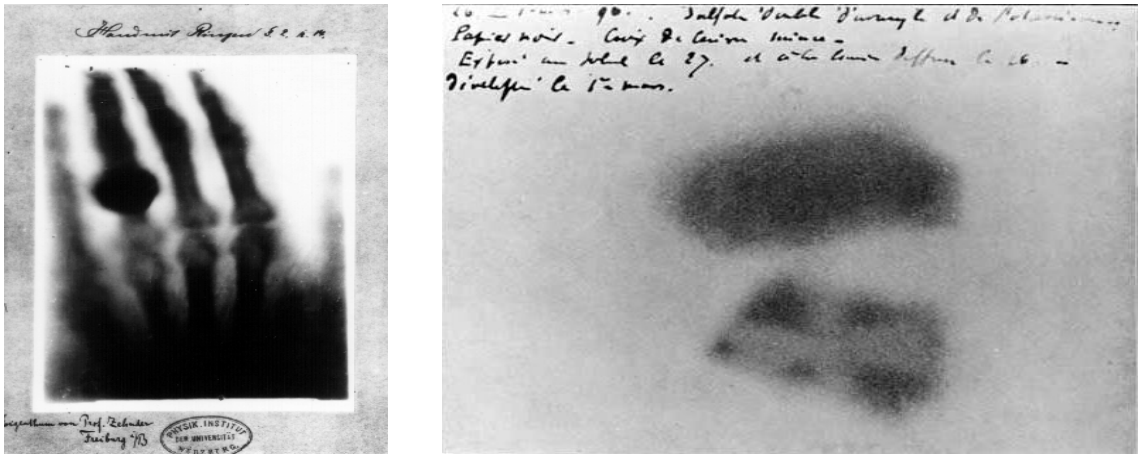

Figure 2. 2 (Left) Hand with Rings: print of first medical X-ray made by W. Röntgen. (Right) Image of Becquerel's photographic plate. The shaded area results from the exposure to radiation from a uranium salt.

In 1897, Thomson showed that cathode rays were composed of negatively charged particles, smaller than atoms. This marks the discovery of the electron, the first known elementary particle. At the same time, Marie Curie [Curie, 1898][iv] realized that uranium is not the only element capable of emitting radiation and discovered a new property of matter, radioactivity.

Radioactivity soon became the subject of intense investigation and by 1899 Ernest Rutherford found two associated forms of radiation, which he called α (protons)[1] and β (electrons). In 1900, Philippe Villard discovered a third, penetrating radiation, which Rutherford named γ -rays.

The experiments carried out by Julius Elster and Hans Geitel on shielded electroscopes lead to the conclusion that the different types of radiation have a penetration power proportional to their energy and even suggested that ionization of air could be caused by penetrating extra-terrestrial radiation.

In the dawn of the 20th century, ambient radiation is a known phenomenon, but the general belief was that it had a telluric origin.

[1] It will be proved later that alpha particles correspond to helium-4 nuclei.

In 1901 Charles Wilson tests if the ionizing radiation has an extra-terrestrial origin. He took measurements of natural radioactivity inside an old railway tunnel expecting attenuation related to the underground conditions. However, due to the observational error, he saw no reduction compared to outside on the surface [Wilson, 1901][v]. The scientific community largely dismissed the theory.

It is in 1909 when Theodor Wulf designed and built a more performant and more transportable electrometer, shown in Figure 2.3. After measuring the ionization of the air in various locations, he concluded that his results were consistent with the hypothesis that the penetrating radiation was caused by radioactive substances in the upper layers of the Earth's crust. Thus, if the radioactivity was coming from the Earth, it should decrease with height.

Figure 2. 3 Wulf's original electroscope.

To validate his hypothesis he designed an experiment, conducted at the Eiffel tower, where he compared the values at the base against those from the top [Wulf, 1910][vi]. Unfortunately, the measurements, despite being correct, could not prove his hypothesis due to the disagreement with an analogue experiment carried out in Valkenbourg [Paul et Robert-Esil, 2009][vii].

Only in 1912, and thanks to two independent experiments, was the extra-terrestrial origin of cosmic rays proven [De Angelis, 2013][viii]. On the one side, the physicist Domenico Pacini (figure 2.4 (Left)) performed a pioneer experiment of underwater measurement of radiation. He observed the radiation strength to decrease 20% when going from the surface to 3 meters underwater (both in a lake and in a sea). He also found a reduction of 30% in the measurements 300m away from the shore compared to measurements on land [Pacini, 1912][ix]. Their results suggested that a meaningful portion of the radiation must be independent of emission from the Earth's crust.

Figure 2. 4 (Left) Domenico Pacini making a measurement in 1910. (Right) V. Hess in a balloon used for his measurements.

On the other side, Viktor Hess (Figure 2.4 (Right)) started in 1911 a new campaign to assess the effect of height in the measurements. But unlike Wulf, he employed balloons to reach grater altitudes. In the measurements performed at an altitude of around 1.100 meters, did not find an essential change in the amount of radiation compared with ground level. Afterwards, in 1912, Hess reached 5.300 meters during a near-total eclipse of the Sun. With the moon blocking much of the Sun's visible radiation, Hess still measured rising radiation at rising altitudes. He stated that: "The results of my observation are best explained by the assumption that a radiation of very great penetrating power enters our atmosphere from above" [Hess, 1912][x].

This event marks the discovery of cosmic rays.

2.2.2 Unraveling the cosmic rays

The cloud chamber, invented by Charles Wilson in 1911 [Wilson, 1911][xi], is an important breakthrough in the history of particle physics and cosmic rays. This device, originally developed to study atmospheric phenomena, made it possible to record the tracks of the particles, visible as trails of droplets, and to photography them. During the first half of the 20th century, experiments that looked at cosmic rays passing through cloud chambers revealed the existence of several fundamental particles.

Nevertheless, after multiple observations of cosmic rays, its nature remained still undetermined. The study of Rutherford on atomic structure shed some light on this issue [Rutherford, 1911][xii]. In his analysis of the wide-angle scattering of α-particles from gold, he concluded that the results demonstrated that the positive charge of the atom was concentrated in a little, central region, the nucleus. A few years later, in 1919, he proclaimed the discovery of the proton as a primary constituent of the nucleus.

During the late twenties, the nature of cosmic rays became a subject of discussion. Whereas Robert Millikan was convinced that the primary cosmic rays were photons released in the synthesis of heavier elements from hydrogen in space and coined the term “cosmic rays”, Arthur Compton stated that the cosmic particles were charged.

Technical developments ran parallel to this fierce debate. In 1929 Hans Geiger and Walter Müller introduced the Geiger-Müller detector [Geiger-Müller, 1929][xiii], which represented a big step forward for the field. The detector consisted of a gas-filled tube capable of registering individual charged particles. A combination of detectors working in coincidence mode allows determination of the path of a cosmic ray.

This technique inspired Bruno Rossi to conceive the coincidence detector shown in Figure 2.5. It confirmed the results that most of the detected cosmic rays were charged particles and had too much energy to be created from gamma rays emitted in the synthesis of elements, dismissing Millikan’s proposition [Rossi, 1930][xiv]. Later, in 1932, he found that 60% of the cosmic rays could pass through a 25-cm piece of lead, could also traverse 1 m of lead. Rossi confirmed that the cosmic ray flux contains a soft component easily absorbed in a few millimeters of lead, and a hard component of charged particles.

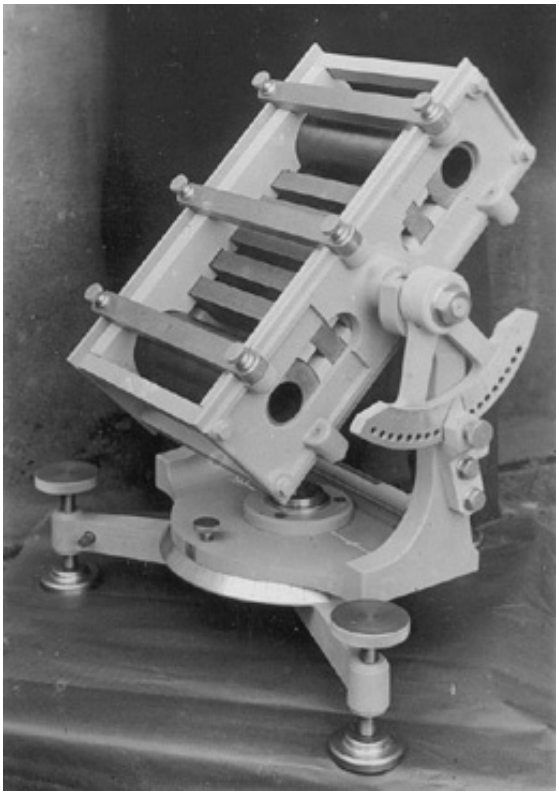

Figure 2. 5 Rossi's Cosmic ray telescope, consisting of two coincidence counters mounted on pivots so measurements could be made in any direction.

Around the same time Jacob Clay, during his trip between Java and the Netherlands, observed a latitude effect in his measurements [Clay, 1927][xv]. He witnessed a drop of cosmic rays' intensity near the equator. This effect follows from the dipole behavior of the Earth's magnetic field, which deflects the charged particles coming from outer space and expels the ones below a certain energy threshold. This effect reaches its limit near the geomagnetic equator and decreases progressively towards the poles. To broaden the scope of the experiment, Arthur Compton led a worldwide measurement campaign to assess the geographic effect. These measurements, shown in Figure 2.6, confirmed the latitude effect that Clay had noticed previously, and hence, provided another proof that cosmic rays are charged particles [Crozon, 2005][xvi].

Another effect was predicted by Bruno Rossi, an asymmetry related to the sign of the charge of cosmic rays. The Earth's magnetic field bends incoming charged particle showers so that if they are more negative, more come from the east than from the west and vice-versa, it is the so-called "east-west effect".

Three independent experiments: [Johnson, 1933][xvii], [Alvarez, 1933][xviii] and [Rossi, 1934a][xix]. found that the intensity is, in fact, greater from the west, proving that most primary cosmic rays are positive. While testing the instrumentation for his East-West experiment, Rossi, discovered the occurrence of extensive showers of particles produced by interactions of cosmic rays in the atmosphere, a phenomenon subsequently studied by Pierre Auger, whose name became associated with this discovery.

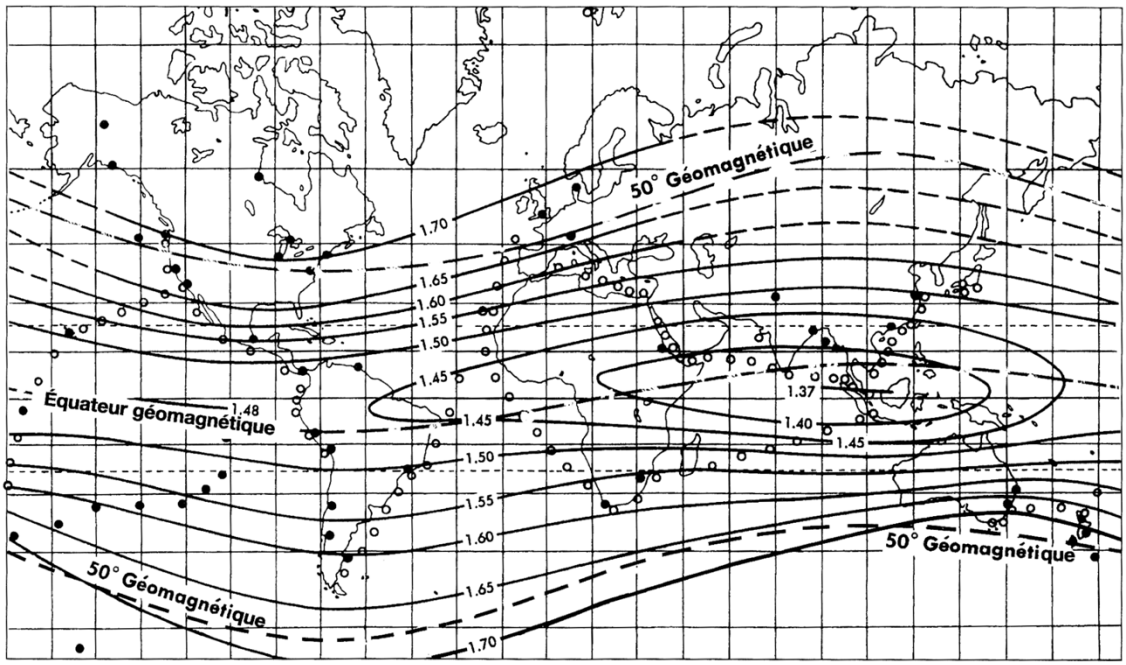

Figure 2. 6 Map with isocosmic lines, the values indicate the number of ions per cm³ and second. The dots represent the measurement stations at sea level.

2.2.3 Cosmic-ray air shower

Rossi noted coincidences between several counters placed in a horizontal plane, far in excess of chance coincidences. He noted in one of his papers: "... it seems that once in a while the recording equipment is struck by very extensive showers of particles, which causes coincidences between the counters, even placed at large distances from one another" [Rossi, 1934b][xx]. This was the first proof of the production of showers of secondary particles.

In 1937 Pierre Auger, unaware of Rossi's former report, detected the same phenomenon while measuring with two Geiger-Müller detectors located many meters apart in coincidence mode to reduce the background noise. The coincidence rate obtained was higher than the expected accidental rate and he started a systematic investigation of the showers. He deployed detectors in Paris, at the Pic du Midi and in Jungfraujoch observatory, the last ones coupled to a cloud chamber.

As seen in Figure 2.7, while the counting rate drops in going from 10 centimeters to 10 meters, the rate decreases faster at larger distances. Auger had recorded "extensive air showers" and he concluded that the observation seemed best described by the theory of electron-photon cascades, with a particle of very high energy starting a cascade at the top of the atmosphere, which rises to a maximum number of particles way down and fades in the atmosphere. Despite his error, Auger succeed to estimate the total energy of the shower, and thus of the primary particle, nearly 10^{15} eV [Auger, 1939][xxi].

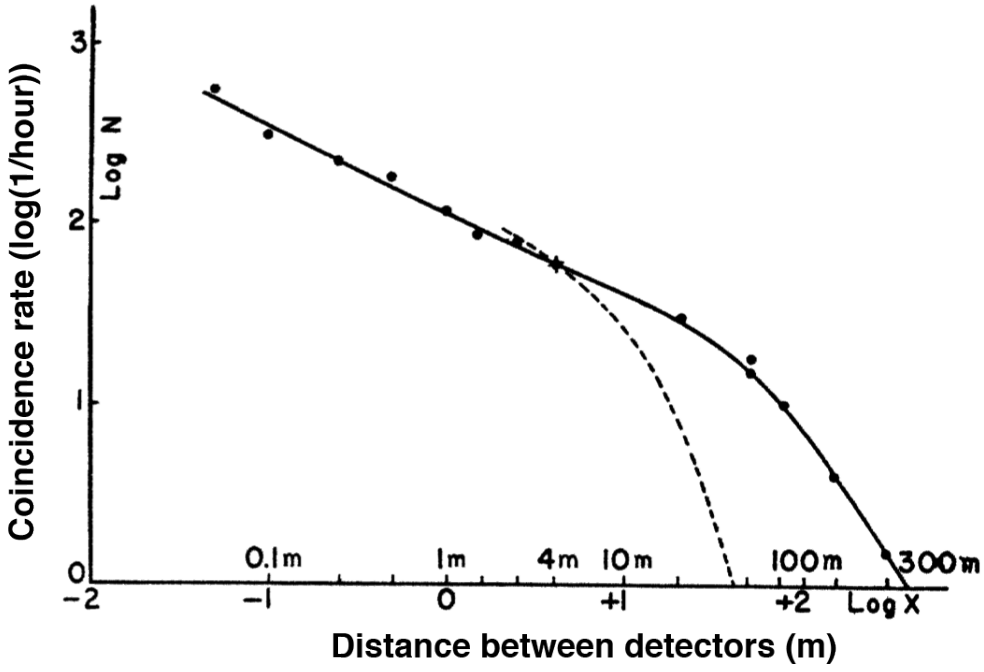

Figure 2. 7 The black dots represent the rate of coincidences per hour of two detectors. The solid line shows a model that fits the experimental data while the dashed line stands for the predicted result considering that the primary particles causing the air shower are electrons or photons.

It was only in 1946 that Auger noticed the different origin of showers. On the one hand the presence of penetrating particles, such as muons, made by Cocconi, Loverdo and Tongiorgi unveil a mesonic component of the air shower. On the other hand, Skobelzyn et al. found coincidences with detectors more than 1 km apart, which could not be explained by the proposed theory [Hillas, 1972][xxii].

2.2.4 Primary particles

The principal components of primary cosmic-ray particles are protons (79%) and helium nucleus (15%) but, as seen in Figure 2.8 from [Gaisser and Satenv, 2008][xxiii], they might also be photons or nucleus from heavier elements.

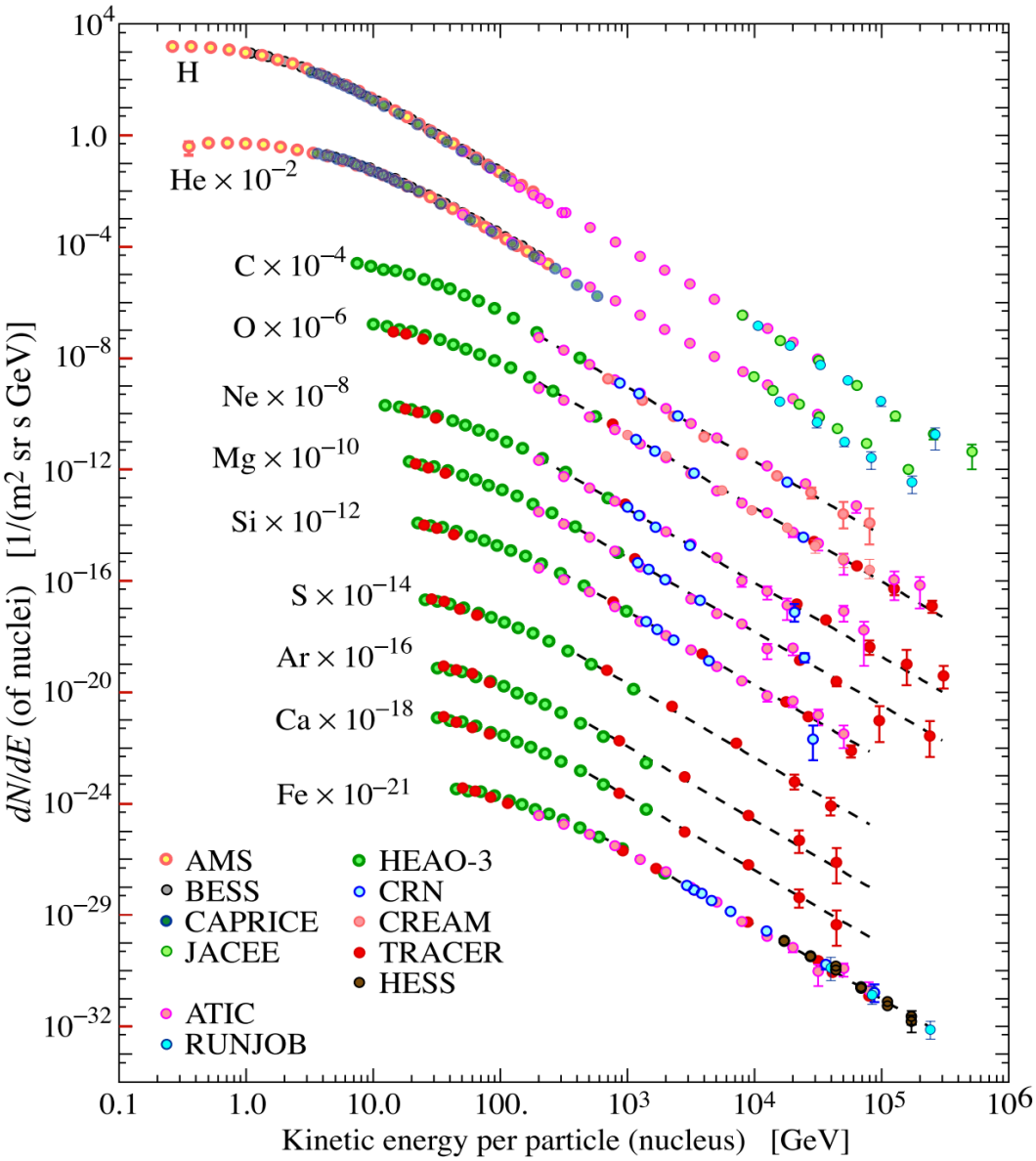

Figure 2. 8 Fluxes by nuclei component of the primary cosmic radiation in particles per energy-per-nucleus are plotted vs energy-per-nucleus.

Big air showers are produced by the interaction of high-energy cosmic primary particles with the atmospheric nuclei, causing a spallation reaction. The large energy spectrum of cosmic primary particles ranges from 10^6 eV to 10^{20} eV as seen in Figure 2.9 from [Grieder, 2001][xxiv].

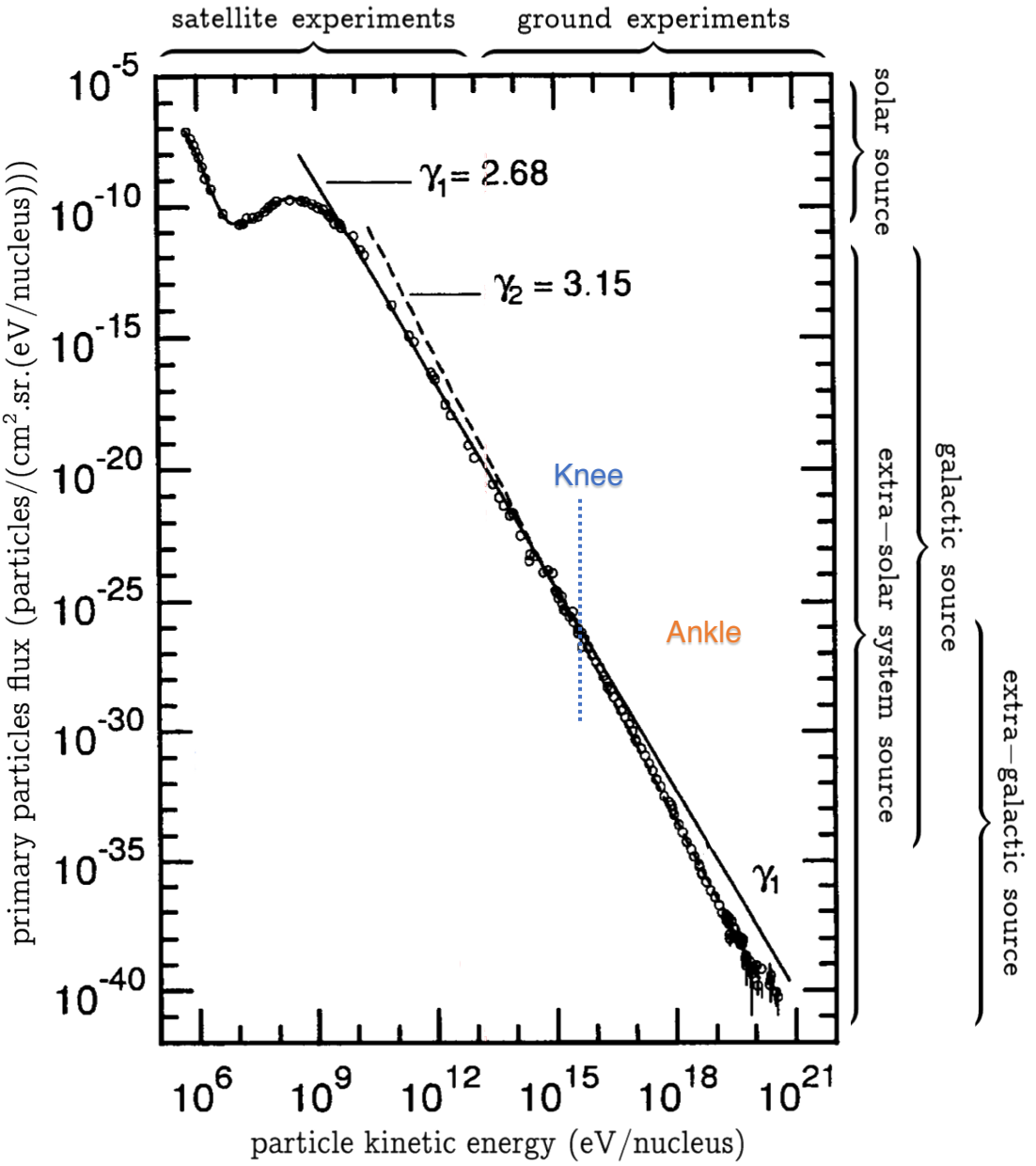

Figure 2. 9 Muon energy spectrum of primary cosmic-ray particles. This figure includes every type of nuclei.

The energy spectrum can be divided into three different zones according to the energy of the primary cosmic-ray particles.

The low-energy particles, up to a few GeV, mainly originate from the Sun and are modulated by the solar winds [Spurio, 2015][xxv]. To measure them, detectors have been installed in the upper layers of the atmosphere in space. The most well-known is the alpha magnetic spectrometer AMS-02 (see Figure

2.10) located on the exterior of the International Space Station [Aguilar, 2013][xxvi]. The size constraint inherent to space equipment is balanced by the high flux of these particles.

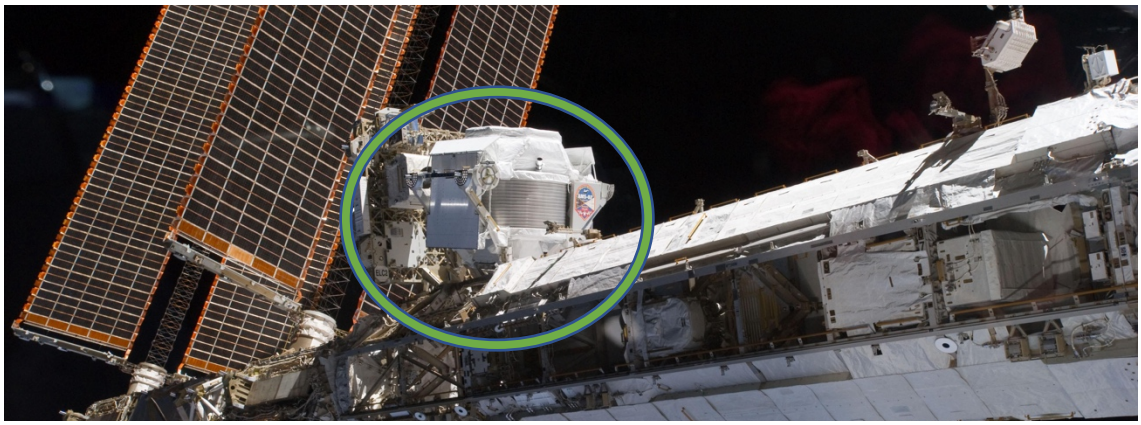

Figure 2. 10 Alpha magnetic spectrometer AMS-02. Picture from NASA-ISS.

The second zone contains the particles with energies ranging from 10 GeV to 10 PeV. They come, in most cases, from outside of the solar system, whose origin is explained by Fermi [Fermi, 1949][xxvii]. He proposed that these particles would be generated by massive stars during the last stellar stage of their lives, one final gigantic explosion called supernova. The protons undergo diffusive shock acceleration and reach high energy when being repeatedly reflected, usually by a magnetic mirror.

As evidenced by Figure 2.9, the flux of primary cosmic-ray particles in this zone, Φ_P, decreases exponentially. The behavior of this flux may be described by the Equation (2.1) proposed by Gaisser [Gaisser, 1990][xxviii].

$$\Phi_P\left(\frac{1}{cm^2 \cdot sr \cdot s}\right) = 1{,}8\left[\frac{GeV}{cm^2 \cdot sr \cdot s}\right] \cdot E[GeV]^{-\gamma} \tag{2.1}$$

Due to the particle heterogeneity, the graph presents two slope discontinuities: one near $5 \cdot 10^{15}$ eV called the “knee” and the other close to 10^{18} eV called the “ankle”. Transitions might be associated with different cosmic sources. The general consensus is that the knee represents the transition from galactic sources (supernova remnants) and extra-galactic sources (AGN, blazars, etc).

Therefore, the value of γ depends on the energy rank considered; for instance, $\gamma \approx 2{,}68$ for the particles with energies ranging from a few keV to 100 TeV and $\gamma \approx 3{,}15$ for higher energies.

The third zone consists of very energetic particles with over 10^{15} eV and their origin remains uncertain to this day. The detection of these events is rare (below 1 particle/(m^2·year)).

2.2.5 Development of an air shower

According to the kind of interacting particle, the air shower has two simultaneous natures: electromagnetic and hadronic [Grieder, 2010][xxix]. The development of an air shower (see Figure 2.11 from [Gosse and Phillips, 2001][xxx]) can be divided into three different components.

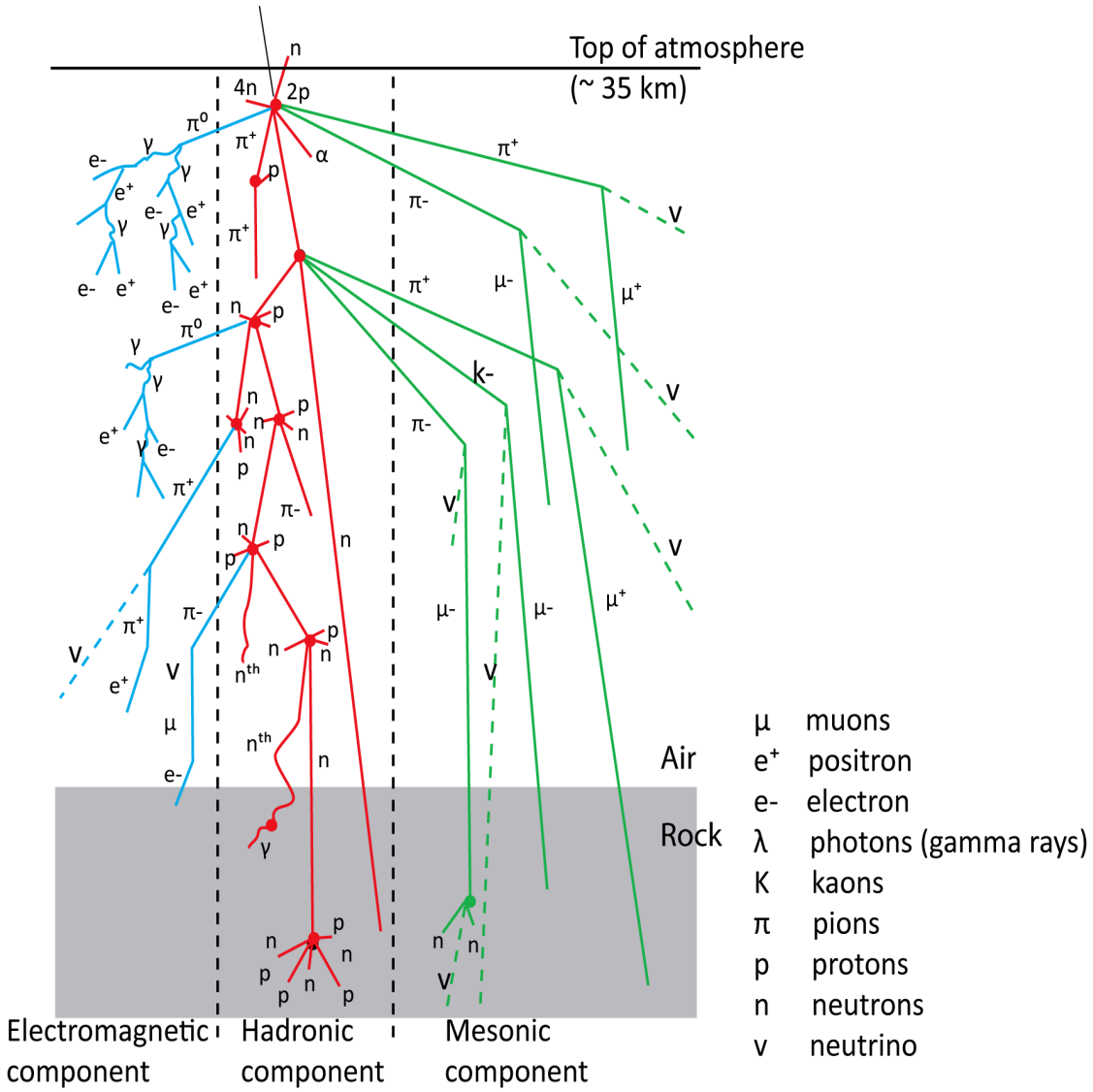

Figure 2. 11 The cosmic ray cascade. Secondary particle production in atmosphere and rock.

1. <u>Hadronic component.</u>

The bulk of air showers are initiated by hadrons. A hadron is a composite particle made up of quarks held together by a strong force. They comprise baryons (e.g. protons and neutrons) and mesons. Due to their high energy and strong interaction, they are highly interacting particles and produce a great number of secondary particles when colliding against the nuclei of the atmospheric atoms (AN), as seen in Equation (2.2).

$$\mathrm{p} + \mathrm{AN} \rightarrow \mathrm{p}, \mathrm{n}, \mathrm{AN}, \pi^0, \pi^{\pm}, K^{\pm} \quad (2.2)$$

where p is a proton, n is a neutron, π are pions and K stands for kaons. The first three products (p, n and AN), allow a sustained chain reaction and increasingly deeper propagation of the air shower into the atmosphere.

The neutral pion π^0 has an extremely short mean lifetime ($8{,}4 \cdot 10^{-14}$ s) and decays into gamma rays (see a more detailed explanation in Point 2, electromagnetic component). Charged pions $\pi^{\pm}$ have a longer half live than the neutral ones (26 ns), and their behavior will be influenced by the atmosphere density. A dense atmosphere will lead to a matter interaction of type (2.2) and create another hadronic air shower. On the contrary, a light atmosphere allows the decay of the pion into a muon μ and a neutrino υ.

$$\pi^{\pm} \rightarrow \mu^{\pm} + \upsilon_{\mu} \, (\overline{\upsilon_{\mu}}) \quad (2.3)$$

The upper layers of the atmosphere favor the decay of pions, but as the atmosphere becomes denser while approaching the ground, the trend reverses and new hadronic showers are created. Therefore, the meteorological variations of the atmosphere may modify in an non-neglectable way the composition of the cosmic ray shower. The kaon interactions are detailed in Point 3, mesonic component.

2. Electromagnetic component.

Neutral pions and other particles, upon decay, transform an important fraction of the hadron's energy into high energy gamma rays. When the, the gamma ray γ is very energetic, it induces a pair production:

$$\gamma + \mathrm{AN} \rightarrow \mathrm{AN} + e^{+} + e^{-} \quad (2.4)$$

These electrons, e (either negative or positive) interact in turn with matter and produce new gamma rays though bremsstrahlung:

$$e^{\pm} + \mathrm{AN} \rightarrow \mathrm{AN} + e^{\pm} + \gamma \quad (2.5)$$

In both cases – Equations (2.4) and (2.5)- γ and e interact with the electric field near the AN. The repetitive pair production and bremsstrahlung process creates an exponential growth of the electromagnetic shower, made of photons and electrons. The passage of the air shower causes air Cherenkov, air fluorescence and radio emission. This process will stop when the resulting photon has an energy close to the electrons rest mass, when the ionization losses will take overtake bremsstrahlung, restraining the growth of the electromagnetic shower.

3. Mesonic component.

The mesonic component consists of kaons and pions that decay into muons, electrons and neutrinos. The decay of pions has been already presented in Equation (2.3). The following reactions show the decay of kaons and muons.

$$K^{\pm} \rightarrow \mu^{\pm} + \upsilon_{\mu}\,(\overline{\upsilon_{\mu}}) \tag{2.7}$$

$$\mu^{\pm} \rightarrow e^{\pm} + \upsilon_{e}(\overline{\upsilon_{e}}) + \overline{\upsilon_{\mu}}\,(\upsilon_{\mu}) \tag{2.8}$$

The large majority of atmospheric muons (~ 90 %) are produced by the pion decay mechanism, while the kaon decay represents less than 1%. The decay of muons in Equation (2.8), producing electrons, also contribute to the electromagnetic component of the air shower.

Figure 2.12, from [Gaisser and Stanev, 2008][xxxi], illustrates the variation of the vertical flux for the major components of the air shower, depending on the atmospheric depth (expressed as the density of the air times the travelled distance, $\frac{g}{cm^2}$). The muon flux reaches its maximum at ~10-15 km of altitude.

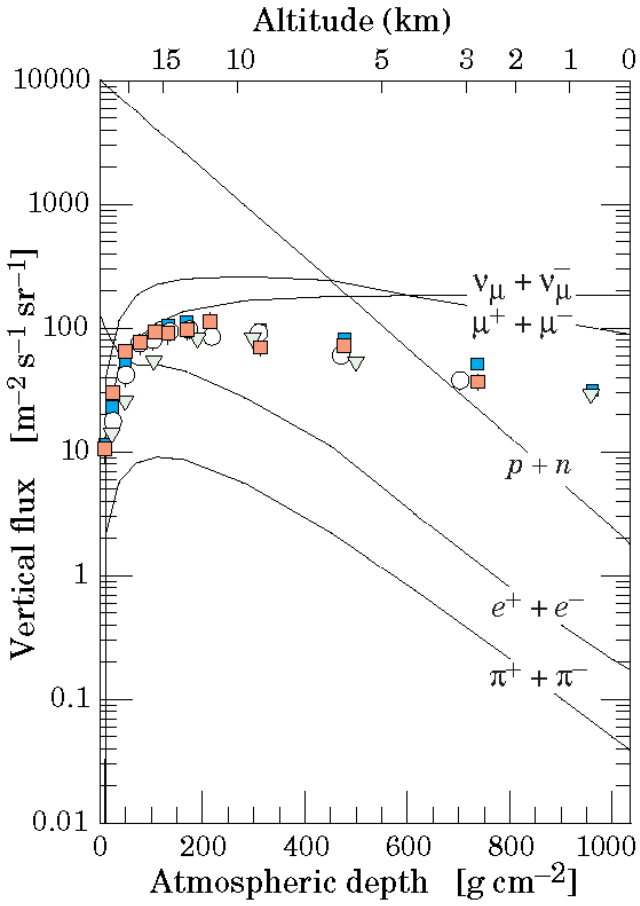

Figure 2. 12 Vertical fluxes for E>1GeV. Points show the μ⁻ measurements.

2.2.6 Cosmic rays at sea level

The extent of the air shower depends mainly on the energy of the initiating particle. Low energy events develop in the high atmosphere and fade out as the atmosphere gets denser, only their muon and neutrino components are able to reach the surface. On the other hand, high energy events reach a maximum potential near ground level; ultra-high-energy cosmic rays (E $>10^{18}$ eV) can generate billions of particles, which spread over a few tens of square kilometers.

The flux and distribution of particles that reach the ground level depends on several factors as seen before. The latitude (North-South effect), the polarity of particles (East-West effect), the altitude and the local weather conditions are among the most important. Table 2.1 shows the percentage of different cosmic rays' components at sea level.

Note that the table doesn't include neutrinos, despite their being 10^6 times more abundant than muons. This is due to the fact that neutrinos are electrically neutral and interact only via the weak subatomic force and gravity: this makes them extremely feebly interactive with matter and therefore extremely hard to detect with regular detectors. Cosmic neutrino detectors must be very large, from several thousands of m^3 on, to detect a significant number of events and are usually underground (e.g. Super-Kamiocande [Fukuda, 2001][xxxii]) or underwater (e.g. Antares [Adrian-Martínez, 2012][xxxiii]) in order to avoid the background radiation such as cosmic muons.

Table 2.1. Cosmic rays components at sea level [Bogdanova, 2006][xxxiv].

Total flux	Muons	Secondary neutrons	Electrons	Protons & Pions
$300\frac{1}{m^2 \cdot s}$	63%	21%	15%	<1%

Muons are the most abundant charged particles at sea level and their role is explained in detail in the next chapter. The nucleonic component, neutrons and protons, at ground level are degraded remnants of the primary cosmic radiation, as seen in Equation (2.2).

The electrons come from the electromagnetic component, also called soft component. While at high altitude the decay of neutral pions is a more important source of electrons, positrons and photons, at sea level muon decay is the dominant source of low-energy electrons. The knock-on electrons (secondary electrons with enough energy to escape from the primary radiation beam and produce further ionization) make a small contribution at low energy as well [Hayakawa, 1969][xxxv].

2.3. The interest of muons

2.3.1 Discovery of muons

The first observation of a muon was in 1936 when Anderson was studying cosmic rays [Anderson and Neddermeyer, 1937][xxxvi]. He detected a particle that, under the influence of a magnetic field, curved differently than known particles.

The experimental setup, shown in Figure 2.13 (from [Leprince-Ringuet, 1945][xxxvii]), consisted of a cloud chamber with a screen inside and a certain magnetic field around the copper cylinder. Charged particle trajectories are modified in a magnetic field, with the curvature depending on the particle's mass and energy (Larmor radius). Since the loss of energy through the screen is known and the setup enables two different measurements (before and after the screen), it allows the calculation of the particle's mass and energy.

The particle coming from point A with a thin, almost straight trajectory and discontinuous track, represents a muon with high energy. Once it crosses the glass screen and loses energy, its track becomes thicker and its Larmor radius smaller.

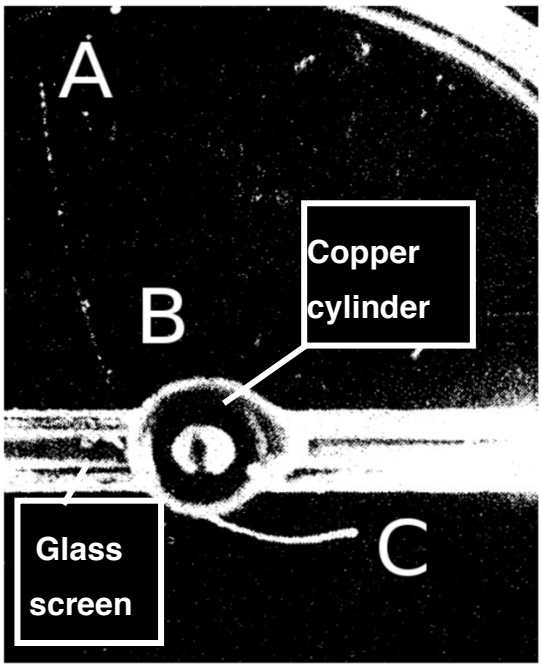

Figure 2. 13 Photo of two tracks with two different energies (A and C) from the same muon inside a cloud chamber under a magnetic field.

By the shape and direction of the curve, Anderson guessed that the particle should have a negative charge and a mass intermediate between the electron and the proton, thus its original name mesotron (from the Greek mes- for middle). The existence of this new particle was confirmed only a year later [Stevenson, 1937][xxxviii]. The discovery of more intermediate particles (pion in 1947) led to the creation of a new family called mesons and the mesotron was renamed "μ-meson".

2.3.2 Muon fundamental properties

Muons are elementary particles, which means that according to present theories, they are not made of other particles or whose substructure is still unknown. As seen in Figure 2.14, the muon is a fermion and it has spin of ½. It belongs to the lepton second generation, which means that it does not undergo strong interactions. On the other hand, they are susceptible to the other fundamental forces: the weak force, the electromagnetic force, and the gravitational force.

It is a negatively charged particle (q= -1 e), but like all elementary particles, the muon has a corresponding antiparticle of reverse charge (+1 e) and identical mass and spin: the antimuon (also named positive muon). Muons are denoted by μ^- and antimuons by μ^+.

Muons have a mass 207 times larger than the electron (0,511 MeV/c^2 vs 105,66 MeV/c^2). Due to their greater mass, they do not emit as much bremsstrahlung radiation as electrons, which allows them to penetrate deeper into matter than electrons for a given energy.

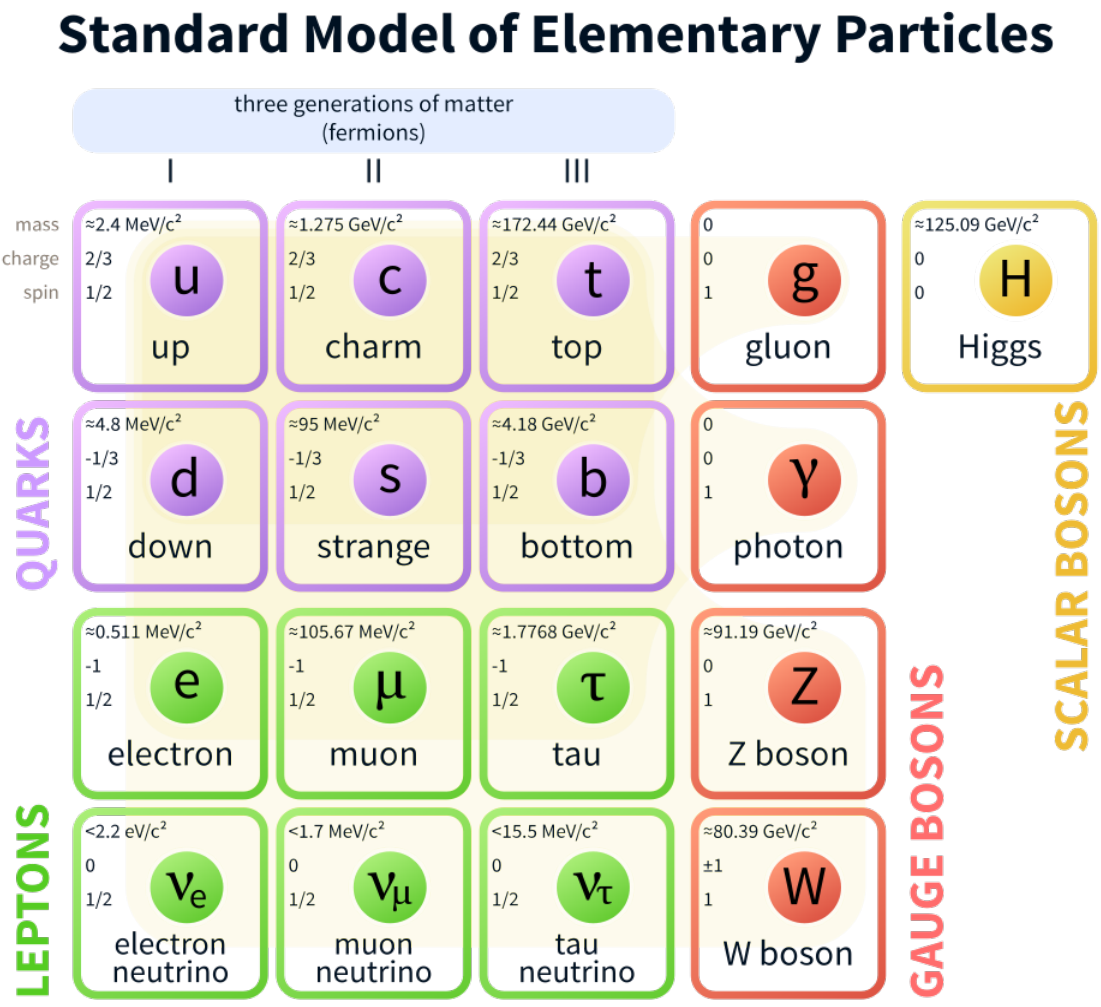

Figure 2. 14 Classification of elementary particles according to the standard model. Source Wikimedia Commons.

Muons are unstable particles with a mean lifetime (average length of time before its decay) of 2,2 μs. If we consider that they travel at 99,98 % of speed of light, a simple calculation would tell us that most shouldn't travel more than a few hundreds of meters. Yet, muons are capable of traveling long distances, for instance a particle with a zenith angle of 60º must cross 30 km of atmosphere to reach the ground.

The explanation of this effect is that muons undergo time dilatation due to their near-light speed [Easwar, 1991][xxxix]. According to the theory of special relativity, the time interval between two events is not invariant from one observer to another, but depends on the relative speeds of the observers' reference frames. The Lorentz transformation, see Equations (2.9) and (2.10), accounts for this effect and provides the cosmic muon mean lifetime in our time frame:

$$\tau = \gamma^L \cdot \tau_0 \tag{2.9}$$

where γ^L (Lorentz factor) is given by the following equation:

$$\gamma^L{}_{muon} = \frac{1}{\sqrt{1-\frac{v^2_{muon}}{c^2}}} \tag{2.10}$$

Solving Equation (2.10) for $v^2_{muon}/c^2 = 0{,}9998$ we obtain γ^L ~70. Therefore, the mean lifetime and reach of the cosmic muon are extended to 154 μs and to ~50 km respectively.

On the other hand, low energy muons (few GeV) have a Lorentz factor γ^L of 2 ~ 10 which induces a mean decay length of ~ 6 km. Since cosmic pions are typically produced at altitudes of 15 km and decay relatively fast, the daughter muons do not reach the sea level but rather decay themselves as shown in Equation (2.8).

2.4. Muon flux characterization towards tomography

2.4.1 Muon flux modeling at sea level

The need to characterize the natural flux of muons plays a major role in using muons to create tomographic images based on absorption. Figure 2.15 (Left), adapted from [Cecchini, 2012][xl], represents the integral fluxes (averaged over the 11-year solar cycle) energy distribution of the main components of cosmic rays arriving at sea level in latitudes ~40º.

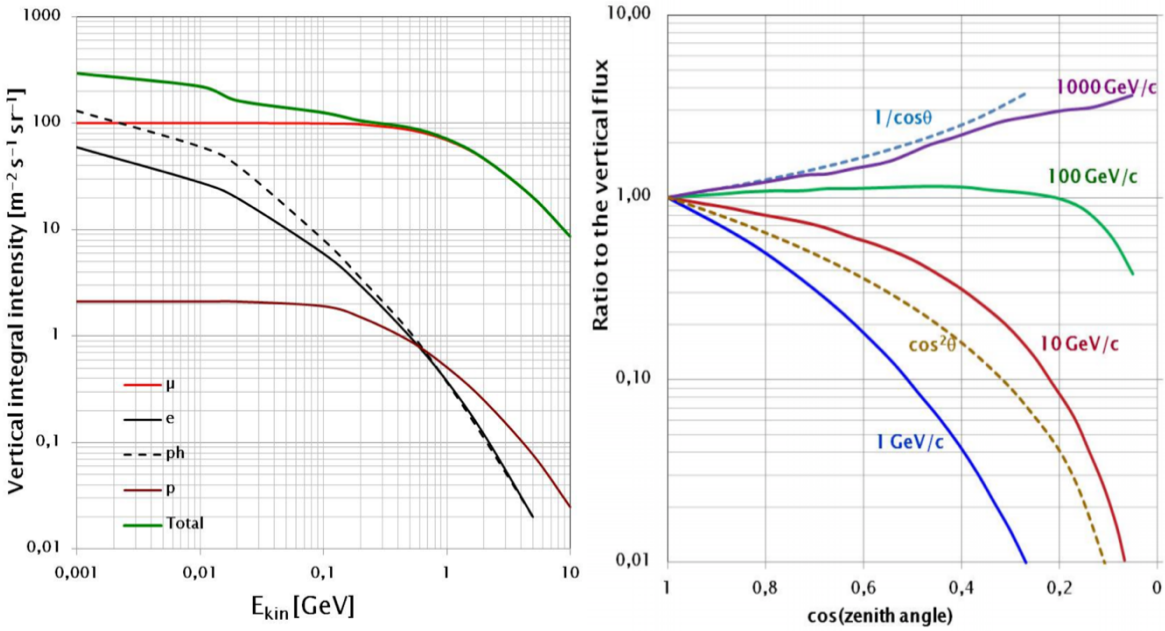

Figure 2. 15 (Left) Averaged integral fluxes of muons, electrons, photons and protons arriving at latitudes ~40°. (Right) Angular distribution of muons at the ground for different muon energies.

It is possible to differentiate three regions according to the muon energy:

A. $E_\mu < 1$ GeV, where the spectrum is close to flat. In this region muon decay and muon energy loss must be taken into account.
B. 1 GeV $< E_\mu <$ $\epsilon_{K,\pi}$, being ϵ_π= 115 GeV and ϵ_K= 850 GeV the critical energies[1] for kaons and pions in the vertical direction respectively [Kellog, 1989][xli]. Over ~100 GeV the energy loss is negligible, and the muon flux follows the same power law as parent mesons.
C. $E_\mu > \epsilon_{K,\pi}$: given the increase in the Lorentz factor and the small thickness of the atmosphere, the kaon and pion decay are suppressed. In this region, the flux of non-vertical muons is higher as seen in Figure 2.15 (Right).

For muons with energy close to 4 GeV (average energy at sea level), the angular distribution is well represented by $\cos^2\theta$. As the zenith angle increases (and therefore the muon's path through the atmosphere), the low energy muons decay before reaching the ground level, increasing the average E_μ for that given angle.

The muon energy and angular distribution is the effect of a convolution of the production spectrum, decay and energy losses in the atmosphere. The equilibrium between decay and interaction is a decisive factor in stablishing the relative importance of the two processes, and is based on the meson component characteristics.

[1] The critical energy is defined as the point where the energy loss contributions from ionization and radiative processes are balanced. More details in Section 2.4.2.

The differential muon flux (Φ_μ) depends on the energy at sea level of the muon (E_μ) and its zenith angle (θ), and is defined as follows:

$$\Phi_\mu(E_\mu, \theta) = \frac{dN_\mu(E_\mu,\theta)}{dA\ dt\ d\Omega\ dE_\mu}\ \frac{muons}{[cm^2 \cdot s \cdot sr \cdot GeV]} \tag{2.11}$$

where dN_μ is the number of muons crossing an area (dA), during a given time (dt) from a certain solid angle ($d\Omega$).

There are three different approaches to quantify the muon flux at sea level:

a) Measures: the direct measurement of the muon flux is the only way to determine it precisely, yet it presents some disadvantages: the detector's efficiency and eventual corrections due to its geometry must be considered and the background noise accounted for.
b) Numerical simulation based on Monte Carlo methods: there are softwares such as CORSIKA (COsmic Ray SImulations for KAscade), which allow the detailed simulation of extensive air showers, including the muon fluxes for different locations and heights [Heck, 1998][xlii].
c) Empirical model: experimental data of muon flux can be fitted, and the parameters of the curve calculated to predict the flux. The limitation of this approach is that the fit is only valid for a certain part of the muon spectrum.

So far it doesn't exist a software or unified model to describe the entire spectrum, hence the user must choose the most convenient model and parameters according to his needs.

Considering the approach (c), one of the most widespread models is that proposed by Gaisser in 1990 and subsequently improved by other contributors, shown in Equation (2.12):

$$\Phi_\mu(E_\mu, \theta) \approx A \cdot E_\mu^{-\gamma} \cdot \left(P_{\pi\mu}(E_\mu, \theta) + P_{k\mu}(E_\mu, \theta) + r_c\right) \cdot W_G(E, \theta) \tag{2.12}$$

where:

- E_μ is the muon energy at sea level in GeV,
- θ is the muon zenith angle in radians,
- A is a normalization factor ($0.14\frac{GeV}{cm^2 \cdot sr \cdot s}$),
- $P_{\pi\mu}$ describes the muons produced by pions: it considers the pion production in the atmosphere $\mathcal{A}_{\pi\mu}$=1, the branching ratio $b_{\pi\mu}$=1 and the pion critical energy $\epsilon_\pi = 115$ GeV. This factor is given as follows:

$$P_{\pi\mu}(E_\mu, \theta) = \frac{b_{\pi\mu} \cdot \mathcal{A}_{\pi\mu}}{1+\frac{1.1 \cdot E_\mu \cdot \cos\theta}{\epsilon_\pi}} \quad (2.13)$$

- $P_{k\mu}$ describes the muons produced by kaons: it considers the kaon production in the atmosphere $\mathcal{A}_{k\mu} = 0{,}085$, the branching ratio $b_{k\mu} = 0{,}635$, and the pion critical energy $\epsilon_\pi = 850$ GeV. This factor is given as follows:

$$P_{k\mu}(E_\mu, \theta) = \frac{b_{k\mu} \cdot \mathcal{A}_{k\mu}}{1+\frac{1.1 \cdot E_\mu \cdot \cos\theta}{\epsilon_k}} \quad (2.14)$$

- r_c refers to the ratio of the prompt[1] muons to pions. This effect wasn't considered in Gaisser's original model, but was introduced by [Tang, 2006][xliii] to reflect the effect of high energy muons. Its contribution is important for our application, as it describes a fraction of the muon spectrum which is likely to be found in underground measurements.
- $W_G(E, \theta)$ is the probability for a muon to reach sea level.

Different estimations of these parameters for specific conditions are provided by several authors. A thorough comparative analysis have been made by [Lesparre, 2010][xliv].

As seen in Figure 2.16, the incident zenith angle (θ) of the muons in the Gaisser model, was defined as the angle between the particle's trajectory and the axis normal to the high atmosphere over the detector.

Given that the Earth is not flat, muons with high incident angles have different apparent angular values. Lesparre proposed Equation (2.15) to account for the Earth's curvature. It describes more accurately the real path of muons with $\theta > 60^o$ along the atmosphere, where the effect of the curvature is non-negligible:

$$cos\theta^* = \sqrt{1 - \frac{1-(cos\theta)^2}{\left(1+\frac{H_{atm}}{R_T}\right)^2}} \quad (2.15)$$

where H_{atm} is the muon production altitude for particles with $\theta > 60^o$ (~32 km) and R_T is the radius of the Earth (~6.370 km).

[1] Prompt muons are generated from charmed particle decay and other so-called prompt or direct processes. Unlike muons originated from pion and kaon decays, they don't show dependence with the zenith angle.

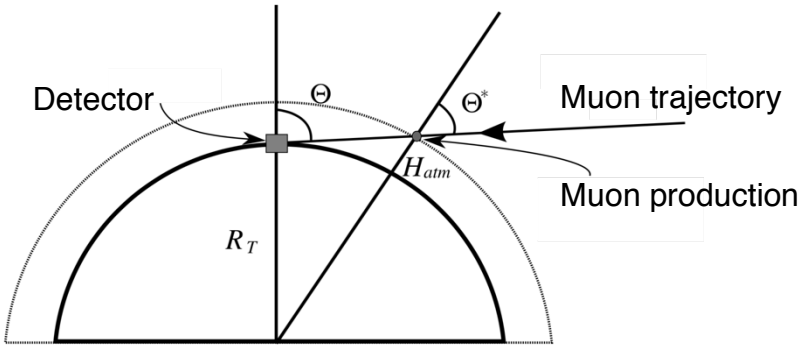

Figure 2. 16 Diagram to illustrate the difference between θ and θ^*. Adapted from Lesparre.

Another simplification assumed by Gaisser was that the energy of the muon arriving at sea level (E_μ) was the same as the energy at the moment of production ($\tilde{E}_\mu$). As seen in the previous section, however, muons lose energy during their atmospheric displacement ($\Delta\mathrm{E}$), given as follows:

$$\tilde{E}_\mu = E_\mu + \Delta\mathrm{E} \tag{2.16}$$

$$\Delta\mathrm{E} = a_{atm} \cdot \left(\frac{\varrho_F}{\cos\,\theta^*} - \varrho_0\right) \tag{2.17}$$

where:

- $\mathrm{a_{atm}}$ is the ionization energy loss ($\sim 2\,\frac{\mathrm{MeV\cdot cm^2}}{\mathrm{g}}$), responsible for 99 % of the total energy loss [Bichsel, 2010][xlv],
- ϱ_F is the atmospheric opacity at sea level (1.030 $\frac{g}{cm^2}$) [Dar, 1983][xlvi],
- ϱ_0 is median opacity of the atmosphere between its external boundary and the muon production altitude (120 $\frac{g}{cm^2}$) [Tang, 2006].

Equation 2.17 takes into consideration that the muons undergo different gradients of density according to their trajectories. The air density changes faster per unit of length traveled for near vertical muons than for the ones with a tilted incident angle.

The muon's probability to reach the sea level, $W_G(E,\theta)$, is associated with the muon decay due to its energy loss and is defined as:

$$W_G = \left(\frac{\varrho_0 \cdot \cos\,\theta^*}{\varrho_F}\right)^{\frac{\gamma_\mu^{-1}}{\cos\theta^* \cdot \tilde{E}_\mu}} \tag{2.18}$$

where γ_μ^{-1}= 1,04 GeV. In consequence, the energy required for a muon to reach the ground is proportional to its incidence angle. The decay phenomenon is observed in particles whose energy is below 1 TeV of energy: beyond this point the particle has a high probability to reach the sea level [Lesparre, 2010].

For a given energy, the muon flux presents a maximum at a characteristic zenith angle. This angle increases with the energy. Therefore, given the modifications to Gaisser's original model detailed above, Equation (2.12) may be rewritten as:

$$\Phi_{\mu}^{s.l.}(E_{\mu},\theta) \approx A \cdot \tilde{E}_{\mu}^{-\gamma} \cdot \left(\frac{b_{\pi\mu} \cdot \mathcal{A}_{\pi\mu}}{1+\frac{1.1 \cdot \tilde{E}_{\mu} \cdot \cos\theta}{\epsilon_{\pi}}} + \frac{b_{k\mu} \cdot \mathcal{A}_{k\mu}}{1+\frac{1.1 \cdot \tilde{E}_{\mu} \cdot \cos\theta}{\epsilon_{k}}} + r_c \right) \cdot \left(\frac{\varrho_0 \cdot \cos\ \theta^*}{\varrho_F} \right)^{\frac{\gamma_{\mu}^{-1}}{\cos\theta^* \cdot \tilde{E}_{\mu}}} \quad (2.19)$$

This model will be used to describe the muon flux at the surface during the present work.

Figure 2.17 shows the differential muon flux ($\frac{\mu}{cm^2 \cdot s \cdot sr \cdot GeV}$) at sea level calculated with Equation (2.19) The flux is shorted by the particle's energy and arrival zenith angle, where 0º represents the zenith and 90º represents the horizontal muons.

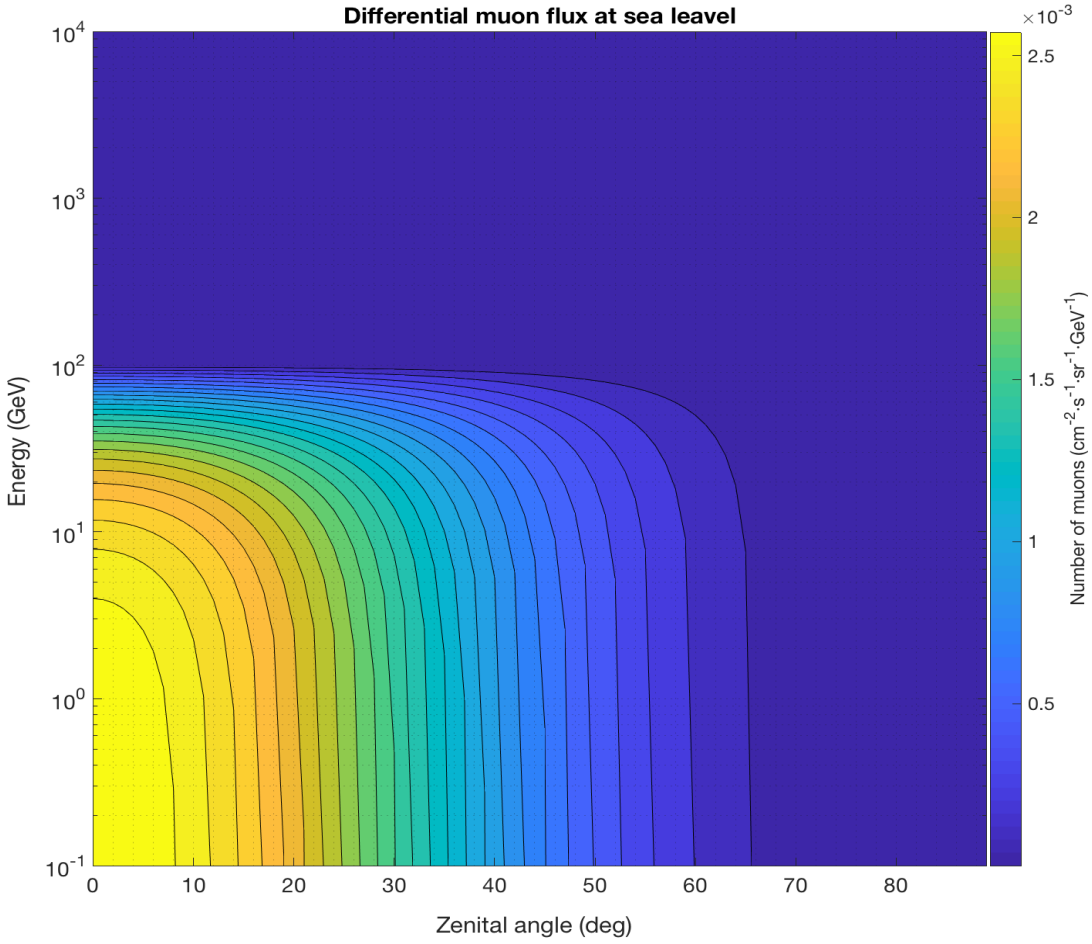

Figure 2. 17 Angular and energy distribution of the differential muon flux at sea level.

The muon detection technology presented in this work is able to reconstruct the trajectory of a muon while it crosses the detector. Yet, it is not capable of determining the energy of the particle recorded. Under this circumstance, the differential flux provided by Equation (2.19) is not directly comparable to the measurement.

To overcome this constraint, the differential muon flux can be integrated over the muon energy as seen in Equation (2.20).

$$\phi(\theta)\ \left(\frac{muons}{cm^2 \cdot sr \cdot s}\right) = \int_{E_\mu}^{\infty} \Phi_\mu^{s.l.}(E,\theta)dE \qquad (2.20)$$

where E_μ is the muon energy at rest, ~0,1 GeV.

Figure 2.18 represents the muon flux integrated over energy calculated with Equation (2.20) for a latitude near the geomagnetic parallel 40º North. It is possible to recognize the sinusoidal shape of the differential flux and the decreasing trend for high zenithal angles. Since only the zenith angles are considered, the East-West effect is not observable in the figure.

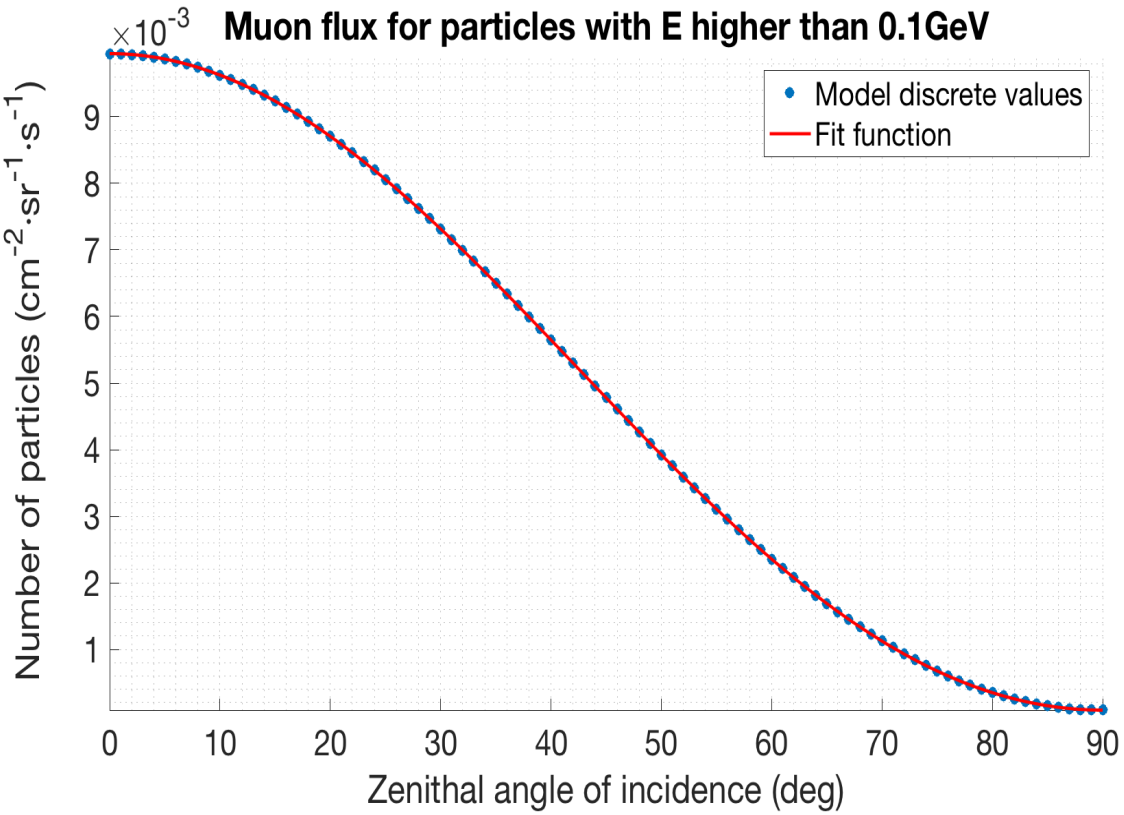

Figure 2. 18 Muon flux integrated over energy at sea level as a function of the zenith angle.

2.4.2 Interaction between muons and matter

As seen in the previous sections, the muon flux is progressively attenuated because of the particle's energy loss. The amount of energy lost depends on the particle's initial energy and the kind of interaction. The most part of losses are due to ionization and radiation (Bremsstrahlung, pair-production and photo-nuclear) reactions.

-Ionization: it is the result from the loss of an electron when a moving charged particle collides with subatomic particles or other atoms.

The mean energy loss ($\frac{dE}{dx}$) due to ionization might be modeled for heavy charged particles with velocities in the range of 0.1 ≤ β_γ ≤ 1.000 via the Bethe-Bloch equation [Amsler, 2010][xlvii]:

$$-\frac{dE}{dx} = K \cdot z^2 \cdot \frac{Z}{A} \cdot \frac{1}{\beta^2} \cdot \left[\frac{1}{2} \cdot ln\left(\frac{2 \cdot m_e \cdot T_{max}(c \cdot \gamma^L \cdot \beta)^2}{I^2}\right) - \beta^2 - \frac{\delta(\beta_\gamma)}{2} - \frac{\delta(\beta \cdot \gamma)}{2}\right] \quad (2.21)$$

where, K = 0,03071 GeV/mwe, z is the charge of the particle, Z and A are respectively the number of protons and nucleons of the medium atoms, c is the speed of light in vacuum, β = v/c is the muon velocity as a fraction of the speed of light, γ^L is the Lorentz factor, m_e is the electron rest mass, m is the particle's mass, I the ionization potential or energy (average energy transmitted to the ejected electron resulting from ionization) and δ is a density effect correction.

T_{max} is the maximum energy transfer, which can be approximated as:

$$T_{max} = \frac{2 \cdot m_e \cdot c^2 \cdot \beta^2 \cdot \gamma^2}{1 + 2 \cdot \gamma \cdot m_e/m + (m_e/m)^2} \quad (2.22)$$

The following radiative effects are also a direct consequence of the passage of muons:

-Bremsstrahlung: the electromagnetic radiation produced by the deceleration of a muon when deflected by the electric field of nearby atoms. In this procedure, the energy lost due to the change of trajectory is emitted in form of a photon. This process is analogue to the one in the air shower production shown in Equation (2.5).

-Pair-production: as seen in Equation (2.4), when the gamma ray created by bremsstrahlung is energetic enough (>1,02 MeV), it can trigger a positron-electron pair production.

-Photo-nuclear: rarer than the previous interaction, it occurs due to the inelastic interaction between the bremsstrahlung gamma ray and a near nucleus.

The average energy loss for these radiative processes increases almost linearly with energy: at TeV muon energies, it represents about 10% of the energy loss rate.

The combined effect of these interactions is shown in Equation (2.23):

$$-\frac{dE}{d\varrho} = a_{ionization}(E) + b(E)_{radiation} \cdot E \qquad (2.23)$$

where $a(E)_{ionization}$ is the energy variation due to ionization characterized by Equation (2.21) and $b(E)_{radiation}$ represents the energy variation due to the radiation processes: pair production, photo-nuclear and principally bremsstrahlung [Bichsel, 2010][xlviii].

Figure 2.19, from [Beringer, 2012][xlix], gives an overview of the contribution from the different interactions to the stopping power (-dE/dρ) of positive muons while going through copper depending on the particle energy.

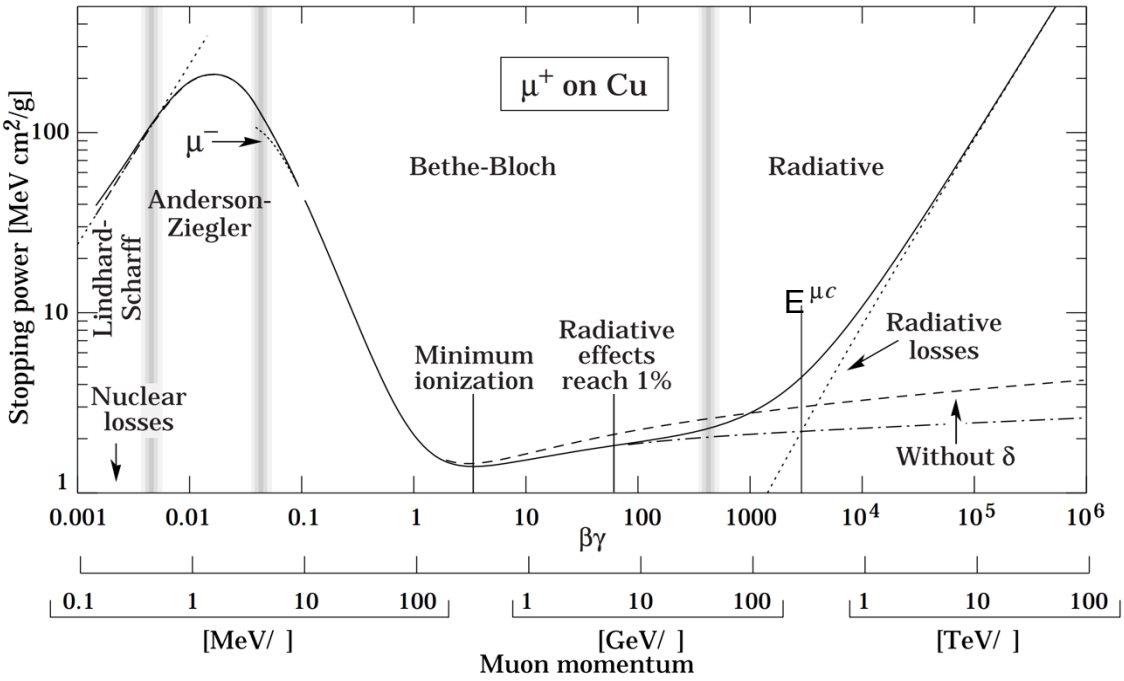

Figure 2. 19 Stopping power (-dE/dx) for positive muons in copper as a function of their momentum. Solid curves indicate the total stopping power and dotted lines illustrate the individual contribution to the energy loss.

The muons lose energy while passing through the atmosphere proportionally to the amount of matter they go through. To quantify this effect, the opacity of the medium is defined as the density (g/cm^3) integrated over the distance traveled (cm). It may be called "interaction length" as well and the standard unit is g/cm^2. Sometimes, particularly when speaking about underground muons, opacity is measured in meters water equivalent (mwe); being the conversion factor 1 mwe = 100 g/cm^2.

The opacity of the atmosphere is about 10 mwe for vertical trajectories and the energy loss for muons is about 0,2 GeV per mwe. During its travel, a muon loses about 2 GeV in passing through the atmosphere, mainly by ionization. The mean energy of muons reaching sea level is about 4 GeV [Nakamura, 2010][l].

2.4.3 Muon flux underground

The present work is focused in the characterization of a muon detection system for subsurface measurements. Under these conditions, the low energy muons are statistically non-significant and thus they will be henceforth neglected.

For the expected range of energies, ionization is the main responsible for the loss of energy. This region starts with a minimum ionization energy and follows a linear trend that continues up to ~1 TeV, where the transition between the ionization and radiative zones begins. The midpoint of the transition occurs at a critical energy ($E_{\mu c}$), which is characteristic of the traversed medium and is defined as the energy where the ionization losses are equal to the radiation losses.

$$E_{\mu c} = \frac{a(E_{\mu c})}{b(E_{\mu c})} \tag{2.24}$$

Beyond $E_{\mu c}$, the radiative loss becomes dominant and the energy loss is proportional to Z·(Z+1)/A for different materials.

The form of the diagram shown in Figure 2.19 is slightly different according to the medium that the muons penetrate. In the case of muons traversing standard rock[1], the shape is analogous to the previous one, but the minimum ionization energy is at 297 MeV and the critical energy $E_{\mu c}$ is 693 GeV [Groom, 2001][li].

With Equation (2.21), it is possible to calculate the energy loss of muons with energies between the minimum ionization energy and ~1 TeV in standard rock:

$$-\frac{dE}{d\varrho} \cong a(E)_{ionization} \cong 250\ \frac{eV \cdot cm^2}{g} \tag{2.25}$$

As a consequence, the muons require a minimal energy to successfully cross a certain opacity in order to balance the energy loss. This so-called minimal energy ($E_{\mu m}$) is calculated by several authors (e.g. Jourde and Lesparre) by integrating Equation (2.21):

$$E_{\mu m}(\varrho) - \int_0^{\varrho} \frac{dE}{d\varrho} d\varrho = E_{\mu} \tag{2.26}$$

were E_{μ} is the rest energy of the muon, 105,66 MeV.

Figure 2.20 shows the minimal amount of energy necessary for a muon to cross a certain length of standard rock, calculated with Equation (2.26).

[1] Standard rock (A=22, Z=11, $\rho = 2{,}65\ {}^{g}/_{cm^3}$)

It is important to note that the energy loss described by Equation (2.21) is a combination of two different behaviors. While the losses due to ionization can be considered as continuous in the energy range considered, the radiative loss is a discrete process. This leads to a statistical distribution of energy loss for high energies. Due to the stochastic nature of the energy loss processes, it becomes necessary to introduce the concept of survival probability W(E,ϱ), which is defined as the probability that a muon with a given energy traverses a certain opacity without being stopped.

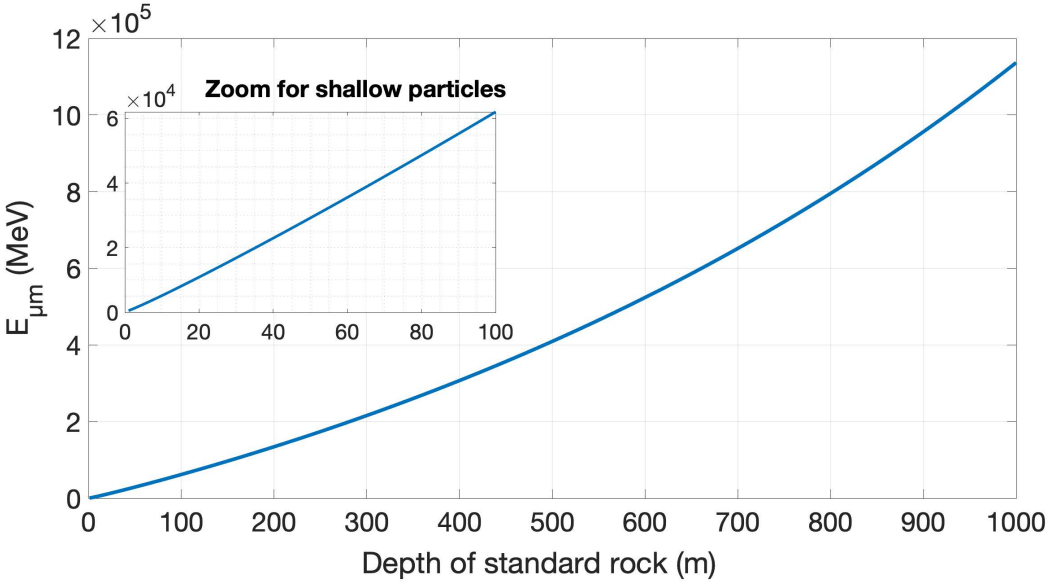

Figure 2. 20 Minimal energy of muons as a function of the length of standard rock's traversed.

The survival probability is connected to the $E_{\mu m}$ through the following relation:

$$W(E_{\mu m}, \varrho) = 0{,}5 \tag{2.27}$$

The survival probability of muons with a certain energy decreases as the opacity gets larger, and is helpful in estimating the evolution of the muon spectrum with depth when the surface flux is known.

The MUon SImulation Code (MUSIC) [Kudryavtsev, 2009][lii] is a Monte Carlo open source code. It is dedicated to the simulation of muon propagation through rock or water and allows approximation of the survival probability and particle energies by providing the depth, rock's composition and density, and the muon initial energy.

Figure 2.21, obtained by [Hivert, 2015][liii] with the MUSIC code using a sample of 10.000 muons per depth, shows the survival probability of muons with different energies while crossing different depths of standard rock.

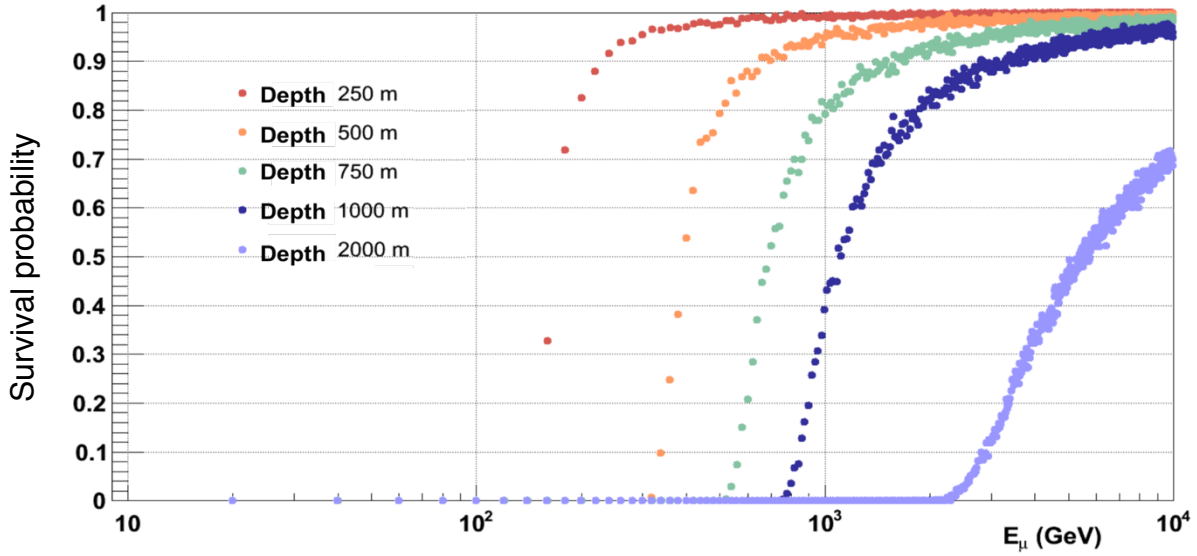

Figure 2. 21 Muon survival probability of muons according to their energy for different depths of standard rock.

By multiplying the survival probabilities with the flux at sea level obtained from Equation (2.19), the underground muon flux can be estimated. Figure 2.22, from [Hivert, 2017][liv], compares the vertical muon flux (θ=0) at sea level against the same flux after crossing 500 m of standard rock. Three different areas can be distinguished: (A) muons with $E_\mu < E_{\mu m}$ are not able to pass through 500 m of standard rock; (B) the muons are partially attenuated by the rock; (C) almost all the muons can reach a 500 m depth of standard rock; for these energies, the muon fluxes at sea level and at 500 m are not significantly different.

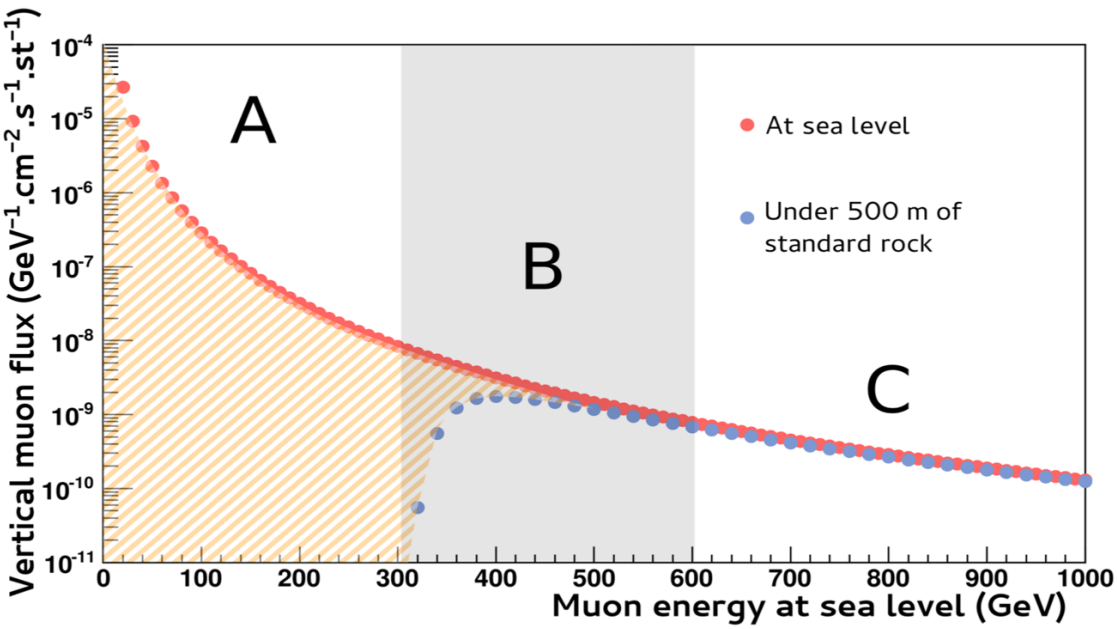

Figure 2. 22 Comparison of the vertical muon fluxes at sea level and at 500 m depth of standard rock.

Analogous to the muon flux at sea level, the integrated muon flux can be obtained with Equation (2.28) for underground conditions:

$$\phi(\varrho,\theta)\ \left(\frac{muons}{cm^2 \cdot sr \cdot s}\right) = \int_0^{\infty} \Phi_{\mu}^{s.l.}(E,\theta) \cdot \mathrm{W}(\mathrm{E},\varrho) dE \qquad (2.28)$$

However, its calculation is very time-consuming due to the Monte-Carlo procedure to obtain the survival probability. A relatively good approximation is to integrate between $E_{\mu m}(\varrho)$ and infinity instead of the entire energy spectrum:

$$\phi(\varrho,\theta)\ \left(\frac{muons}{cm^2 \cdot sr \cdot s}\right) = \int_{E_{\mu m}(\varrho)}^{\infty} \Phi_{\mu}^{s.l.}(E,\theta) dE \qquad (2.29)$$

Unlike Equation (2.20) for open sky measurements, Equation (2.29) takes the opacity into consideration. Note that the lower limit of the integral is the muon minimal energy for a certain opacity, instead of the muon rest energy.

The muon flux attenuation is the most important parameter in performing muon transmission tomography, but another factor should be taken into consideration when imaging large volumes. Muons interact with matter by Coulomb scattering, which deflects their trajectories. While low-energy particles present in the first meters of depth are more sensitive to this interaction, the scattering probability increases with the medium opacity as well. Ideally, a flat topography and homogeneous medium lead to the balance between missing scattered muons and incoming muons resulting from the scattering at the neighboring points.

In real life, the work of [Hivert, 2015] demonstrated that density heterogeneities will lead to trajectory variations on the order of a few cm for several hundreds of mwe crossed, because of the muon scattering.

Due to the limited opacity of the targets analyzed during the present work, this effect will not be taken into account, but its influence shouldn't be neglected systematically.

2.5. Conclusion

Primary cosmic rays from deep space hit the upper atmosphere and produce a shower of secondary particles, including muons. These charged particles, created naturally all around us, have a set of properties which allow them to propagate up to several hundreds of meters underground. The muon flux decreases progressively, with an absorption correlated with the medium opacity, and may be used as a vector of information.

Absorption based muon tomography uses on the decrease of the muon flux with depth increase to calculate the density of the matter crossed, which allows the creation of density chart inside big unreachable volumes.

In order to do so, the muon flux characterization, both at ground level and underground, is primordial. The empirical models described herein allow estimation of estimate this flux as a starting point for the tomography.

2.6. References

[i]Coulomb, C. A. (1785). Troisième mémoire sur l' électricité et le magnétisme. Mémoires de l'Académie des Sciences, 612 638.

[ii]Röntgen, W. C. (1896). On a New Kind of Rays. Science, 3, 227-231.

[iii]Becquerel, A. H. (1903). On radioactivity, a new property of matter. Nobel Lecture 11/12/1903

[iv]Curie, M. (1898). Rayons émis par les composés de l'uranium et du thorium. Comptes Rendus de l'Académie des Sciences, 126, 1101-1103.

[v]Wilson, C. T. R. (1901). On the ionisation of atmospheric air. Proceedings of the Royal Society of London, 68, 151 161. DOI :10.1098/rspl.1901.0032.

[vi]Wulf, T. (1910). Observations on the radiation of high di usion capacity on the Ei el Tower. Physikalische Zeitschrift, 11, 811-813.

[vii]Paul, J. et J. Robert-Esil (2009). Le roman des rayons cosmiques. Ellipses, Paris.

[viii]De Angelis, A., Giglietto, N. and Stramaglia, S. (2010) Domenico Pacini, the forgotten pioneer of the discovery of cosmic rays. Nuovo Cimento, 33, p. 713

[ix]Pacini, D. (1912). La radiazione penetrante alla super cie ed in seno alle acque. Il Nuovo Cimento, 3, 93 100. DOI :10.1007/BF02957440.

[x]Hess, V. (1912). Über Beobachtungen der durchdringenden Strahlung bei Sieben Freiballon- fahrten. Physikalische Zeitschrift, 13, 1084-1091.

[xi]Wilson, C. T. R. (1911). On a Method of Making Visible the Paths of Ionising Particles through a Gas. Proceedings of the Royal Society of London A: Mathematical, Physical and Engineering Sciences, 85, 285-288.

[xii]Rutherford, E. (1911). The Scattering of α and β Particles by Matter and the Structure of the Atom, Philosophical Magazine. Series 6, vol. 21.

[xiii]Geiger, H. & Müller, W. (1928). Elektronenzählrohr zur Messung schwächster Aktivitäten. Naturwissenschaften, 16, 617-618.

[xiv]Rossi, B. (1930). On the magnetic de ection of cosmic rays. Phys. Rev., 36, 606.

[xv] Clay, J. (1927). Penetrating radiation. Proceedings of the Amsterdam Academy of Sciences, 30, 1115-1127.

[xvi]Crozon, M. (2005). Quand le ciel nous bombarde... Qu'est-ce que les rayons cosmiques? Vuibert, Paris.

[xvii] Johnson, T. (1933). The Azimuthal Asymmetry of the Cosmic Radiation. Physical Review. 43 (10): 834–835. DOI:10.1103/PhysRev.43.834.

[xviii] Alvarez, L.; Compton, A. (1933). A Positively Charged Component of Cosmic Rays. Physical Review. 43 (10): 835–836. DOI:10.1103/PhysRev.43.835.

[xix]Rossi, B. (1934a). Directional Measurements on the Cosmic Rays Near the Geomagnetic Equator. Phys. Rev., 45, 212-214. DOI :10.1103/PhysRev.45.212.

[xx]Rossi, B. (1934b). Misure sulla distribuzione angolare di intensita della radiazione penetrante all'Asmara. Ricerca Scientifica. 5 (1): 579–589.

[xxi] Auger, P. (1939). Extensive cosmic-ray showers. Reviews of Modern Physics, 11, 288 291. DOI :10.1103/RevModPhys.11.288.

[xxii]Hillas, M. (1972). Cosmic Rays: The Commonwealth and International Library: Selected Readings in Physics. Pergamon Press Ltd.

[xxiii] Gaisser, T. et T. Stanev (2008). Cosmic Rays in the Review of Particle Properties, S. Eidelman et al. Physics Letters B 592, 254–260.

[xxiv] Grieder, P.K.F. (2001) Cosmic Rays at Earth, Elsevier Science.

[xxv] Spurio, M. (2015). Particles and Astrophysics. Astronomy and Astrophysics Library. Springer International Publishing, Cham.

[xxvi] Aguilar, M. et al. (2013). First Result from the Alpha Magnetic Spectrometer on the In- ternational Space Station : Precision Measurement of the Positron Fraction in Primary Cosmic Rays of 0.5 350 GeV. Phys. Rev. Lett., 110, 141102. DOI :10.1103/PhysRev- Lett.110.141102.

[xxvii] Fermi, E. (1949). On the Origin of Cosmic Radiation. Phys. Rev., 75, 1169 1174. DOI :10.1103/PhysRev.75.1169.

[xxviii] Gaisser, T. K. (1990). Cosmic Rays and Particle Physics. New York, Cambridge university press edition.

[xxix] Grieder, P. K. F. (2010). Extensive Air Showers. Springer-Verlag Berlin Heidelberg. DOI : 10.1007/978-3-540-76941-5_1.

[xxx] Gosse J. C., Phillips, F. M. (2001). Terrestrial in situ cosmogenic nuclides: theory and application. Quat. Sci. Rev. Vol 20, 14, 1475-1560

[xxxi] Gaisser, T. et T. Stanev (2008). Cosmic Rays in the Review of Particle Properties, S. Eidelman et al. Physics Letters B 592, 254–260.

[xxxii] Fukuda, S. et al (2001). Solar ^{8}B and hep Neutrino Measurements from 1258 Days of Super-Kamiokande Data. Phys. Rev. Lett. 86, 5651

[xxxiii] Adrian-MArtínez, S. et al (2012). Measurement of atmospheric neutrino oscillations with the ANTARES neutrino telescope. Physics Letters B. 714 (2–5): 224–230

[xxxiv] Bogdanova, L., M. Gavrilov, V. Kornoukhov, et A. Starostin (2006). Cosmic muon flux at shallow depths underground. Physics of Atomic Nuclei 69(8), 1293–1298.

[xxxv] Hayakawa, S (1969). Cosmic Ray Physics, Wiley, Interscience, New York.

[xxxvi] Neddermeyer, S. H., Anderson, C. D. (1937). Note on the Nature of Cosmic-Ray Particles. Phys. Rev. 51 (10): 884–886

[xxxvii] Leprince-Ringuet, L. (1945). Les rayons cosmiques. Albin Michel, Paris.

[xxxviii] Street, J.; Stevenson, E. (1937). New Evidence for the Existence of a Particle of Mass Intermediate Between the Proton and Electron. Phys. Rev. 52 (9): 1003.

[xxxix] Easwar, N. and MacIntire, D. (1991). Study of the effect of relativistic time dilation on cosmic ray muon flux—An undergraduate modern physics experiment. Am. J. Phys.59, 589

[xl] Cecchini, S. and Spurio, M. (2012) Geosci. Instrum. Method. Data Syst. 1 185-196

[xli] Kellogg, R., H. Kasha, et R. Larsen (1978). Momentum spectra, charge ratio, and zenith-angle dependence of cosmic-ray muons. Physical Review D 17(1), 98–113.

[xlii] Heck, D., Knapp, J., Capdevielle, J.N., Schatz, G. and Thouw, T. (1998) CORSIKA: A Monte Carlo Code to Simulate Extensive Air Showers. V + 90 p., TIB Hannover, D-30167 Hannover (Germany).

[xliii] Tang, A., Horton-Smith, G., Kudryavtsev, V. A. & Tonazzo, A. (2006). Muon simulations for super-kamiokande, kamland, and chooz. Phys. Rev. D74, 053007 (DOI:10.1103/PhysRevD.74.053007)

[xliv] Lesparre, N. (2010). Geophysical muon imaging: feasibility and limits. Geophys. J. Int. 183 (2010) 1348

[xlv] Bichsel, H., Groom, D.-E. and Klein, S.-R. (2010). Passage of particles through matter. Review of Particle Physics, Amsler C. et al. Physics Letters B 667, 267–280

[xlvi] Dar, A. (1983). Atmospheric Neutrinos, Astrophysical Neutrons, and Proton-Decay Experiments. Physical Review Letters 51(3), 227–230.

[xlvii] Amsler, C. et al., (2010) Passage of particles through matter. PL B667, 1. http://pdg.lbl.gov

[xlviii] Bichsel, H., Groom, D.-E. and Klein, S.-R. (2010). Passage of particles through matter. Review of Particle Physics, Amsler C. et al. Physics Letters B 667, 267–280.

[xlix] Beringer, J. et al. (2012). Review of particle Physics, Vol 86. Phys.Rev. D.

[l] Nakamura K. and Particle Data Group (2010). Review of Particle Physics. J. Phys. G: Nucl. Part. Phys. 37 075021

[li] Groom, D., Mokhov, N. & Striganov, S. (2001). Muon stopping power and range tables 10 MeV-100 TeV. Atomic data and nuclear data tables, 78, 183 356. DOI :10.1006/adnd.2001.0861.

[lii] Kudryavtsev, V. (2009). Muon simulation codes MUSIC and MUSUN for underground physics. Computer Physics Communications, 180, 339 346.

[liii] Hivert, F. (2015). Caractérisation de la densité des roches et de ses variations spatiales et temporelles à partir des muons : application au Laboratoire Souterrain à Bas Bruit (LSBB). Doctoral dissertation.

[liv] Hivert, F., Lázaro Roche, I., Decitre, J-B., Brunner, J., Busto, J. and Gaffet, S. (2017). Muography sensitivity to hydrogeological rock density perturbation: roles of the absorption and scattering on the muon flux measurement reliability. Near Surface Geophysics. Vol 15, No 2, 121 - 129

Chapter 3. Muon detection for imaging applications.

Chapter 3 abstract

There exist several ways to detect muons, each with different arguments for and against depending on the targeted application. The broad scope of methods available nowadays has led to the design of application-oriented detectors in order to enhance their performance.

Micromegas-like detectors have proven to be a versatile tool for temporal monitoring of large volumes with a compact size, light weight, relative low cost and ground and underground operation capabilities. Nowadays, there are different setups based on Micromegas readout planes capable of performing muon tomography measurements in different domains.

There are two main techniques for muon tomography: transmission and scattering. Both of them rely on the direction-sensitive measurement of the cosmic muon flux. Due to the intrinsic limitations of each technique, only transmission appears suitable to image large volumes.

Muography provides reliable, original and independent information relatively to the physics of the measures produced by the seismic, gravimetry or resistivity soundings of the Earth for instance. It is thus as a complementary method in several disciplines, it eases the resolution of the inverse problem to obtain in situ the density distribution of the targeted volume.

3.1. Muon detection technologies

Ever since the discovery of muons in 1936, several technologies have proven their capability to react to the passage of these particles though them or to measure the effects produced by their movement. This section provides an overview of the most employed methods nowadays to detect muons, as well as their differentiating features and main applications.

3.1.1 Visual detection

The visual detection technologies allow the direct visualization of the particle's trajectory in a temporary or permanent way.

As seen in Chapter 2, the first technology capable of identifying muons was the cloud chamber. It consists of a sealed compartment containing a supersaturated vapor of water or alcohol. Charged particles collide with the gaseous mixture and create electrostatic forces. This originates condensation centers that lead to the formation of a trail of droplets, visible for a few seconds. The data acquisition relies on the analysis of photographic images of the trails. The chamber provides information about the particle due to the characteristic shapes of the trails. It is possible to determine, when subjected to magnetic field, the particle's direction, speed, quantity of movement and sign of electric charge.

Cloud chambers were widely used before the introduction in the late '60s of the multiwire proportional chamber [Sauli, 1977][i]. Charpak's invention, awarded with the Nobel prize in 1992, would revolutionize particle detection. With computer science booming, it made the data acquisition quick, automated and electronic. The slow response speed relegated cloud chambers to the background, which ended up mainly as educational tools to illustrate particle physics to the general public.

Another technique based on making the particle's tracks visible, this time in a permanent way though, is the nuclear emulsion. The principle of functioning is based on high sensitive photographic films.

The emulsion films used for muography are usually made of silver bromide crystals interspersed in a gel. Traversing ionizing particles sensitize the crystals and create a latent image. A development is therefore necessary to fix the image. In this process the metallic silver coalesces onto the sensitized site, growing folded micrometric filaments, named grains. These structures are visible as dark spheroids on a bright background. The alignment of grains reveals the path of the particle in the medium, and films of 20~30 µm become 3D a tracking detector with a sub-micrometric precision and good angular precision (few mrad). Figure 3.1 from [Bozza, 2017][ii], shows an automatized microscope scanning the nuclear film at different depths, by varying its focal distance.

Unfortunately, nuclear emulsion films are sensitive from their production to their development and the latent image may fade out if the environmental conditions are not appropriate (i.e. hot temperatures and high humidity). The lack of time trigger or event time information (unlike electronic detectors) complicate the data analysis and motivates the use of a double-coating configuration in order to filter the non-desired data.

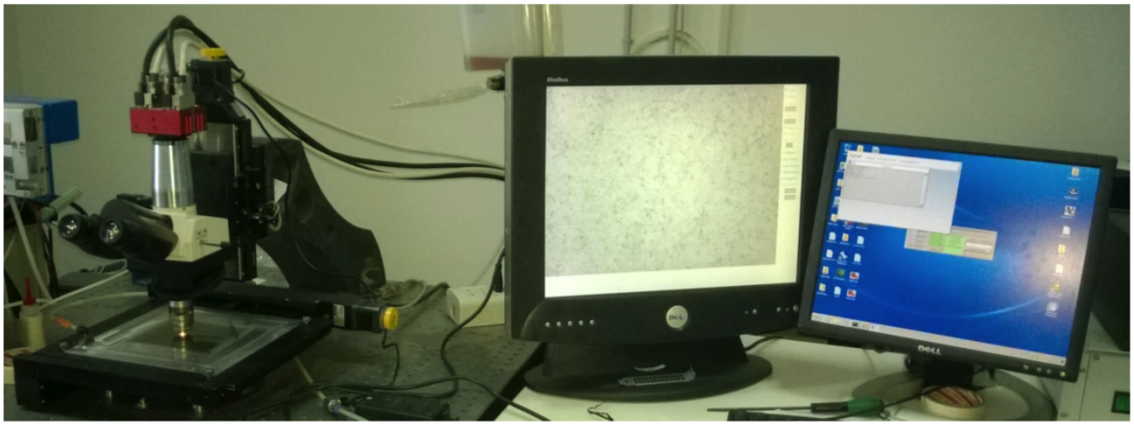

Figure 3. 1 Readout robot analyzing a nuclear emulsion with an automatic microscope.

This technique has been employed in the last decade to successfully image volumes in domains such as archeology [Morishima,2017][iii], volcanology [Tanaka, 2017][iv] or nuclear reactors [Morishima,2012][v]. It is especially interesting when a power supply is not available, or the instrumented area presents a difficult access.

In conclusion, the assets of the nuclear emulsion are its sub-micrometric 3D spatial resolution, the lightness of plates required for the measurement, it allows a modular assembly and doesn't need a power source to record data. On the other hand, this technique is sensitive to environmental parameters and lacks timing information of the particle's passage, making the temporal monitoring extremely hard. Nowadays, the focus is on improving the readout speed to minimize the considerable time elapsed between the acquisition and the results.

Another family of visual detectors take advantage of the Cherenkov light produced along the muon path and can be seen in Figure 3.2 from [Catalano, 2016][vi]. The characteristic ring-like image (Figure 3.2 (Left)) produce by muons has been previously employed for optical calibration of telescopes. More recently, Catalano has proposed a new approach to study the interior of volcanoes by the use of Cherenkov telescopes (Figure 3.2(Right)) to detect the relativistic cosmic-ray muons that survive after crossing Mount Etna [Catalano, 2016].

The muons with an energy higher than the threshold value (~ 5 GeV in the atmosphere at sea level) produce Cherenkov light. This radiation occurs in the visible and ultraviolet regions of the electromagnetic spectrum. These photons are reflected by the primary mirror of the telescope onto secondary mirror which focuses them onto the camera

The resulting annular pattern contains all the essential information to reconstruct the particle direction and energy.

This technique offers the advantage of a negligible background and a good spatial resolution (~0,14 deg). The downsides reside in the weight and size of the telescope (analogue to a shipping container), which makes difficult the transport and deployment of the telescope in certain study sites, and the complications to acquire data in broad daylight.

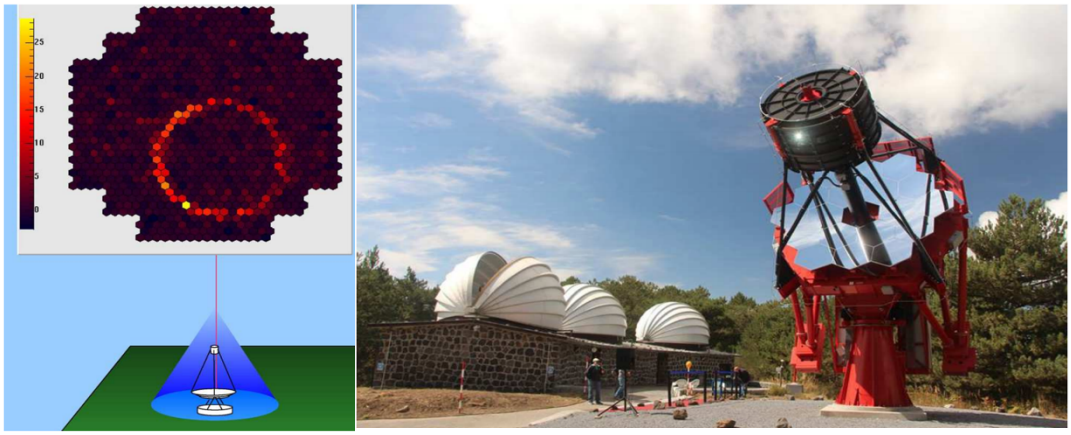

Figure 3. 2 (Left) Muon ring images with Cherenkov telescope. (Right) ASTRI SST-2M telescope proposed for muon tomography.

3.1.2 Hodoscopes

Hodoscopes are instruments that determine the trajectories of passing charged particles. Hodoscopes are typically made up of many segments; the combination of segments detecting an event is then used to infer the passage point of the particle through the device.

Typically, the detection segments are composed of scintillating material, which emits light when a charged particle passes through it. In terms of material, there are two main groups according to its nature: organic and inorganic. Both rely on the emission of a photon due to the transition of an electron from an excited state to a less energetic state. The first case takes advantage of the electronic properties of organic polymers, while the second case relies on the electronic bandgap structure of a semiconductor glass.

The organic scintillators are the most widely used for muography purposes and they can be both in liquid or plastic forms, which makes them very versatile to fit different experimental configurations.

The scintillation light is usually converted into exploitable signal by means of a photomultiplier tube (PMT). The PMT is a vacuum tube consisting of:

- an input window to let the photons pass,
- a photocathode to convert photons into electrons (also known as photoelectrons),
- focusing electrodes to focus and accelerate the photoelectrons towards the dynodes,
- dynodes (electron multipliers) to create successive electron cascades by means of secondary electron emission
- and an anode to collect the output signal.

The PMT multiplies the current produced by incident light and provides a low-noise, high frequency (few ns) response.

Some experimental setup configurations may include wavelength shifting optical fibers between the scintillator and the PMT to adapt the light spectrum.

For some systems the strength of the light can be proportional to the deposited energy. The deposited energy can be determined by calibrations, which then can be used to infer information about the original particle's energy.

When a segment measures a significant amount of light, the experimenter can suppose that a particle passed through that segment. The segments are generally disposed in a matrix-like configuration to reconstruct the point of passage in two dimensions and at least two separated layers are required to determine the tridimensional trajectory of the particle.

In reality, dummy tracks originated by random coincidence events or background radiation (especially while performing surface measurements) are a non-negligible source of noise due to their capacity to blur the relevant information. The two main approaches to reduce the noise so generated are:

- the incorporation of additional planes of detection to restrict accidental coincidences
- shielding layers (steel or lead for example) between detection planes to block low energy ionizing particles such as electrons or positrons.

As a consequence, the hodoscopes used for muon tomography are relatively heavy and bulky, for instance the telescope of Figure 3.3 weights ~700 kg, more than a half of which is due to the lead shielding [Jourde, 2015][vii].

Figure 3. 3 Muon telescope from Diaphane project composed of aligned scintillator planes.

Hodoscopes are reliable and sturdy detectors for tracking charged particles. However, their spatial resolution is limited by the segment size. In applications where the spatial resolution is very important, hodoscopes have been superseded by other detectors such as nuclear emulsion films and gaseous detectors.

3.1.3 Gaseous detectors

Historically, gaseous detectors were the first devices permitting detection of charged particles. The single wire counter, invented in 1908 by Rutherford and Geiger [Rutherford, 1908][viii], was based on Townsend avalanches, which appear in gases subject to a high enough electric field [Townsend, 1901][ix].

Townsend avalanches originate when free electrons (called primary electrons) in a gas undergo strong acceleration. Due to collisions with atoms and molecules, the primary electrons produce secondary electrons via impact ionization. These secondary electrons are also accelerated and collide with the near gas atoms and molecules, releasing more electrons in every stage. Hence, a single primary electron can trigger an avalanche of electrons and the charge is amplified with a certain multiplication factor, called the gas gain.

Wire counters have a cylindrically shaped hollow cathode with a thin anode wire along the central axis. A narrow region of strong electric field is generated around the wire. The electron avalanches are developed in this region within a radius of a few wire diameters. These early detectors could reach a gas gain of ~100. In the initial stages, these detectors were not position sensitive, but afterwards some advanced designs were capable of detecting where along the wire the primary electron was liberated.

In the decades of 1950-1960, the first two-dimensional position-sensitive gas detectors were introduced: the spark and streamer parallel-plate chambers. Both consisted of two parallel metallic electrodes coupled to a separated triggering detector. When the trigger is activated after the passage of a charged particle, a short pulse of high voltage is applied between the electrodes. The primary electrons can, depending on the high voltage applied, either produce avalanches or, at higher voltages, sparks and streamers (see Section 4.9.3 for more details).

The sparks and streamers were photographed or filmed to determine the position of the passing particles [Chikovani, 1964][x]. The superposition of several detectors allows the visualization of the particle's tracks in three dimensions. Nevertheless, the complication and low rate operation of these detectors restricted their applications.

The next breakthrough came with the invention of the multiwire proportional chamber invented by Georges Charpak and colleagues in 1968, seen in Figure 3.4 [Charpak, 1968][xi]. This device contains an anode plane made of parallel wires, with a pitch of a few mm, located between two metallic cathodes. The chamber is filled with a carefully chosen gas, such as an argon/methane mix, and the detector operates in an avalanche mode (the different modes are detailed in Section 4.9.2). The signals are recorded on the nearest wire and present a charge proportional to the ionization effect of the detected particle.

Figure 3. 4 From left to right, Georges Charpak, Fabio Sauli and Jean-Claude Santiard working on a multiwire chamber in 1970. Image from CERN document server, original ref.: 8-8-70.

While performing high time resolution measurements of the current pulses of the wires, and taking into account the drift time of ions, it is possible to infer the distance at which the particle passed the wire. This increases the accuracy of the path reconstruction and is known as a drift chamber.

In 1970-1980s, the parallel-plate-type detectors made a come-back thanks to the invention of the resistive plate chambers (RPC) which replaced the metallic electrodes with resistive ones [Parkhomenchuk, 1971][xii]. The RPC have become widely used as muon detectors due to the large area of coverage (of order m^2), time resolution of ~ns and space resolution of order cm. A particular model of RPC made with low resistivity glass plates (GRPC), as seen in Figure 3.5 from [Raveendrababu, 2016][xiii], present interesting features for tracking muons [Cârloganu, 2013][xiv].

Nowadays, a team of the University of Louvain is developing a gas-tight mini-GRPC detector, focused in applications with challenging available volumes [Wuyckens, 2018][xv].

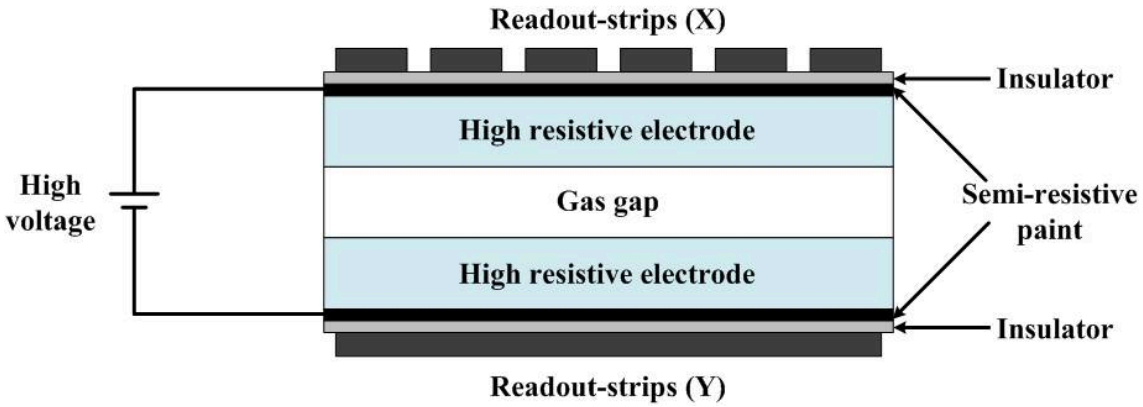

Figure 3. 5 Schematic section of a Resistive Plate Chamber.

Micropattern detectors represent the newest family of avalanche gaseous detectors. The invention of the microstrip gas counter (MSGC) at the end of the 1980s [Oed, 1988][xvi] was the starting point of this now well-known family. The MSGC is made of alternating anode and cathode strips with a pitch of less than 1 mm over an insulator (e.g., glass surface or PCB).

For the first time, microelectronic technology was applied in the manufacturing of gaseous detectors. Its main advantage was to offer a large area planar detector with small gaps between the electrodes. This enabled the operation at significantly lower voltages than the classical detectors. Despite the very limited applications nowadays, the most important contribution was to trigger a chain of developments and collective efforts, which led to the conception of a new generation of micropattern gaseous detectors.

In 1992 Charpak and collaborators developed the micromesh gaseous detector structure (MICROMEGAS) detector as an evolution of the multiwire proportional chamber [Charpak, 1994][xvii]. Micromegas is a micro-pattern gas detector (MPGD) that detects particles by amplifying the charges created by the ionization of the gas, usually a noble-gas-based blend. It consists of a two-stage parallel plate avalanche chamber with a sub-millimetric amplification gap. Both spaces are physically separated by a micromesh. Regularly-spaced insulating supports attach (in bulk versions) and keep constant the distance between this mesh and the anode plane made of printed copper tracks.

The more recent Micromegas [Giomataris, 2006][xviii] includes a resistive layer acting as spark protection to reduce the discharge current, preventing the front-end electronics from being damaged [Alexopoulos, 2011][xix]. The detailed description of the Micromegas readout plane, used for the present work, would exceed the scope of this chapter and can be found in Chapter 5.

Another member of the MPGD family used for detecting muons is the gas electron multiplier (GEM). The GEM, as seen in Figure 3.6 from [Francke, 2004][xx], is a hole-type detector made of dielectric sheets metalized on both sides with a matrix of holes through it. The voltage applied between the metalized electrodes produces a strong electric field inside the holes.

The electric field is sufficiently strong for triggering the avalanche of primary electrons. This detector has several unique features such as the possibility to operate in avalanche mode to increase the maximum achievable gain or the possibility to combine a GEM with other gaseous detectors.

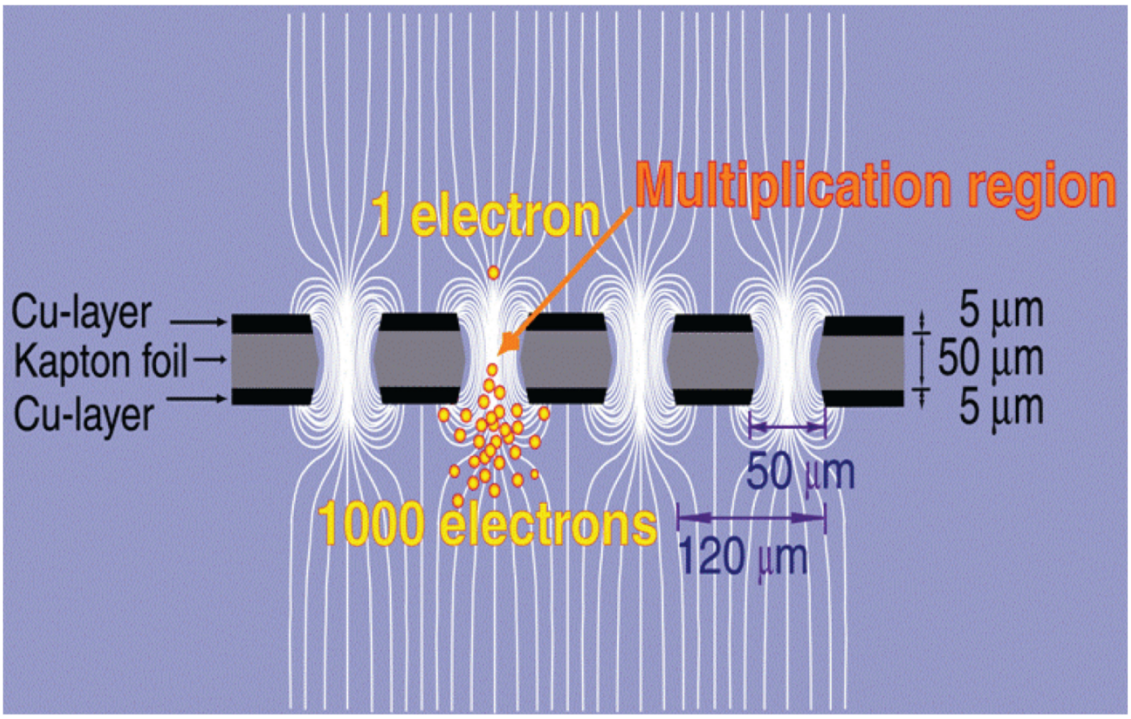

Figure 3. 6 Schematic drawing of a GEM detector and the principle of its operation.

Despite the great variety of gaseous detectors, all are based on the same principle. The incident radiation ionizes a gas and releases primary electrons. These primary electrons are either detected directly or trigger subsequent avalanches in regions of the detector with a strong electric field. The electrical signals, so generated and amplified, are large enough to allow detection even of relatively weak primary ionization.

These relatively light and compact detectors provide a good spatial (the values may vary between different configurations) and time resolution and allow the temporal data monitoring. On the other hand, a gaseous detector's performance depends on both the quality of the gas and environmental parameters such as temperature or pressure that must be monitored and/or compensated to get a steady measurement.

3.2. Tomography

Nowadays imaging techniques allow the knowledge and mapping of certain physical properties of the medium below its surface with non-invasive methods and permit its temporal monitoring. Properties like electrical conductivity, strength, deformation, water content, porosity or density might be deduced by the influence in measurable variables such as electrical current, velocity of propagation, absorption of acoustic and electromagnetic waves and variation of the gravitational field.

Tomography aims at inferring the distribution of these physical properties inside the volume to be monitored, on the basis of information provided by external measurements.

3.2.1 Density tomography in geophysics

The density distribution is essential to understand and anticipate the physical behavior of a solid in many domains of Earth sciences. It makes possible to identify potential zones of brittleness and the temporal evolution gives precious information about the dynamics of processes inside the monitored volume.

In geophysics, there are already robust techniques (e.g. electrical resistivity and gravimetry) used to map the subsoil structure. They provide an excellent referent to validate the original data coming from muon measurements. Moreover, muon tomography provides complementary and independent information which expands the available information.

- Electrical resistivity: The basic principle for electrical methods is the different conductivity of distinct kinds of soil. Stone might impede the flow of electricity, while the organic deposits might conduct electricity more easily than surrounding soils. In most systems, there is an injection of current into the ground using a pair of metallic current probes. This current creates a potential difference in the ground which is recorded by other electrodes, called voltage or potential probes. The measured voltage can be converted into an apparent resistivity value. In general, larger probe spacing results in a greater depth of investigation, but at the cost of sensitivity and spatial resolution.

The apparent resistivity can provide a range of information regarding the material being tested. Different types of soil compositions have different resistivities. Nevertheless, this is not a direct measurement of density. Different soils with different densities or under different circumstances (water content for instance) may have the same apparent resistivity. This non-unicity of the model complicates the interpretation of the electrical resistivity results by themselves.

In this framework, muon tomography provides alternative and independent information to reduce the degrees of freedom of the system and validate the model, such as in the work presented by [Lesparre, 2012][xxi] and [Portal, 2013][xxii].

- Gravimetry: Gravimetry is the measurement of the integrated strength of a gravity (g) field. Multiple measurements in space allows 3D inversion of the g distribution to obtain the medium density. Gravimetry is subject to several factors that affect the quality of the measure, such as latitude, altitude, nearby relief, atmospheric load and instrumental drift. It is necessary to balance out these

effects in order to isolate and map the g distribution, from which the density map can be deduced.

The coupling of gravimetry with tomographic muon measurements in the field of volcanology is well documented in the work of [Lesparre, 2012], [Portal, 2013], [Cârloganu, 2013], [Nishiyama, 2014][xxiii] and [Jourde, 2015][xxiv] among others.

A main advantage of the joint muon-gravity inversion concerns the improvement of the resolution obtained in the deeper parts of the density model. Despite the fact that this part is not directly sampled by muon tomography, a piece of information obtained by the muon data is transferred to the deep regions of the model integrated by the gravity measurements.

3.2.2 Muon tomography principle

Muon tomography aims at determining the density distribution of geological bodies by measuring their screening effect on the natural flux of cosmic muons. There are two kinds of muographic techniques depending on the muon interaction taken into account to model their transmission across the matter: (i) absorption of muon flux taking into account the energy loss and the scattering of the muons during their interactions with the atoms during their transmission across the matter, and (ii) the signature of the deviation of the muons induced by scattering against matter with high Z values. Energy loss and scattering of muons take place simultaneously, independently of the matter being traversed. However, their contribution varies depending on the case. The current work is focused in rectilinear transmission or absorption muography[1].

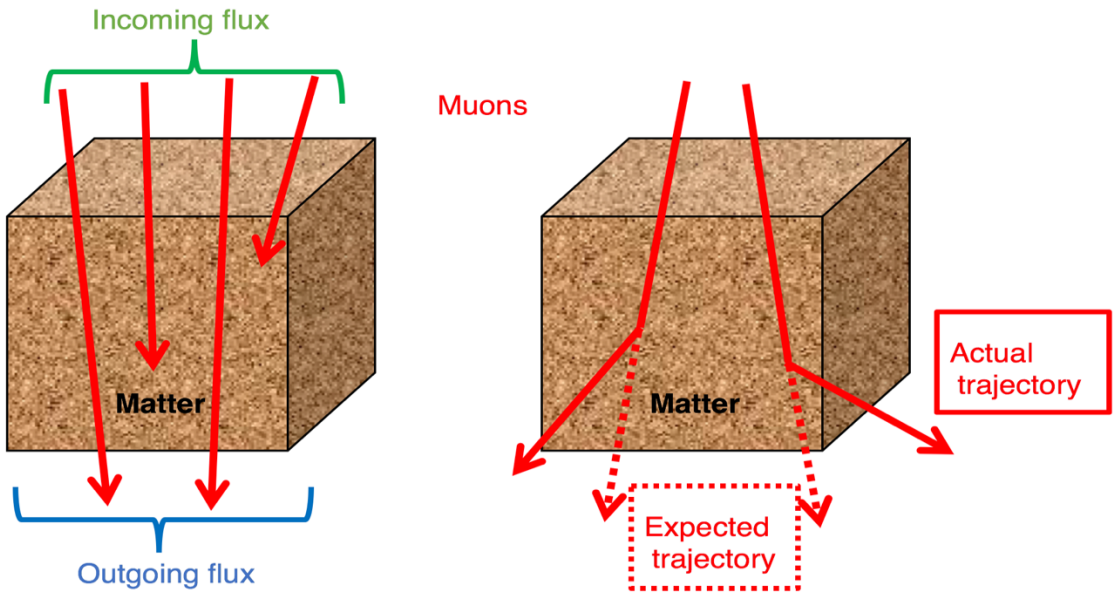

Figure 3. 7 (Left) Principle of transmission tomography due to the muon flux attenuation because of the loss of energy. (Right) Principle of scattering tomography due to the deviation of the muon.

[1] Transmission muography or muon radiography are often used as synonyms.

- Transmission or absorption muography: Because of the energy loss, a muon has only a certain probability to cross a given amount of material. As seen in Figure 3.7 (Left), the initial muon flux decreases after the passage of the muon through the matter. The minimal amount of energy necessary for a muon to successfully cross a certain depth of standard rock and its survival probabilities have been previously discussed in Section 2.4.3.

The fraction of muons that cross a material is mostly determined by the integrated density over the path length, called opacity. The experimental measurements of the muon flux in different directions through an object from a given point of view (the location of the muon detector), gives access to a map of the object's mean opacity along these directions. If the dimensions of the object are known, the integrated density might be obtained. This technique is possible thanks to the wide energy distribution of cosmic muons, allowing some of them to cross several hundred meters of rock.

Measurements from one single point of view enable the creation of 2D maps of an object. Nevertheless, by merging different 2D projections it is possible to obtain 3D information. This can be achieved either with one muon detector and successive measures from different locations or by encircling the object to image with several instruments.

A muography telescope suitable for transmission consists of one or several detectors that reconstruct the muon trajectory to infer its path through the object to image. The telescope, located downstream from the object, extrapolates the trajectory of the muons passing through the detector towards the object. Another possible configuration requires an additional telescope upstream the object, acting as a constraint to identify non-crossing muons [Procureur, 2018][xxv].

In both cases, the resulting muography image is composed of the accumulation of many muon tracks. The sharpness and accuracy of the image will depend on the angular resolution of the telescope, the scattering within the object and between the object and the telescope, and the inherent noise of the instrument itself.

- Deviation or scattering muography: The multiple Coulomb scattering originating from the interaction of muons with the nuclei of matter, seen in Figure 3.7 (Right), is dependent on the atomic number Z. An experimental setup suitable for scattering muography requires 2 trackers to measure the muon trajectory before and after crossing the structure. This allows determination of the diffusion angle and position of individual muons through the structure. The analysis of the spatial distribution and magnitude of muon scattering events provides information about the internal composition of structures. This technique is particularly useful in discriminating between materials of high, medium, and low atomic number, Z [Gnanvo, 2010][xxvi].

Compared to the transmission mode, the deviation muography mode requires installation of telescopes stacked on both sides of the object. The imaging time in this mode is usually much smaller. However, these two modes aim at different applications. Scattering muography is mostly valid for modest opacity, as the technique is only capable of reconstructing one scattering point. Objects inducing multiple scattering will produce images with artifacts.

3.2.3 Overview of forward and inverse problems

There are two different approaches to assess the interaction of muons with matter inside the object intended for imaging.

A direct approach takes into consideration the incoming muon flux falling upon the volume to image and applies physical theories to predict the outgoing flux by taking into account the matter properties (i.e., density distribution and material composition) and the volume's geometry and dimensions. This problem of predicting the result of measurements is called the forward modelling.

On the other hand, the inverse approach, best-known as inverse problem, aims at inferring the physical properties of matter via the measurement of muons [Tarantola, 1982][xxvii].

While the forward problem has (in deterministic physics) a unique solution, the inverse problem does not. As an example, consider measurements of the surviving muons after the passage of an obstacle: given the distribution of mass inside the obstacle, one can unequivocally predict the number of muons that will succeed in crossing the obstacle (forward problem), but there are different distributions of mass for the obstacle that give exactly the same outcome, and thus different valid solutions.

The scientific procedure for the study of a physical system in order to solve the inverse problem can be divided into the three different steps:

a) Parameterization of the geological target: establishing of a minimal amount of model parameters (e.g. sub-volumes with fixed density) whose values completely characterize the geological target
b) Forward modeling: implement the physical laws allowing to predict the results of measurements.
c) Iterative inverse modeling: make perturbation of the parameter values of the model in order to minimize the misfit between the measurements done and the modelled ones.

The inverse problem is an iteration process between the different steps, where the knowledge of the geological properties of the volume helps to create a more robust model and to converge faster to a solution for this problem [Tarantola, 2005][xxviii]. There is a strong feedback between these steps, and a good improvement in one of them is usually followed by advances in the other two.

The inverse problems have the particularity of being often unstable; by repeating the inversion of a given data set, the results may show important divergences. Thus, it is possible that the result of the inversion (despite being a valid solution) doesn't show a good agreement with reality [Pitt, 2002][xxix]. Regularization methods can be used to minimize this undesirable effect, but the most effective asset is to acquire as much data as possible to enhance the inversion stability to get a strongly coherent result [Demoment, 2001][xxx].

The resolution of the inverse problem to obtain precise density measurement requires dedicated Monte Carlo (MC) simulations. The inefficiency of classical MC simulations for large volumes and distant ~1 m^2 detectors leads

to very time- and resource-consuming calculations to estimate the muon flux crossing the object and the detector. A recent approach to enhance the resolution of the inverse problem is based on backwards MC techniques [Niess, 2017][xxxi]. This technique consists of simulating the muon flux starting from the detection plane towards the targeted volume. This guarantees to sample only useful events and increases the performance of the simulation.

3.3. Transmission muography through years, evolution and applications

The first tomographic application for muon measurements was proposed by George at the beginning of the 1950s [George, 1955][xxxii] to determine the overburden of a tunnel in an Australian mine by the measurement of the cosmic muon flux. Geiger counters were deployed both on surface and inside the mine to determinate the overburden induced by the ice at surface level. The measure established an opacity of 163±8 mwe, which was validated by the result of the drilling and sampling at the same site (175±6 mwe). At the time, George could determine the significant differences of soil thickness in different directions by moving the experimental setup. However, his detector was neither reliable nor precise enough to find density heterogeneities related to the presence of ores.

In the late 1960s, the Nobel Prize laureate, Luis Alvarez installed tracking detectors in the Belzoni chamber inside the pyramid of Kahfre. The objective was to reveal the existence of any void in the overlaying rock structure, indicator of the presence of hidden crypts or chambers. The experimental setup, seen in Figure 3.8 from [Alvarez, 1970][xxxiii], consisted in a stack of two spark chambers (1.8 m × 1.8 m) and three scintillators, one on the top and 2 at the bottom. An iron shield was included between the two lower scintillators to filter low energy particles. The acceptance of the detector covered 19 % of the volume of the pyramid.

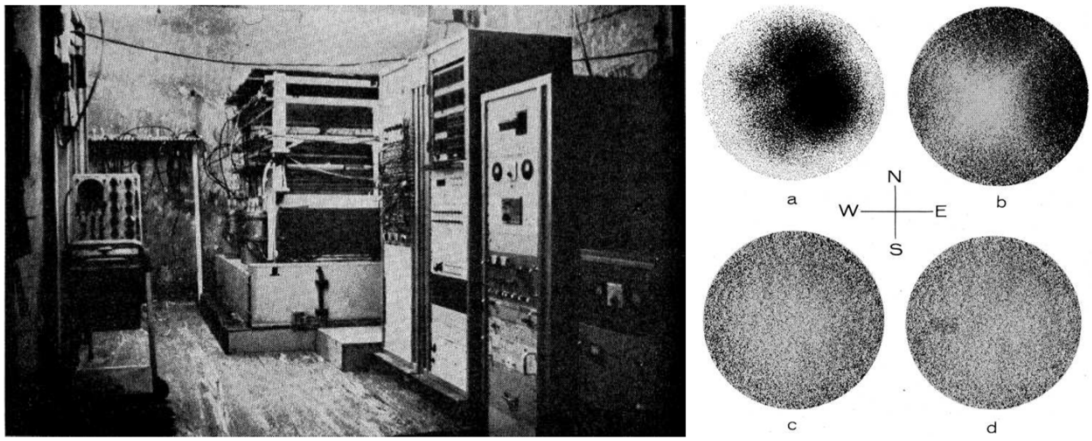

Figure 3. 8 (Left) Experimental setup of Alvarez inside the pyramid of Kahfre. (Right). The measured scatter plots (a) without any correction, (b) with correction for detector acceptance and (c) with correction on the surface heterogeneities of the pyramid; (d) is the result of the Monte Carlo simulation including the Kings' chamber.

The experiment recorded more than 10^6 muons, and the detector could determine the pyramid's corners location with a precision within 1 meter (Figure 3.8 (Right) b). Furthermore, a Monte Carlo simulation of the measurement was also performed (Figure 3.8 (Right) d). According to the results (Figure 3.8 (Right) c), the existence of a hidden chamber inside the explored volume was not confirmed.

In 2015, the Heritage Innovation Preservation (HIP) Institute launched a new scientific mission to probe the heart of the largest pyramids of Egypt with non-destructive techniques. In this occasion, three different technologies for transmission muography were installed in parallel. On the one hand, the University of Nagoya installed nuclear emulsion plates inside the Queen's chamber. On the other hand, KEK placed a scintillator hodoscope at the same location. Finally, the CEA installed three Genetic Multiplexed Micromegas based telescopes outside of the pyramid.

The analysis, seen in Figure 3.9 from from [Morishima, 2017][xxxiv], revealed a void, called ScanPyramids' Big Void. It was detected with a high confidence by three different muon detection technologies and three independent analyses. First observed by the Nagoya team, then confirmed by the other two teams, this finding represented a great leap forward for muography in terms of technology visibility among the non-scientific public.

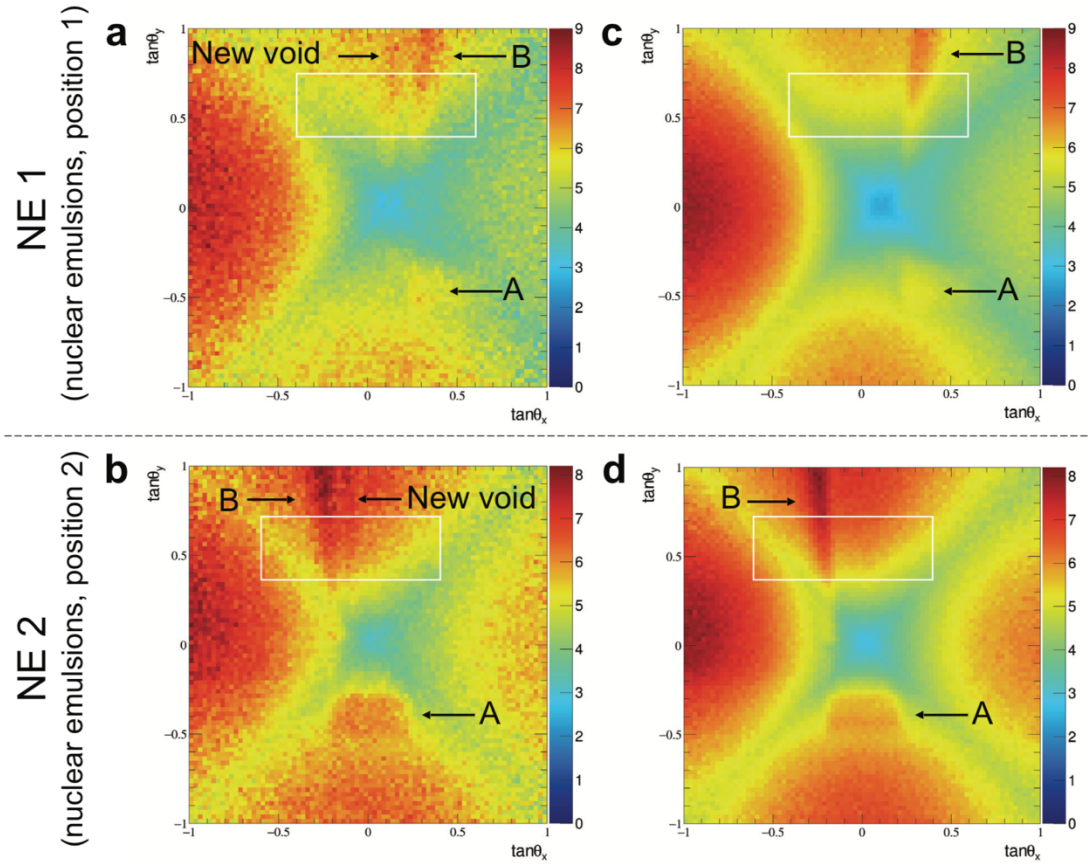

Figure 3. 9 Nagoya team ScaPyramid's results: figures (a) and (b) are the experimental measurements and (c) and (d) the result of MC simulations. A & B areas represent known cavities: King's chamber and Grand Gallery respectively.

Currently, there are other groups working in archeology with different muon techniques such as:

- METROPOLIS project, which uses scintillator hodoscopes in order to monitor the Bourbonic tunnel at mount Echia site in Italy [Saracino, 2017][xxxv].

- The *Universidad Nacional Autonoma de México* is searching for hidden chambers at the Teotihuacan Pyramid of the Sun with multiwire proportional chambers [Menchaca-Rocha, 2011][xxxvi].

Other than archeology, volcanology was among the firsts scientific disciplines to include muography in its toolbox.

In 1995, Nagamine proposed muography to image the inside of volcanic edifices [Nagamine, 1995][xxxvii], and eventually to predict eruptions. He conceived a plastic scintillator hodoscope with an adjustable acceptance by playing with the relative distance between the two detection planes. The first results allowed to successfully recognize the profile of Mt. Tsukuba, a non-volcanic site.

A few years later, the team of Hiroyuki Tanaka performed the first muographic measurements of an active volcano at Mt. Asama. The shielding layer between the detection planes allowed the discrimination of low energy radiation, and thus noise reduction [Tanaka, 2001][xxxviii]. The acquired data in this campaign and in 2003 was in good agreement with MC simulations and revealed the presence of the volcanic crater, as seen in green in Figure 3.10 from [Tanaka, 2003][xxxix].

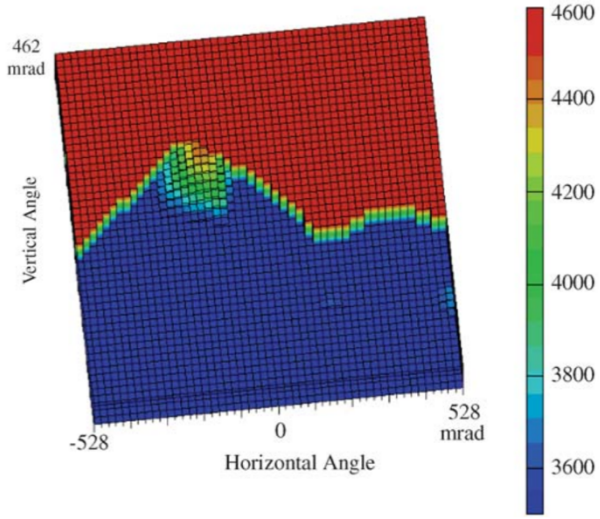

Figure 3. 10 Muon radiography of Mt. Asama. The green concavity represents the volcanic crater. It is visible thanks to the higher muon flux compared to the rest of the mountain (blue).

After the eruption of 2004, Mt. Asama could not be accessed, and conventional geophysical methods, such as electromagnetic and seismic techniques could not be performed. Tanaka et al. deployed nuclear emulsion detectors with the aim of detecting the differences due to the eruption. The results of their measurements, shown in Figure 3.11 from [Tanaka, 2007][xl], permitted identification of structural changes in the volcano associated with the eruption.

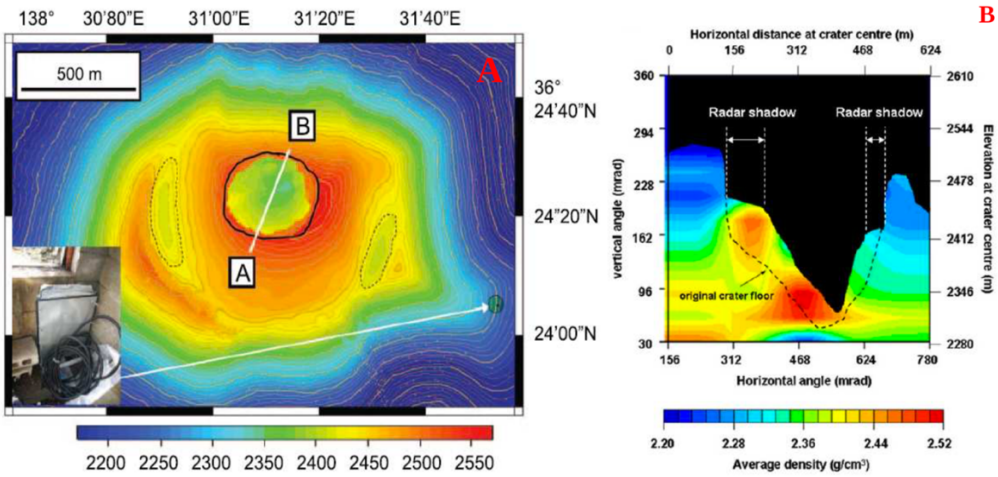

Figure 3. 11 (A) Map of the Asama volcano with the location of the emulsion cloud chamber with an arrow. The section AB shows the plane of the density distribution plotted in panel B. The solid black line shows the summit crater. (B) Reconstructed average density distribution of the summit crater, showing the solidified magma (red zone) at the crater floor.

The black dotted line in Figure 3.11(B) shows the original crater floor, visible in Figure 3.10. It Is possible to recognize the solidified magma region, and the low-density zone just below the magma, associated with the magma conduit.

Despite the success of achieving the first muographic image of an active volcano, the emulsion cloud chambers are not applicable to perform live measurements of the density distribution of volcanoes due to the offline analysis. The real-time measurement of the lava movement inside the volcano is essential to predict the future eruptions.

The next innovative experiment was performed at Satsuma-Iwojima, during an eruption period. It obtained for the first time sequential muon radiographic images about the magma dynamics. The higher density magma ascended in the crater and the flow of the lower density volcanic gases was faster than the magma body. This observation was consistent with the models of volcanology [Shinobara, 2012][xli].

This was the starting point for several projects that will use different muon technologies to image volcanos:

- DIAPHANE project, born in 2008 in order to monitor the active volcanos at the French Antilles, with a particular focus on the Soufrière volcano at Guadeloupe island [Gilbert, 2010][xlii].

-TOMUVOL, created in 2009 to monitor the biggest volcanic region of Europe, in Auvergne, France. The monitored object is the Puy de Dôme volcano due to its proximity to the city of Clermont-Ferrand [Cârloganu, 2013].

-MU-RAY collaboration, from 2010, intends to perform volcano radiography, in particular at Mt. Stromboli, Mt. Vesuvius and Mt. Etna [Ambrosino, 2014][xliii].

The above experiments help to prove the added value of muon radiography for underground cavity research and for subsurface density mapping. However, the application-oriented development of particle detectors is necessary to fully exploit the potential of this technique.

Muography has proven to be useful in the field of civil engineering as well. In 2005 the French electric company EDF studied a technique in order to estimate the snow cover thickness of mountains, in order to predict the rise of water downstream due to the melt [Paquet, 2006][xliv].

Another example is the radiography of the Saclay water tower seen in Figure 3.12 from [Bouteille, 2017][xlv]. It is possible to observe both the evolution of the water level of the reservoir and the structural elements of the construction.

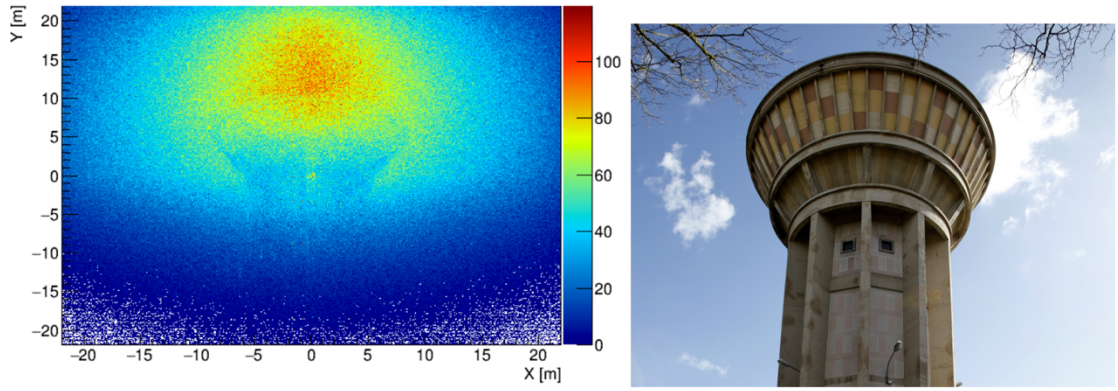

(a) Muograph. (b) Photograph.

Figure 3. 12 Muon radiography of the water tank of Saclay and an illustrative picture of the structure.

A recent application for muon tomography aims at monitoring the Carbon Capture and Storage (CCS) [Kudryavtsev, 2012][xlvi]. CCS has been proposed to minimize the greenhouse effect produced by the carbon dioxide.

A way to prevent the release of CO_2 into the atmosphere is by capturing CO_2 emissions at the source, mainly from power stations. Once compressed into a liquid, it could be stored typically 1.5 - 3.5 km beneath the seabed in depleted oil or gas fields, or saline aquifers.

Nevertheless, a challenge of CCS is the capability of measuring how full the underground storage sites are, and to understand the migration of CO_2 once stored underground.

The Sheffield University is developing a borehole muon detector, capable of fitting inside a 20 cm diameter hole and resistant to elevated temperatures (over 40º C). Currently, after a preliminary phase of simulations, there is a prototype of detector being tested at the Boulby underground laboratory [Thompson, 2014][xlvii].

To conclude, Table 3.1 summarizes the main projects working on muon tomography based on transmission, sorted by technology, which are today working on transmission-based muon tomography.

Table 3.1. Summary of the main projects working on muon tomography based on transmission, the technology used and its foreseen applications.

Detector family	Technology	Project	Foreseen application
Visual detection	Nuclear emulsion film	Nagoya Univ. (Japan)	Nuclear reactor imaging
	Nuclear emulsion film	Scan pyramids Nagoya Univ. (Japan)	Archeology
	Nuclear emulsion film	Bern Univ. (Switzerland)	Glacier mapping
	Nuclear emulsion film	Involcan-Iter-ERI (Spain-Japan)	Volcanology
	Cherenkov telescope	Astri (Italy)	Volcanology
Scintillator hodoscope	Plastic scintillators	Muraves - Metropolis (Italy – Belgium - Japan)	Volcanology Archeology
	Plastic scintillators	DIAPHANE (France)	Volcanology Civil structures
	Borehole plastic scintillators	Deep carbon (U.K.)	CO_2 storage monit.
	Plastic scintillators	Kyushu Univ. (Japan)	Civil structures Education
	Plastic scintillators	CRM GeoTomography (Canada)	Geophysics

Detector family	Technology	Project	Foreseen application
Gaseous detector	Glass resistive plate chambers	TOMUVOL (France)	Volcanology
	Small gas-tight glass resistive chambers	Université catholique de Louvain (Belgium)	Muography in confined spaces
	Thick Gas Electron Multiplier	Sun Beam Lingacom (Israel)	Geophysics
	Multiwire proportional chamber	UNAM Univ. (Mexico)	Archeology
	Multiwire proportional chamber	REGARD (Hungary)	Geophysics
	Genetic multiplexing multilayer Micromegas	Scan pyramids CEA (France)	Archeology Civil structures
	Micromegas in Time Projection Chamber	T2DM2 (France)	Geophysics Hydrogeology Civil structures

3.4. Conclusion

Through the years, several devices have allowed muon detection based on different physical principles of its interaction with matter. Muon detection has evolved in parallel to major breakthroughs, such as the incorporation of computers in the data acquisition and analysis processes or the components industrial fabrication and miniaturization. Today there is a broad range of muon detection technologies with different assets depending on the targeted application.

Regarding the present work, the Micromegas family of detectors provide a versatile tool to perform temporal monitoring of the muon flux with a compact and light detector. Different configurations of Micromegas detectors, such as the multilayer detector or the time projection chamber, are currently used to perform muon tomography measurements in different domains.

Muography provides reliable, original and independent information. Used as a complementary method in several disciplines (e.g., volcanology, nuclear management or geological surveys), eases the resolution of the inverse problem to obtain the density distribution.

3.5. References

[i] F. Sauli (1977). Principles of operation of multiwire proportional and drift chambers. CERN 77-09.

[ii]Bozza, C. et al. (2017). Nuclear emulsion techniques for muography. Annals of geophysics, 60, 1, S0109

[iii] Morishima, K., Procureur, S. et al. (2017) Discovery of a big void in Khufu's Pyramid by observation of cosmic-ray muons. Nature Vol. 552, 386

[iv] Tanaka, H.K.M., et al. (2007). High resolution imaging in the inhomogeneous crust with cosmic-ray muon radiography: the density structure below the volcanic crater floor of Mt. Asama, Japan. Earth Planet. Sci. Lett. 263 104.

[v] Morishima, K., et al. (2012). First demonstration of cosmic ray muon radiography of reactor cores with nuclear emulsions based on an automated high-speed scanning technology. Proceedings of the 26th Workshop on Radiation Detectors and Their Uses in KEK, 27-36.

[vi]Catalano, O., Del Santo, M., Mineo, T., Cusumano, G., Maccarone, M.C., Pareschib, G. (2016). Volcanoes muon imaging using Cherenkov telescopes. Nucl. Instr. Meth. Phys. Res. Section A. Vol. 807, 5-12

[vii] Jourde, K. (2015) Un nouvel outil pour mieux comprendre les systèmes volcaniques: la tomographie par muons, application à la Soufrière de Guadeloupe. Doctoral dissertation.

[viii] Rutherford, E., & Geiger, H. (1908). An electrical method of counting the number of α -particles from radio-active substances. Proceedings of the Royal Society of London. Series A, 81, 141–161. doi:10.1098/ rspa.1908.0065

[ix] Townsend, J. S., & Kirkby, P. J. et al. (1901). Conductivity produced in hydrogen and carbonic acid gas by the motion of negatively charged ions. Phi. Mag., &. Journal of Science, 1, 630–642

[x] Chikovanii, G. E., Roinishviki, V. N., & Mikhailov, V. A. (1964). Operation mechanism of the track spark chamber. Nuclear Instruments and Methods, 29, 261–269. doi:10.1016/0029-554X(64)90378-7

[xi] Charpak, G., Bouclier, R., & Bressani, T. et al. (1968). The use of multiwire proportional counters to select and localize charged particles. Nuclear Instruments and Methods, 62, 262–268. doi:10.1016/0029- 554X(68)90371-6

[xii] Parkhomenchuk, V. V., Pestov, Y. N., & Pertovykh, N. V. (1971). A spark counter with large area. Nuclear Instruments and Methods, 93, 269–270. doi:10.1016/0029-554X(71)90475-7

[xiii] Raveendraba, k. et al. (2016) Study of glass properties as electrode for RPC. Conference proceedings of 13th Workshop on Resistive Plate Chambers and Related Detectors (RPC2016). doi: 10.1088/1748-0221/11/07/C07007

[xiv] Cârloganu, C. et al. (2013). Towards a muon radiography of the Puy de Dôme. Geosci. Instrum. Method. Data Syst., 2, 55–60

[xv] Wuyckens, S., Giammanco, A., Demin, P. and Cortina Gil, E. (2018). A portable muon telescope based on small and gas-tight Resistive Gas Chambers. arXiv:1806.06602v1

[xvi] Oed, A. (1988). Position-sensitive detector with microstrip anode for electron multiplication with gases. Nuclear Instruments and Methods in Physics Research, 251, 35.

[xvii] Charpak, G., Crotty, I., & Giomataris, Y. et al. (1994). A high-rate, high-resolution asymmetric wire chamber with microstrip readout. Nuclear Instruments and Methods in Physics Research, A346, 506–509. doi:10.1016/0168-9002(94)90585-1

[xviii] Y. Giomataris et al. (2006). Micromegas in a Bulk. Nucl.Instrum.Meth. A560, 405-408

[xix] T Alexopoulos et al. (2011). A spark-resistant bulk-micromegas chamber for high-rate applications. Nucl. Instr. Meth. Phys. Res. Section A. Vol. 640.1, 110–118.

[xx] Francke, T. snd Peskov, V. (2014). Innovative Applications and Developments of Micro-Pattern Gaseous Detectors. Engineering Science Reference. ISBN 978-1-4666-6014-4

[xxi] Lesparre, N., Gibert, D., Marteau, J., Komorowski, J. C., Nicollin, F. & Coutant, O. (2012). Density muon radiography of La Soufriere of Guadeloupe volcano: comparison with geological, electrical resistivity and gravity data. Geophysical Journal International, 190, 1008-1019. DOI :10.1111/j.1365-246X.2012.05546.x.

[xxii] Portal, A., Labazuy, P., Lénat, J. F., Béné, S., Boivin, P., Busato, E., Cârloganu, C., Comba- ret, C., Dupieux, P., Fehr, F., Gay, P., Laktineh, I., Miallier, D., Mirabito, L., Niess, V. & Vulpescu, B. (2013). Inner structure of the Puy de Dôme volcano: cross-comparison of geophysical models (ERT, gravimetry, muon imaging). Geoscienti c Instrumentation, Methods Data Systems, 2, 47-54. DOI :10.5194/gi-2-47-2013.

[xxiii] Nishiyama, R., Tanaka, Y., Okubo, S., Oshima, H., Tanaka, H. K. M. & Maekawa, T. (2014). Integrated processing of muon radiography and gravity anomaly data toward the realiza- tion of high-resolution 3-D density structural analysis of volcanoes; case study of Showa- Shinzan lava dome, Usu, Japan. Journal of Geophysical Research: Solid Earth, 119, 699-710. DOI :10.1002/2013JB010234.

[xxiv] Jourde, K., Gibert, D., and Marteau, J. (2015). Improvement of density models of geological structures by fusion of gravity data and cosmic muon radiographies. Geosci. Instrum. Method. Data Syst., 4, 177–188.

[xxv] Procureur, S. (2018). Muon imaging: Principles, technologies and applications. Nucl. Instr. Meth. Phys. Res. Section A. Vol. 878, 169-179

[xxvi] Gnanvo, K. et al. (2010). Detection and Imaging of High-Z Materials with a Muon Tomography Station Using GEM Detectors. CERN RD51-Note-2010-004

[xxvii] Tarantola, A. et B. Valette (1982). Inverse problems= quest for information. Journal of Geophysics 50(3), 150–170.

[xxviii]Tarantola, A. (2005). Inverse problem theory and methods for model parameter estimation. Society for Industrial and Applied Mathematics, Philadelphia.

[xxix] Pitt, M. et I. Myung (2002). When a good fit can be bad. Trends in cognitive sciences 6 (10), 421–425.

[xxx] Demoment, G. et Y. Goussard (2001). Approche bayésienne pour les problèmes inverses, Chapitre Inversion dans un cadre probabiliste, pp. 59–77. Hermès - Lavoisier, Paris.

[xxxi] Niess, V. et al. (2017). Backward Monte-Carlo applied to muon transport. arXiv:1705.05636v2.

[xxxii] George, E. P. (1955). Cosmic rays measure overburden of tunnel. Commonwealth Engineer, 455-457.

[xxxiii] Alvarez, L. W., Anderson, J. A., Bedwei, F. E., Burkhard, J., Fakhry, A., Girgis, A., Go- neid, A., Hassan, F., Iverson, D., Lynch, G., Miligy, Z., Moussa, A. H., Mohammed & Yazolino, L. (1970). Search for hidden chambers in pyramids. Science, 167, 832-839. DOI :10.1126/science.167.3919.832.

[xxxiv] Morishima, K. et al. (2017) Discovery of a big void in Khufu's Pyramid by observation of cosmic-ray muons. Nature. Vol. 552, 386–390. doi:10.1038/nature24647

[xxxv] Saracino, G., et al. (2017). Imaging of underground cavities with cosmic-ray muons from observations at Mt. Echia (Naples). Scient. Reports. Vol 7, 1181. doi:10.1038/s41598-017-01277-3

[xxxvi] Menchaca-Rocha, A. (2011). Searching for cavities in the Teotihuacan Pyramid of the Sun using cosmic muons experiments and instrumentation. International Cosmic Ray Conference. Vol. 4. 325.

[xxxvii] Nagamine, K., Iwasaki, M., Shimomura, K., and Ishida, K. (1995). Method of probing inner structure of geophysical substance with the horizontal cosmic-ray muons and possible application to volcanic eruption prediction. Nucl. Instr. Meth. Phys. Res Section A, 356(2), 585–595.

[xxxviii] Tanaka, H., Nagamine, K., Kawamura, N., Nakamura, S. N., Ishida, K., and Shimomura, K. (2001). Development of the cosmic-ray muon detection system for probing internal-structure of a volcano. Hyperfine interactions, 138 (1-4), 521–526.

[xxxix] Tanaka, H., Nagamine, K., Kawamura, N., Nakamura, S., Ishida, K., and Shimomura, K. (2003). Development of a two-fold segmented detection system for near horizontally cosmic-ray muons to probe the internal structure of a volcano. Nucl. Instr. Meth. Phys. Res Section A 507(3), 657–669.

[xl] Tanaka, H., Nakano, T., Takahashi, S., Yoshida, J. & Niwa, K. (2007). Development of an emulsion imaging system for cosmic-ray muon radiography to explore the internal structure of a volcano, Mt. Asama. Meth. Phys. Res Section A, 575, 489 497. DOI :10.1016/j.nima.2007.02.104.

[xli] Shinohara, H. & Tanaka, H., 2012. Conduit magma con- vection of a rhyolitic magma: Constraints from cosmic- ray muon radiography of Iwodake, Satsuma-Iwojima volcano, Japan, Earth and Planet. Sci. Lett., 349–350, 87–97.

[xlii] Gibert, D., Beauducel, F., Déclais, Y., Lesparre, N., Marteau, J., Nicollin, F., and Tarantola, A. (2010). Muon tomography : Plans for observations in the Lesser Antilles. Earth, Planets and Space, 62(2) :153–165.

[xliii] Ambrosino, F., Anastasio, A., Basta, D., Bonechi, L., Brianzi, M., Bross, A., Callier, S., Caputo, A., Ciaranfi, R., Cimmino, L., D'Alessandro, R., D'Auria, L., Taille, C. d. L., Energico, S., Garufi, F., Giudicepietro, F., Lauria, A., Macedonio, G., Martini, M., Masone, V., Mattone, C., Montesi, M. C., Noli, P.,

Orazi, M., Passeggio, G., Peluso, R., Pla-Dalmau, A., Raux, L., Rubinov, P., Saracino, G., Scarlini, E., Scarpato, G., Sekhniaidze, G., Starodubtsev, O., Strolin, P., Taketa, A., Tanaka, H. K. M., Vanzanella, A., and Viliani, L. (2014). The MU-RAY project : detector technology and first data from Mt. Vesuvius. Journal of Instrumentation, 9(02), C02029–C02029.

[xliv] Paquet, E. and Laval, M. (2006). Experience feedback and future prospects for the use of EDF's Cosmic-Ray Snow Gauges.

[xlv] Bouteille, S. (2017). Développement et application de détecteurs gazeux à micro-pistes pour la tomographie muonique. Doctoral dissertation.

[xlvi] Kudryavtsev, V., Spooner, N., Gluyas, J., Fung, C. & Coleman, M. (2012). Monitoring sub- surface CO2 emplacement and security of storage using muon tomography. International journal of greenhouse gas control, 11, 21 24. DOI :10.1016/j.ijggc.2012.07.023.

[xlvii] Thompson, L. F. et al. (2014). The application of muon tomography to carbon storage monitoring. 4th EAGE CO_2 Geological Storage Workshop 2014.

Chapter 4. Physics of the detector.

Chapter 4 abstract

This chapter describes the physical principles and processes that enable the muon detection and reconstruction of its trajectory with a gaseous detector composed of time projection chamber (TPC) with a Micromegas readout plane.

When a muon enters the conversion and drift volume of the TPC, it creates along its track clusters of electron-ion pairs. The primary electrons so created are driven by an electric field to the position sensitive amplification structure, i.e. the Micromegas detector, where the electric field strength reaches significantly higher values. In this region the primary electrons experience an avalanche multiplication which enables the detection of signals generated by a small number of primary electrons.

The choice of gas mixture is a key parameter in enhancing the detection performance. The number, type and proportion of its components will influence the response of the detector during the entire signal formation process from the primary electron yield to the gain. The electric fields, present in both the drift volume and amplification gap, play a major role in the charge transport and multiplication.

A harmony between these elements is therefore required in order to meet a set of physical and technical constraints, with the aim of designing an optimized detector suitable for muon tomography as well as establishing the operational parameters according to the acquisition conditions.

4.1. Parameters that affect the physical processes

Numerous parameters influence the signal formation processes and affect the signal formation. Several authors have performed studies on the causality between a parameter variation and the change in the detector's performance. To cite some relevant examples, the gas and environmental variable parameters have been assessed by [Adloff, 2009][i], the humidity and dust effect on the leakage current were studied by [Wang, 2013][ii] and the micromesh geometrical aspects have been considered by [Kuger, 2017] [iii].

Each parameter might potentially affect multiple processes and in turn, each process is influenced by multiple parameters and affects several characteristics. Figure 4.1 summarizes the most impacting interactions of this system of dependencies.

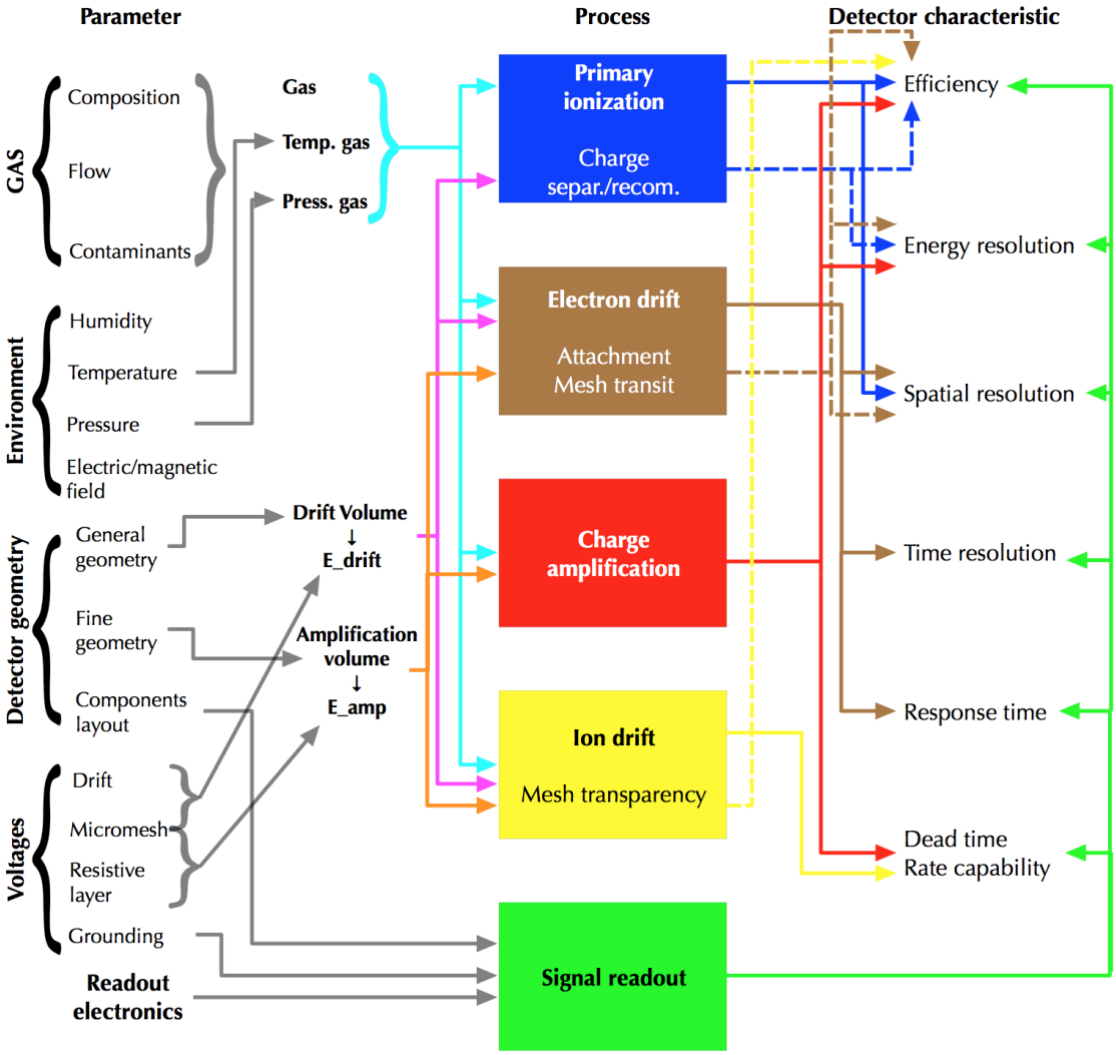

Figure 4. 1 Schematic flowchart with the MUST² detector physics processes. The parameters that affect the processes are listed at the left and the effects in the detector characteristics are on the right.

4.2. Time projection chamber

The Time Projection Chamber (TPC) idea was made possible thanks to the development of the Multi Wire Proportional Chamber (MWPC). The MWPC represents a powerful tool for particle identification and tracking. It provides the energy loss rate (stopping power dE/dx) and, in some cases, the particle energy. They have good spatial and time resolution, scalability, low material budget and high trigger rate capabilities. By including two superposed perpendicular wire planes, it is possible to infer the 3D spatial information. A stack of planes can be used to register slices of the ionization path.

A method to simplify this structure was proposed by David Nygren only six years after the invention of the MWPC [Nygren, 1978][iv]. He developed a technique to reconstruct the ionization path by projecting the electrons associated with the incident particle passage in a single detector. To do so, a constant electric field is applied inside a gaseous chamber, with the readout plane in the anode end. In this so-called time projection chamber, whose working principle is sketched in Figure 4.2, the electric drift field does not have to be very strong to avoid charge amplification, but intense enough to drive as orthogonally as possible the primary charges through the chamber towards the readout plane.

Despite the near-light speed of particles like muons traversing the time projection chamber, the much slower drift speed of electrons inside the gas allows the detector to quantify time differences with fast-enough front-end electronics. These relative delays, of a few tens of ns in our case, are generated during the drift of the primary charges to the readout plane. Hence, if the drift speed is constant, the delays are proportional to the relative distances between the particular positions where ionization was produced when projected on the drift field axis. The correct interpretation of these time differences allows the full three-dimensional reconstruction of the track.

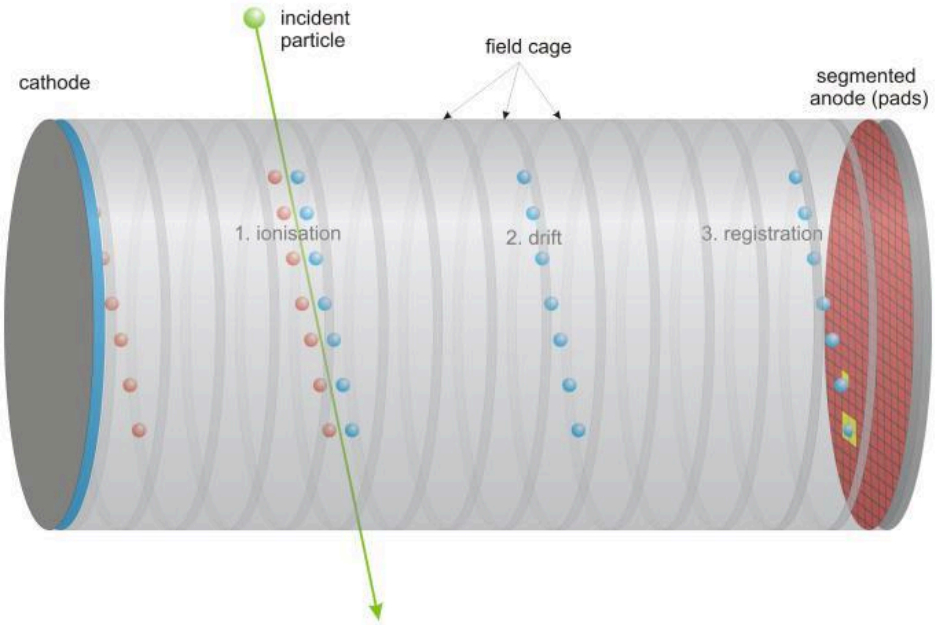

Figure 4. 2 Working principle of a TPC. Figure from LCTPC.org by O. Schäfer.

4.3. Gaseous detectors, principle of operation

The detection of a particle requires energy deposition by the traversing particle in the detector. Avalanche gaseous detectors were the first devices capable of detecting a low number of primary electrons created by ionization of a gas. This is due to the charge amplification produced when primary electrons trigger an avalanche of secondary electrons, ions, and photons in the detector region immersed in strong enough electric field. Electron multipliers are ideal noise free amplifiers, capable of amplifying a single electron with a gain[1] of up to $G=10^7$, and theoretically with no output signal in the absence of radiation. The signal formation in gaseous detectors covers a sequence of different physical processes and presents similarities between the different detector's families.

Figure 4.3 shows a simulation of the gas ionization after the passage of one charged particle and the subsequent electron transport under the operation conditions, for the geometry corresponding to the detector used in the present work[2]. The simulation was done with the software Garfield [Veenhof, 2010] [v].

In it, it is possible to differentiate the following characteristic regions explained above:

1) Conversion of the incident radiation (green line) into primary electrons (green dots) and ions. This conversion can happen and trigger signal formation anywhere in the detection volume, including the amplification zone.
2) Drift region of the TPC, where the primary electrons drift towards a multiplication region (electron paths in yellow line).
3) Level of the micromesh, which acts as a porous frontier between the drift and amplification zones.
4) Amplification zone where the primary electrons create many secondary electrons (brown dots), these secondary electrons drift towards the readout plane.
5) Collection electrode structure, capable of transmitting the signal to the readout electronics.

[1] The gain (G) is defined as the ratio between the number of primary electrons and secondary electrons.

[2] Gas blend: Isobutane 2%, CF_4 10% and Argon QS, E_{drift}= 600 V/cm, E_{amp}= 33 kV/cm, TPC height: 5 cm, amplification gap: 128 μm

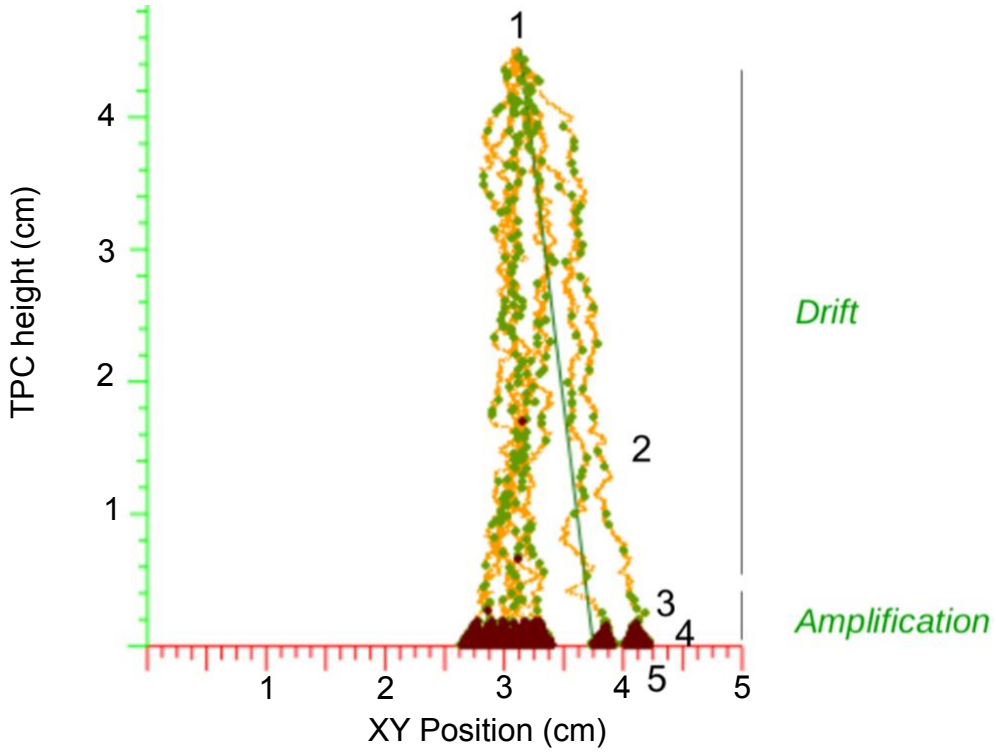

Figure 4. 3 Simulation of the passage of a muon inside the MUST[2] detector.

- Conversion and drift zone: In the first stage, the presence of an electric field ($\vec{E}_{drift}$) prevents electron-ion pairs from recombining and allows the signal development. The strength and shape of $\vec{E}_{drift}$ are designed to optimize the electron drift in terms of speed, diffusion[3] and trajectory deflection. Primary electrons are accelerated along the field lines, acquire momentum and will likely scatter with other gas constituents. Characteristic values for the drift process are the mean drift velocity, and the transversal (D_T) and longitudinal diffusion (D_L) of electrons.

- Amplification zone: The drifting electrons are guided to the amplification volume of higher field strength ($\vec{E}_{amp}$), where they accumulate more energy in-between collisions and hence become more likely to cause ionization. Each released electron is accelerated in turn and can cause further ionization leading to the formation of an electron avalanche (see Section 4.9.1 for more details). This charge amplification process is stopped once the electrons are either captured by a cation or the electrode, or the electric field strength is sufficiently reduced to provoke ionizing collisions. The output signal amplitude process depends in part on the electron yield resulting from this amplification process. A group of these secondary electrons created by one primary electron is called a cluster.

In parallel to the fast electrons travelling to the resistive anode of the Micromegas readout plane, the remaining ions drift slowly towards the cathode,

[3] Diffusion is the process of particles being deviated from a straight trajectory because of the multiple scattering caused by interactions such as collisions.

in our case the micromesh. This charge separation and subsequent movement induces a charge on both electrodes. The micromesh can also be used as a complementary readout structure when connected to electronics that allows measuring the current and processing it into a charge signal.

Although the secondary electrons resulting from the signal amplification might be collected on a readout electrode, the measured signal mainly depends on the relative movement of the charges in the amplification zone. The charge spread along the resistive layer during the discharge of the electrode is characterized by the Shockley–Ramo theorem. This theorem proposes that each charge q moving in the vicinity of an electrode at a speed v inside an electric field E will induce on the electrode a charge Q following Equation (4.1).

$$Q = \int E \cdot q \cdot v \, dt \tag{4.1}$$

4.4. Gas ionization

Primary electrons are produced by diverse mechanisms as seen in Figures 4.3 and 4.4. This process has several dependences: (i) the type of the gas compounds, (ii) the type of the ionizing particle, and (iii) the strength of the particular energy deposition. An incoming particle might stochastically ionize the gas when its energy exceeds the ionization potential of the gas, in which case it creates along its track -and nearby- a number of delta rays, (i.e. the secondary electrons kicked out from the gas atoms and molecules with enough energy to escape a significant distance away from the primary radiation trajectory and produce further ionization). These low energy delta electrons produce short and very dense ionization tracks as they slow down in the gas, and release in turn new electron-ion pairs. The result is dense clusters of electron-ion pairs along the track of the primary radiation.

Another mechanism for primary electron production is when a charged particle kicks out electrons from an inner shell of the atoms or molecules. This triggers a chain of phenomena, fluorescent photon emission and expulsion of Auger electrons.

The arbitrariness of this process is translated into discontinuous tracks with eventually large distances between two successive ionizations created by the same particle, mainly with large angle tracks (far from the orthogonal axis of the detector readout plane). This effect can be seen in the Figure 4.3 from [Kuger, 2017], where the arrival of secondary electrons is discontinuous.

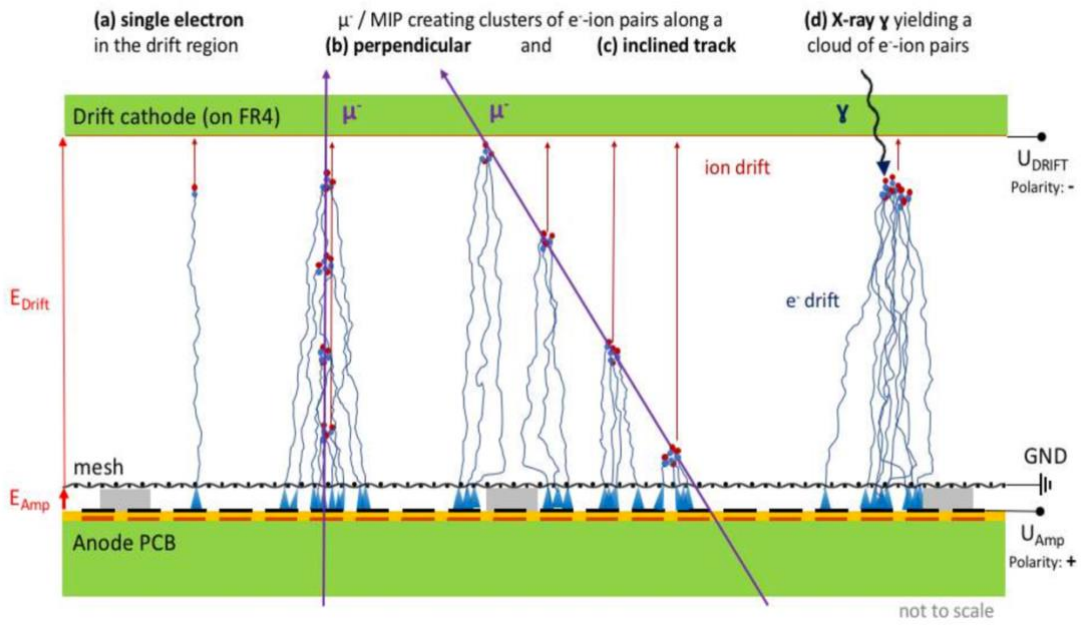

Figure 4. 4 Schematic section of a Micromegas detector, primary ionization and signal formation processes for different event types: (a) a single electron inserted in the detector; (b) perpendicularly or (c) inclined trespassing MIP; (d) electron-ion cloud caused by an X-ray photon. Blue dots and lines represent electrons while red is for cations.

The ionization yield is primarily determined by the gas mixture. The total number of produced electrons (N_T) can be calculated from the following relation:

$$N_T = \frac{dE/dx}{W_I} \tag{4.2}$$

where dE/dx is the deposited energy inside the detector volume and W_I is the mean energy required to produce an electron-ion pair. Table 4.1 provides an overview of the gas properties of the noble gas and compounds used in different gas blends to operate the detector MUST[2].

When the detector contains a gas blend instead of a pure gas, the interaction of the incoming particle with a homogeneous gas mixture can be seen as a successive transition through layers of a pure gas. The mean energy loss can be obtained by a weighted summation of the *i* components (Bragg rule of stopping power additivity), where the weighting factors p_i correspond to their proportion:

$$-\frac{dE}{dx} = \sum_i p_i \cdot \left(-\frac{dE}{dx}\right)_i \tag{4.3}$$

Table 4.1. Properties of gases at NTP (20ºC, 1 atm). E_X: first excitation energy; E_I: ionization energy; W_I average energy to produce an electron-ion pair; $dE/dx|_{min}$: differential energy loss; N_P: primary and N_T: total number of electron-ion pairs per cm for a unit charge minimum ionizing particle. Data from [Patrignani, 2016][vi].

Gas	Density $mg \cdot cm^{-3}$	E_X eV	E_I eV	W_I eV	$dE/dx\|_{min}$ $keV \cdot cm^{-1}$	N_P cm^{-1}	N_T cm^{-1}
Ar	1.66	11.6	15.7	26	2.53	25	97
CO_2	1.84	7.0	13.8	34	3.35	35	100
CF_4	3.78	10.0	16.0	54	6.38	63	120
iC_4H_{10}	2.49	6.5	10.6	26	5.67	90	220

The same principle can be applied to the average number of primaries N_P and total ionization N_T per path length, as well as for the average energy per electron-ion pair W_I. The fluctuation in the number of independent primary ionization processes is determined by Poisson statistics with $\sigma(N_P) = \sqrt{N_P}$. In our case, a Micromegas with a 5 cm height conversion and drift space, filled with Ar:CF_4:iC_4H_{10} (88:10:2), an average of 161.3 ± 12.7 primary interactions with the gas are expected heterogeneously distributed along a perpendicular track as the one seen in Figure 4.3 (b).

4.5. Signal strength

The signal strength (S) is used to define the charge deposited in the gas volume by a muon traversing a gaseous detector operated in a proportional mode[4], such as the Micromegas, and is directly related, among other parameters, to the gain of the detector, G.

In order to infer the deposited energy in the detector, the electronics must maintain the proportionality between S and the charge created in the detector's amplification stage and can be represented by the conversion factor $c_{r/o}$. In our case, the information relative to the passage of the muon is transferred to the detector in the TPC. Yet S is proportional to the amount primary electrons arriving in the amplification region. This is due to the fact that the majority of the charge is created in the amplification gap and collected on the resistive layer anode (electrons) and the micromesh (majority of cations). A small portion of the total number of ions, those generated in the conversion and drift volume, is collected in the drift cathode.

Theoretically, all primary electrons created during the primary ionization (N_T) should contribute to S. However, several processes contribute to a decrease

[4] The produced charge is proportional to the deposited charge by the muon.

in primary electrons before they reach the amplification zone or trigger an avalanche. This fraction of electrons lost (L) reduces the total charge yield during amplification, and thus the signal strength.

$$S = N_T \cdot (1 - L) \cdot G \cdot c_{r/o} \quad (4.4)$$

The electron loss is mainly due to three processes: recombination after primary ionization (R), attachment to gas constituents during scattering (A) and neutralization of the electrons (N). On the one hand, the origin and consequences of A is detailed in Section 4.7. On the other hand, in Micromegas-like detectors, the passage of electrons through the micromesh represents a critical stage for N and a fraction of electrons may be neutralized in this boundary zone. The fraction of surviving electrons (1 − N) is commonly called electron transparency (T) and its effect is seen in Section 4.8. Therefore (4.4) may be rewritten as:

$$S = N_T \cdot (1 - R) \cdot (1 - A) \cdot T \cdot G \cdot c_{r/o} \quad (4.5)$$

Unfortunately, the validity of the factorization (4.5) is limited due to the assumption of independence of the processes. While their independence is ensured on a per electron level, it is not guaranteed for variables summing over several electrons or processes undergoing interactions, such as R or A losses. Process factorization describes well enough a single electron response signal, but systems involving multiple electrons are commonly treated numerically to consider the possible interactions between the processes.

During the present work, to overcome the aforementioned constraint, the software MAGBOLTZ has been used [Biagi, 1999][vii]. It numerically solves the Boltzmann transport equations for electrons in gas mixtures under the influence of electric and magnetic fields, and takes into account the interactions between the processes of energy loss.

4.6. Drift of electrons and ions: gas choice

A detailed description of all the processes involved during the ion transport inside the detector would exceed the scope of this thesis. Therefore, only the basic considerations are considered in order to provide a general understanding of the matter.

Because of the electron production, positive ions (cations) are also generated in the gas volume at two different stages, gas ionization and amplification. Cations created by primary ionization in the conversion/drift volume are usually guided to the drift cathode and neutralized, while the primary electrons are utilized to create a signal. On the other hand, the movement of the cations within the amplification zone should be taken into account to characterize adequately the behavior of the detector: while the processes for electrons and ions are similar, ions move several orders of magnitude more slowly in the gas,

because of their larger mass. Their probability to undergo a scattering process is drastically reduced compared to electrons in the same electric field.

By applying Equation (4.1) in the case of a detector under a constant electric field, the charge Q will depend on the distance travelled by each charge. Since most of the ionizations happen de facto in the vicinity of the anode plane in the amplification zone (128 μm thick), the fast electrons will produce a prompt signal, and the cations a longer tail which represent as seen in Figure 4.5 found in [Bouteille, 2017][viii].

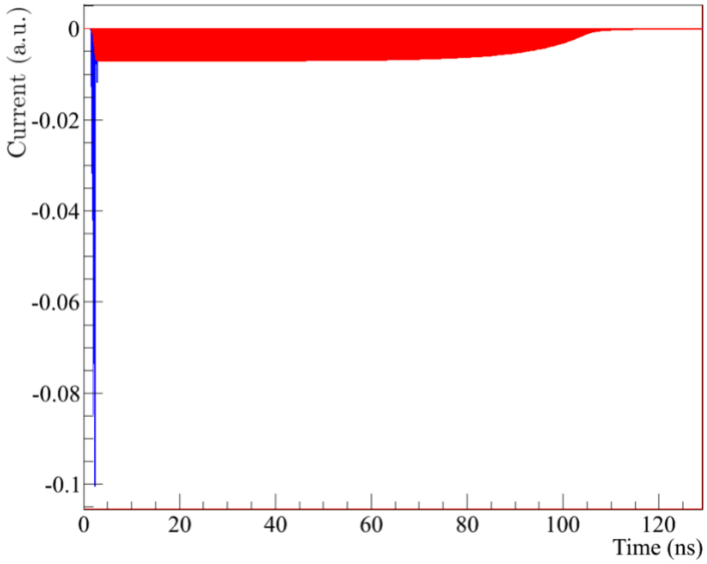

Figure 4. 5 Typical signals induced by electrons (blue) and ions (red) in a Micromegas detector.

The drift of the electrons through the detector towards the anode (readout plane) is a key process for a TPC. The deviation suffered by the electrons from the theoretical projection point, compared to its actual arrival position at the readout plane ($\sigma_{x,y}$), and the deviation of the expected arrival time (σ_t) produces a diffusion of the topological information that affects the TPC imaging accuracy (see Figure 4.2).

Electrons are not constantly accelerated by the $\vec{E}_{drift}$, but instead rapidly reach a steady drift velocity ($\vec{v}_d$), which manifests itself macroscopically. This drift speed can be more easily described by

$$\overrightarrow{v_d} = \mu_{ion} \cdot \vec{E}_{drift} \tag{4.6}$$

where μ_{ion} is the gas-dependent ion mobility, which does not vary with the electric field over a wide electric field range and is not significantly influenced by the mixture of the molecular gases. On the other hand, μ_{ion} depends on the pressure and temperature of the gas through the expression:

$$\mu_{ion}(P,T) = \mu_{ion}(P_0,T_0) \cdot {}^{T}/_{T_0} \cdot {}^{P_0}/_{P} \tag{4.7}$$

Mobilities for several ions in argon at Normal Temperature and Pressure (NTP) conditions are compiled in Table 4.2; the CO_2 is included due to the gas blend Ar:CO_2 (93:7) used punctually during an experiment to test the self-trigger induced by the micromesh. The mobility of ions in mixtures of gas can be obtained with Blanc's law:

$$1/\mu_{ion} = \sum_{j=1}^{n} p_j/\mu_{ionj} \tag{4.8}$$

where p_j is the volume fraction of gas j in the mixture and μ_{ionj} in the mobility of the ion in the gas j.

Table 4.2: Mobility of ions in argon at NTP (20ºC, 1 atm).

Main gas	Ion precursor	μ_{ion} $cm^2/(V \cdot s)$	Source
Argon	$self$	1.7	[McDaniel, 1973][ix]
	iC_4H_{10}[5]	1.56 2.15	[Schultz, 1977][x] [Yamashita, 1992][xi]
	CF_4	1.10	[Santos, 2017][xii]
	CO_2	1.72	[McDaniel, 1973]

The goal while running a TPC is to look for the highest mobility to rapidly flush the ions and minimize the deformation of the electric field. This further has a positive influence on the discharge probability, as a quick drain of space charge reduces the streamer formation probability (see Section 4.9.3 for more details about the streamer formation).

From the electron point of view, the optimum scenario is a gas that allows a long mean free path (low cross section) and hence, with a low possibility to absorb the electron. The electrons would be able to reach high velocities and be only driven by the drift field with small deviations. Unfortunately, low cross section and ease of ionization are frequently conflicting features for a simple gas, therefore mixtures are frequently used.

The most common choice is a gas mixture based in a noble gas with addition of a, usually small, amount of quencher[6] gas. The gas mixtures of the type Ar + CF_4 + hydrocarbon are recommended for applications in high rate drift

[5] The discrepancy of values is due to the assumption or not of the Blanc's law by the authors.

[6] Quenching refers to any process which decreases the fluorescence intensity.

chambers in terms of space charge problems [Yamashita, 1992]. The gas blend chosen for the current experience, Ar:CF_4:iC_4H_{10} (88:10:2), follows this strategy.

Although the pure argon gas has a low probability of interaction with muons, its tendency to elastic collisions produces an undesirable effect due to the dispersion of the direction of the electron's velocity in each collision. The cross section has a minimum at very low drift fields due to a quantum interaction between the electron and the gas molecule wave lengths, named the Ramsauer-Townsend minimum, which is related to a maximum in the drift velocity. On the other hand, the quench gas, CF_4 in our case, yields higher drift velocities; a high $\vec{E}_{drift}$ is however needed to balance out the high cross section.

Based on this strategy of combining gases with complementary properties, the interaction between the mean free path and the efficiency of the reset mechanism makes the drift speed as a function of the electric field develop a peak whose amplitude and position depend on the mixture composition: the higher the quench fraction, the faster the gas can be, but stronger $\vec{E}_{drift}$ are needed. This peak is clearly revealed in Figure 4.6 for green and purple gas mixtures.

The presence of isobutane, iC_4H_{10}, in the mixture is doubly justified due to its contribution to the amplification properties of the gas and to the important improvement of the pure noble gases drift features. Unfortunately, the elastic cross section of isobutane is also very high in contrast to CF_4. In consequence, even with higher fractions of isobutane, drift velocities larger than ~5 cm/μs cannot be surpassed in two-component argon-isobutane mixtures.

The minimal drift speed required to record the entire signal produced in the TPC (5 cm height) within a suitable time window for the chosen electronics (around 675 ns per event) is ~7,7 cm/μs. Therefore, a mixture of the three components is required for the correct operation of the detector.

Nowadays, with a better understanding of electron gas interaction processes on a microscopic level, and the availability of libraries with the different gases cross sections, the use of algorithms to calculate and predict drift properties becomes more and more affordable and widespread. In the present work, electron drift velocities and diffusion coefficients as a function of the electric field have been calculated with MAGBOLTZ. Figure 4.6 shows the result of simulations of electron drift speed depending on the electric field for different gas mixtures. The red dotted line represents the electric field necessary to obtain the maximal drift speed of the electrons with the gas mixture chosen for the MUST^2 detector, Ar:CF_4:iC_4H_{10} (88:10:2). The relatively flat zone close to highlighted point suggests that small variations in the drift electric field have a small impact in the electron drift speed.

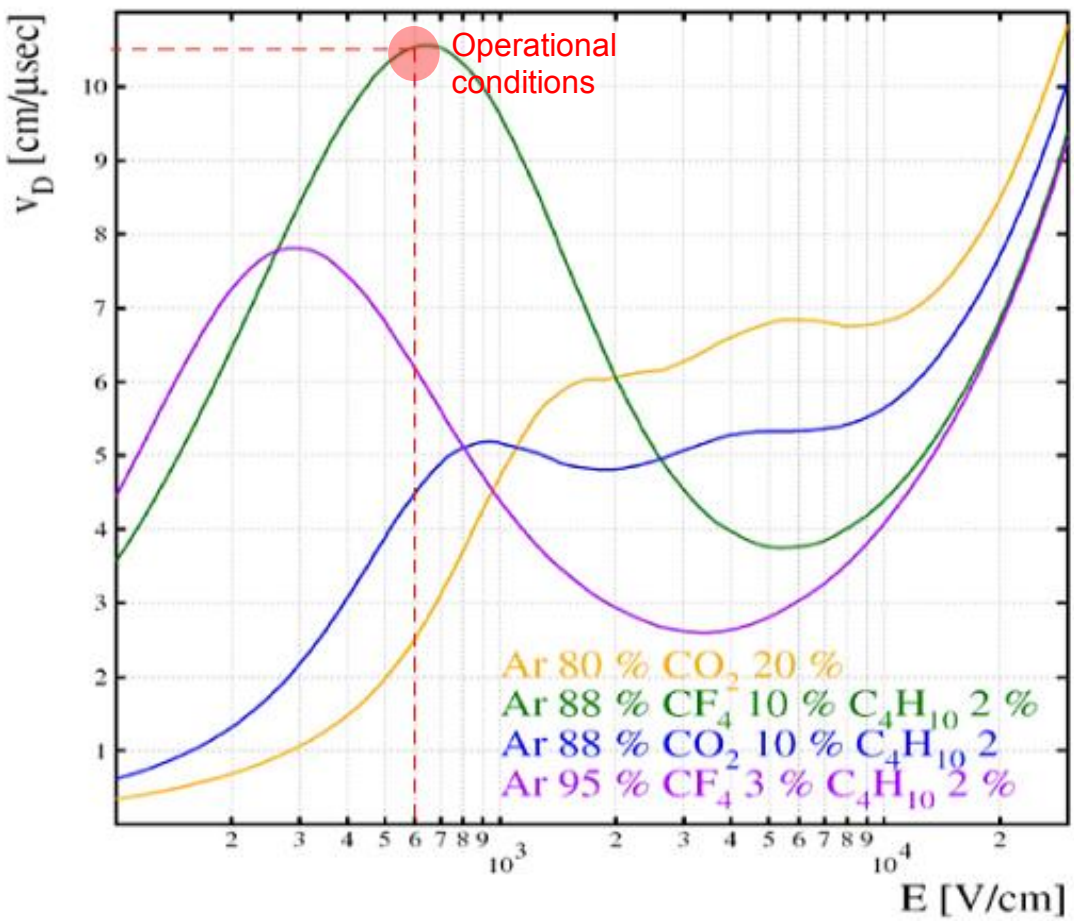

Figure 4. 6 Electron drift velocities as a function of the electric field for different gas mixtures calculated with MAGBOLTZ. The red dotted line marks the electronic drift velocity for the TPC operational conditions.

Section 5.3, dedicated to the gas characterization, provides more information about the simulations carried out in order to characterize the drift speed of the electrons in gas mixtures of Ar:CF_4:iC_4H_{10} with different proportions. The longitudinal (σ_z) and transversal ($\sigma_{x,y}$) diffusion of the electrons as a function of the $\vec{E}$ are also presented and discussed.

4.7. Effects of gas contamination

Apart from the gas mixture selection, the gas contamination can have a large impact on the attachment of electrons. The gas mixture in the detection volume may contain impurities as a result of an inaccurate gas fabrication process, out-gassing of components, the defective air-tightness of the gas circuit or an insufficient air-purge before operation. The main source of external contamination in our experimental setup is the (humid) atmospheric air. As seen in Equation (4.5) the loss of electrons by attachment (A) contributes to the loss of information. TPCs are especially sensitive to this effect due to their longer drift path.

The most abundant element in air, N_2, and other noble gases do not have electron attachment mechanisms. The contribution of minor components such as H_2 and CF_4 in atmospheric air is minuscule and its impact negligible. On the other hand, oxygen-based compounds such as O_2, H_2O and CO_2, give the largest attachment contribution to electron absorption as a result of the following processes:

$$e^- + O_2 \rightarrow O_2^- \quad (4.9)$$

$$e^- + O_2 \rightarrow O^- + O \quad (4.10)$$

$$e^- + H_2O \rightarrow H + OH^- \quad (4.11)$$

$$e^- + H_2O \rightarrow H_2 + O^- \quad (4.12)$$

$$e^- + H_2O \rightarrow HO + H^- \quad (4.13)$$

$$e^- + CO_2 \rightarrow CO + O^- \quad (4.14)$$

For electron scattering energies of 0.1-1.0 eV attachment losses are dominated by (4.9) [Biagi, 2015][xiii]. Therefore, electron losses by Oxygen contaminations are prevalent during drift in low electric fields (<500 kV/cm). For electron scattering energies >3 eV, dissociative attachments become more frequent [Itikawa, 2015][xiv]. While the total cross section maximum for (4.10) and (4.13) are higher, these processes have a higher energy threshold than (4.14). A rather large contamination with water vapor would contribute only with very strong drift fields ≥ 2 kV/cm.

Simulations by [Kuger, 2017] show that even the presence of 0.1% O_2 has an impact on the electron yield in low drift fields, with attachment losses over 10% for E_{drift} = 600 V/cm.

On the other hand, the presence of H_2O below 1% has a small effect on the general drift velocities and diffusion coefficients, and their effect on the attachment is expected to be unimportant. Unfortunately, the presence of humidity increases the probability of discharges between the micromesh and the resistive layer, with a series of unwanted consequences as described in Section 4.9.3.

With the aim to minimize the undesirable effects of the two aforementioned contaminants, the gas circuit includes specific filters for O_2 and H_20.

4.8. Mesh transparency

Many of the Micromegas assets derive from the division of the detector's volume into two subvolumes: the drift and the amplification regions. Nevertheless, a physical barrier, the micromesh, is placed between them. Introduced in Section 4.5, the mesh transparency (also known as electron transmission in early publications) refers to the survival probability of electrons while traversing this structure.

The micromesh is conceived to allow the electrons to pass, but some will be neutralized by the grounded mesh wires, with the subsequent loss of

information. The opposite phenomenon, but less probable occurs for ions: most of them will be collected in the micromesh but some can pass through it to the drift volume. We will pay special attention to primary electrons transiting from the drift volume to the amplification gap.

Figure 4.7 shows a zoom near the micromesh of a 2D electrostatic simulation of the MUST^2 detector with a carbon sputtered resistive layer. The reddish curves represent the isovoltage lines, its values inside the amplification gap vary from 0V (grounded micromesh) to +440V at the resistive layer stripes. The scale goes to -3kV due to the TPC simulation, also considered. Black traces indicate the field lines, which reveal the most probable path for the charge drift towards the resistive anode or drift cathode for electrons and cations respectively.

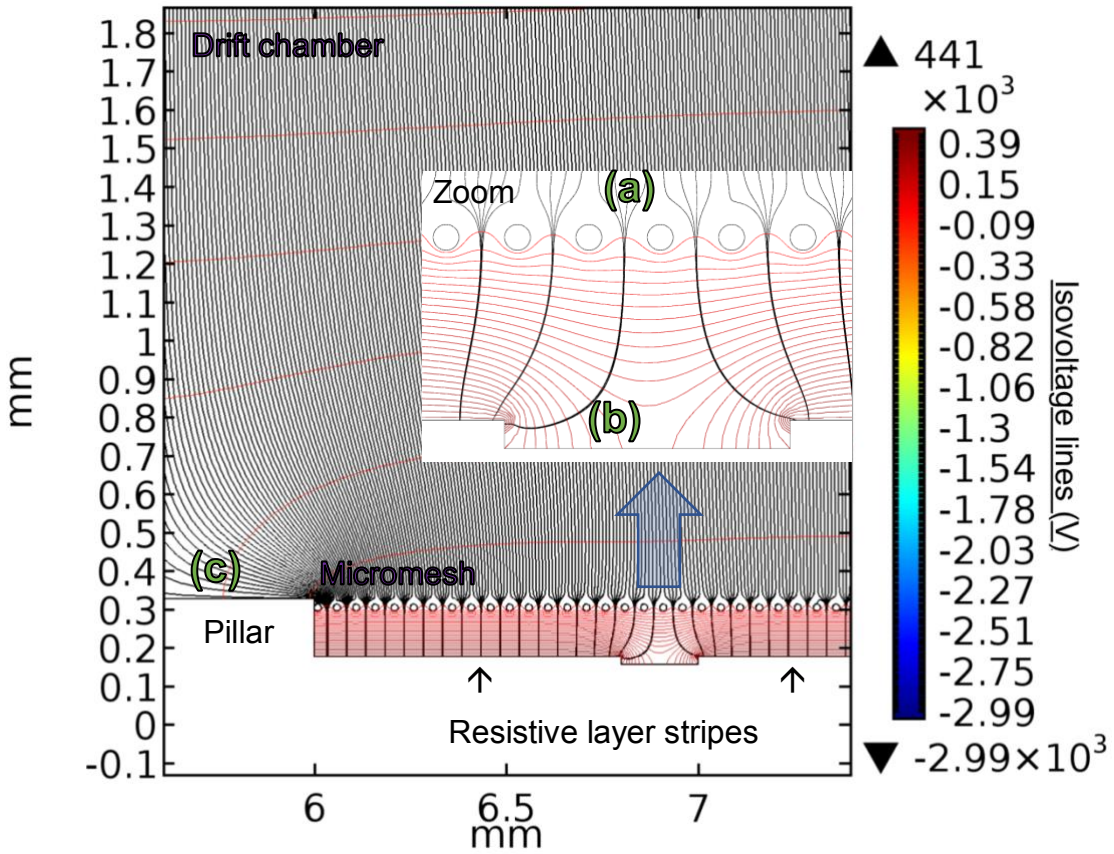

Figure 4. 7 Electrostatic simulation near the micromesh, performed with COMSOL multiphysics®[xv].

It is possible to appreciate the funnel-like distortion of the field lines near the micromesh (a) due to the transition between $\vec{E}_{drift} \rightarrow \vec{E}_{amp}$. Punctual distortions close to the resistive layer stripes (b) and the pillars that hold the micromesh are also noticeable (c).

The analytic description of the transparency of Micromegas detectors has been approached by assessing the fraction Ω_{mesh} of field lines terminating on the wire or mesh compared to the total originating from the cathode. The Micromegas case is not suitable for a two dimensions simplification [Bunemann, 1949][xvi],

instead an approximation by two successive grids of crossed wires with the same values for $\vec{E}_{drift}$ and $\vec{E}_{amp}$ was proposed by [Sauli, 2014][xvii] as follows:

$$T \leq (1 - \Omega_{mesh})^2 \tag{4.15}$$

where:

$$\Omega_{mesh}(E_{drift}, E_{amp}, \rho) = \frac{(E_{drift} + E_{amp})}{\pi \cdot E_{drift}} \cdot \sqrt{\rho^2 - \left(\frac{E_{amp} - E_{drift}}{E_{drift} + E_{amp}}\right)^2} - \\ - \frac{(E_{amp} - E_{drift})}{\pi \cdot E_{drift}} \cdot cos^{-1} \cdot \left(\frac{E_{amp} - E_{drift}}{E_{drift} + E_{amp}} \cdot \frac{1}{\rho}\right) \tag{4.16}$$

and $\rho = 2\pi r/p$ is a geometrical factor with r the radius of the wire and p the pitch of the micromesh. The expression (4.16) is valid within the range ${}^{1-\rho}/_{1+\rho} < {}^{E_{amp}}/_{E_{drift}} < {}^{1+\rho}/_{1-\rho}$. For values of ${}^{E_{amp}}/_{E_{drift}}$ above the upper limit, the transparency tends towards 1. In our case, the geometrical factor of the micromesh $\rho = 2 \cdot \pi \cdot 9\mu m/63\mu m \approx 0{,}898$ and the upper limit is therefore 18,5. Given an electric field ratio ${}^{E_{amp}}/_{E_{drift}}$ ≈50-55[7], the theoretical transparency is optimal.

Nevertheless, the analytic approach neglects the effect of electron scattering during the drift. To take these effects into account, a full simulation of the microscopic processes is be required.

To characterize the electron movement across three dimensional woven meshes, the COMSOL Multiphysics® software has been used as simulation tool. The AC/DC Electrostatic module has been used along with the module for the transport of diluted species. The first module creates the electric field framework, and the second simulates the drift of electrons by analogy to the mass transport of a dissolved species (solute species) or a component in a gas mixture.

The simulation was carried out by modeling a unit cell of 1cm^2 that contains all the representative readout elements: resistive layer stripes and X and Y readout stripes. The mesh geometry was simplified due to the requirement of computing resources to simulate its actual shape of interwoven wires.

Instead of a woven mesh, the micromesh is represented as a grid-like flat volume made of 18 µm thick stainless-steel, with squares holes of 63 µm side. The amplification gap thickness is 128 µm and the drift distance 5 mm.

The chamber was flushed with Ar:CF_4:iC_4H_{10} (88:10:2). The gas mixture's traverse and longitudinal diffusion coefficients have been calculated with the

[7] The ratio considers E_{drift}= 600 V/cm and E_{amp} ≈ 30-33 kV/cm, which corresponds to V_{drift}= -3000 V and V_{res}= 380-420 V.

Garfield software for the detailed simulation of two- and three-dimensional drift chambers.

The drift electric field has been fixed to 600 V/cm for the reasons detailed in Section 4.6, and the ratio E_{amp}/E_{drift} has been sampled by varying E_{amp}.

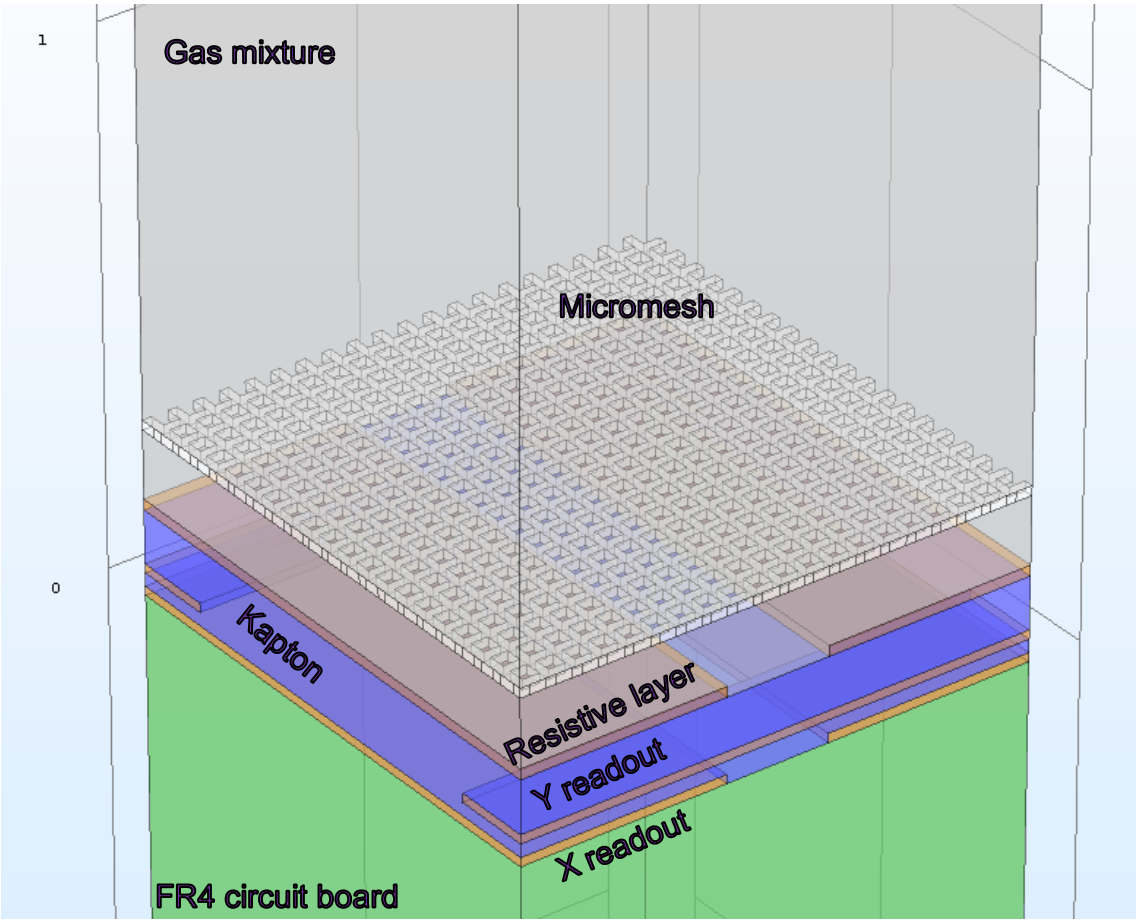

Figure 4. 8 Scheme of the unit cell of the Micromegas detector. Performed with COMSOL multiphysics®.

The determination of the electron transparency was accomplished by placing two probes within the assessed volume, the first one in the micromesh volume and the second one comprising the rest of the gas volume. Transparency was calculated as the ratio between the number of electrons into the amplification gap compared to total number of electrons produced.

Figure 4.9 summarizes the results of the transparency simulations. Larger values of the electric field ratio lead to better transparency values. Nevertheless, if the E_{drift} has to remain constant, the rise of E_{amp} may lead to the creation of sparks, streamers or other undesirable process presented in Section 4.9.

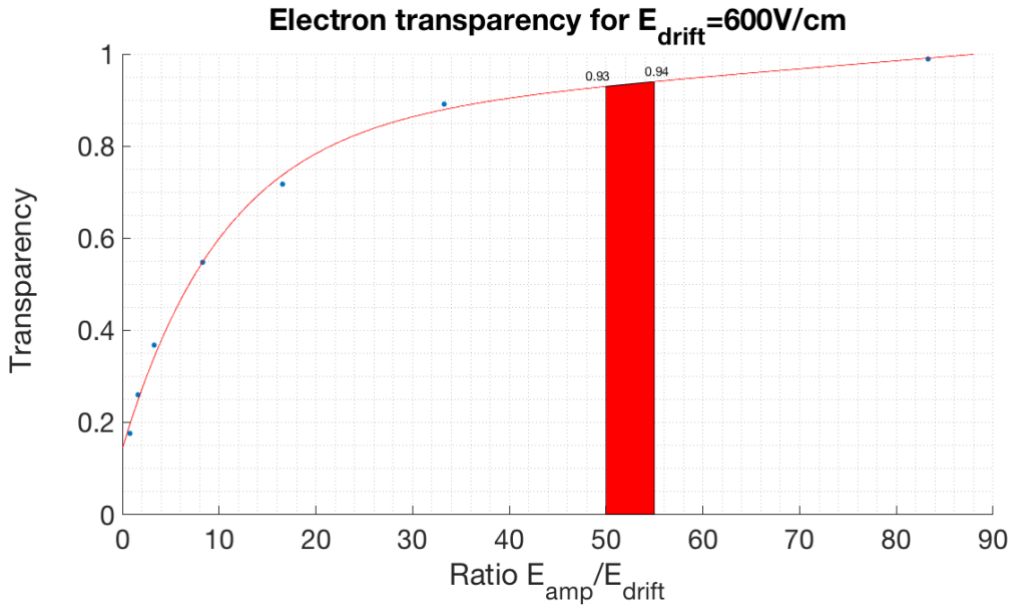

Figure 4. 9 Results of transparency simulations.

For the technical reasons stated above, the operation zone of the MUST[2] is in the interval of field ratios between 50 and 55. The calculated values of transparency for this region of interest vary from 93 to 94 ± 9,6%. The values here presented are consistent with the results obtained by [Kuger, 2017], who performed a detailed simulation of different kinds of mesh models under different electric fields and gas mixtures.

Square wires are much simpler to model than woven meshes and less time-consuming when performing simulations. Nevertheless, when compared against experimental data, this kind of coarse approach leads to simulated transparencies lower than the actual experimental measures [Nikolopoulos, 2011][xviii]. In reality, for the type of mesh used (geometrical parameters and interweave), the low drift electric field (< 700 V/cm) and high ratio E_{amp}/E_{drift}, the detector transparency is very close to 1 and its effect can be neglected for the current application.

4.9. Avalanche multiplication

The primary electrons created by radiation in the drift/conversion region are transported by an electric field to the multiplication structure where the electric field strength reaches significantly larger values. In this region the primary electrons experience avalanche multiplication.

4.9.1 Gain

The survival electrons entering into the amplification gap of the detector (n_0), also called signal electrons, undergo acceleration within a strong electric field (E_{amp}). They can accumulate enough energy between collisions to cause ionization, thus releasing an additional free electron. As seen in Section 4.4, a free electron can acquire sufficient kinetic energy E_k to ionize the gas atoms or molecules via inelastic collisions (if $E_k > E_i$) so that after the collision another free electron appear in the gas.

Repetition of this charge amplification process by the initial, as well as the newly released electrons, causes a cascade of electron multiplication, typically referred to as an electron avalanche, first discovered by J. Townsend [Townsend, 1901][xix].

Mathematically this avalanche process can be described by:

$$\frac{dn_e(x)}{dx} = \alpha \cdot n_e \tag{4.17}$$

where $n_e(x)$ is the number of avalanche electrons at a given position x along the amplification direction, and α is the first Townsend coefficient. The total number of electrons created in the avalanche after passing a distance d will be:

$$N_e = n_0 \cdot exp\left(\int_0^d \alpha \cdot dx\right) \tag{4.18}$$

Thus, when the electric field is uniform, α is constant and the number of electrons reaching the anode (N_e) depends on the distance between the two electrodes (d) and the number of electrons that trigger the avalanche:

$$N_e = n_0 \cdot e^{\alpha \cdot d} \tag{4.19}$$

Considering the gain (G) as the ratio of the number of signal-to-produced-electrons, Equation (4.19) can be rewritten as follows:

$$G = e^{\alpha \cdot d} \tag{4.20}$$

Nevertheless, the Micromegas amplification gap does not behave like a perfect parallel plate device due to the micro-mesh and cathode non-flat geometry. As a consequence, the distance parameter between electrodes does not define accurately the system and the amplification field presents heterogeneities.

The generalized form of the reduced first Townsend coefficient is given by the expression [Davidov, 2006][xx]:

$$\frac{\alpha}{\rho} = A \cdot exp\left(\frac{-B \cdot \rho}{E}\right) \tag{4.21}$$

where ρ is the molecular density of the gas and A and B are parameters depending on the gas type and electric field range.

During operation, the larger number of photons emitted in radiant de-excitation increases as well. A photo-electric effect at the cathode of the Micromegas detector, the micromesh, frees an electron which in turn triggers a secondary avalanche. These secondary avalanches occur potentially delayed and displaced with respect to the initial avalanche due to the distance travelled by the photon (unaffected by the electric field) and they are often experimentally not distinguishable.

Therefore, a measured gas gain G_{exp} is biased by the statistical occurrence of secondary avalanches:

$$G_{exp} = \frac{G}{1-\beta \cdot G} \tag{4.22}$$

where β is the second Townsend coefficient, representing the mean probability to trigger a secondary avalanche per electron in the initial avalanche.

The mean gain G and its relative variance are the two macroscopic measurable parameters for assessing the electron amplification. Correctly setting the gain of the detector is a prerequisite for its successful operation.

The gain variance inherent to the stochasticity of the process, on the other hand, is the determining factor for the detector's energy resolution. Gain variance might be accurately modeled by a Polya distribution [Eggenberger, 1923][xxi].

The targeted application for the MUST^2 detector, muon transmission tomography, relies on the determination of the origin and flux of incoming muons and does not require mandatorily to determining the energy loss of the muons.

4.9.2 Operation modes

The performance of gaseous detectors is strongly reliant on the gain. The same detector can behave in different modes by varying the electric field:

1. Recombination region (G < 1): with a very low electric field, the separation of the primary electron-ion pairs is not entirely possible, and a fraction of the charge-pairs recombine.
2. Ionization chamber mode or Unity-gain (G = 1): with an electric field near the recombination threshold, only the electron-ion pair created by primary ionization is measured.
3. Proportional region (G ≈ 10^3 - 10^5): with an electric field larger than the amplification threshold, primary electrons succeed to trigger avalanches of stable mean gain and gain fluctuation. The integrated charge is proportional to the initial number of signal electrons; thus, it is possible to infer the deposited energy of the traversing particle.
4. Range of limited proportionality (G ≈ 10^5-10^8): the proportionality between deposited energy and signal is gradually lost due to the electric field distortion caused by the accumulation of ions near the anodes and the additional avalanches with nonlinear effects.
5. Saturation or Geiger-Müller mode (G ≈ 10^8 - 10^9): the total charge collected saturates, and the electric field between the fast electron avalanche and the ions dominate the amplification process, which allows for recombination processes associated with a photon emission. These photons, not affected

by the electric field, may trigger secondary avalanches. As a consequence, the amplification spreads along the anode and eventually causes a breakdown of the voltage, impeding temporarily the amplification until the field is restored. The electric field strength reduction becomes too important, and results in a self-quenching of the avalanche.

6. Discharge region ($G > 10^9$): if the power source responsible for the electric field does not have a current cutoff protection, the ions density becomes sufficiently high that the electrons go freely from cathode to anode and cause a discharge. These sparks can cause irreversible damage to the detector.

The values of gain between modes are dependent on the geometry of the amplification zone and may differ between different configurations. The reference values presented above refer to the Micromegas detectors of the ATLAS experiment [Kuger, 2017].

Figure 4.10 from [Silva, 2015][xxii], illustrates the different modes or regimes of operation of gaseous detectors. The pulse size is proportional to the gain of the detector, and the applied voltage may differ depending on the type of detector.

Micromegas based detectors operate usually with a gain near 10^4, thus in the proportional region and distant from the sparking zone as seen in the previous section. Nevertheless, certain circumstances may foster the appearance of sparks during normal operation, such as the presence of impurities in the amplification gap, local distortions of the micromesh or humidity among others.

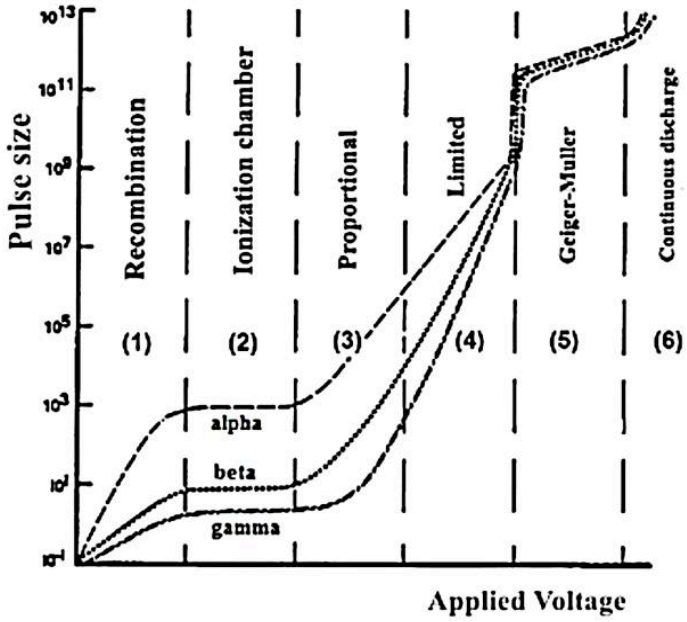

Figure 4. 10 Six-region curve for gas-filled detectors.

4.9.3 Discharges

One of the main disadvantages of the Micromegas technology, before the incorporation of the resistive layer, was the vulnerability to discharges. These violent discharges, often referred to as sparks, cause a voltage drop, rendering the detector less efficient until the potential difference is restored, and may also

cause irreversible damage at both the micromesh and the readout tracks. The high current can damage the downstream readout electronics as well.

The Paschen law predicts the theoretical breakdown voltage as a function of the distance between electrodes, type of gas between them and its pressure:

$$V_B = \frac{B \cdot p \cdot d}{\ln(A \cdot p \cdot d) - ln\left[ln\left(1+\frac{1}{\gamma_{se}}\right)\right]} \tag{4.23}$$

where V_B is the breakdown voltage, p is the gas pressure, d is the gap distance between electrodes, γ_{se} is the secondary-electron-emission coefficient, A is the saturation ionization in the gas at a particular E/p (reduced electric field value), and B is related to the excitation and ionization energies [Paschen, 1889][xxiii].

By means of Equation (4.23), it is possible to obtain Figure 4.11 (Image adapted from [Wittenberg, 1962][xxiv]), which shows the theoretical breakdown voltage of several gases under different conditions of pressure and electrode distance. For instance, considering a constant distance of 100 µm between the micromesh and the resistive layer, and an atmospheric pressure of 760 mmHg, the green dotted line marks the breakdown voltage in dry air, 927V. On the other hand, the black dotted line represents the same geometry, but with argon instead of air at 790 mmHg (30 mmHg is the typical overpressure of the TPC volume). In this case the breakdown voltage drops to near 450V.

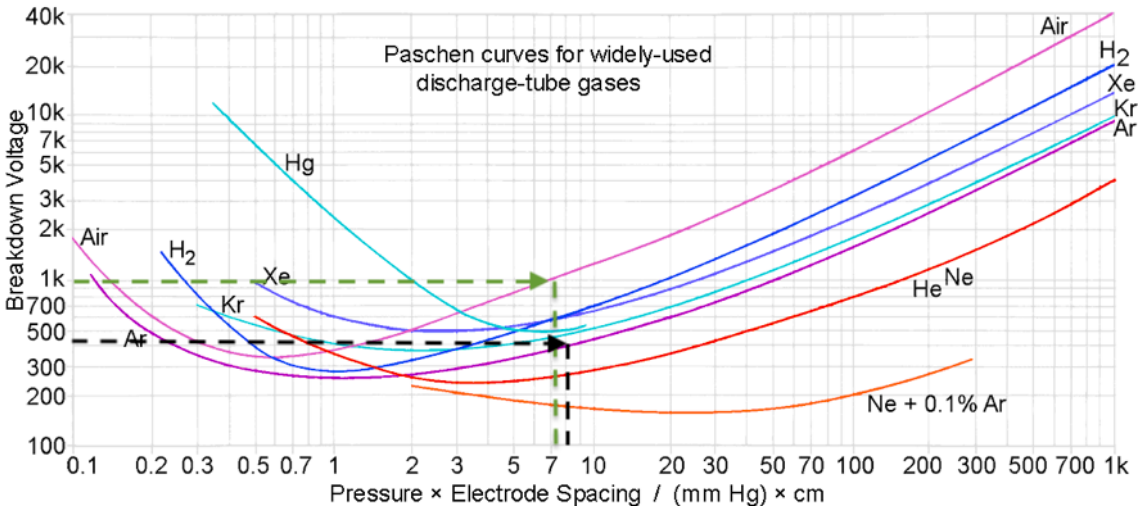

Figure 4. 11 Paschen's law breakdown curves for various gases.

The knowledge of the breakdown voltage is particularly meaningful for the present work in two scenarios:

- Detector benchmarking tests: after its fabrication, a detector undergoes a process of quality control in open air to identify construction errors that may lead to its malfunction. Smaller than expected breakdown voltages indicate the presence of contaminating particles or defective areas that should be removed or neutralized.

- The presence of sparks during detector operation may shed some light on the gas quality or environmental parameters during the acquisition. Besides the damage to the detector, the presence of sparks leads to electric field instabilities that alter the amplification stage, and thus the signal strength. The stability of the electric field is critical to maintaining the dead time as small as possible (Typically between 10^{-3} and 10^{-2} s). In addition, the breakdown voltage sets a physical limit to the detector operational parameters.

Another mechanism of spark formation has been introduced in the previous section. When the detector's gain exceeds a gain of ~10^8, the avalanche reaches a critical size, called the Raether limit [Raether, 1964][xxv] and leads to the formation of a streamer.

Figure 4.12 shows a schematic illustration of streamer development. When the total charge in the avalanche is close to the Raether limit (T_0 in the picture), the field lines near the primary avalanche undergo a focusing effect and start to bend towards the primary avalanche.

In T_1, secondary electrons created adjacent to the primary avalanche move towards it and generate secondary avalanches. In T_2, the secondary avalanches create a fast-moving thin plasma filament inside the gas volume, called a streamer.

When the streamer reaches the resistive layer, it creates a conductive trail and produces a discharge and local drop of the electric field.

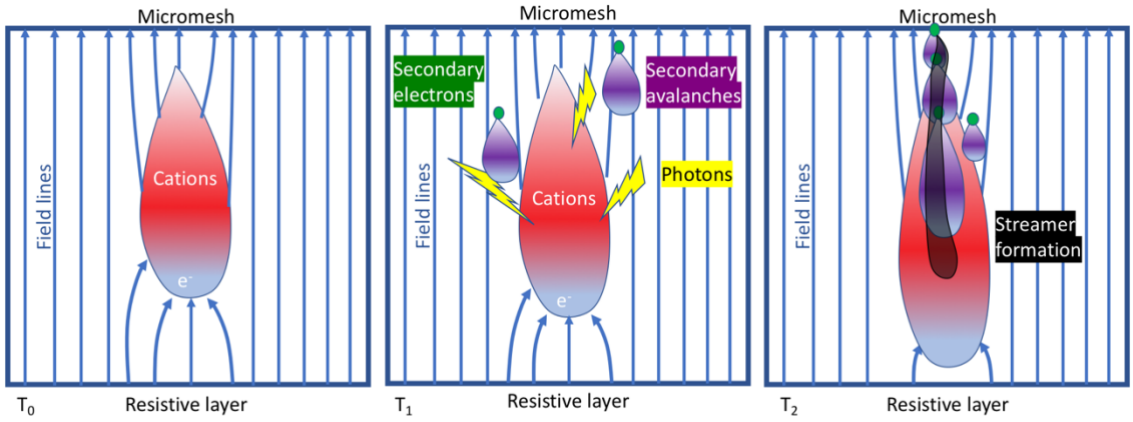

Figure 4. 12 Schematic illustration of streamer development process.

Actually, Micromegas-like detectors, seldom reach gains over 10^5 because of the mechanism explained above. Derived avalanches are started by a secondary photon, which induces a photo-electron in a gas molecule or the mesh material.

The choice of gas components, as seen in Section 4.6, is crucial in order to minimize this undesirable effect. The quencher component of the gas must have a good absorption cross section for these photons, and lead to the excitation of non-radiative states (rotational, vibrational). In the absence of a quench component, pure argon would break down before achieving G > 10^3 in typical microbulks [Dafni, 2009][xxvi].

4.10. References

[i] Adloff, C., Chefdeville M. et al. (2009). Environmental study of a Micromegas detector. pp.19. in2p3-00413881

[ii] Wang, B. Et al. (2013). Study on the effect of humidity and dust on leakage current of bulk micro-MEGAS detector. arXiv:1309.6439v1

[iii] Kuger, F. (2017). Signal Formation Processes in Micromegas Detectors and Quality Control for large size Detector Construction for the ATLAS New Small Wheel. Doctoral dissertation.

[iv] Nygren, D.R. and Marx, J.N. (1978). The Time Projection Chamber, Physics Today 31,46. 20

[v] Veenhof, R. (2010) Garfield - simulation of gaseous detectors. http://cern.ch/garfield

[vi] Patrignani, C. et al. (2016) Review of Particle Physics. Chin. Phys., C40(10)

[vii] Biagi, S.F. (1999). A description of the Magboltz program, with results compared to experiment. Nucl. Instr. and Meth. A 421 (1999) 234-240

[viii] Bouteille, S. (2017). Développement et application de détecteurs gazeux à micro-pistes pour la tomographie muonique. Doctoral dissertation.

[ix] MacDaniel, E. W. and Mason, E. A. (1973). The Mobility and Diffusion of Ions in Gases. Wiley.

[x] Schultz, G. et al. (1977). Mobilities of positive ions in some gas mixtures used in proportional and drift chambers. Rev. Physyque Appliquée 12, 67.

[xi] Yamashita, T. et al. (1992). Measurements of electron drift velocities and positive ions mobilities for gases containing CF_4 II. Nucl. Instr. and Meth. A317,213.

[xii] Santos, M.A.G. et al. (2017). Ion mobility studies for the ILC experiment. Presentation at CERN RD51 collaboration meeting.

[xiii] Biagi database (v8.9), www.lxcat.net, retrieved on April, 2018

[xiv] Itikawa database, www.lxcat.net, retrieved on April, 2018

[xv] "COMSOL Multiphysics Reference Manual, version 5.2", COMSOL, Inc, www.comsol.com

[xvi] Bunemann, O., et al. (1949) Design of grid ionization cham- bers. Canadian Journal of research A, 27:191–206

[xvii] Sauli, F. (2014) Gaseous Radiation Detectors. Cambridge University Press, Cambridge, 1st edition.

[xviii] Nikolopoulos, K. et al. (2011). Electron transparency of a Micromegas mesh. Journal of instrumentation, Vol 6.

[xix] Townsend, J. S., Kirkby, P. J. et al. (1901). Conductivity produced in hydrogen and carbonic acid gas by the motion of negatively charged ions. Ph Mag., &. Journal of Science, Vol 1, 630–642.

[xx] Davidov, Y.I. (2006). On the first Townsend coefficient at high electric field. IEEE Transactions on Nuclear Science. Vol 53. Issue 5.

[xxi] F. Eggenberger and G. Polya. (1923). Über die Statistik verketteter Vorgänge. Z. Angew Math. Mech, 4:279–289.

[xxii] Silva, M. (2015). Evolution of Ionizing Radiation Research. Mitsuru Nenoi, ISBN 978-953-51-2167-1. DOI: 10.5772/60914

[xxiii] Paschen, F. (1889). Ueber die zum Funkenübergang in Luft, Wasserstoff und Kohlensäure bei verschiedenen Drucken erforderliche Potentialdifferenz. Annalen der Physik 273.5, 69–96.

[xxiv] Wittenberg, H.H. (1962). Gas tube design. From electron tube design, RCA Electron tube division. 792-817

[xxv] Raether, H. (1964). Electron avalanches and breakdown in gases. London: Butterworths.

[xxvi] Dafni, T. et al. (2009). Energy resolution of alpha particles in a Micromegas detector at high pressure, Nucl. Instrum. Meth. A 608. Vol. 259. 77, 95-98.

Chapter 5. Technology description and developments.

Chapter 5 abstract

The present chapter aims at describing the design choices and the reasons that motivated them, in adapting existing tools in order to match the project requirements and goals. It also covers the development of innovative solutions to fill in the technological gaps encountered during the construction process.

Section 1 provide a brief summary of the Micromegas detector origins and the distinctive factors between its different versions as well as the reasons that motivated its selection for this work. Section 2 provides a detailed description of the specifications and manufacturing of the detector's readout which was used during the work.

As seen in Chapter 4, the gas management plays a major role in the performance of the detector. The results of the numerical simulations of the gas physical properties, relevant for the detector design and operation, are presented in Section 3. Section 4 provides a walkthrough of the gas conditioning system, which is coupled to the detector and responsible for the gas quality. It controls the gas flow and pressure, and prevents contaminants from entering into the detection volume.

Section 5 depicts the numerical simulations of the electric field conducted to minimize the artifacts related to the electric field distortions within the TPC, and to design the field homogenizer elements. The angular resolution of the MUST^2 is also discussed. The assembly process of the detector is illustrated in Section 6 together with the benchmark tests before its approval.

Section 7 provides a description of the two different kinds of instrumentation tested with the MUST^2 detector for retrieving and storing the data associated with the passage of muons.

Last but not least, some detectors used in the present work malfunctioned or manifested contamination symptoms during the experiments. Section 8 summarizes the servicing process carried out to recover, when possible, the faulty units.

5.1. Introduction

5.1.1 MUST^2 functioning principle

As mentioned in Chapter 1, the MUon Survey Tomography based on Micromegas detectors for Unreachable Sites Technology (MUST^2) camera is a gaseous muon detector. Conceived both for ground- and underground operation, it is a compact, portable and robust tool for geophysics and civil engineering. The detector consists of a thin TPC (detailed in Section 4.2) with a Micromegas readout plane. This innovative combination presents interesting distinctive features, allowing a wide angular acceptance of the detector with a light weight and reduced volume, hence iswell adapted for confined spaces or underground operation.

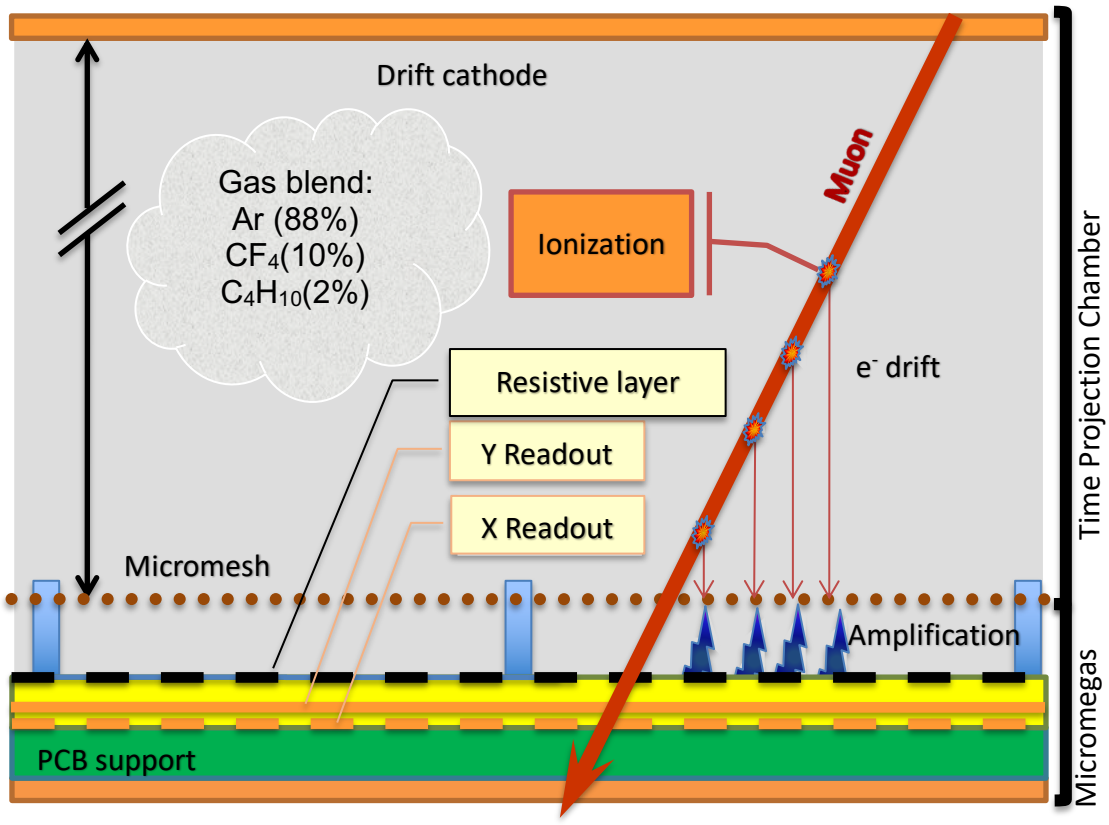

Figure 5. 1 Schematic cross-section of the MUST^2 to illustrate its functioning principle.

As seen in Figure 5.1, when the muon enters the conversion and drift chamber, it ionizes the gas. The generated electrons will drift orthogonally towards the micromesh under the influence of the electric field in this region. Once the electron passes the micromesh, it enters the amplification gap with a much stronger electric field, where it undergoes acceleration that creates an avalanche effect which amplifies the charge. The charge displacement induces a signal by capacitive coupling in both the micromesh and the readout tracks. The first signal can be used to command the acquisition instrumentation and the second one for the image reconstruction.

5.1.2 Micromegas, a member of MPGD

A century after the discovery of the gas amplification basic principle, gaseous detectors are widely used in applications where a large coverage area is required with a low materials budget. The development of photolithography and microprocessing techniques in the circuit board industry have led to a transition in the field of gaseous detectors during the last decades from wire structures to Micro-Pattern Gas Detector (MPGD). Figure 5.2 shows the timeline for several most spread MPGD technologies.

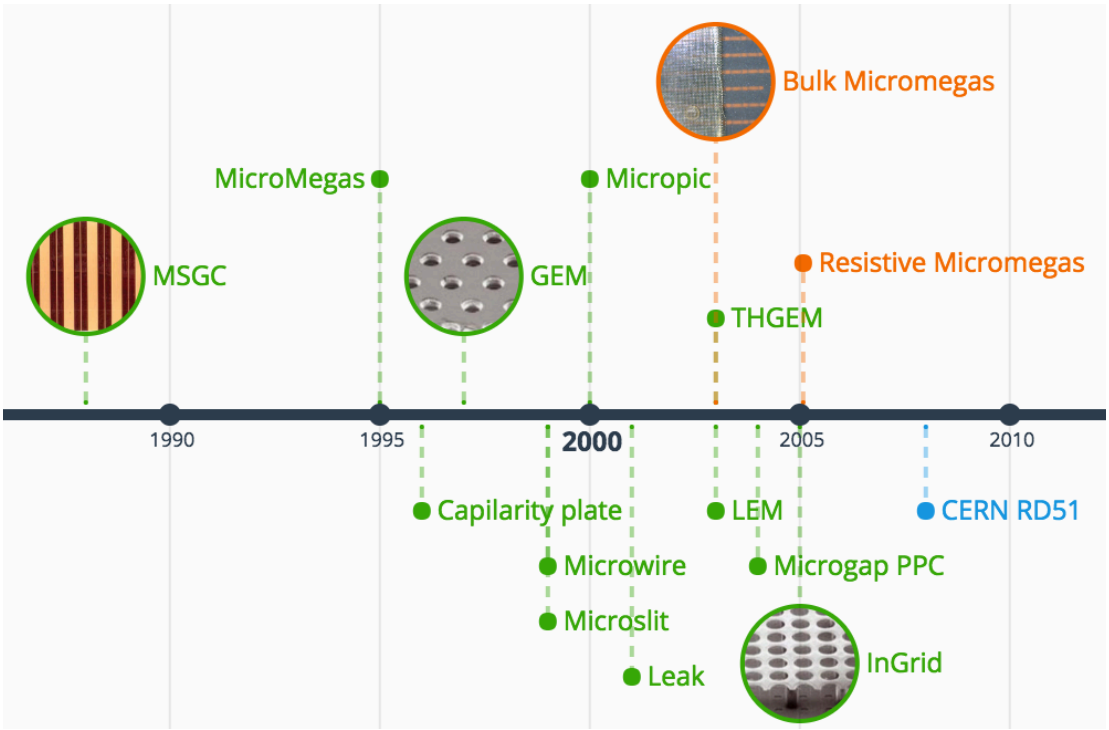

Figure 5. 2 Timeline of the MPGD technology developments. In blue, the creation RD51 CERN research group dedicated to the development of MPGD technologies.

The first MPGD was the Micro Strip Gas Counter (MSGC) conceived by Oed [Oed, 1986][i]. It consisted basically of a MWPC, but instead of wires it had metallic printed strips in a glass base. Later, many original MPGDs structures have developed from this initial idea. Two main designs have emerged, because of ease in manufacturing, operational stability and superior performances for tracking applications: the Gas Electron Multiplier (GEM) [Sauli, 1997][ii] and the Micromegas [Giomataris, 1996][iii]. This established two subgroups in turn: strip-and-hole and micromesh based MPGDs. Figure 5.3 illustrates the family tree with the most relevant MPGDs.

MPGDs are nowadays employed in several nuclear and high-energy physics experiments, medical imaging instruments and geophysics, but many more applications are foreseen. They outperform traditional wire chambers in terms of rate capability, time and position resolution, granularity, stability and radiation hardness [Duarte, 2010][iv].

Micromegas-like detectors are good candidates for muon tracking purposes due to their high spatial resolution (down to ~10 μm, typically 100 μm) [Derré, 2001][v], fast response to signals (down to ~10-20 ps, typically 10 ns) at high counting rates [Papaevangelou, 2018][vi].

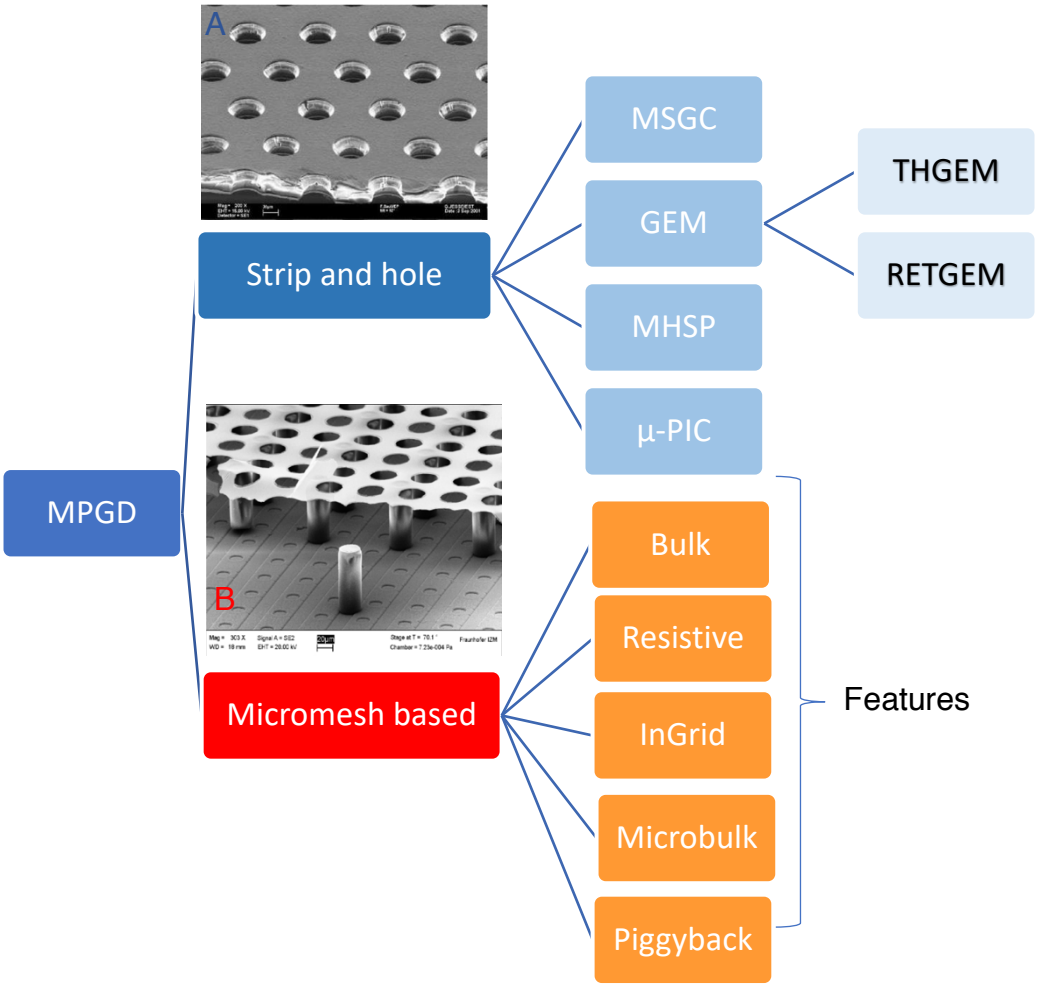

Figure 5. 3 Family tree of MPGD. Image A: GEM structure taken with an electron microscope (from CERN GDD group). Image B: InGrid detector observed with an electron microscope (image from H van der Graaf).

5.1.2 Bulk resistive Micromegas

As seen in Figure 5.3, the Micromegas family offers several options that can be combined according to the nature and layout of its characteristic elements, i.e. micromesh and readout anode. Table 5.1 summarizes the hardware differences between members of this family and their distinctive features.

Table 5.1. Comparative table of Micromegas-based detectors' features.

	Bulk	Resistive	MicroBulk	InGrid	Piggyback
Hardware difference	Woven wire micromesh integrated to the anode through pillars	Resistive layer between the micromesh and the anode	The mesh is printed in Kapton® film, thinner than bulk	Aluminum microgrid integrated onto a pixel detector	The resistive layer is deposited on a thin ceramic substrate
Distinctive features	Robustness Industrialized	Spark protection	High energy resolution	Best energy resolution	Large dynamic range of resistivity

The current work aims at the development of a pre-industrial tool, therefore both commercial availability and verified robustness of components play a major role in the decision-making.

Having this in mind, the Micromegas bulk-type detectors (invented only a few years after the standard Micromegas [Giomataris, 2006][vii]) benefit from the manufacturing machinery and processes used by the Printed Circuit Board (PCB) industry to fix the micromesh at a permanent and constant distance above the readout plane. This kind of detector is characterized by its robustness and large area coverage (up to 2-3 m^2). It has been widely used since 2005, and are foreseen in large scale particle physics experiments such as the Large Hadron Collider at CERN [Bianco, 2016][viii].

The pioneer manufacturers, CEA and CERN MPGD workshops, have made significant efforts since 2012 towards the detector industrialization. The goal is to transfer the know-how and outsource the production of bulk-Micromegas to industrial partners, e.g., the PCB manufacturers Elvia in France and Eltos in Italy.

On the other hand, the formation of discharges, detailed in Section 4.9.3, brings a series of undesirable effects that might lead, in the worst-case scenario, to permanent damage of the Micromegas detector or the downstream electronics. The incorporation of resistive layers between the micromesh and the readout anode, developed between 2005 and 2013, can convert bulk-Micromegas anodes into spark-resistant detectors, while maintaining their precision and preventing the hardware from harmful consequences.

Due to the factors explained above, the T2DM2 project commissioned a batch of 6 bulk-Micromegas resistive detectors in 2013. Four of these were assigned to the CERN's MPGD workshop; the remaining two, to Elvia.

In 2014, the project received the first 4 units from CERN. The two units awarded to Elvia encountered production issues during the resistive layer pressing, and had to be resent to the CERN's workshop for completion. The 5th detector was delivered in 2015.

At the time, recent advances in resistive layer manufacturing gave to the project a unique opportunity to slightly modify the structure of the 6th unit before its completion. A new technique, mastered by the Kobe University in order to produce big Diamond Like Coated Resistive Layers (DLCRL), motivated the upgrade of the former resistive layer made with the technique of screen printing. Finally, the 6th detector with a DLCRL was delivered in 2016.

5.2. Micromegas readout plane

5.2.1 Elements and layout

In order to evaluate the size of the Micromegas readout plane for the MUST^2 detector, two conflicting aspects have been taken into account. On the one hand, in order to minimize the acquisition time, the active surface of detection must be maximized. On the other, the transportability is compromised by its large size, the fabrication process becomes technically challenging, and the cost to instrument the device increases.

The width of the Micromegas plane has been established by the constraints associated with the manufacturing process. The majority of standard equipment used for printing circuit boards are capable of handling panels of width up to a maximum of 600 mm.

As for the length, the maximal dimension is given by considering the practical aspects of transport (a length similar to the 1200 mm of a standard pallet), in-situ deployment at the LSBB, and required instrumentation.

The actual external dimensions of the MUST^2 Micromegas readout plane are 555 x 1.155 mm^2, which enables its fabrication with standard equipment. These dimensions come from the addition of the surface occupied by the readout tracks, plus the necessary space to host the drift field cage and the electronics interface.

All six detectors commissioned by T2DM2 present the same readout and connectivity configuration. Figure 5.4 shows the location of the following elements:

-Micromesh. This element acts as a frontier between the conversion/drift zone and the amplification gap. A distinguishing feature of the MUST^2 Micromegas readout plane is that the micromesh is isolated from the TPC frame.

The only ground connection possible is the designated pad to retrieve the signal from the mesh, with the aim of creating a trigger signal associated with the muon passage.

-Readout tracks. Placed in two superimposed surfaces shifted 90º, they provide hit position information in the coordinate orthogonal to their plane. They contain a series of copper tracks that are parallel beneath the active detection zone, and converge in groups of 128 tracks to the front-end electronics connector interface.

The lower Y readout plane contains 512 channels of 0.7 mm width and 1 mm pitch grouped in 4 connectors, while the upper X readout plane contains with 1.024 channels of 0.3 mm width and 1 mm pitch grouped in 8 connectors.

The difference of width between the tracks of the two readout planes is motivated by the layout of the layers. The lower readout layer, the Y plane, is farther from the resistive layer where the capacitive signal is generated. The width of the Y tracks is maximized in order to get as much signal as possible.

On the other hand, the upper X readout layer produces an undesirable screening effect; the track width must be as narrow as possible while keeping a minimal size to receive the signal.

-Resistive layer. The anode spark-protection element. As mentioned above, two different resistive layers have been used in the present work: screen printed and diamond like coating.

Another distinguishing feature of the MUST^2 Micromegas readout plane is the fact that that the resistive layer is divided longitudinally into four equal sections. Each section is electrically-isolated from its neighbors and allows the four different sectors to operate independently. This feature has proven to be especially useful when certain areas of the detector present malfunction due to aging or assembly problems.

-TPC ground connector. This copper pad enables the electrical connection of the time projection chamber to the ground outside of the detector's sealed volume.

According to the distribution of the previously cited elements, the absolute area can be divided in turn into two regions:

-Active surface of detection. The part of the detector capable of producing a measurable output associated with the muon passage. It corresponds to the region where the readout tracks, resistive layer and micromesh are aligned, and measures 1.024x512 mm^2 (86,5% of the Micromegas readout plane area).

-Service or rim area. The part surrounding the active surface, and insensitive to the muon passage. This area contains the necessary electrical or mechanical connections between elements for the detector operation.

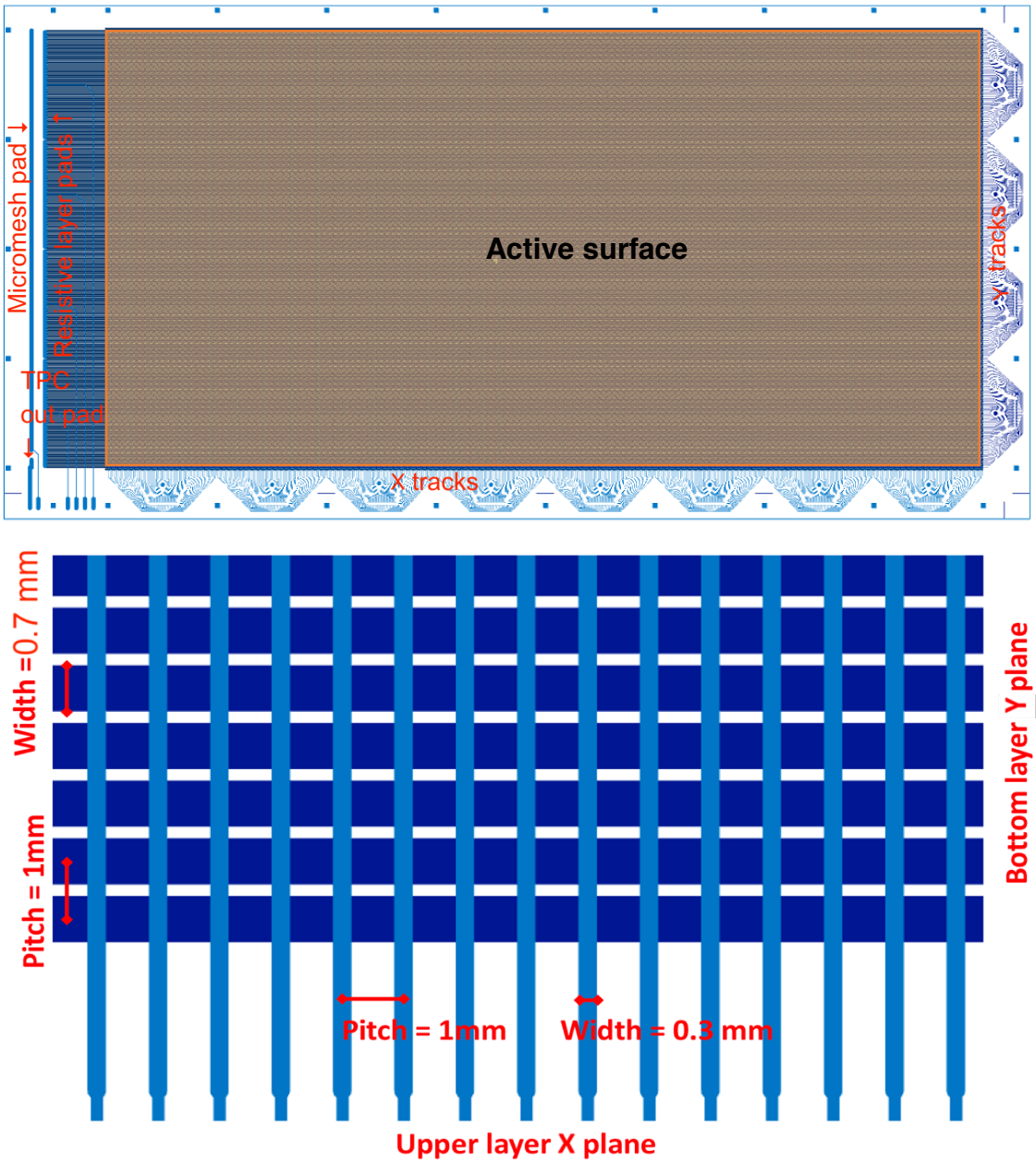

Figure 5. 4(Up) Overview of the MUST² Micromegas detection plane. (Down) Zoom of the readout tracks and their dimensions.

Since the Micromegas readout plane is meant in this work for a single-plane tracking device, the anode must be capable of retrieving the 2D position of the ionization associated with the particle passage. To do so, there are two classical approaches:

- Pixel-based detectors: the active surface is divided into a matrix of readout pads, each instrumented individually to provide the position directly. The main disadvantage is the large number of channels necessary in order to cover a large are with good spatial resolution. Experiments, such as ASACUSA, are

making electrical connections between pads to form discontinuous strips track in order to reduce the number of instrumented channels [Radics, 2015][ix].

- Strip-based detector: the active surface contains a series of copper tracks which provide information about the position across the strip direction. In order to retrieve the position in 2D, a second readout layer with strips placed perpendicularly can be superimposed.

This method has two drawbacks, the first is associated with the non-uniqueness of XY track correspondences during simultaneous events. The second is related to the signal transmission between the resistive layer and the readout track by capacitive coupling: the charge signal is split between the two readout layers, and each layer has a different behavior that must be balanced by adapting the geometry of the elements to get a similar output from the two readout planes.

Recently, other advanced techniques to reduce the number of instrumented channels in MPGDs have emerged based on channel layout multiplexing, such as the Micromegas genetic multiplexing [Procureur,2013][x].

The readout granularity is the most important factor in determining the reachable spatial resolution of a MPGD detector. To determine the density and distribution of tracks necessary to achieve a minimal spatial resolution of 1 mm, two factors are taken into consideration: the large active area of the detector and the number of channels read by the selected electronics. With these in mind, the selected configuration (seen in Figure 5.4 (Up)) allows grouping the channels into groups of 128 tracks, which is the most convenient interface for the master-slave APV25 hybrid cards (see Section 5.7 for more details about the electronics).

The total number of instrumented channels per detector, 1.537, can be read by a single standard combination of analog-to-digital converter (ADC) and front-end concentrator (FEC) from the CERN's RD51 Scalable Readout System (SRS).

Regarding the track geometry, readout tracks perform two basic functions: collect the signal related to the muon passage and route it to the interface connector in the outer part of the detector. As seen in Figure 5.4 (Down), the section of the readout tracks is not equal between the two planes nor constant along their length.

As for the variable section and geometry of the readout track along its path, once it exceeds the active surface of detection, the track acts as an electrical nexus with the front-end electronics and its path is defined by its position and the shape of the 128-pin Panasonic interface connector.

5.2.2 Production process

A key component of the MUST² detector is its resistive bulk-Micromegas readout plane. This anode board carries the two superimposed layers of readout tracks produced by workshops using photo-lithographic etching, the protective resistive layer and the built-in amplification gap delimited by the micromesh embedded in the support pillars. The schematic cross-section view of the readout plane is shown in Figure 5.5 (Up) the values in parentheses correspond to the height of the layer.

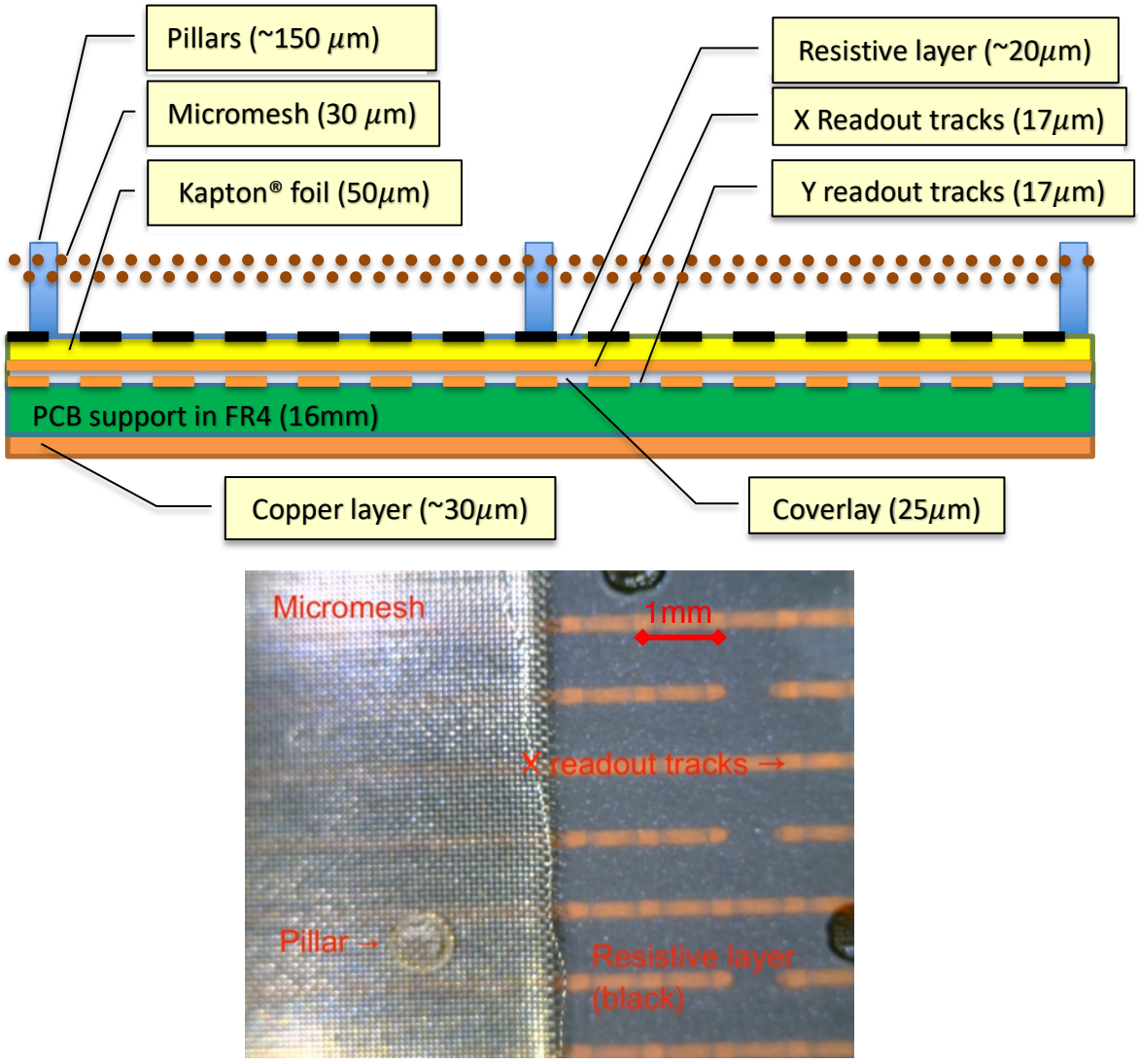

Figure 5. 5(Up) Schematic cross-section view of the Micromegas readout plane. (Down) Magnified view of the active surface of the MUST² with the micromesh partially removed.

Figure 5.5 (Down) shows a magnified view of the readout plane with the micromesh partially removed, in which it is possible to identify: the stainless-steel micromesh (grey weave in the left half), the support pillars, the resistive layer made by screen printing and the X readout plane (vertical stripes below the resistive layer). The Y readout plane is not visible in the picture because it of its alignment with the resistive layer.

The production process of the Micromegas plane used by the MUST² detector is presented in the figure 5.6.

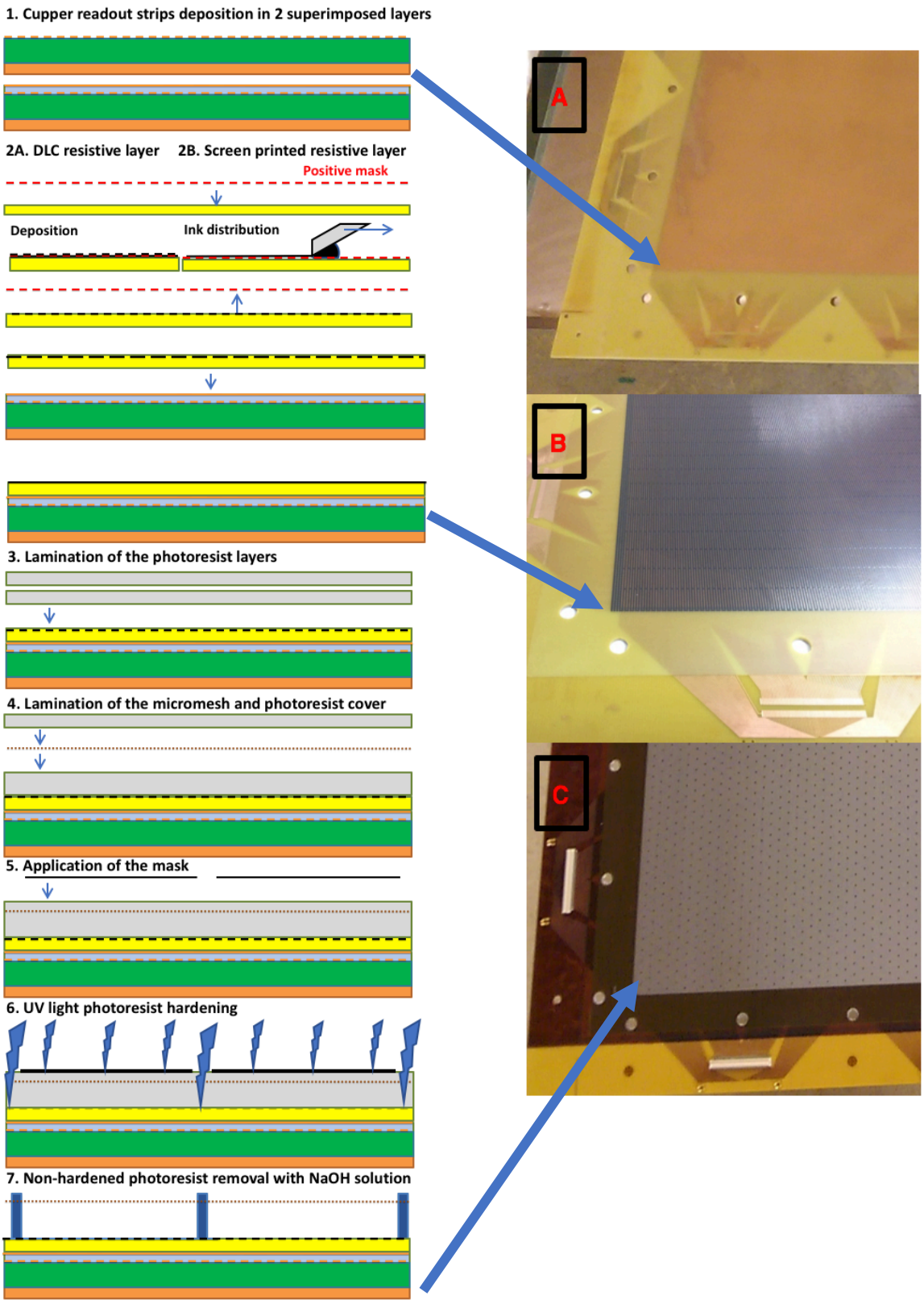

Figure 5. 6(Left) Diagram of the production process of the MUST² readout plane. (Right) Images of the readout plane during different stages.

The production process follows a multi-step work-flow analogue to the fabrication process of standard bulk-Micromegas detectors, described in detail by [Kuger, 2018][xi] and [Delbart, 2010][xii].

1. Readout strips and connector pads. Production starts with a fiber glass epoxy (FR4, 1,6 mm thick) panel, which acts as a support for the copper readout pattern. The Y lower readout plane is etched into the 17 µm thin copper layer previously deposited on the FR4 board via classical photo-lithographic methods. Then, a coverlay layer is placed over the Y readout plane and the procedure is repeated to etch the X higher readout plane. The process takes place within a temperature- and humidity-controlled environment. The expansion of the base material due to the temperature and humidity changes is taken into account while designing the mask's pattern so the final product will match the specifications. For the connector pads, to guarantee the conductivity between them and the elements such as the resistive layer or the micromesh (see Figure 5.4 (Up)), the copper pad is covered with a noble metal material, such as silver paste. At this point the detection board has the appearance shown in Figure 5.6 (A).

2. Resistive layer. During this work two different resistive layer techniques have been tested: one produced by DLC coating, the other by screen printing. Screen printing is the conventional technique for making resistive electrodes with patterns requiring sub-100 µm accuracy. It uses carbon-doped black-loaded paste, mostly made from graphite, resin and solvent. A negative mask is placed over the substrate foil, the paste is distributed with a squeegee and the excess removed. The targeted resistivity of the layer and its thickness is achieved by adjusting the composition and viscosity of the paste, the permeability of mask, and the pressure and speed applied by the squeegee during the paste application. The drawback of this method is due to the liquid nature of the paste: the resulting pattern has a bump-like cross section and the boundaries of the stripes are not sharp.

On the other hand, the DLC technique consists of a vacuum deposition of carbon particles of molecular size with an amorphous structure over the substrate foil with a negative mask. The surface resistivity and thickness can be controlled by determining the exposure time to the carbon atoms. This technique presents some convenient advantages for Micromegas applications, such as better accuracy of the tracks (< 10 µm) and absence of surface irregularities. In return, the production of DLC patterns is quite complex and expensive.

In both cases, a ladder pattern[1] is applied over a 50 µm thick layer of Kapton® foil: the thickness of the resistive material is ~10-15 µm in the case of screen printing, and ~70 nm for DLC. Once the paste is hardened the pattern mask is removed and only the exposed areas remain coated. Afterwards, the Kapton® foil is glued (with a precission of ~10 µm) on the readout side of the PCB with a 25 µm thick Akaflex® glue layer under high pressure and heat.

[1] The ladder patter consists of long tracks of 0,8 mm tick, superimposed on the Y readout strips and with side connections every 2 cm to allow the interconnexion of resistive strips and minimize the apparition of dead zones in case of or damage or not enough accuracy during the construction.

The surface resistivity is 100 MΩ/□[2] for the two different layers. At this point the detection board has the appearance shown in Figure 5.6 (B).

3. Bulk Micromegas mesh integration. Once the resistive layer is fixed, the micromesh is embedded on top of the Micromegas plane. During the lamination process, the micromesh is held in place by an external frame with a tension of ~10 N/m.

First, two layers of 64 μm photoresist coverlay, like Varcel® or Pyralux®, are placed over the resistive layer with μm precision. This guarantees the flatness of the micromesh, and leads to a uniform micromegas amplification gap of 128 μm. Then the micromesh is laminated on top and covered with an additional layer of coverlay. This material is the precursor of the pillars that attach and keep the micromesh in place. The supports are about 1 mm diameter, and spaced of 6 mm apart, creating a triangular pattern over the active surface. The loss of active surface of detection due to the presence of pillars is 2,5%.

In order to fill the holes of the micromesh and fuse the coverlay layers, the lamination is made at high pressure and temperatures of 90ºC to provoke the partial melt of the coverlay. The full stack is then hardened at the pillars' positions using a mask and UV light, and the entire anode is developed with NaOH to remove all non-hardened material. The micromesh then is held by a 15 mm coverlay border surrounding the detector's active area to harden, after which it's is cut to its final 55 × 115 cm^2 dimensions. At this point the detection board has the appearance shown in Figure 5.6 (C).

The micromesh chosen for the micromegas readout plane is made of stainless-steel with a plain weave pattern as shown in Figure 5.7. The height is 30 μm, the pitch distance p = 63,5 μm and the wire diameter is d = 18 μm, which leads to an aperture a = 45,5 μm.

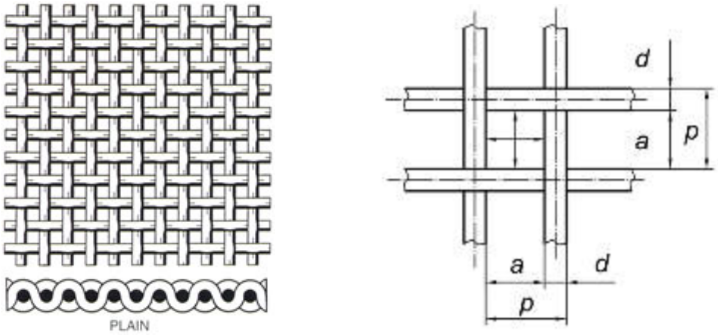

Figure 5. 7 Schematic of the plain weave pattern and the geometrical parameters required to define its unit cell. Image from [ISO9044:1999][xiii]

This micromesh is actually a commercial woven wired mesh, and has proven to be an affordable and technologically viable choice for large area Micromegas with a good performance in terms of electron transparency.

[2] The resistivity measured between two opposite sides of a square does not depend on the square size. Sheet resistance is a special case of resistivity for a uniform sheet thickness, its unit (ohms per square, Ω/□) is dimensionally equal to an ohm but exclusively used for sheet resistance.

5.2.3 Spatial resolution

The simplest hit position reconstruction can be made when the signal of a single strip exceeds an established threshold level. Nevertheless, in a Micromegas-like readout, this case is mostly applicable in a situation when an event is induced by a single electron and with no transverse diffusion.

As seen in Section 4.4, the ionization induced by a muon usually produces a higher number of signal electrons. Moreover, these signal electrons undergo scattering processes along their drift in the TPC, resulting in a shift of their position before triggering the avalanche in the amplification zone. In consequence, the charge induced on the readout tracks by the muon passage is often distributed over several strips. This effect can be used to improve the achievable spatial resolution for hit reconstruction; with a sufficient charge sensitivity and adequate temporal sampling of the readout electronics, the charge-over-position-over-time information of a hit can be used for a centroid reconstruction method.

Numerical simulations of the detector charge dispersion made with the Garfield++ software can help to estimate the spatial resolution. Since a full simulation of the detector physics would be excessively time consuming, electron drifts are not fully simulated. Instead, the results from the gas simulation presented in Section 5.3 are used to characterize the electrons after their drift in the TPC. Gaussian distributions are used with mean and variance depending on the drift length, gas nature and electric field; only then is amplification fully simulated. Regarding the geometry of the simulation, only a finite zone containing 20 strips of 1mm pitch in the upper readout plane is considered. The results of the charge dispersion along the X direction during the electron drift are shown in Figure 5.8. The dispersion depends on the square root of the drift distance of the electron [Ferbel, 1991][xiv]. The simulated dispersion shows good agreement with the required spatial resolution for the MUST^2 micromegas readout, with value of ~0,4 mm.

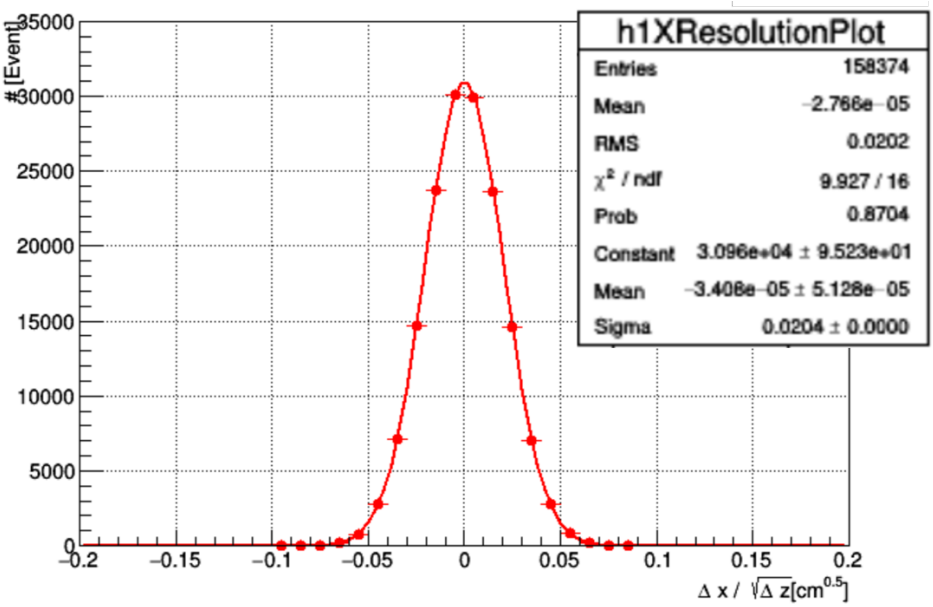

Figure 5. 8 Simulation of signal dispersion along the X axis as a function of the square root of the electron drift distance ($\sqrt{Z}$).

5.3. Gas characterization

As seen in the previous chapter, the choice of gas has important implications in the detector's physical processes leading to the creation of an exploitable signal associated with a muon passage.

Simulations provide valuable predictions of important gas characteristics such as:

- Mean longitudinal diffusion. This affects the duration of propagation of the electron, and thus the TPC capabilities of the detector.

- Mean transverse diffusion. This measures the shift of the electron between the original nadir at the beginning of its displacement and the actual arrival point at the amplification plane.

- Mean drift velocity. Despite the fact that muons travel close to the speed of light, the drift velocity of the primary electrons produced by the gas ionization after its passage in the time projection chamber allows controlling the speed of the process. This drift speed ($\overrightarrow{v_d}$) is dependent upon the gas blend and the electric field.

Ideally, the gas selected for the current application, Ar:CF_4:iC_4H_{10} (88:10:2), should present low diffusion values to improve the precision of the TPC, and a high drift speed for the signal to fit completely whithin the electronics sampling. Simulation of the electron drift has been made with MAGBOLTZ [Biagi, 1999]. This software solves the transport equations for electrons in gas mixtures under the influence of electric and magnetic fields, and calculates drift, diffusion, gain and attachment of electrons in gases.

When working with non-standard gas mixtures, the suppliers are required to prepare tailor-made blends, and might be unable to guarantee the exact composition required. Once the gas mixture is created, it undergoes a precise chemical analysis to determine the true composition of the mixture. Deviations of up to 1% in composition are usual.

For this reason, several similar gas mixture compositions have been simulated for a range of 100 V/cm ≤ E_{drift} ≤ 1.000 V/cm, the environmental parameters have been set to 20ºC and 1 atm. In real-life conditions, the variation of these parameters leads to changes in the drift speed and diffusion. The dependence of electron diffusion (D) of pressure (P) and temperature (T), is characterized by the following equation:

$$D = \frac{2}{3\cdot\sqrt{\pi}} \cdot \frac{1}{P\cdot\sigma_0} \cdot \sqrt{\frac{(k_B\cdot T)^3}{m_e}} \tag{5.1}$$

where σ_0 is the cross section of the electron-gas interaction, k_B is the Boltzmann constant and m_e is the mass of the electron. The results of the simulation for the three aforementioned characteristics are presented in Figures 5.9 and 5.10. The error on the integration of MAGBOLTZ scales with the square root of the number of collisions. This parameter has been set to 10 for better than 0.5 % accuracy.

The data highlighted in red represents values for the targeted gas composition. The rest of the series allows estimation of and correction for the drift speed and diffusion of electrons as a function of the real gas composition.

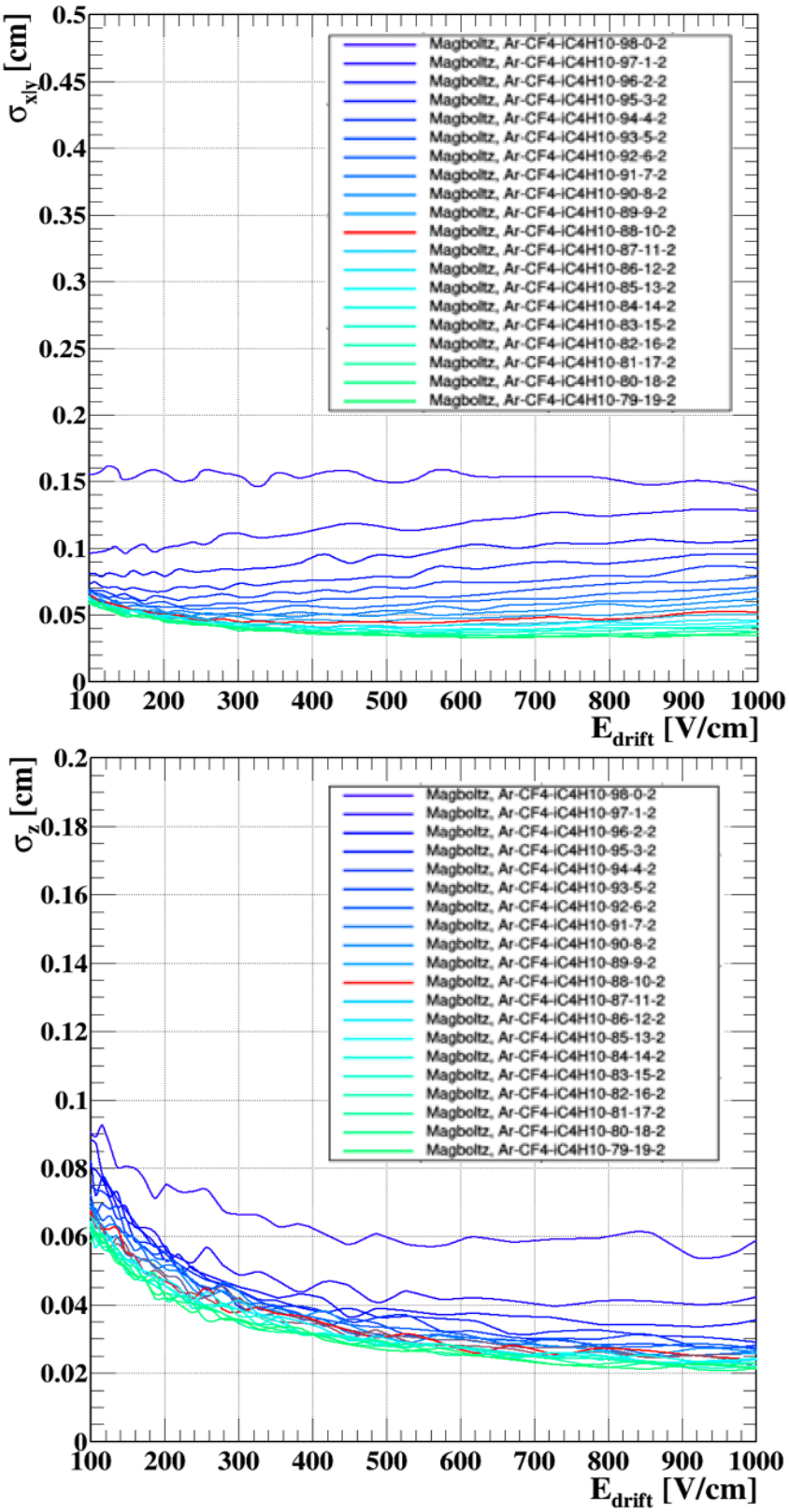

Figure 5. 9 Simulation results for longitudinal (Down) and transverse diffusion (Up) as a function of the drift electric field.

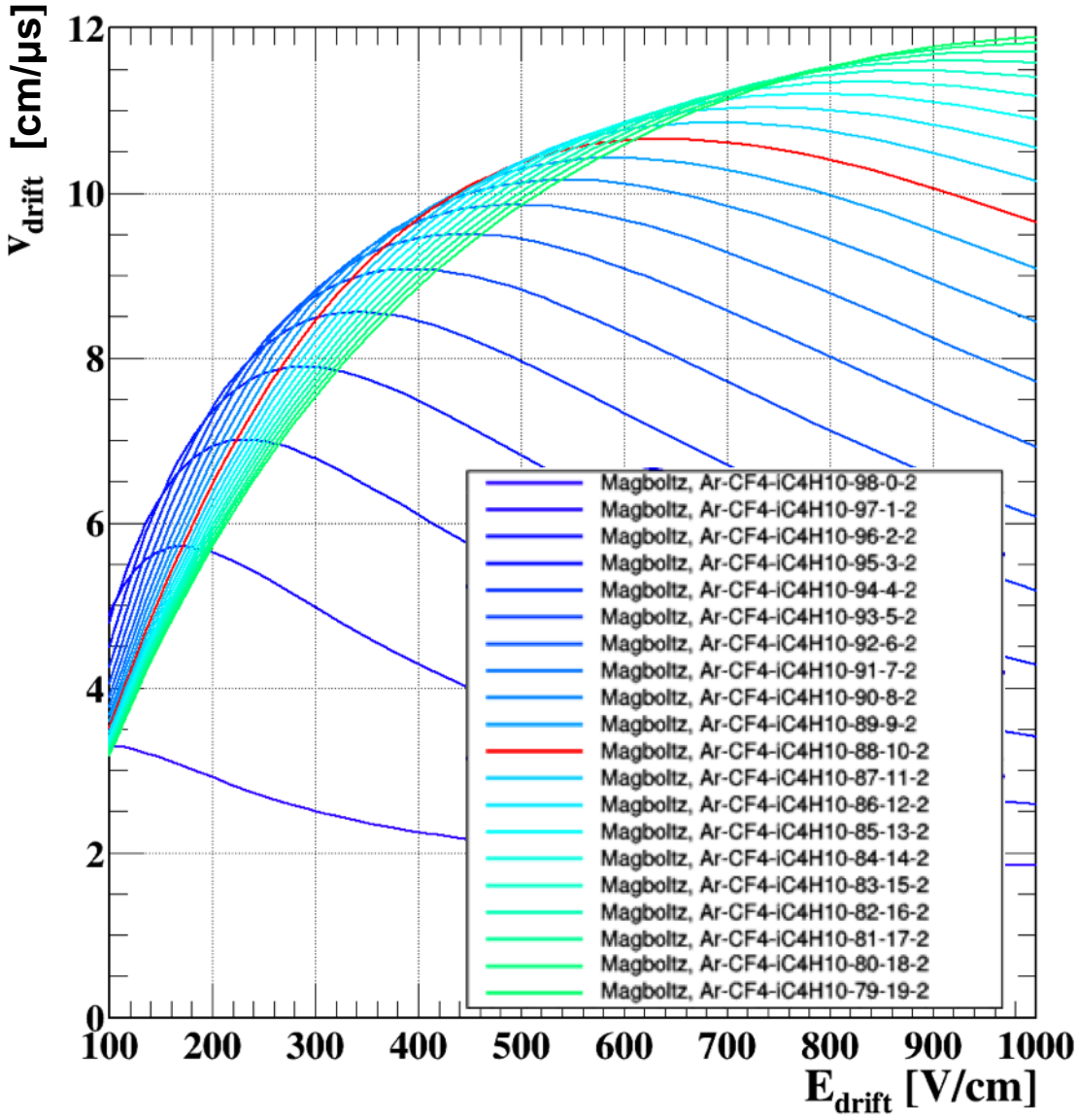

Figure 5. 10 Simulation results the electron mean drift velocity speed as a function of the drift electric field.

The longitudinal and transverse mean drift distances for the operational E_{drift} = 600 V/cm are reasonably low (better than 0,5 mm, half of the pitch distance) and in good agreement with the detector spatial resolution.

Another interesting feature of this gas blend is that the drift speed near 600 V/cm is nearly constant. Small fluctuations of E_{drift} during the detector operation should have little-to-no effect in the mean electron drift speed, which eases the data analysis while reconstructing the muon track.

The gas mixture presents a high mean drift velocity, 10,7 cm/μs under standard operational conditions. This means that the most distant electrons (generated at the top of the TPC 5 cm away) will take ~467 ns to reach the amplification gap.

Since the SRS readout electronics, used for most of the project (see Section 5.7.2), is capable of recording data during 675 ns for a single event, the drift speed meets the requirements for this configuration.

To quantify the length of the signal generated in the TPC, Figure 5.11 shows the distribution of the number of time bins containing signal over the stablished threshold in the X and Y coordinates during an acquisition of 144.973 events with Ar:CF_4:iC_4H_{10} (88:10:2) and E_{drift} = 600 V/cm.

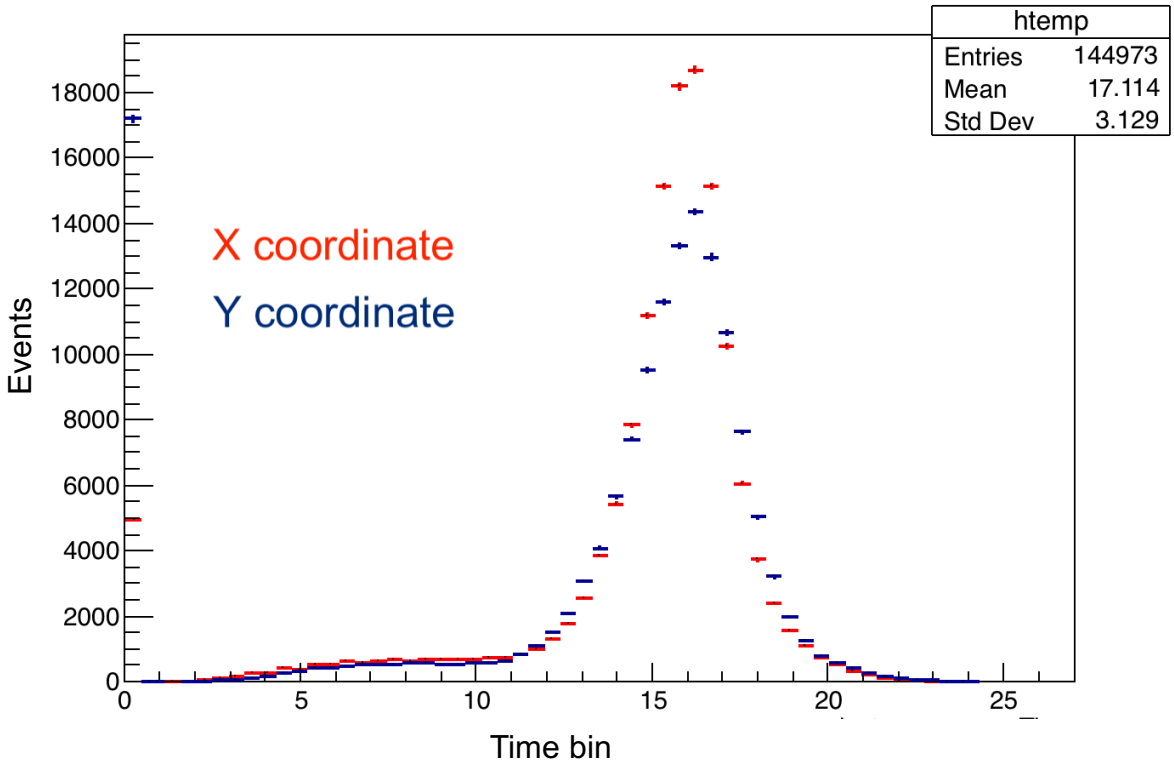

Figure 5. 11 Number of time bins with signal over threshold.

The signal length duration is homogeneous in the two coordinates, the amplitude in the Y coordinate is however lower due to the induced charge difference between the readout planes. The value of 17,114±3,129 time slots corresponds to 427,85±78,22 ns, which is in good agreement with the above estimated value.

5.4. Gas management

The performance of the detector is dictated by the quality of the gas and its homogeneous distribution inside the detection volume. Gas parameters (e.g., fine composition, flow, contaminants, pressure, etc.) affect directly the physical processes that lead to the signal creation. More specifically, as seen in Section 4.7, the presence of contaminants such as O_2 and H_20 produces an attenuation of the signal strength.

To minimize the undesirable effects associated with the gas management, an auxiliary system coupled to the detector has been designed. The Gas Conditioner system (GC) consists mainly of a regulable system of gas filtering and recirculation; it also keeps the pressure inside the detection volume steady in order to compensate for possible gas leaks along the system, or the gas expansion/contraction due to temperature changes. The GC, as seen in Figure 5.12 (Right), has been designed to fit inside a sturdy trolley to be deployed along with the detector in harsh environments.

The GC is controlled by a logic controller that allows the device to be operated both locally and remotely via an ethernet connection. This logic controller retrieves the temperature and gas flow values at two different points of the gas circuit, and adjusts the pump speed to regulate the gas flow.

Thus, the GC components shown in Figure 5.12 (Left) can be divided into two subgroups according to their function:

- Gas transport.
- Flow control and monitoring.

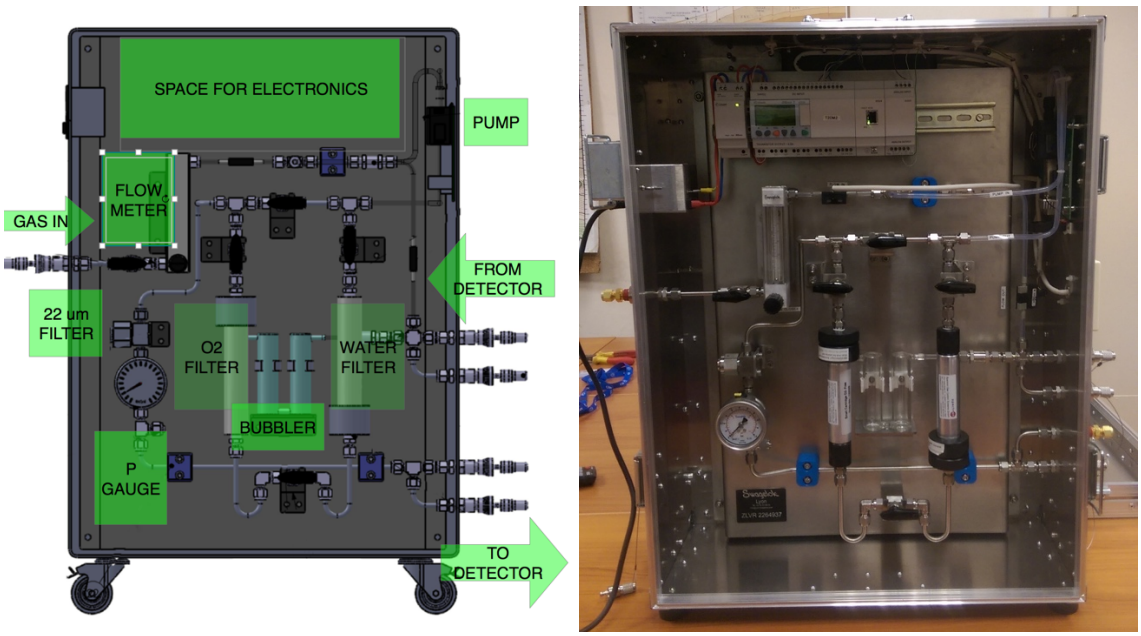

Figure 5. 12(Left) 3D model of the GC with its components identified. (Right) View of the GC trolley without the cover.

5.4.1 Gas circuit

The schematized gas transport process is presented in Figure 5.13. The dark blue line shows the gas path, while the light blue line indicates the gas release from the recirculation loop.

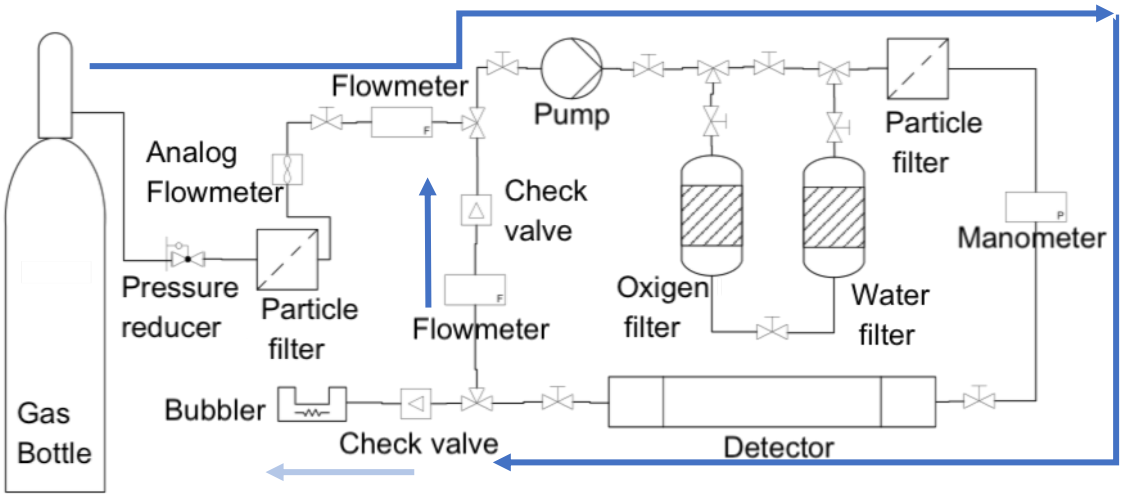

Figure 5. 13 Flow diagram of the gas circuit.

The gas circuit begins with the gas source, in this case a high-pressure gas bottle. The gas passes through a pressure reducer, where the pressure is set to the desired level, usually ~100 mbar. Just afterwards is a first 22 µm particle filter, coupled to the pressure reducer to prevent the entry of fine particles into the circuit.

The filter is connected to the gas conditioner box (seen in Figure 5.12 Right) through a Teflon PFA 6 mm tube with Swagelok quick connectors. This kind of connector allows its connection/disconnection as many times as necessary while ensuring the gas tightness of the line. Their dead volume is extremely low, and air inclusion can be neglected.

The first component inside the GC case is an analog flow meter, to provide a direct read of the gas input, and to permit adjustment of the input flow manually. Afterwards, there is a digital flow meter connected to the logic controller that regulates the pump speed. The pump generates a pressure gradient that drives the gas recirculation.Following the pump, the gas enters into the contaminant filter section. Two in-line consumable cartridges filter the water vapor and oxygen present in the gas. A series of valves allows bypassing the gas path, and the servicing of these elements without exposing the entire gas line.

Afterwards is a second 22 µm particle filter. This redundant element is included inside the gas loop to capture the particles that might enter into the circuit from the granular nature of the filter cartridges, or after their substitution. Next to the filter, there is a manometer to monitor the pressure of the system. At this point the gas line goes directly to the detector, so if we consider negligible the pressure drop due to the short length of the Teflon tube, the manometer provides a measure of the pressure inside the detector.

The direction of the gas feed to the detector is interchangeable: both sides can act equally as input/output just by switching the gas tubes. To enhance the gas distribution inside the detector, the gas input/output connectors located in the metallic frame of the TPC have been split into two points evenly separated from the frame's border and the other connector respectively. Figure 5.14 (Up) illustrates the position of the gas connectors with respect to the TPC frame.

Once the gas crosses the TPC frame, it enters into the gap between the metallic frame and the electric field homogenizer cage (see Section 5.5). A pattern of 1mm diameter holes has been made in the two PCBs located in front of the input/output faces to increase the gas diffusion towards the drift volume. Figure 5.14 (Down) shows a magnified view of the holes in the electric field homogenizer PCB.

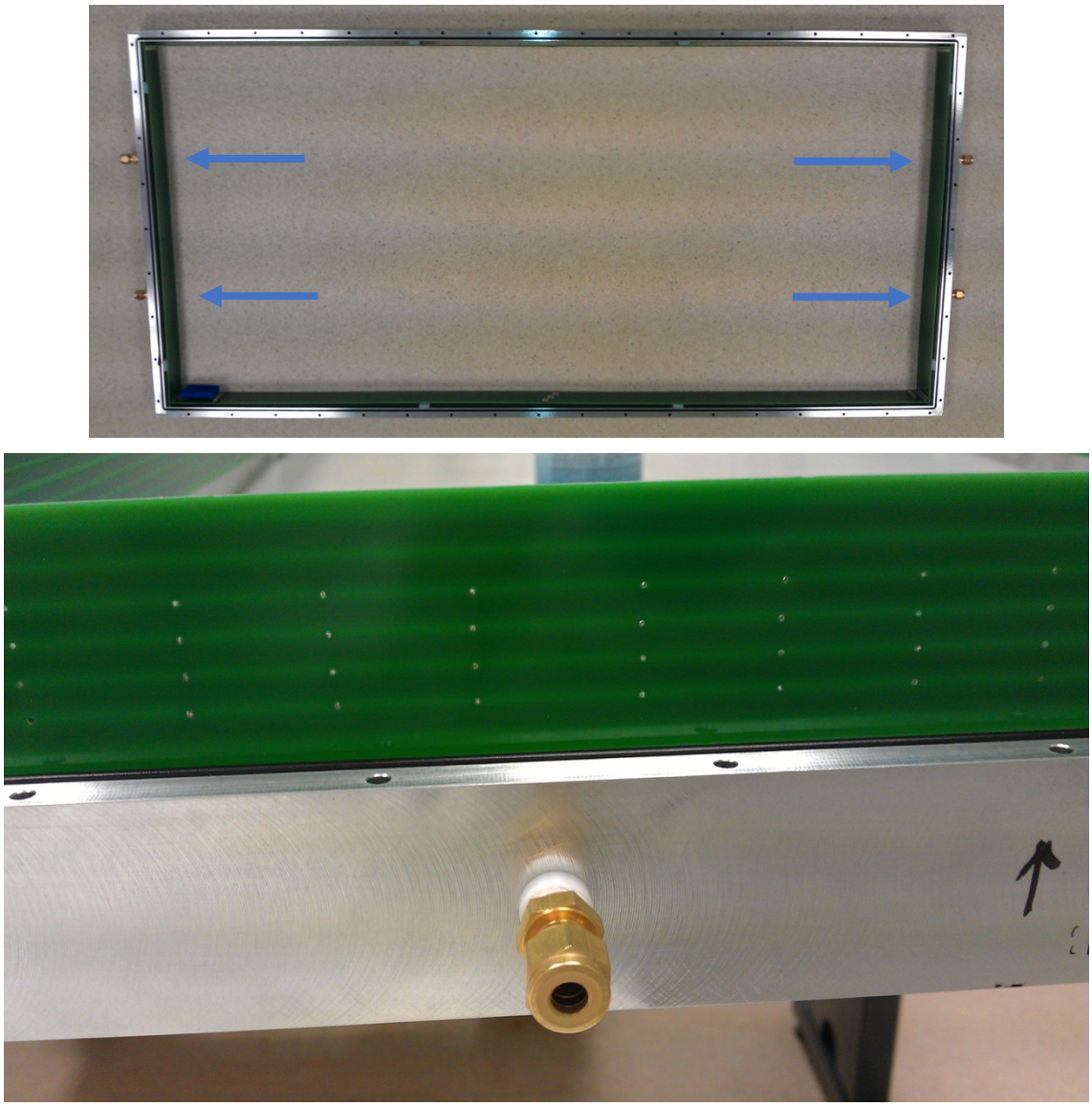

Figure 5. 14(Up) Gas input/output connections in the frame of the PTC (Down) Detail of the gas diffusion hole pattern.

After the detector, the gas line splits into two. The first one, dedicated to release the overpressure of the detector, contains a check valve with an opening pressure of ~60 mbar, followed by a bubbler. The bubbler, filled with paraffin oil, has the double function of enabling the visual detection of the released gas, and avoiding the air backflow into the gas circuit.

The second line after the detector conducts the gas to the second digital flow meter, which quantifies the amount of gas recirculated and closes the gas loop. A check valve with an opening pressure of ~20 mbar controls the direction of the gas.

5.4.2 Flow control and monitoring

Management of the gas flow is made by a Crouzet XD26 logic controller with two extension modules to respectively provide ethernet access and produce analog output signals. This setup is shown in Figure 5.15.

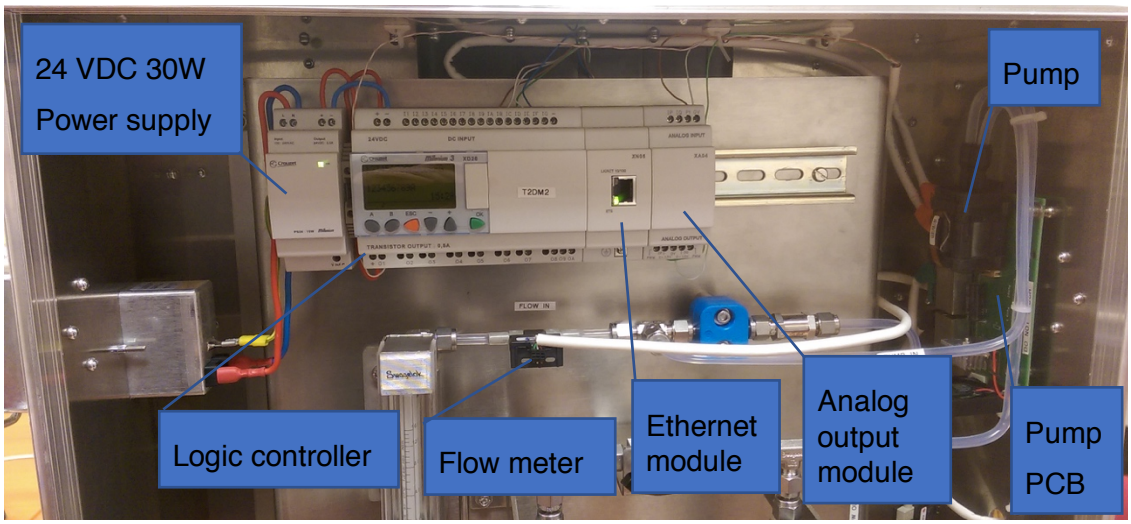

Figure 5. 15 View of the GC's logic controller.

The program of the logic controller has been made with the M3 software, and provides two operation modes -manual and automatic- that can be used locally and remotely.

The manual mode enables the operator to adjust *in situ* and directly the pump speed from the logic controller interface, as well as visualize all data monitored by the GC. The automatic mode adjusts automatically the pump speed to maintain the gas flow within the preset limits.

This logic controller is not capable of recording the environmental data: it uses the measured values to control the gas flow. The environmental parameters during the data acquisition are recorded with another detector.

Figure 5.16 shows the PCB specially designed to host, feed and control the pump, and to gather all connections between the logic controller and the sensors. The connectivity chosen for the GC is based on 8P8C modular connectors due to their availability and proven performance with Category 5e cables and custom pinout configuration.

The circuit contains 9 ports for the following purposes:

- Two to power and control up to two pumps (1 operational and 1 spare).

- Two to power and control the flow meters.

- One to power and control the thermocouple.

- One to power and control the pressure sensor.

- One to gather all inputs from the power source and logic controller.

- One to gather all outputs with signals to the logic controller.

- One, in reserve: it can be used for any of the previous functions.

The PCB also contains the following elements:

- One LED light which remains on as long as the board is powered.

- Two aluminum capacitors (105deg 1000uF 25V) for electrical protection.

- One voltage transformer (TO220 12V 1,5A) to convert from 24VDC to 12VDC, as necessary to power the sensors.

- Two pads to solder the Molex connector (Molex 0526100672 FFC/FPC) necessary to connect the pumps.

- One resistor for the voltage transformer GND connection.

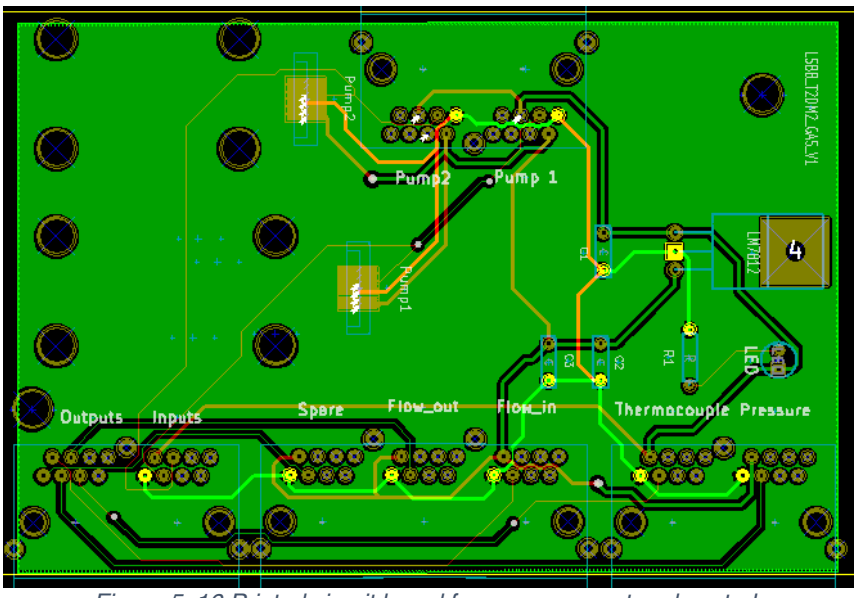

Figure 5. 16 Printed circuit board for pump support and control.

5.5. Time projection chamber design

The TPC covers the space between the drift cathode and the micromesh. It provides information about the time component, also called longitudinal coordinate. It permits the identification of spatial points along a particle trajectory: X-Y coordinates are obtained from the readout plane and the Z coordinate from the drift time. The measurement of the third coordinate requires a precise knowledge of the drift velocity as seen in the previous section.

The TPC walls must provide a gas-tight envelope, and insure appropriate electrical isolation of the detection volume from the rest of the detector.

The design of the time projection chamber requires a balance between angular resolution and technical convenience.

On the one hand, taller chambers provide better angular resolutions, but present some disadvantages in return:

- The voltage required to reach the operational E_{drift} increases proportionally with the height of the chamber.

- The shape of $\vec{E}_{drift}$ deviates in absence of an auxiliary field cage. This deflects the drifting electrons from the desired orthogonal trajectories.

- The spatial resolution decreases due to electron diffusion.

A TPC height of 5 cm has been chosen in view of the following factors:

- The voltage necessary for the drift cathode in order to achieve E_{drift}= 600 V/cm is -3.000 V, which is within the standard range of commercial high voltage power supplies.

- As seen in Section 5.3, the electron mean drift time from the most unfavorable part of the TPC remains compatible with the electronics acquisition time window.

- The spatial resolution degradation due to diffusion is acceptable (the same order as the resolution).

- The expected angular resolution of the detector is better than 1,1º for muons with incident angles to the readout plane larger than 10º, which matches the values required to perform muon imaging. In turn, the angular constraint can be diminished with a correct positioning of the detector towards the target.

- The volume and weight of the detector remains in good agreement with the desired values for field transportability.

The drawbacks associated with this choice are:

-The need to integrate an electric field homogenizer within the TPC.

-The gas volume of the MUST detector is ~29,5 L, resulting in long filling times prior to operation.

5.5.1 TPC frame

The material chosen for the mechanical part of the TPC is aluminum, due to its light weight, low price, ease of machinability, good anti-corrosion properties and good conductivity.

The frame is composed of 4 elements made of 2 different pieces. The pieces are aligned thanks to a central flat guide bolt, and then attached by two conical head screws as seen in Figure 5.17. Once the frame is assembled, it has a rectangular shape with 1.155 mm x 555 mm external perimeter, 50 mm height and 15 mm thickness.

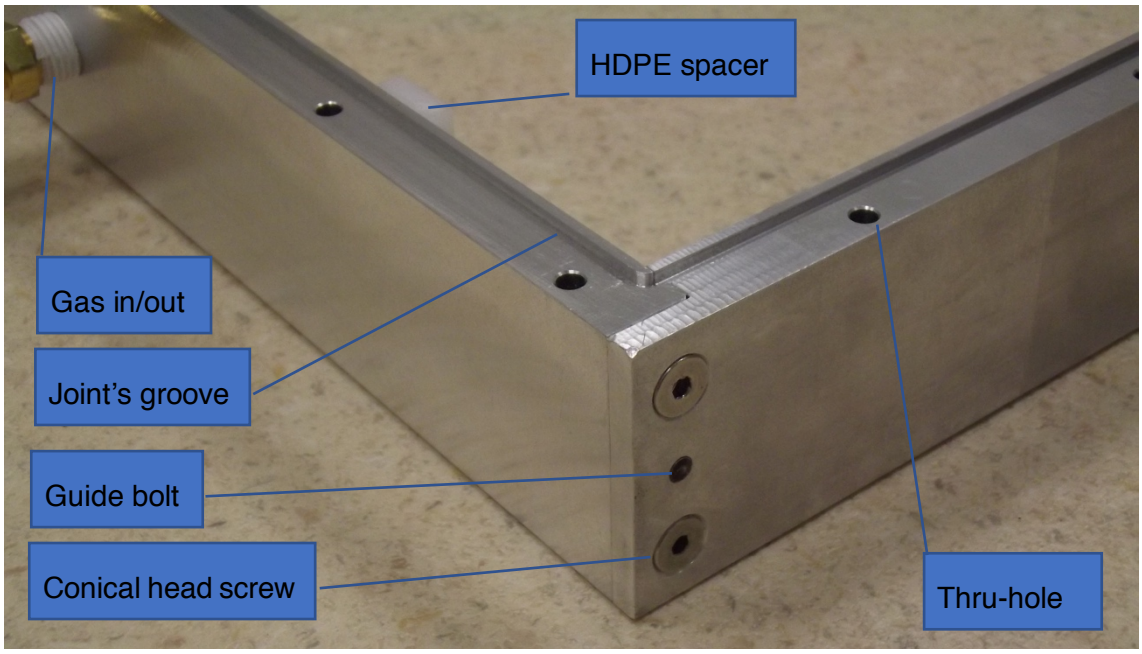

Figure 5. 17 Detail of the corner of the TPC frame.

The frame contains a pattern of thru-holes along its perimeter to let pass the screws that will secure the stack of elements defining the detector. There are also some high-density polyethylene (HDPE) spacers. The role of these components is to attach the PCB elements from the electric field homogenizer and to maintain them parallel to the metallic frame.

To reinforce the gas-tightness of the frame the following measures have been taken:

- Incorporation of Loctite 518 joint paste at the corner joint surfaces between frame pieces.

- The gas in/out connectors' thread is covered with Teflon tape to lubricate and seal the contact between parts.

- The frame has a groove loop in both up and down faces to host a cylindrical joint. This joint is responsible for the gas-tightness along the detector's perimeter. The upper face of the frame is in contact with the drift cathode, while the lower face is in contact with the Micromegas readout plane.

5.5.2 Drift cathode board

The MUST^2 drift cathode board has the following features:

- A polarized surface on the inner side of the TPC, to induce the electric field necessary for the electron drift.

- An external face completely covered with copper, to ground all external surfaces of the detector.

- This board, along with the metallic frame and the micromegas detector, defines the gas-thigh detection volume.

- Makes possible the electrical contact between the high voltage power supply and the drift cathode.

The drift cathode board consist in a 1,6 mm thick FR4 panel with 30 µm copper depositions on both faces. The perimeter of the board contains a pattern of holes for the assembly of the piece. The drift electrode of the inner face, seen in Figure 5.18, has the same shape as the active area of the Micromegas readout plane and is placed directly above it.

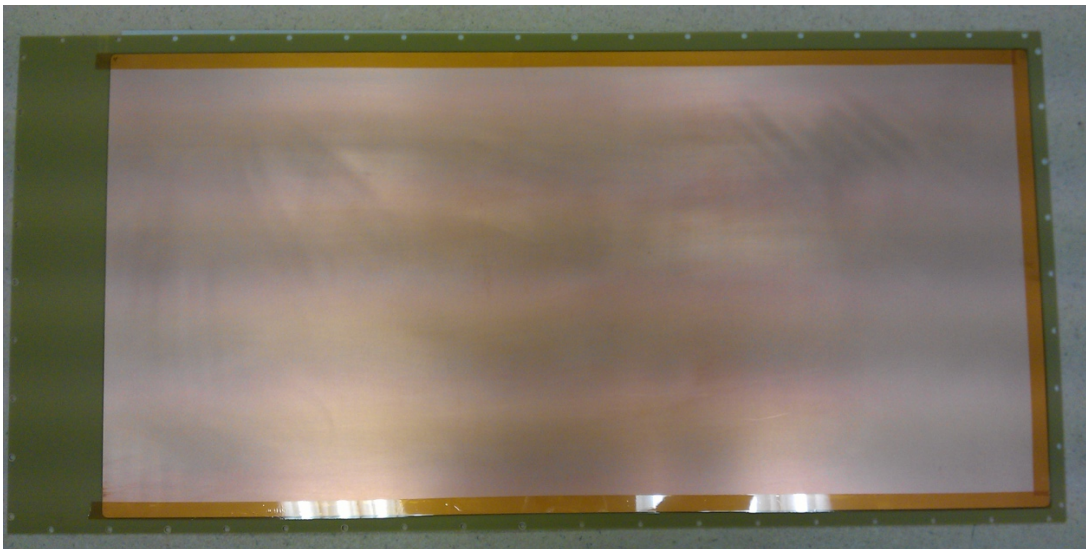

Figure 5. 18 Drift cathode of the time projection chamber.

The theoretical distance between the drift cathode and the metallic frame is 1 cm. Nevertheless, while operating at -3.000 V, sparks between the two elements have been noticed, due to their proximity once the detector is assembled. This design flaw has been resolved by placing Kapton® tape on the three sides of the cathode that are next to the frame.

The external face of the board contains a copper pad isolated from the remainder of this surface. The pad is connected to the drift cathode through the board, and acts as the entry point for the high voltage line, which polarizes the electrode. The electrical connection is made by means of a passive, second order low-pass RC filter in order to reduce the instrumental noise.

5.5.3 Electric field

Field homogeneity is of major importance in obtaining a straight projection of the particle path during TPC operation. The shape of the electric field inside the TPC has been simulated with two different software packages -QuickField and COMSOL multiphysics®- both yielding equivalent results. The first scenario considers a TPC without electric field homogenizers, a drift cathode polarized at -3.000 V and a grounded Micromesh. Figure 5.19 shows the result of the simulation made with COMSOL multiphysics®: the field lines allow visualizition of the shape of $\vec{E}_{drift}$, and represent the most probable path of the electrons generated inside the drift volume.

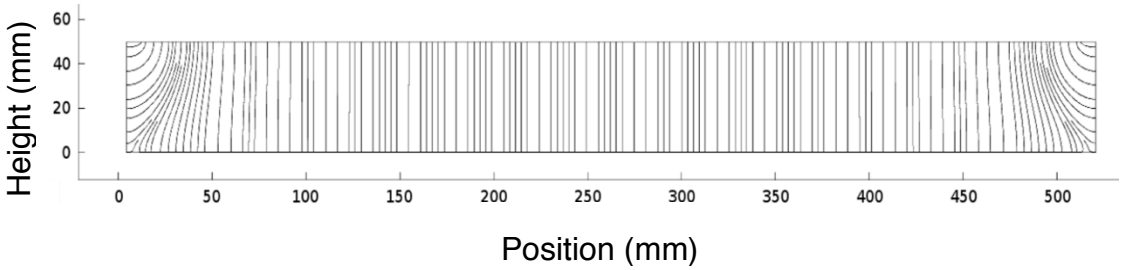

Figure 5. 19 Electric field lines inside the TPC without field homogenizer.

Figure 5.20 shows the results of 3 simulations obtained with the QuickField software. The three images present a zoom of the TPC near the metallic frame. The color indicates the voltage ranging from 0 to -3.000 V. The purple lines illustrate the path of 10 electrons released at different points of the TPC.

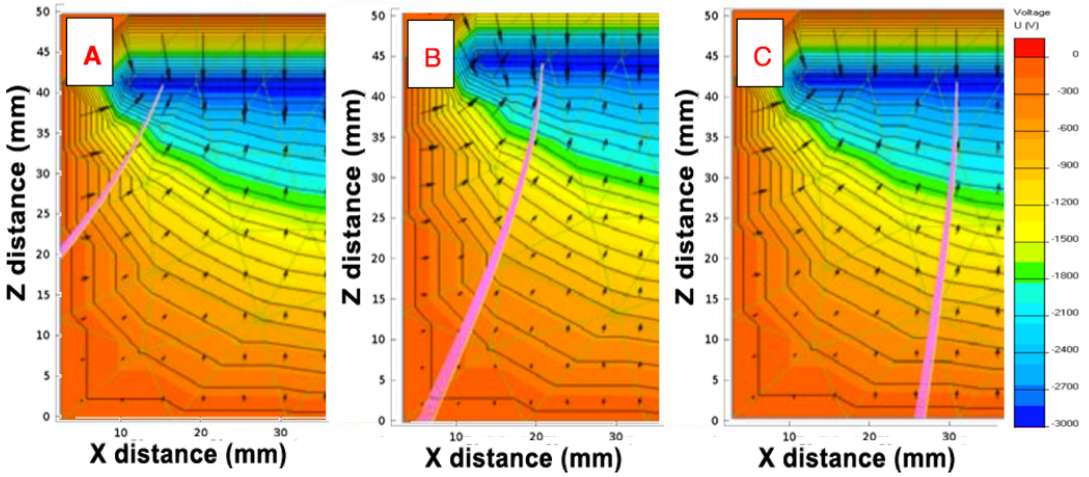

Figure 5. 20 Electron path simulation inside the TPC without field homogenizer.

The figures reveal important electric field distortions near the TPC frame. The non-orthogonality of the field lines to the detection plane cannot be neglected in the first 60 mm around the metallic frame[3], which results in an alteration of over 16% of the active surface.

[3] The horizontal deviation of the field lines for from the top to the bottom of the TPC is bigger than 1 mm, the readout pitch distance.

To minimize the electric field distortions predicted by the simulations, it is necessary to include an electric field cage inside the TPC. The role of this element is to define a uniform electrostatic field in the gas volume. To do so, a series of polarized conductors was placed along the frame perimeter to produce a progressive reduction of the voltage from the drift cathode to the micromesh.

The system based on printed circuit boards has been chosen because of the following factors:

- The PCB provides a self-supporting element in which the conductive elements remain immutable.

- Their mechanical stability enables the fixation to the metallic frame and reduces the need of servicing.

- PCBs are easy to design and fabricate, allowing custom design.

The PCB contains a series of equal, evenly-spaced copper tracks interconnected via resistors to create a polarized cage around the drift volume.

Three different track configurations have been simulated with COMSOL Multiphysics® to assess the effect of the number and size of the copper tracks. Figure 5.21 shows the electric field with no electric field homogenizer, and a PCB containing 6 tracks, 12 tracks and 24 tracks.

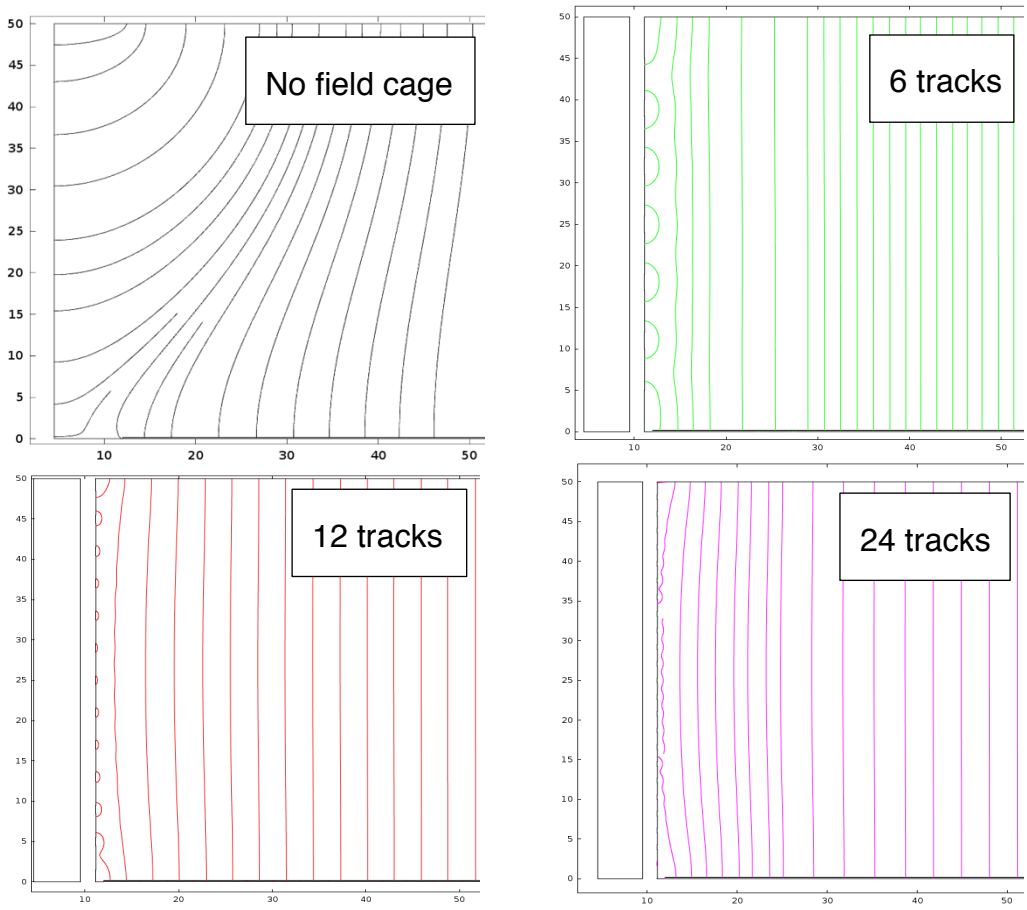

Figure 5. 21 Electric field simulation of three different PCB configurations.

As seen in Figure 5.21, incrementing the of number of copper tracks beyond a certain threshold yields no significant improvement in the electric field homogeneity. Therefore, a PCB with 6 copper tracks has been chosen for practical reasons. Fewer tracks implies less resistors to connect them, easing the soldering and layout of the components due to the lager tack size. Nevertheless, for devices below 6 divisions the electric field is not homogeneous enough. All resistors used for the track connections are the same, creating a uniformly-decreasing polarizing cascade. The high value of the resistors, 300 MΩ each and 2,1 GΩ in total, provides a current consumption on the order of 1,4 mA.

Figure 5.22, analogue to 5.19, represents the TPC with the electric field homogenizer. The path of the simulated electrons reveals a reduction of the deviation due to the electric field heterogeneities in the zones near the frame.

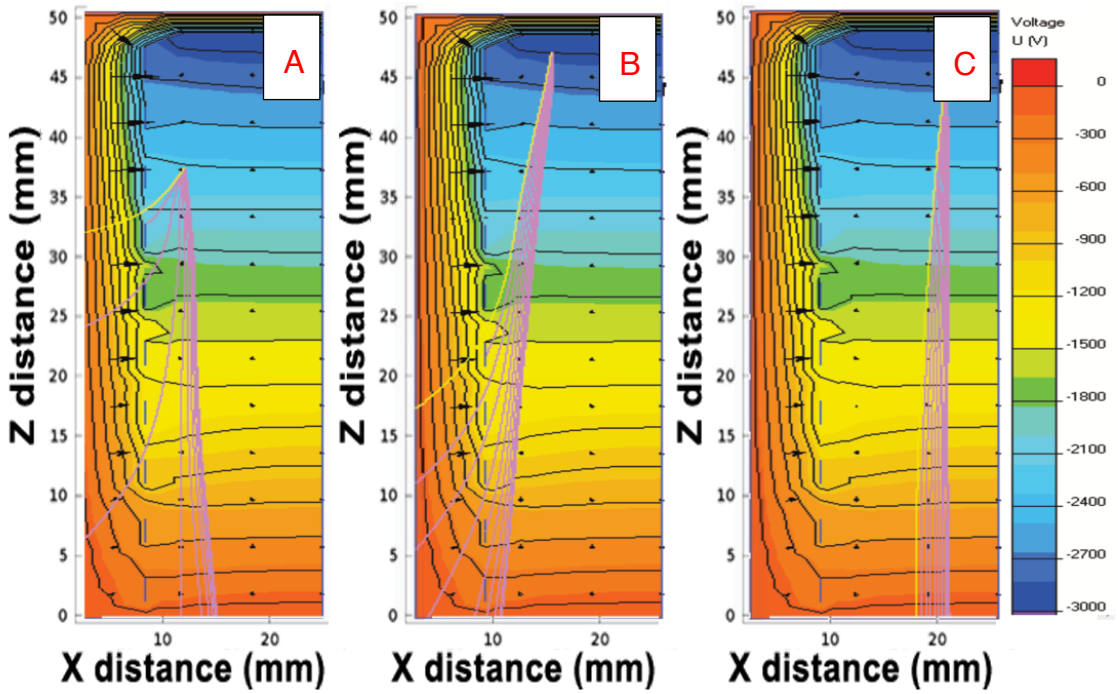

Figure 5. 22 Electron path simulation inside the TPC with the field homogenizer.

5.5.4 Angular resolution

The angular resolution provides an estimation of the error made in calculating the incident angle of the particle to the readout plane. It is influenced by the gas properties, which affect the temporal resolution and geometric parameters, such as the spatial resolution of the Micromegas readout plane (as seen in Section 5.2.3) and the height of the TPC. The reconstruction of the muon trajectory requires a minimum number of points in order to provide a reliable outcome.

This number is a parameter for the data reconstruction algorithm presented in the Chapter 6. The choice of this parameter influences the reconstruction efficiency and the robustness of the reconstruction. Nevertheless, a hard limit of 3 points is required in a less demanding scenario.

The angular resolution of the detector is dependent on the length of the projection of the muon trajectory over the readout plane. This length is in turn dependent of the muon incident angle of arrival. Figure 5.23 shows the maximal theoretical number of readout channels (considering the X and Y readout planes) intersected by the projection of the muon trajectory within the TPC as a function of its zenith and azimuth angles. The azimuth 0º represents the axis of the Y readout tracks.

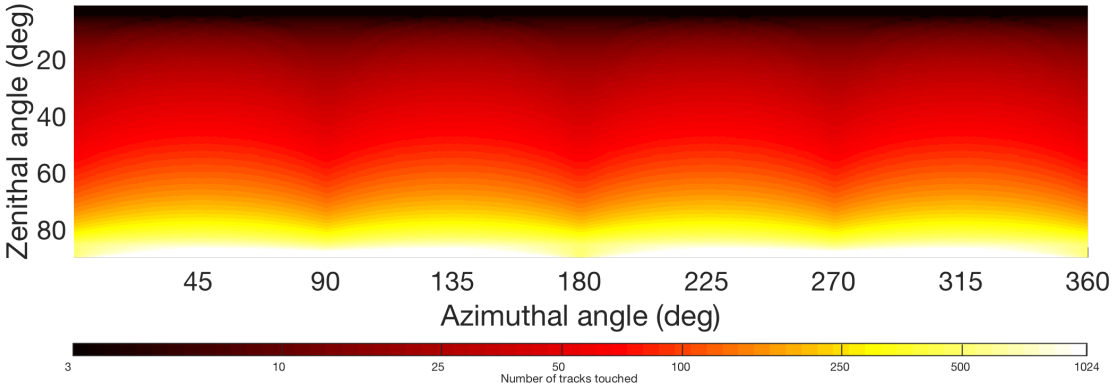

Figure 5. 23 Maximal number of readout channels intersecting the muon trajectory projection as a function of its zenith and azimuth arrival angles.

The figure shows that muons with trajectories with θ<~10º and azimuths near multiples of 90º, intersect less readout tracks so that the angle reconstruction is more difficult. Figure 5.24 shows the simulated detector's angular resolution as a function of the distance between the most distant hit channels associated with the same muon passage, which is in turn dependent of the incident angle of the muon arrival to the readout plane. The angular resolution increases with tilted tracks as more strips are hit.

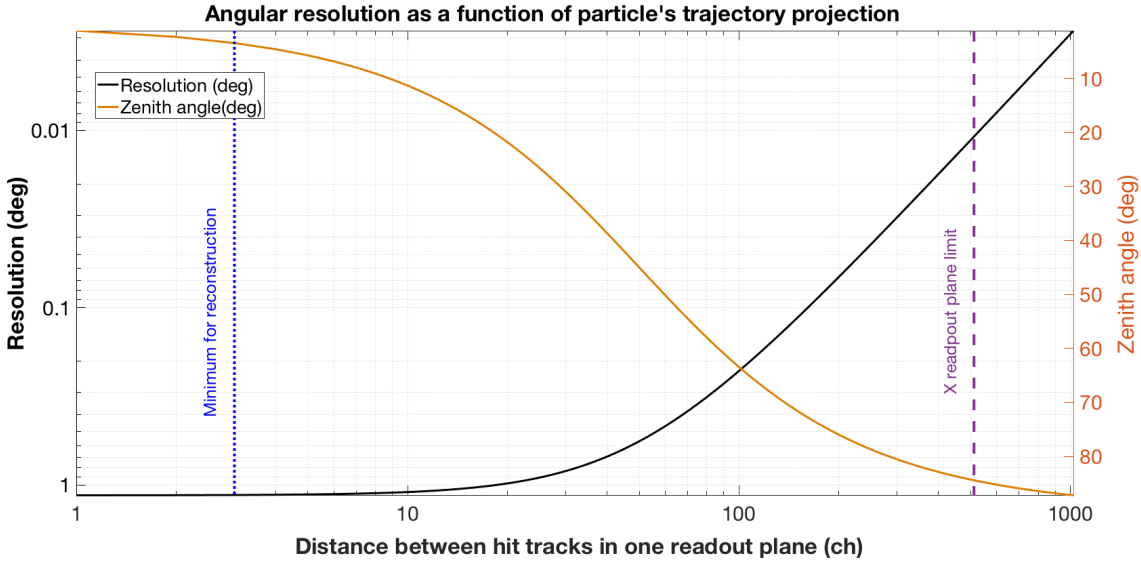

Figure 5. 24 Angular resolution of the MUST² detector as a function of the muon's trajectory projection over the readout plane.

5.6. Assembly

The Micromegas readout plane performance can be compromised by the presence of small particles, such as dust, in the amplification gap. Foreign bodies boost the discharges between the micromesh and the resistive anode, and trigger current leaks with annoying consequences. To minimize this, the Micromegas readout plane is protected with a melamine plate immediately following its production, and the assembly of the MUST^2 detector is made in the clean room of the Low Background Noise Laboratory.

The assembly of the detector is made in a series of steps to minimize the exposure of the readout plane to contaminants.

- Time projection chamber. The time projection chamber is composed of the drift cathode, the metallic frame and the electric field homogenizer.

The metallic frame is the first element to be assembled as it hosts the electric field homogenizer. The short sides of the metallic frame, as seen in Figure 5.25, contain the brass gas connectors and a diffusion plate. On top of it, the plastic spacers are attached with nylon screws, as also the long side pieces.

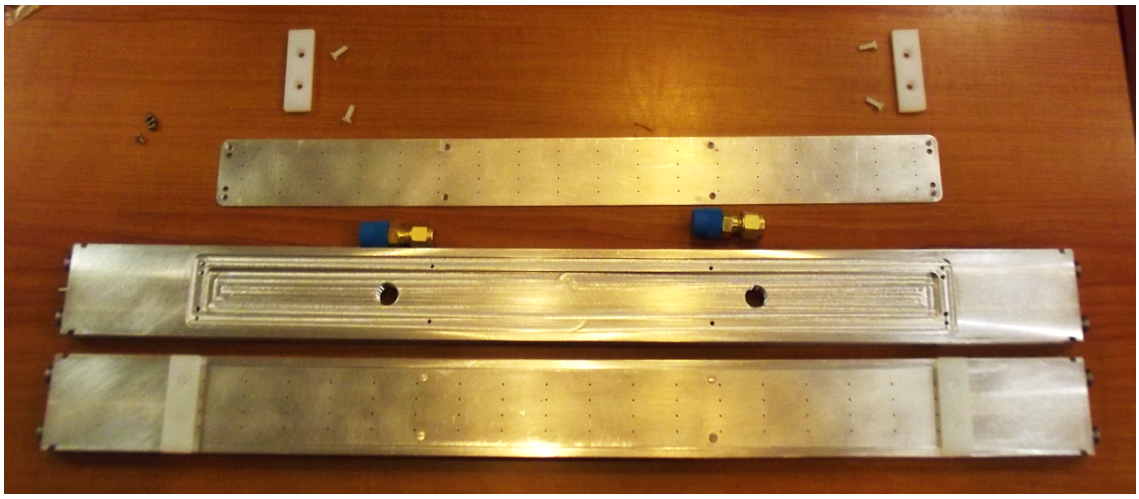

Figure 5. 25 Components of the short side of the metallic frame.

The next step is to assemble the four sides of the TPC frame. Loctite 518 is added in to the contact surfaces between metallic parts to improve the gas-tightness of the joint, and the excess removed. The result is seen in Figure 5.26.

The metallic frame is now ready to host the electric field homogenizer. Due to the PCB size limitations and given the large size of the detector, it has been impossible to create one single PCB board for the entire drift cage. Two different male/female pieces (see Figure 5.27 (A)) have been created so they can be combined in groups of 6 to obtain a board frame that fits perfectly inside the drift cage. The PCBs are mechanically attached to the TPC metallic frame by plastic spacers.

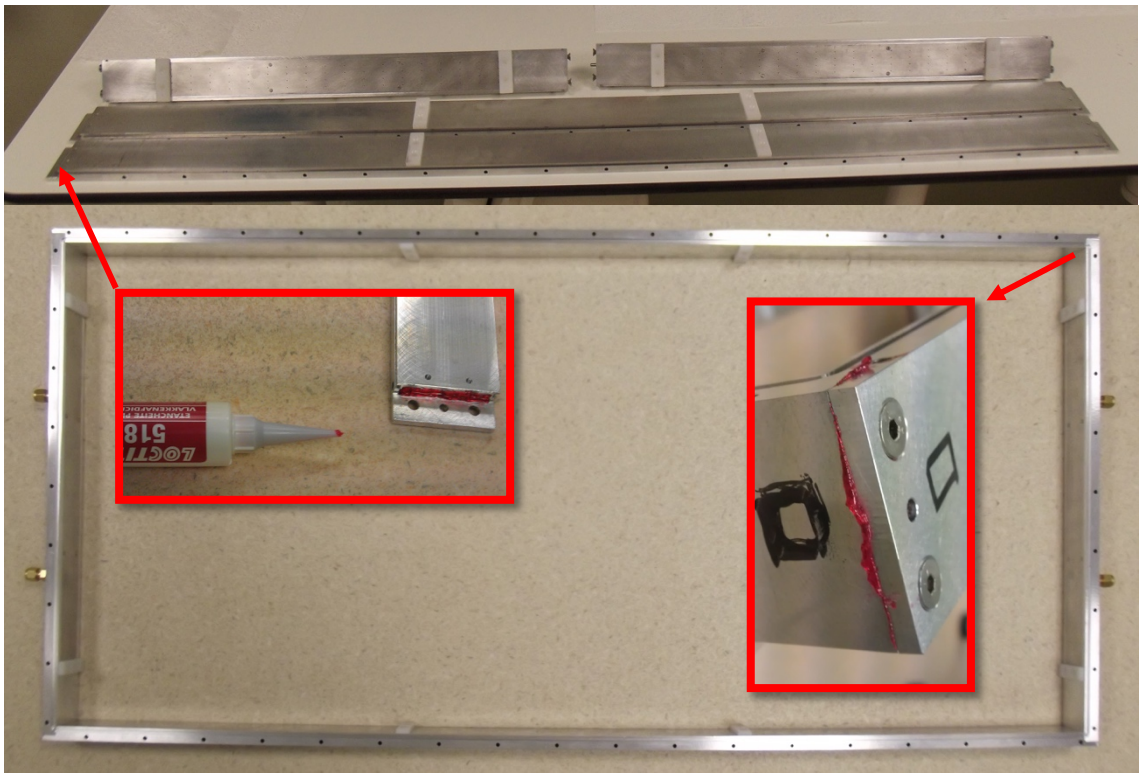

Figure 5. 26 TPC metallic frame.

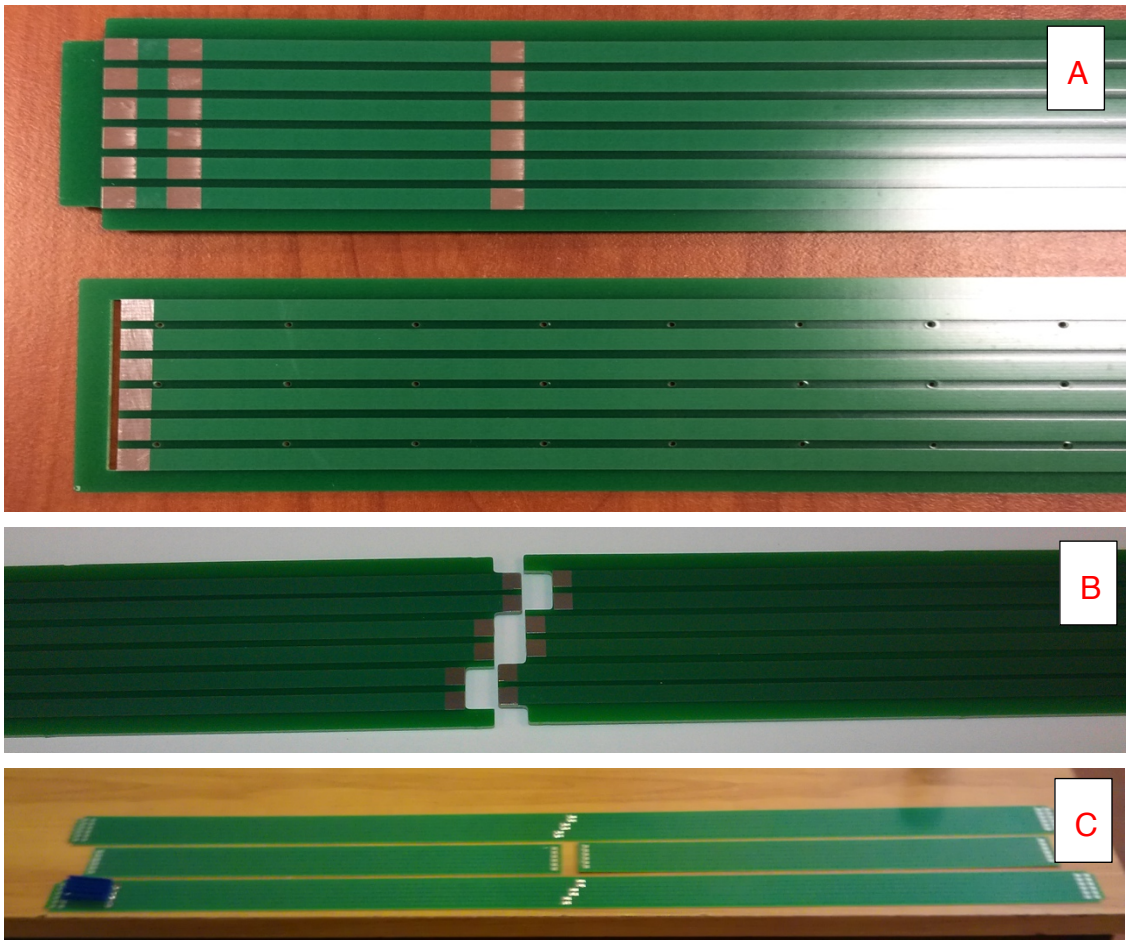

Figure 5. 27 Electric field cage PCB components.

Figure 5.27 (A) provides a global view of the corner connection of the different boards; the bare copper pads on the bands are for soldering the resistors and the boards between them. Figure 5.27 (B) shows the detail of the junction between the two boards which form the long side of the detector. Both pieces have the same geometry and they can be assembled together. The zig-zag design has been chosen to avoid mechanical stress on the soldered connection.

Figure 5.27 (C) shows the long frames already soldered and with the resistors. A complete view of the frame with the electric field cage can be found in Figure 5.14. (Up).

- Micromegas readout preparation. While most of the groups using this kind of readout plane try to make a good ground connection of the micromesh, the MUST^2 aims at being able to recover the mesh signal to provide a trigger signal for the electronics associated with the muon passage. Due to the fabrication process, the Micromegas detector presents some particularities that require being addressed.

After the fixation of the micromesh via the coverlay frame, the micromesh is cut all along the external perimeter and around the thru-holes for the screws that hold the detector together. Sometimes, microscopic 18 µm stainless-steel wires from the tore micromesh remain near these zones. These wires, in contact with the grounded aluminum TPC frame, reduce the amplitude of the signal collected in the dedicated micromesh pad. To avoid this, the contact zone between the fame and the coverlay is covered with Kapton® foil as seen in Figure 5.28. A similar effect is observed in the field cage pad, the current from the electric field homogenizer partially leaing to the micromesh because of the excess of tin when soldering the resistor. A small patch of Kapton prevents the electrical leakage.

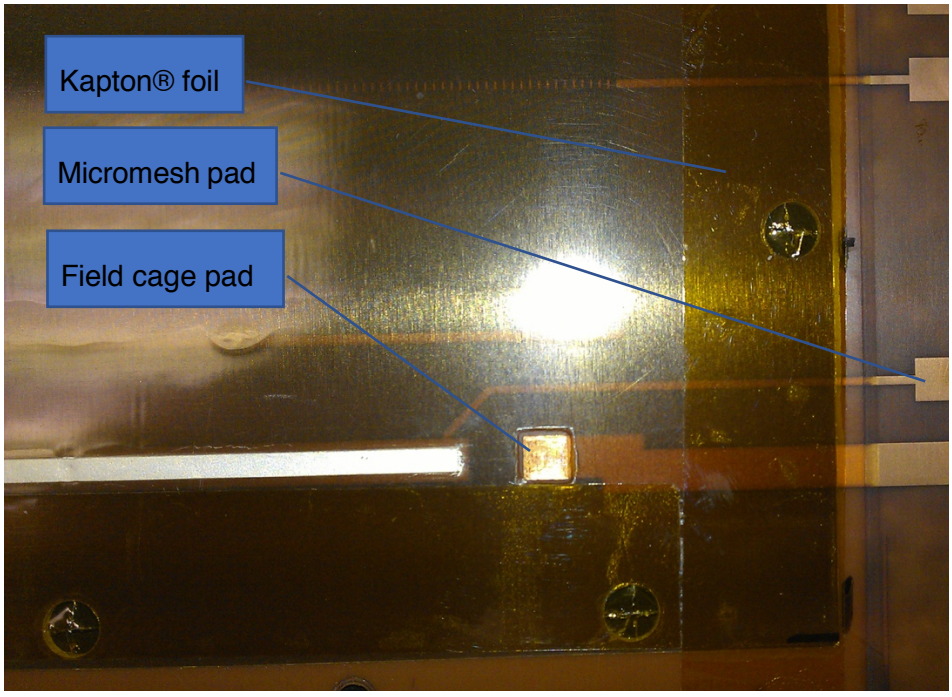

Figure 5. 28 Detail of the Kapton® foil added to isolate the micromesh.

In the same spirit, the base of the inox screws has been covered with insulating material as seen in Figure 5.29.

A steel auxiliary frame of 1 cm is placed below the Micromegas readout plane, in order to evenly distribute the pressure of the screws, increasing the gas-tightness and adding some rigidity to the structure.

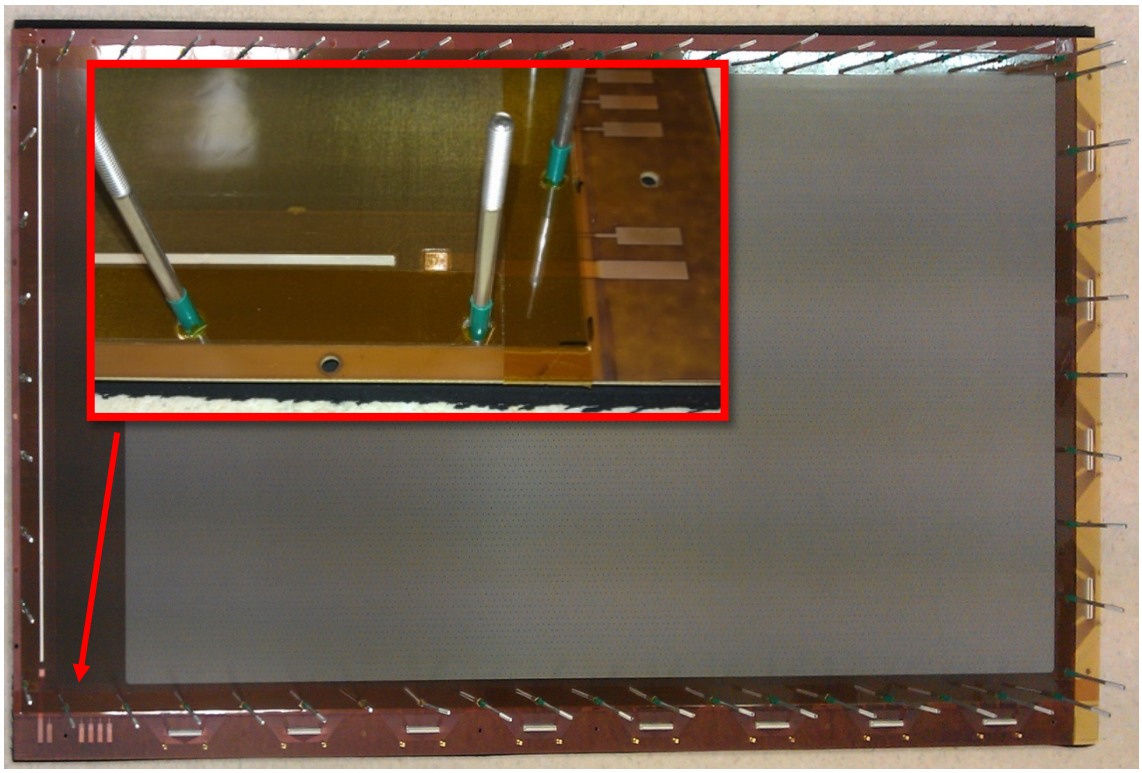

Figure 5. 29 Modified screws with insulating material.

- Assembly. The next step is the covering of the Micromegas readout plane with the drift cage. A toric rubber joint of 3,5 mm diameter is placed in the groove in both faces of the metallic frame. Until this moment, the readout plane has remained protected by the melamine plate; the protection is removed just before the incorporation of the metallic frame, and the covering process speed should be adapted to the grade of the clean room.

Once the metallic frame is in place, the lowest resistor of the field homogenizer element is soldered to the dedicated pad of the Micromegas detector, as seen in Figure 5.30 (A). The drift cathode board is then placed on top of the metallic frame. The contact of the electric field cage with the drift cathode is made thanks to a openable connector soldered in the upper resistor and the drift electrode as seen in figure 5.30 (B).

The upper auxiliary frame is seated, and the nuts are tightened following a star-pattern sequence. In this process, the screws must be kept immobile and only the nuts turned in order to avoid damaging the insulator in the base of the screws.

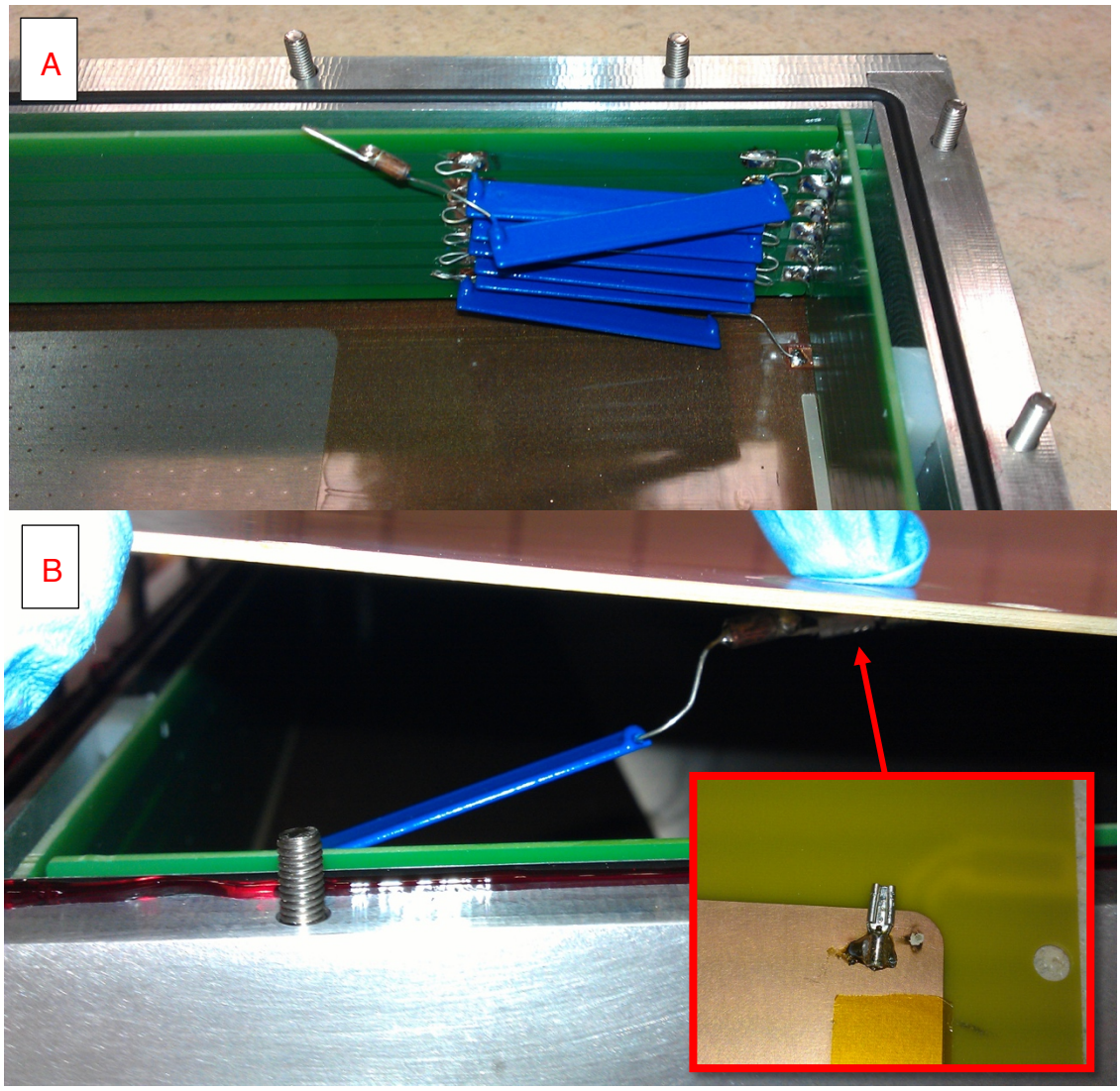

Figure 5. 30 Electrical connections of the electric field homogenizer.

The tightening process of the nuts is delicate due to the slight deformation of the readout plane resulting from the pressure applied by the frames. To monitor possible faults, the external surface of the detector and the resistive layer are grounded, the floating micromesh is polarized and the current monitored (see Figure 5.31). Current leaks indicate unwanted contacts to the ground (most of the time through the screws or the metallic frame), or leaks to the resistive layer due to the local distortion of the amplification gap near the external perimeter. A compromise must be reached between the gas-tightness and the electrical leakages.

Once the detector is closed, a passive, second order low-pass RC filter is applied to the high voltage line which polarizes the drift cathode, as seen in Figure 5.32. A copper protection cage has been added to avoid sparks while manipulating the detector, and to prevent accidental discharges.

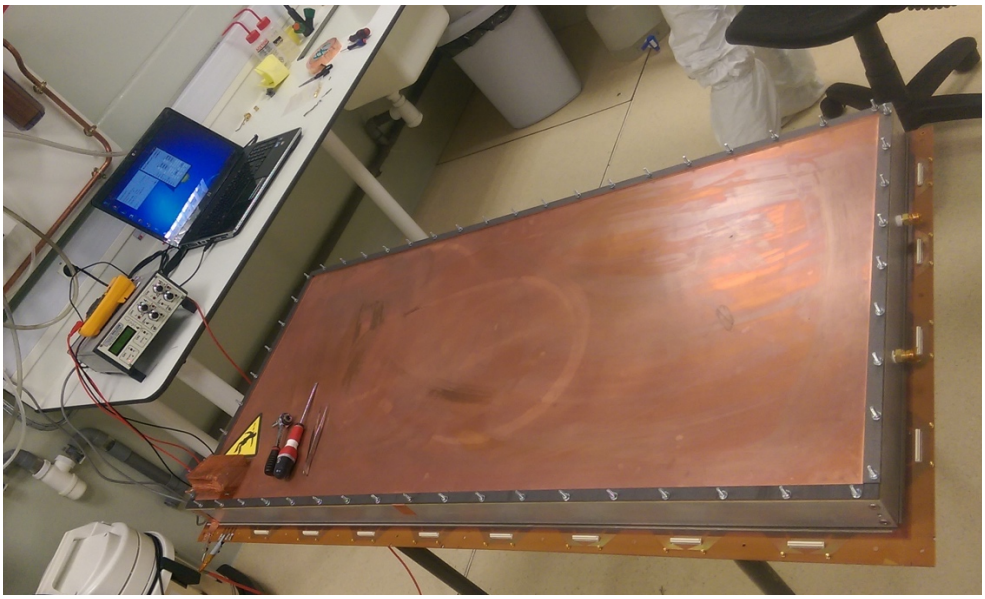

Figure 5. 31 Current monitoring while closing the detector.

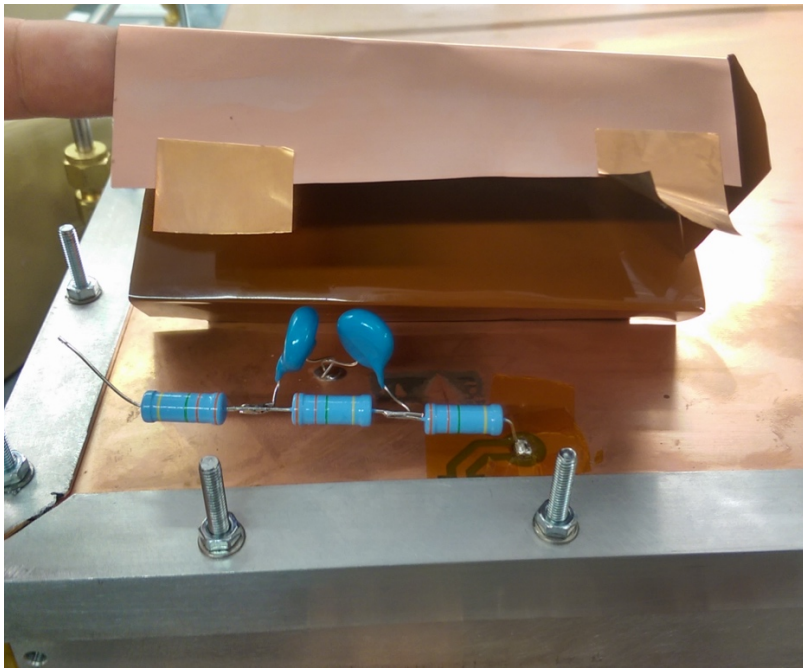

Figure 5. 32 Filter for the drift electric field cage and copper protection.

- Boxing up. The detector is placed inside a protection box for its transport and operation, as seen in Figure 5.33. Two gas quick-connectors are attached to the box and the connection is made with a stainless-steel tube of 6 mm diameter. To power the detector, a series of panel connectors is also placed: two SHV for the high voltage (drift cathode and resistive layer) and one BNC for the micromesh output. The electronics front-end cards are installed inside the box, and their wires enter the box via cable glands.

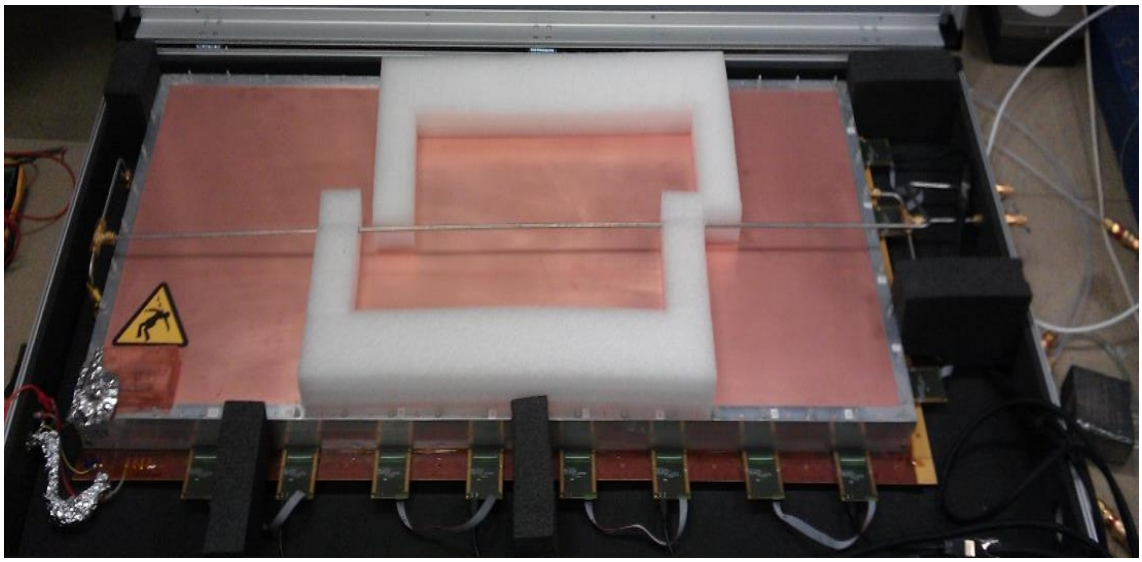

Figure 5. 33 MUST² fully assembled.

5.7. Instrumentation

During the present work, the data has been acquired with the CERN Scalable Readout System (SRS) and an external trigger provided by two scintillators in coincidence. A second data acquisition electronics, developed by the CEA's Irfu[4], has also been successfully tested, along with different trigger configurations.

5.7.1 CERN readout electronics: Scalable Readout System

The SRS, developed in the framework of the RD51 collaboration at CERN [Pinto, 2010][xv], aims at providing an easy-to-use, portable readout system for micropattern gaseous detectors.

Figure 5.34 represents a simplified version of all elements of the acquisition chain, consisting of APV25 front-end hybrid[5] cards, an ADC converter, a Frontend Concentrator (FEC), the Scalable Readout unit (SRU, only for network configurations) and the Data Acquisition Computer.

The interface of the APV25 hybrid card with the micromegas readout plane is made through a 130 pin Panasonic connector with two gold coated-connectors for the ground connection and mechanical fixation.

The hybrid cards are based on the custom-designed APV25 chip [Martoiu, 2013][xvi], which contains 128 channels of preamplifier and shaper which drive an analogue memory into which samples are written at 40MHz. All channels are AC coupled and protected against discharges via fast diodes.

[4] Institute of Research into the Fundamental laws of Universe.

[5] The term hybrid makes reference to the mixed analog and digital signals on the front-end boards.

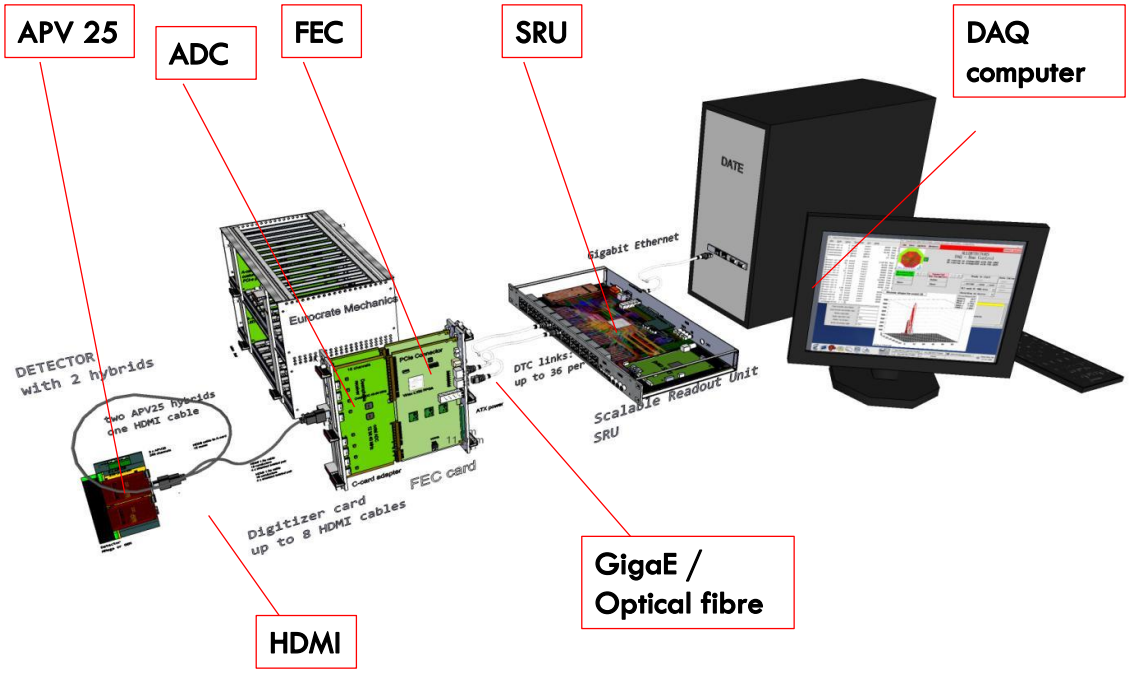

Figure 5. 34 Schema of SRS electronics. Source: RD51 collaboration.

The front-end boards operate in master/slave tandems and are connected between them via a flat cable. The so-called master card, additionally contains the PLL25 Application-Specific Integrated Circuit (ASIC), which unties the 40 MHz bunch clock and the trigger signals, which are fed to the hybrid board over a single differential line pair. The trigger signal is provided by a missing clock tick. The control and parallel readout of the two front-end hybrid cards is made with a single HDMI. The maximal length of the HDMI cable between the APV25 and the ADC converter is 25m.

The ADC converter, with a capacity of 8 HDMI ports (up to 2.048 instrumented channels), contains two octal 12-bit 40 MHz ADCs for digitization of the raw analog data. The ADC-card is coupled via PCI connectors to the FEC card. This field-programmable gate array (FPGA), provides readout flow control, as well as digital baseline suppression and data preprocessing. The combination of ADC and FEC cards is called a SRS combo and both components are hosted and powered by a crate. The external trigger signal is provided with a LEMO 00 coaxial connector carrying a NIM pulse and sent downstream to the APV25 cards.

The interface to the Data Acquisition (DAQ) Computer is realized via optic fiber (up to 100 Gb) or copper-based (up to 10 Gb) Gigabit Ethernet, according to the transceiver chosen. For readout of systems with more than 2048 channels, a switch-like unit can be added to synchronize clock and trigger between different FEC cards. In our case, with a detector of 1.536 channels in standalone operation, this has not been necessary.

<<Due to the synchronous transmission of the asynchronous trigger to the APV25 hybrid cards, the recorded time-resolved charge signals are afflicted with a 25 ns jitter. Nevertheless, in applications where the absolute signal timing is needed, the jitter can be corrected>> [Bortfeldt, 2014][xvii].

5.7.2 CEA Readout electronics

In the last stage of the project, and with to the partnership between IRIS Instruments and the CEA's IRFU, a compatibility test between the electronics developed by the CEA for the CLAS12 experiment and the MUST^2 has been performed. The compatibility between detectors and electronics is not straightforward in some cases. The different behavior of Micromegas detectors with unlike layout results into the heterogeneity of signal parameters, such as width of the signal or its charge.

The tested electronics consisted of a Front-End Unit (FEU) containing eight Dead-time less REadout ASIC for Micromegas (DREAM) chips, each being capable of reading 64 electronic channels, resulting in up to 512 channels per FEU.

Unlike the SRS, where the front-end electronics is located next to the Micromegas plane, connection with the DREAM chips is made through non-standard micro-coaxial cables with 64 channels each. As seen in Figure 5.35, an adapter (green card) was used between the Panasonic 130 pin connector and two 64 channel wires (divided into 4 flat blue cables with 32 channels each). The length of the micro-coax cable has been tested up to 2,2 m, beyond this point the, high capacitance of the readout tracks plus wire (over 200 pF) can become a problem [Bouteille, 2017][xviii].

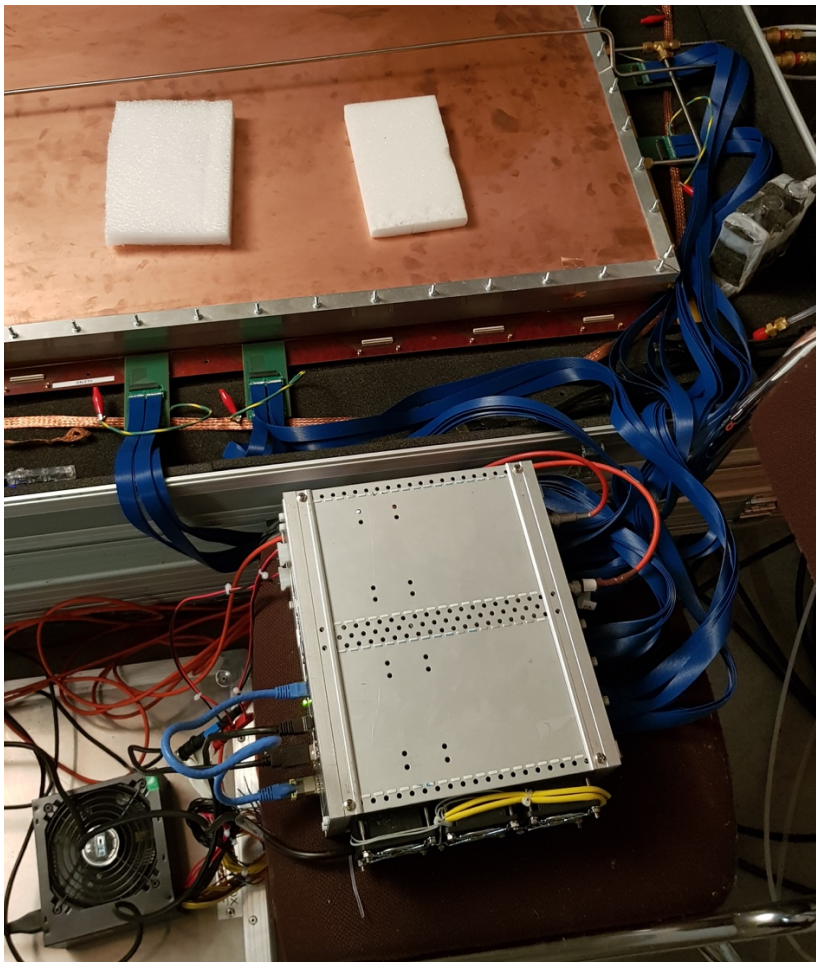

Figure 5. 35 MUST^2 detector instrumented with CEA electronics.

Each channel is connected to a programable charge sensitive amplifier (CSA), where the signal output is filtered and shaped. The chip contains prior the CSA a decoupling capacitor as circuit protection to avoid spark damage. The CSA gain has a dynamic range going of 50 - 600 fC (4 values), which has been key in overcoming the capacitance differences due to different track geometries or layouts.

The resulting amplitude is continuously stored in a circular buffer: when the trigger occurs, the analog memory is read and digitalized by an external 12-bit ADC, and then sent for storage at a frequency of up to 20 MHz.

5.7.3 Data acquisition trigger

The creation of a reliable trigger associated with the muon passage through the detector plays a major role in the electronics performance. During the present work, the four kinds of trigger presented in Figure 5.36 have been tested.

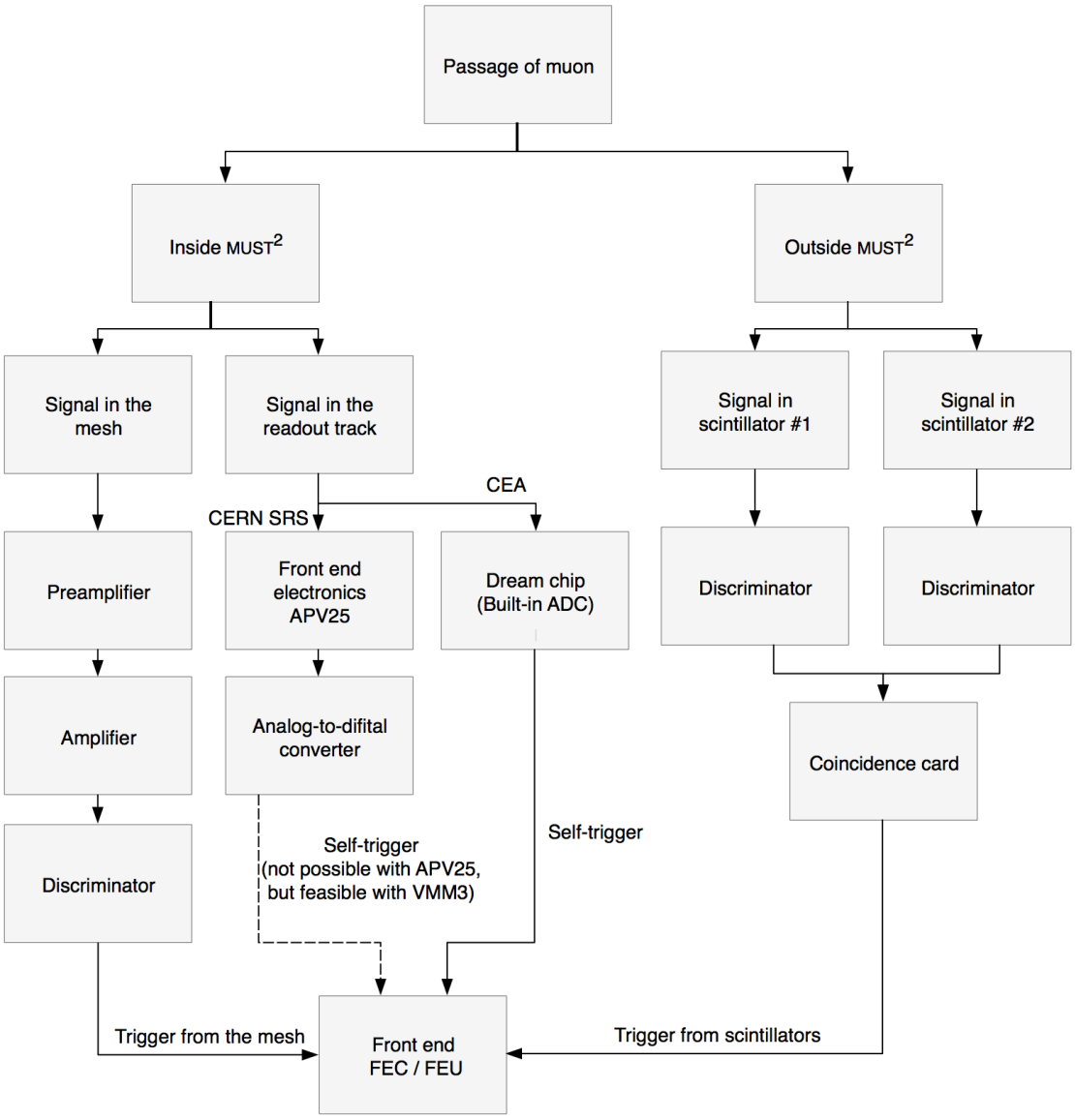

Figure 5. 36 Flow chart of data triggering.

- External trigger. The external trigger consists of the creation of a standardized signal pulse (NIM in case of the SRS FEC, TTL for the CEA's FEU) to prompt the FPGA to perform the data logging by means of two auxiliary scintillators aligned with the MUST^2 detector.

The scintillators used during the tests have roughly the same surface as the MUST^2 detector (1000 x 500 x 10 mm) and they are made of polystyrene-based plastic (UPS-923A) covered with light reflecting film and black vinyl. Each has a Hamamatsu R6094 PMT mounted on its short side; each, as seen in Figure 5.37, is encased by a protection box of the same surface as the MUST^2, one and in the same position to ease the material stacking.

Figure 5. 37 Scintillators used for external trigger.

Both scintillators are powered with a two-channel high voltage power supply iseg NHQ 214M at ~ -1.100 V. The output of the scintillator is sent to an Ortec 584 discriminator module, which produces a NIM pulse of ~50 ns each time that the input signal exceeds the stablished threshold value. This NIM pulses are collected by a LeCroy 465 coincidence module which generates the NIM signal to trigger the FPGA.

- Internal trigger from micromesh. The main difference compared with the previous trigger chain is the absence of auxiliary detectors. This mode of operation theoretically permits a standalone acquisition.

Two experimental setups have been tested. In the first, the mesh signal is recovered with an Ortec 142C preamplifier, then amplified with an Ortec 474 timing filter amplifier. The amplified signal is sent to an oscilloscope triggered by the scintillators.

Nevertheless, the low signal-to-noise ratio retrieved from the mesh, and high instrumental noise during the tests have hampered the creation of a steady trigger with this setup.

The second experimental setup relies on a CERN pickup box seen in Figure 5.38. This preamplifier-shaper tool has been specifically designed to trigger the SRS readout on passage of particles though MPGD detectors. This test was performed at the RD51 workshop and a different gas mixture, Ar:CO_2 (93:7) was tested due to the lack of the regular blend in these facilities.

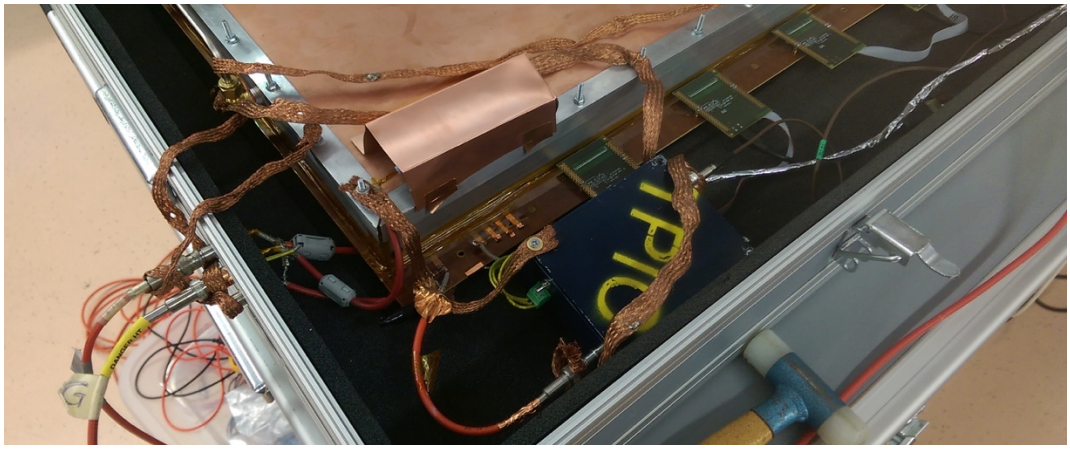

Figure 5. 38 CERN pickup box.

Figure 5.39 shows two captures from the oscilloscope used to monitor the experiment during runs of 5 minutes. The oscilloscope is triggered with a coincidence signal of two scintillators placed below and above the MUST[2] detector. The upper half shows a histogram of maximum signal amplitude, while the bottom half shows the signal from the pickup box and the trigger pulse.

The resistive layer is polarized to 560 V in both cases. Figure 5.39 (A) shows the signal when the drift voltage is off (meaning signal amplification but no electron drift in the TPC). On the other hand, Figure 5.39 (B) shows the signal when for E_{drift}= 600 V/cm.

It is possible to see the instrumental noise peak around 204 mV in both images, and the signal appearance once the TPC is active. This test validates the physical origin of the recorded data.

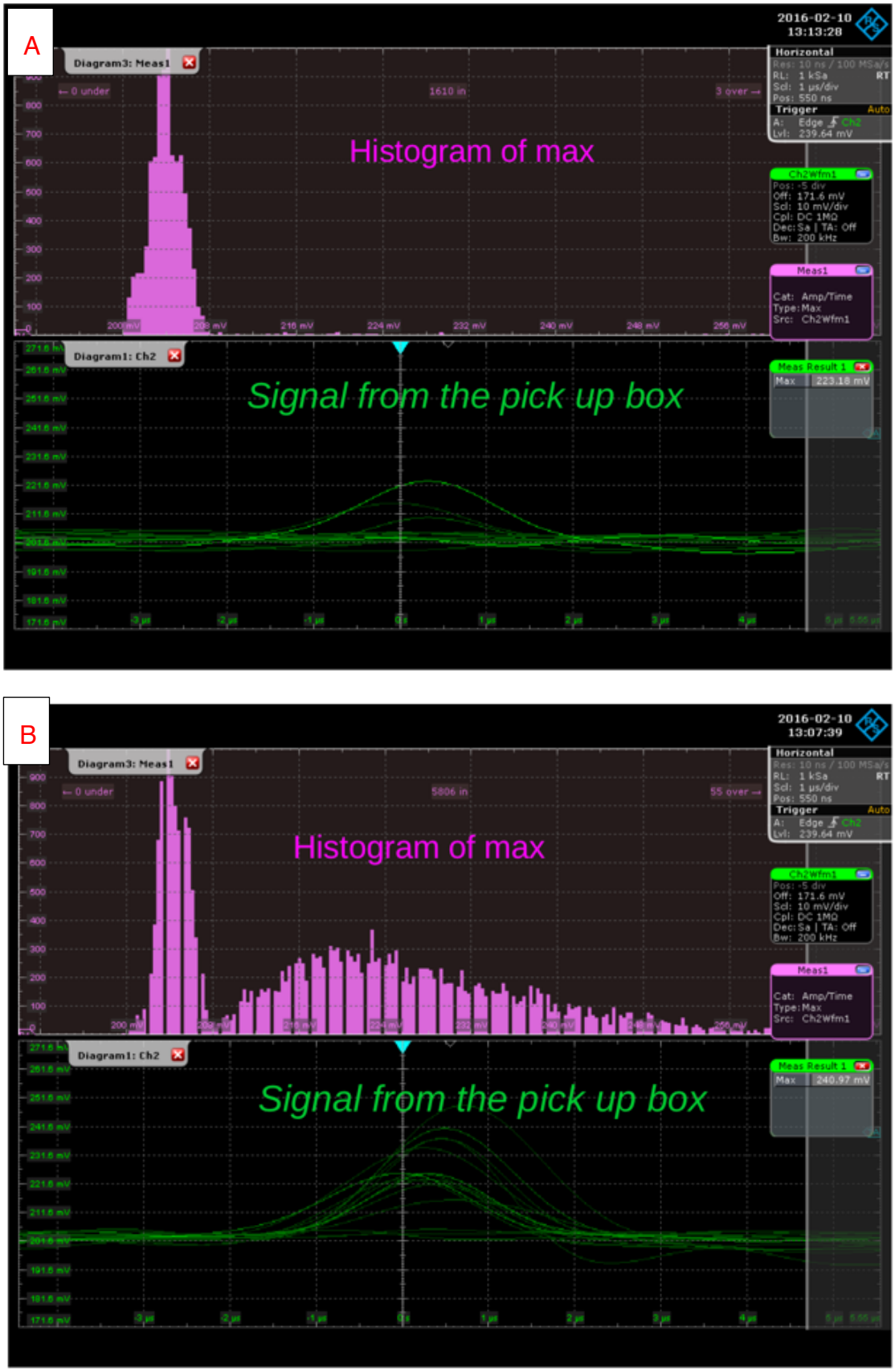

Figure 5. 39 Signal recovered from the micromesh with the drift voltage off (A) and on (B).

Figure 5.40 shows the good agreement between the mesh signal as the voltage of the resistive layer increases. This parameter presents a direct influence in the gain of the detector, the amplitude of the signal and the number of events recorded increases. These tests have demonstrated the potential feasibility of the self-trigger operation. Nevertheless, the drift speed of the gas used for the experiment is slower than our preferred mixture, and the signal exceeds the acquisition time-window. Therefore, the data analysis of this dataset is hence inconclusive. Further complementary testing is required in order to fully validate this approach.

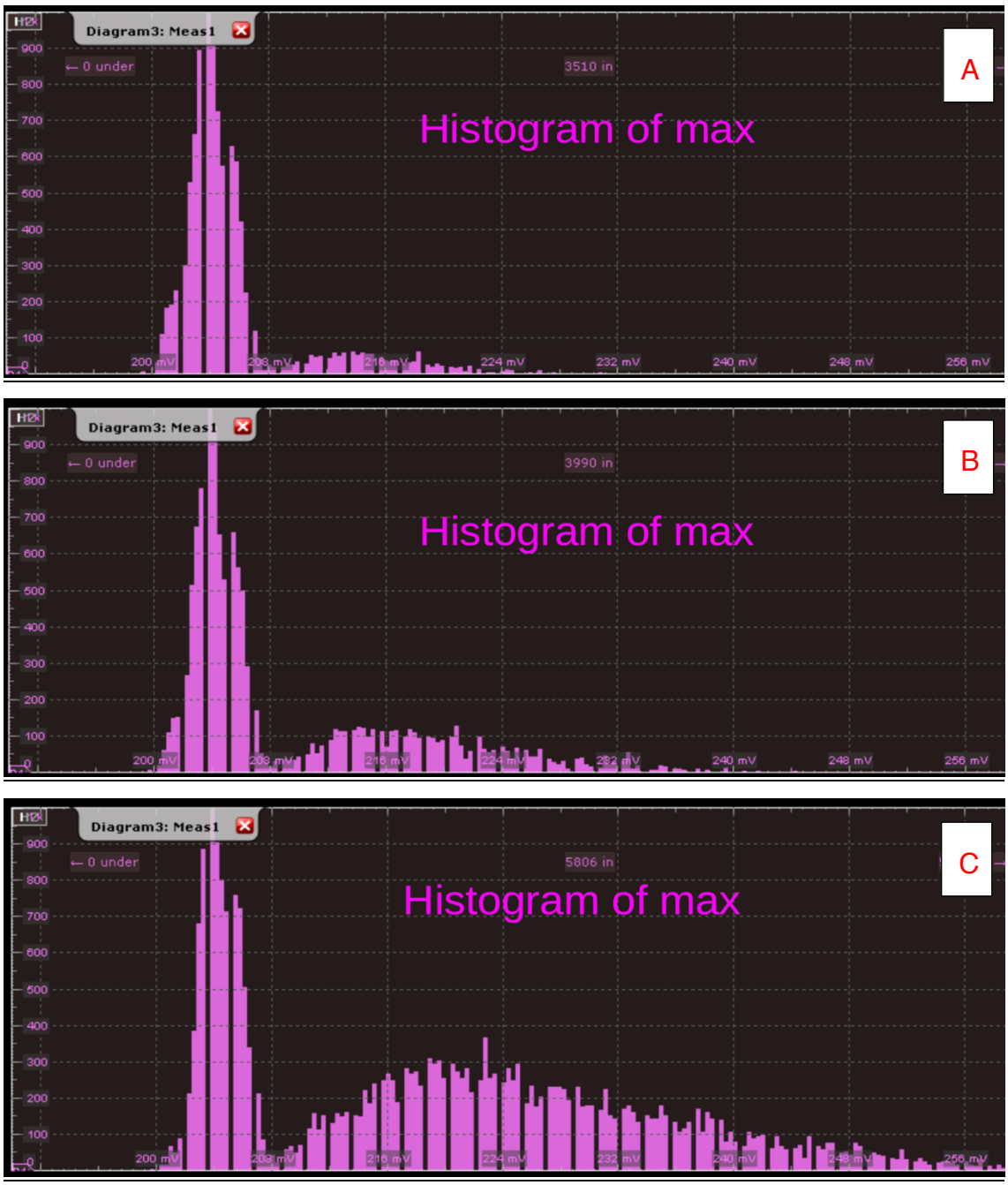

Figure 5. 40 Signal recovered from the micromesh for E_{drift} = 600 V/cm and a resistive layer voltage of 510 V (A), 530 V (B) and 560V (C).

- Internal trigger from readout tracks with CEA electronics. An interesting feature of this electronics is the self-trigger capability.

The filtered signal of each readout channel is compared to a programmable threshold value. The outputs are summed to obtain multiplicity information: if the multiplicity exceeds a programmable threshold, the differential output is triggered. This signal can be used to elaborate, outside the chip, a signal which can be used as a trigger for DREAM, furnishing a custom trigger configuration with no auxiliary detectors.

- Internal trigger from readout tracks with SRS electronics. This kind of trigger is not currently possible with the selected APV25 front-end electronics. Nevertheless, the new family of boards soon available, VMM3, allows this feature [Muller, 2018][xix].

5.8. Servicing

5.8.1 Contamination symptoms

As mentioned previously, Micromegas readout planes are prone to contamination in the amplification gap. If the detector starts losing performance, either locally or in general, it may suffer from contamination issues. This effect may be caused by several sources and appear at the outset or during operation. The first case is related to pollution during the assembly of the TPC, whereas the second one occurs as a consequence of the presence of humidity and/or particles in suspension smaller than 20 μm in the gas flow. The contaminants decrease the resistance between the micromesh and the resistive layer, which ideally should be infinite and in fact ranges from 10 to 100 GΩ. The resistance drop discharges the polarized resistive area through the grounded micromesh, reducing drastically the electric field and hence reducing the signal amplification. To prevent permanent damage to the readout plane, it is good practice to set a low current limitation in the resistive layer power supply (150-200 nA).

A recognizable symptom associated with a serious contamination problem is the vanishing of events in the affected area due to the drop of the amplification field and the rise of the current to feed the resistive layer. Figure 5.41 shows the 2D histogram of 5.000 detected events in a partially contaminated detector. The lower half of the detector is not able to detect the passage of particles due to the loss of gain in this section. If the current leakage is due to the presence of a small particle, such as dust, it might disappear without a user interaction; the current leaks produced in the contaminated point come to vaporize the contaminant in some cases by electric pyrolysis and self-regulate the leakage problem.

This scenario is illustrated in Figure 5.42. Both images represent a 2D histogram of the detected points in an acquisition immediately following the closing of the TPC. This dataset corresponds to the experiment for validating the self-trigger from the micromesh described in Section 5.7.3. The active zone of the detector was limited to the zone between Y channels 128 to 256 and X channels 1 to 1.024.

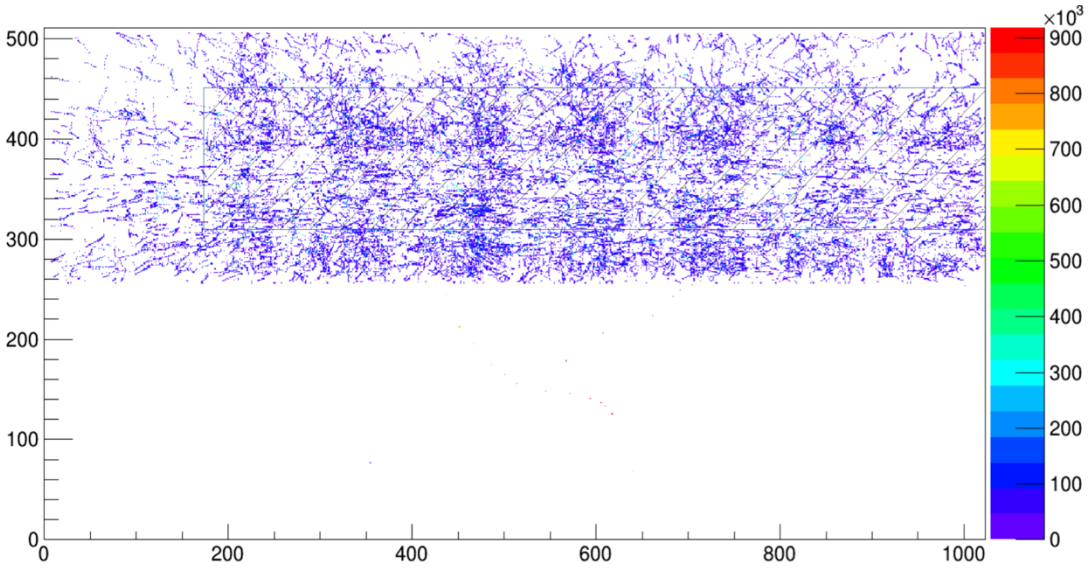

Figure 5. 41 Characteristic behavior from a detector presenting a current leakage in the lower half.

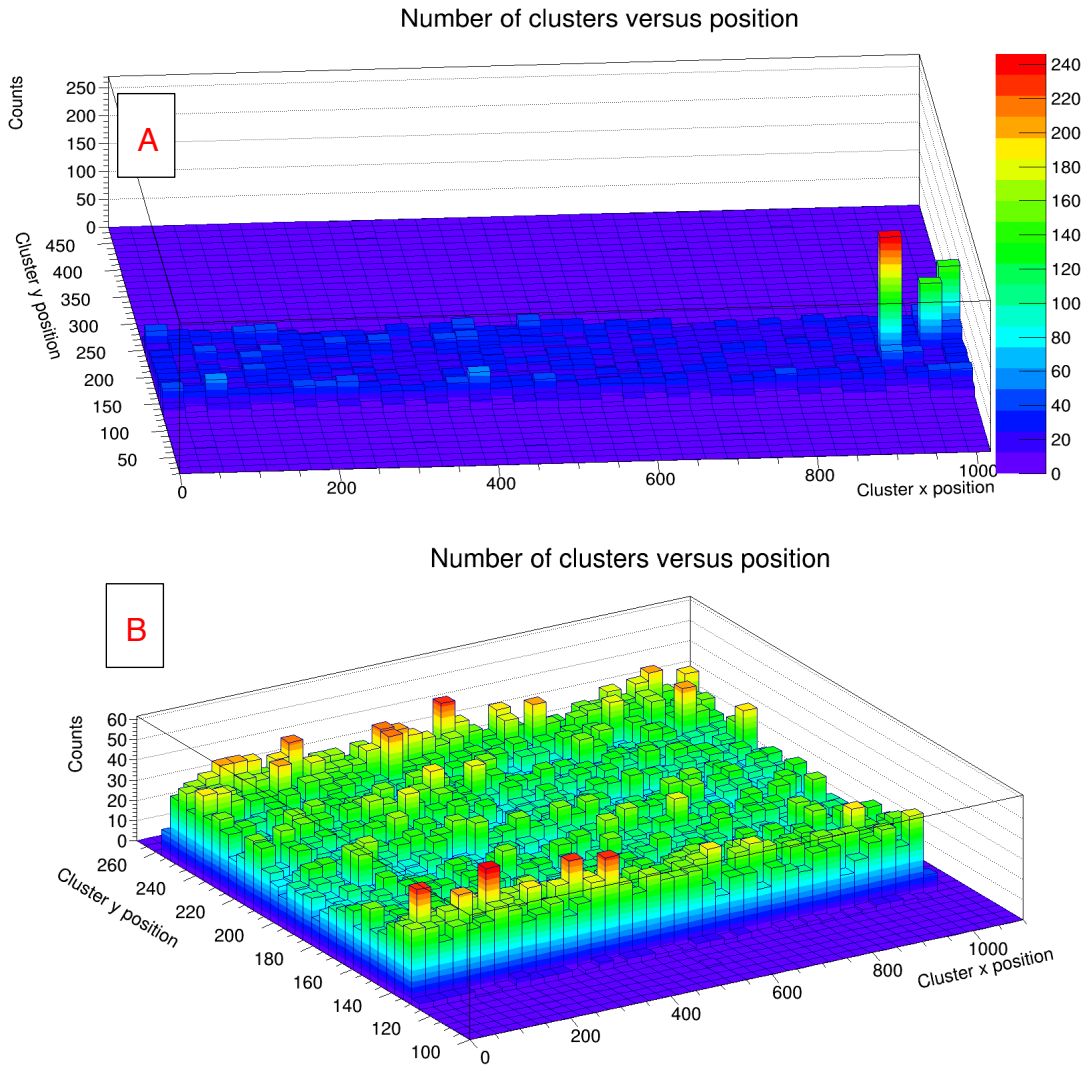

Figure 5. 42 Current leak points(A) disappear after 3h of operation (B) due to the self-cleaning of the detector by electric pyrolysis

Figure 5.42 (A) presents 3 points with abnormally high detection rates located near the detector frame, probably due to the presence of particles after a service operation in this zone (exchange of the gas line). After 3 h, Figure 5.42 (B) shows that the high detection rates at the same points has drastically decreased to the average.

5.8.2 Cleaning protocol

Once the lack of performance has been established and related to the presence of impurities in the amplification gap, the cleaning protocol to follow is the one shown in Figure 5.43.

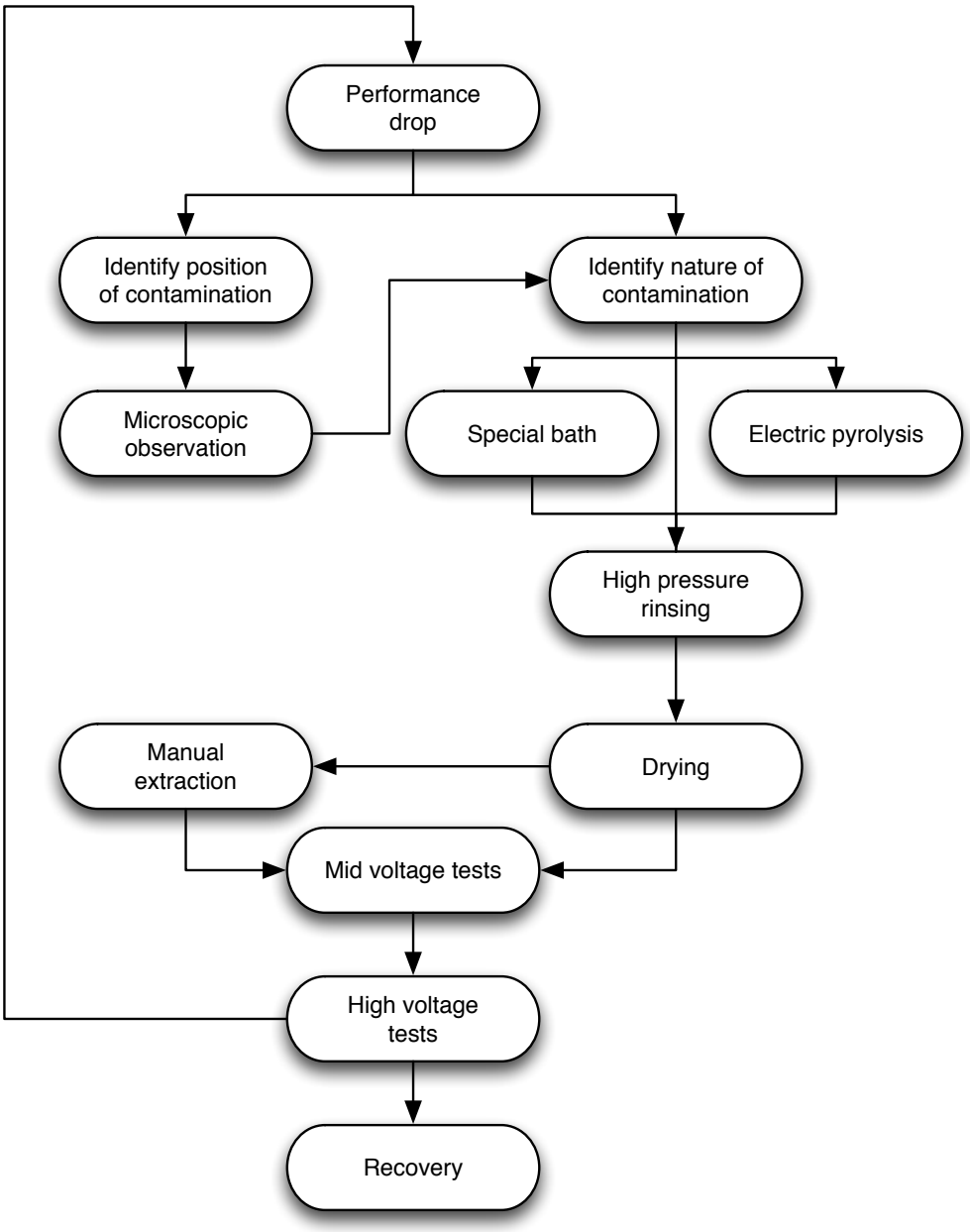

Figure 5. 43 Flow diagram of the Micromegas cleaning protocol.

The first step is to identify the affected area using different means. The 2D histograms such as in Figures 5.41 and 5.42 give hints as to the position of the contaminated zone. Another technique is to measure the leak current between the resistive layer by sectors (phase) and the micromesh (ground): typical values of the leak current should not exceed 20 nA in air for 650 V in air. In some cases, a direct observation with a microscope can be made to identify the cause of the problem.

It is not always possible to identify the cause and position of the problem, especially with humidity. In this case it is possible to proceed directly with the cleaning. The procedure for cleaning the detector includes different stages depending on the contaminant, and the steps should be conducted in order of increasing roughness to avoid damaging the detector as much as possible.

The first and less invasive technique is to try removing the contaminants by rinsing with pressurized water. The servicing must be done in a wet area with a source of deionized water and a pumping system to provide the pressure necessary to clean beneath the micromesh.

As seen in Figure 5.44 (A), a superficial cleaning is made to move all the contaminants settled over the mesh. This is performed from a distance of at least 1 m. Keeping a threshold distance is important to not apply too much pressure, which could push more contaminants inside the amplification gap. The sweep should be done in downwards movements to help the water stream in removing the impurities. Once completed, a horizontal sweep is convenient to concentrate in a single corner. After the superficial cleaning, comes the cleaning of the amplification gap. The threshold distance to the detector should be reduced to 20 cm to penetrate the micromesh and push the particles downwards. Afterwards, the Micromegas readout plane is placed into an oven at ~80º C for about 30 minutes, as see in Figure 5.44 (B).

At this point and after a visual inspection it is possible to proceed to a manual extraction of the identified contaminants. To do so, a small incision is performed in the micromesh and the foreign body is withdrawn. The affected zone is then covered with resin in order to avoid the connection between the ripped micromesh and the resistive layer. The result of this process can be seen in Figure 5.45.

Another technique is to submerge the detection plane into cleaning baths made of (per order of increasing roughness): soapy water, solvents (alcohol or ketone), sodium permanganate or solution of NaOH at 15% and 60ºC (same as for removing the coverlay). The bath facility of the CERN MPGD workshop can be seen in Figure 5.46.

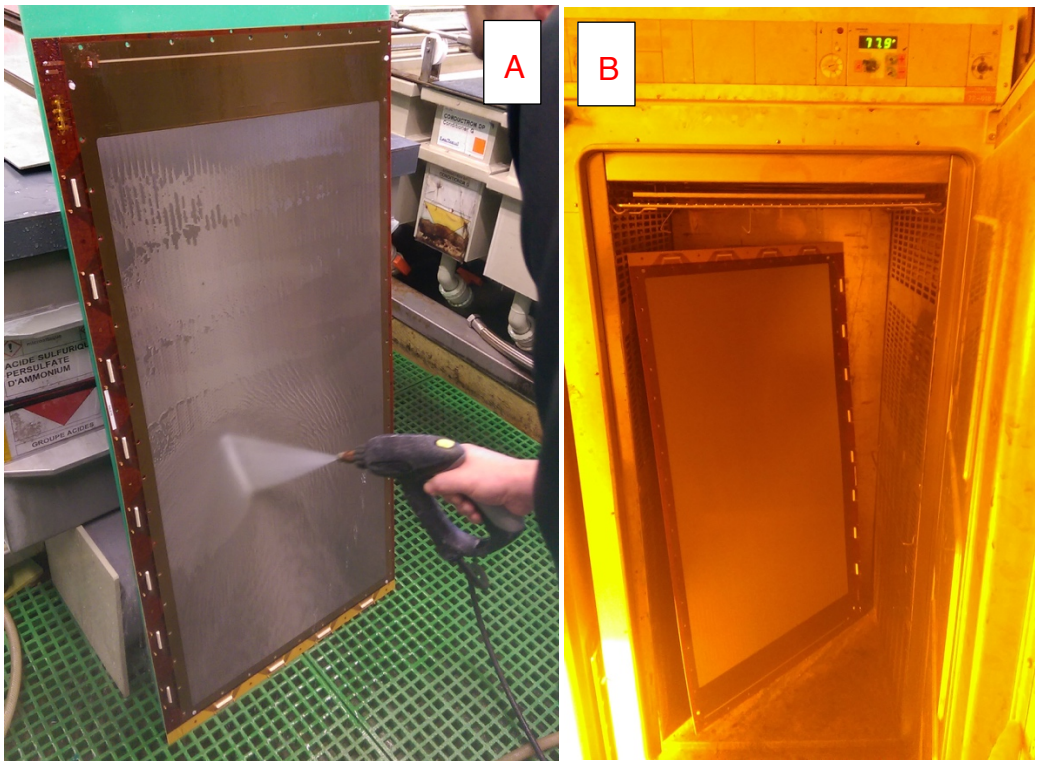

Figure 5. 44 Cleaning of the Micromegas readout plane with pressurized water and drying.

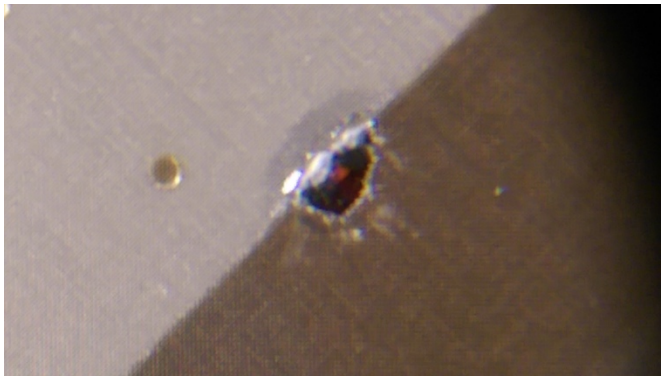

Figure 5. 45 Micromesh consolidated after body extraction.

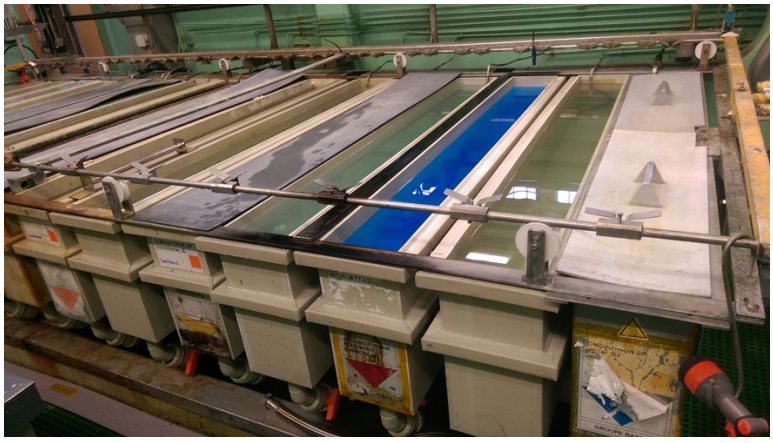

Figure 5. 46 Cleaning baths at MPGD workshop.

Once the cleaning is completed, it is possible to run a high voltage test. This examination consists of monitoring the breakdown voltage between the resistive layer and the micromesh at its four different sections. This test is done in a clean room with air. The theoretical maximal breakdown value is given by the Paschen's law as explained in Section 4.9.3, and must be remembered that the amplification gap height ranges from 100 to 128 µm. In general, breakdown voltages over 900 V are considered excellent.

Table 5.2 provides the measured breakdown voltages after the assembly of two detectors as a reference, one made by CERN and the second made partially by Elvia and finished by the CERN.

Table 5.2. Breakdown voltages for two different detectors.

	Zone #1	Zone #2	Zone #3	Zone #4
CERN made detector	850 V	780 V	925 V	925V
Elvia/CERN detector	783 V	850 V	852 V	830 V

5.9. References

[i] Oed, A. (1988) Position-sensitive detector with microstrip anode for electron multi- plication with gases, Nucl. Instrum. meth. A 263, 351. 20-22

[ii] Sauli, F. (1997) GEM: A new concept for electron amplification in gas detectors. Nucl. Instrum. Meth. A 386, 531

[iii] Giomataris, Y. et al. (1996). MICROMEGAS: a high-granularity position-sensitive gaseous detector for high particle-flux environments Nucl. Instrum. Meth. A 376, 29

[iv] Duarte Pinto, S. (2010). Micropattern gas detector technologies and applications. The work of the RD51 collaboration. arXiv:1011.5529v1. DOI:10.1109/NSSMIC.2010.5873870

[v] J. Derré et al. (2001). Statial resolution in Micromegas detectors, Nucl. Instrum. and Meth. A 459 523-531. s

[vi] Papaevangelou, T. et al. (2018) Fast Timing for High-Rate Environments with Micromegas. EPJ Web of Conferences 174, 02002

[vii] Giomataris, I. et al. (2006). Micromegas in a bulk. Nucl. Instrum. meth. A 560. 405-408

[viii] Bianco, M. (2016). Micromegas detectors for the muon spectrometer upgrade of the ATLAS experiment. Nucl. Instrum. meth. A 824. 496-500

[ix] Radics, B. et al. (2015) The ASACUSA Micromegas Tracker: A cylindrical, bulk Micromegas detector for antimatter research. Rev. Sci. Instrum. 86, 083304

[x] Procureur, S., Dupré, R. And Aune, S. (2013). Genetic multiplexing and first results with a 50×50 cm^2 Micromegas. Nucl. Instrum. meth. A 729. 888-894

[xi] Kuger, F., Iengo, P. (2018) Design, construction and quality control of resistive-Micromegas anode boards for the ATLAS experiment. EPJ Web of Conferences 174, 01013

[xii] Delbart, A. (2010). Production and calibration of 9 m^2 of bulk-micromegas detectors for the readout of the ND280/TPCs of the T2K experiment. Nucl. Instrum. meth. A 623. 105-107

[xiii] International Organization for Standardization (1999). Industrial woven wire cloth - Technical requirements and testing. ISO 9044:1999(E),

[xiv] Ferbel.T (1991). Experimental Techniques In High-energy Nuclear And Particle Physics (2^{nd} Edition). World Scientific

[xv] Pinto, S.D. (2010). Micropattern gas detector technologies and applications, the work of the RD51 collaboration. In Nuclear Science Symposium Conference Record (NSS/MIC), 2010 IEEE, 802–807

[xvi]Martoiu, S., Muller, H., Tarazona, A. and Toledo J. (2013). Development of the scalable readout system for micro-pattern gas detectors and other applications. JINST, 8 (03):C03015.

[xvii] Bortfeldt, J. (2014). Development of Floating Strip Micromegas Detectors. Doctoral dissertation.

[xviii] Bouteille, S. (2017). Développement et application de détecteurs gazeux à micro-pistes pour la tomographie muonique. Doctoral dissertation.

[xix] Muller, H. (2018), Scalable Readout Systems in 2018. RD51 Collaboration Meeting and the topical workshop on “MPGD Stability”.

Chapter 6. Data acquisition and analysis.

Chapter 6 abstract

Chapter 6 describes the different software tools used for recording the data and its subsequent analysis, with the aim of providing an overall comprehension of the data management process including: acquisition, preanalysis, analysis and data filtering techniques.

The data acquisition and preanalysis were made with software developed for the electronics used during most of the present work, the CERN Scalable Readout System electronics.

On the other hand, the muon trajectory reconstruction is made via the algorithm created by T. Serre. This algorithm is capable of retrieving the time, 2D position, zenith (θ) and azimuth (φ) angles for most of the muons traversing the detector. A detailed description of its functioning is presented and its limitations discussed.

As a result of the conditions required to reconstruct the trajectory, the MUST^2 presents some “blind zones” where the trajectories cannot be calculated, yet, their influence on the muon flux measurement can be minimized with a detector correctly positioned towards the target.

The track reconstruction algorithm still has room for improvement, such as the fine tuning the development of the centroid technique to reduce the blind zone. The analysis of further data will help in order to enhance the robustness of the results.

Lastly, the current analysis chain represents a bottleneck in terms of computing time. One possible solution is presented to partially overcome this limitation.

6.1. Introduction

Once the passage of the muon is established by the trigger, as seen in the previous chapter, the data logging begins. Figure 6.1 presents a flow diagram of the data management. This process has been subdivided into three consecutive stages according to the software used: data acquisition, preanalysis and analysis.

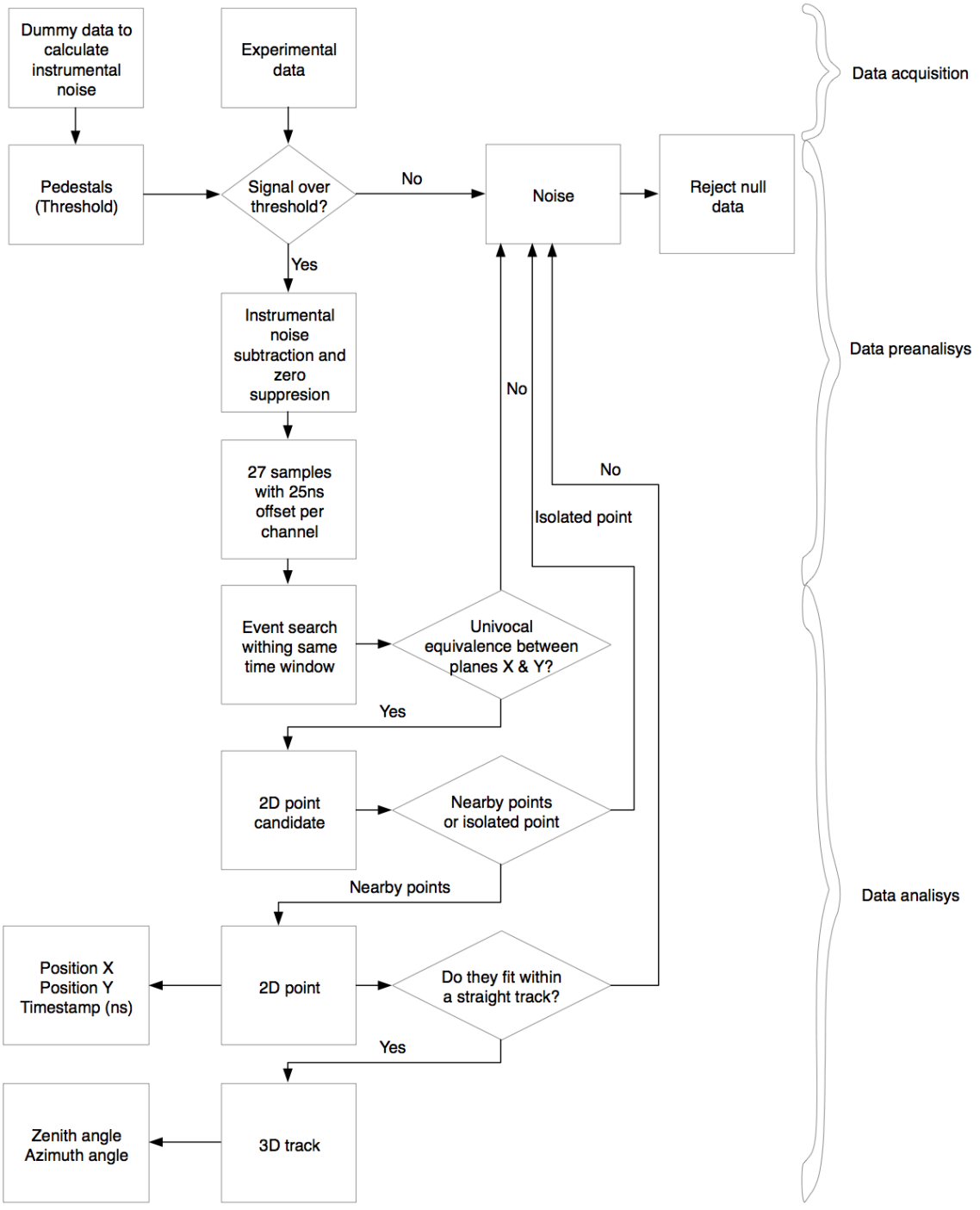

Figure 6. 1 Flowchart of the data analysis process.

The existence of preliminary software associated with the selected SRS electronics conditions the data acquisition (DAQ) and analysis process. The electronics offers a set of firmware, slow control and DAQ tools ready to use with no further development required.

Nevertheless, the limited scope of these tools (originally meant for different applications), and the impossibility to withdraw directly the required information, has motivated the creation of new data analysis algorithms for trajectory reconstruction.

Figure 6.2 shows the different software used in each stage and its function, as well as the format of the data file.

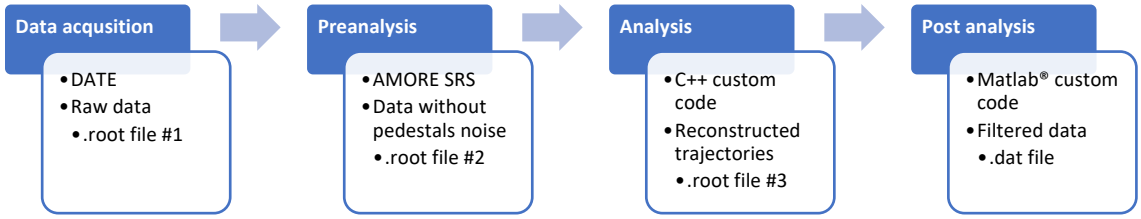

Figure 6. 2 Files created during the data analysis process.

6.2. Data acquisition

6.2.1 Slow control

The electronics slow control is in charge of setting all the configurable parameters of the electronics, such as the trigger source, data window length or latency. The slow control configuration of the SRS electronics can be done with different tools provided by the RD51 collaboration or directly through the ALICE Data Acquisition and Test Environment (DATE) software.

6.2.2 Pedestal noise

The pedestal level represents the intrinsic noise of every acquisition channel. As these values can evolve with time, it is good practice to redo pedestal runs frequently or after hardware modifications.

During this work, the pedestal runs have been made with all equipment on, but with a high latency[1]. This offset prevents the signal from being logged, which would artificially increase the pedestal level and decrease the detection efficiency. This run allows reproduction of the noise conditions during the acquisition in a reliable way. A limited number of events (500-1.000) is enough to provide a robust statistic of the channel instrumental noise.

[1] Time interval between the trigger signal arrival and the signal logging. See Section 7.2.2 for more details.

Figure 6.3 shows a typical view of the pedestal root mean square (RMS) noise of one APV25; generally values below 10 ADC counts[2] represent a low noise level. Figure 6.4 shows the pedestal RMS values of all channels of the detector. The noise in the Y plane is slightly higher, consistent with the longer track lengths.

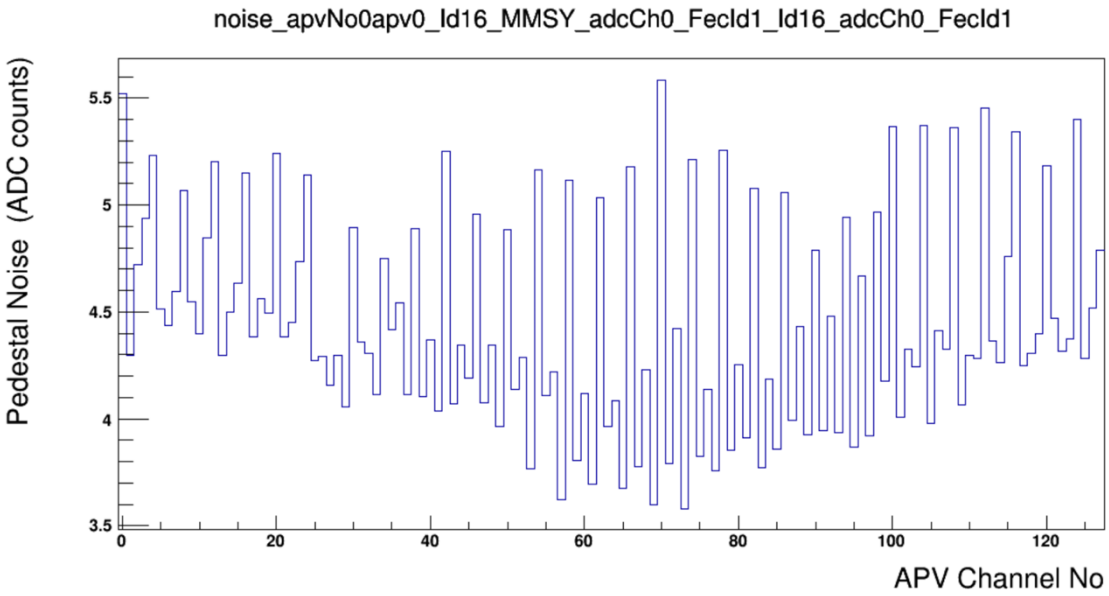

Figure 6. 3 Pedestal RMS noise values for the 128 channels of a given APV25 card.

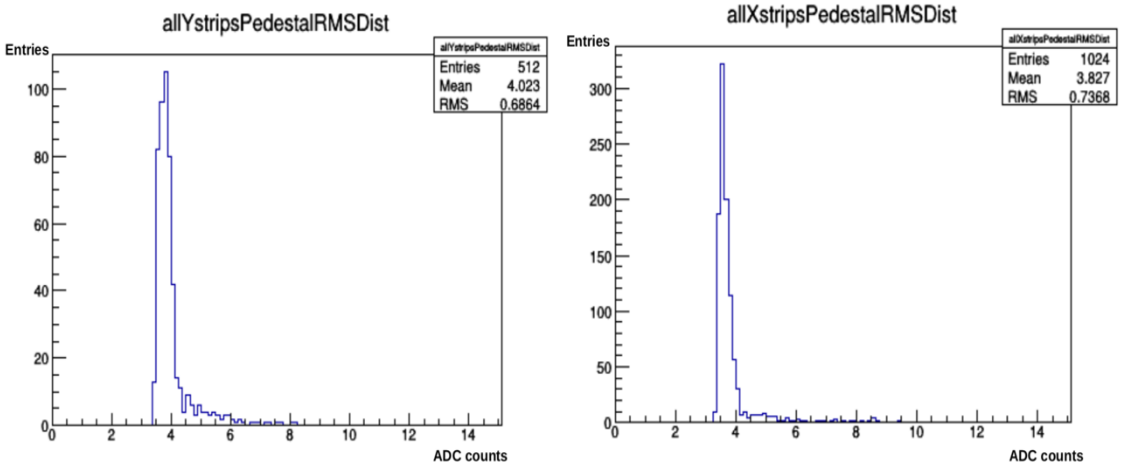

Figure 6. 4 Pedestal RMS noise values for all the detector channels. Each figure represents a readout plane.

[2] ADC counts are the digital number output by the ADC, proportional to the measured charge.

6.2.3 Experimental data

The software chosen to acquire data is the DATE framework, developed by the ALICE collaboration [ALICE collaboration, 2008][i]. The software has been designed to run on UNIX platforms connected by an IP-capable network, and sharing a common file system such as NFS. DATE performs different functions:

- The local data concentrator collects event fragments transferred by the detector data links into its main memory and reassembles these event fragments into subevents. It also does local data recording if used in a standalone mode, as in the present work.

- The global data collector puts together all the sub-events from the same event, builds the full event and archives it to the mass storage system.

- The DATE run-control manages and synchronizes the processes running in the local data concentrator and the global data collector.

These features weren't used in the present work, but present interest for networks of detectors where the data requires synchronization.

The monitoring programs, such as AMORE (detailed in the next section) receive streaming data. They can be executed on any machine accessible via the network.

DATE offers a graphic interface to configure the slow control of the SRS electronics in an acquisition and store the data. It allows the simultaneous operation of several detectors, and also gives basic information on the current run such as event rate and total number of recorded events.

The data stored locally in the DAQ machine is a ROOT file that contains all raw information (i.e. 27 samples for all instrumented channels, regardless of the channel threshold level and the instrumental noise).

6.3. Preanalysis

The preanalysis is the first stage of the data analysis process. It removes all unnecessary information from the raw ROOT file created by DATE.

This process is done by the AMORE code, a data monitoring software system developed for ALICE experiments [Haller, 2009][ii]. It is based on the data analysis framework ROOT, developed by CERN and uses the DATE monitoring library [ROOT][iii]. Amore executes topology-dependent processes for detector-specific decoding, and analysis of raw data samples, called agents. These agents allow to:

- Process the raw data of pedestal run. The file so generated is a pedestal ROOT file that contains the pedestal RMS noise and offset for each APV25 channel in form of a histogram.

- Visualize both live and stored raw data acquired with DATE.

- Filter the raw data by comparing it against the pedestal file to withdraw the APV25 instrumental noise.

Unfortunately, the agents are not configured for multicore processing, so the speed of the preanalysis is limited by the frequency of the processor.

The ROOT file created by the AMORE agent contains all relevant hit information prior to the track reconstruction, i.e. the time stamp, card ID, and 27 samples of the signal for each channel. A hit is defined as a readout track with a reading, whose mean ADC count value over the 27 samples, larger than the product of the threshold parameter σ and the pedestal RMS noise; the σ parameter can be tuned by the user, with typical values during this work being σ ∈ [15-20].

Figure 6.5 shows an example of the data after preanalysis, where void events are removed. The two figures represent the signal evolution associated with the same event recorded two different APV25 cards, one in the X plane and the other in the Y plane. The signal is divided into 27 time bins of 25 ns that contain the information of all 128 channels of the card. The vertical bars act as time-bin spacers. From the figure, it is possible to appreciate the signal amplitude difference between the X and Y readout planes.

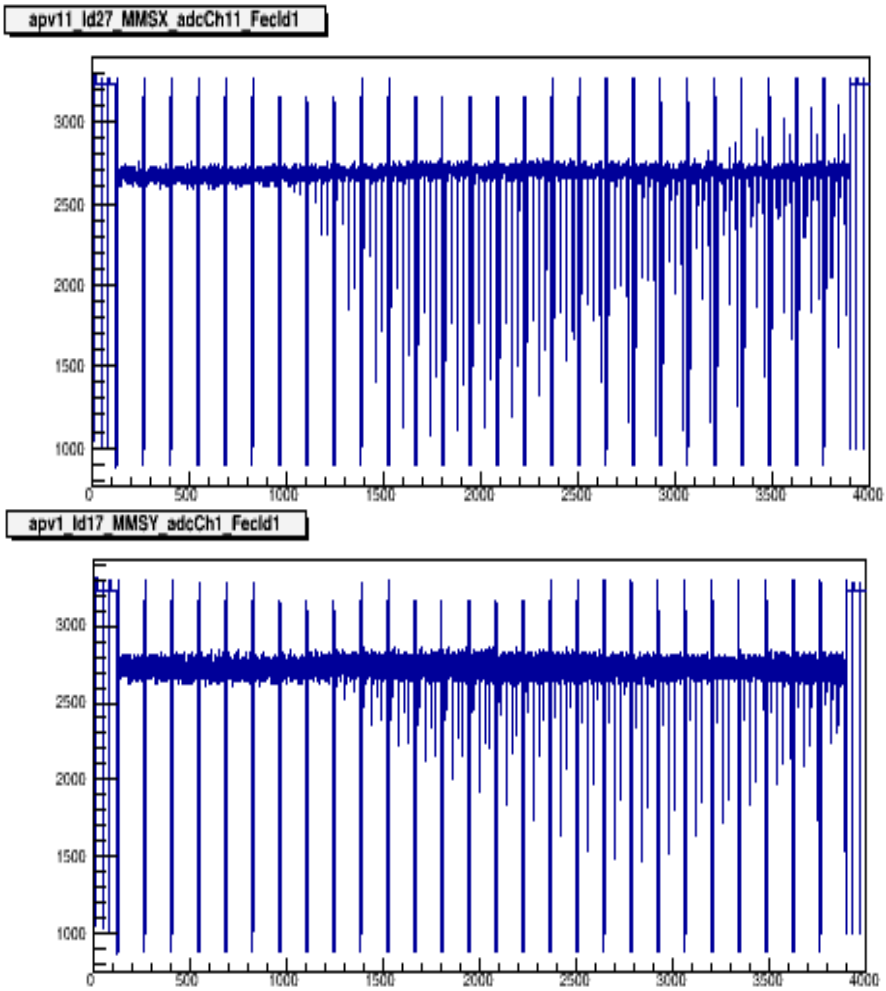

Figure 6. 5 Signal from one event recorded by two APV25 cards in the X and Y plane respectively.

6.4. Analysis

The Muon Trajectory Reconstruction Algorithm (MTRA), developed by T. Serre with the reconstruction parameters tuned by the author, aims at retrieving the muon trajectory with the highest precision on its trajectory, and to reject backgrounds such as ambient radioactivity and electronical noise.

6.4.1 Hit determination

The hit determination, made in the first instance by AMORE, is checked by the MTRA. The hits are discarded in two scenarios:

- Presence of two maximums during the 27 time samples, as seen in Figure 6.6. Hits with one bin with an ADC counts greater than 0,5 X the maximum bin, and distant by at least 7 bins are rejected.

- Signal saturation: when more than 5 contiguous bins are higher than 1.500 ADC counts (the maximal measurable value is 1.750 ADC counts) during 5 bins, as seen in Figure 6.7.

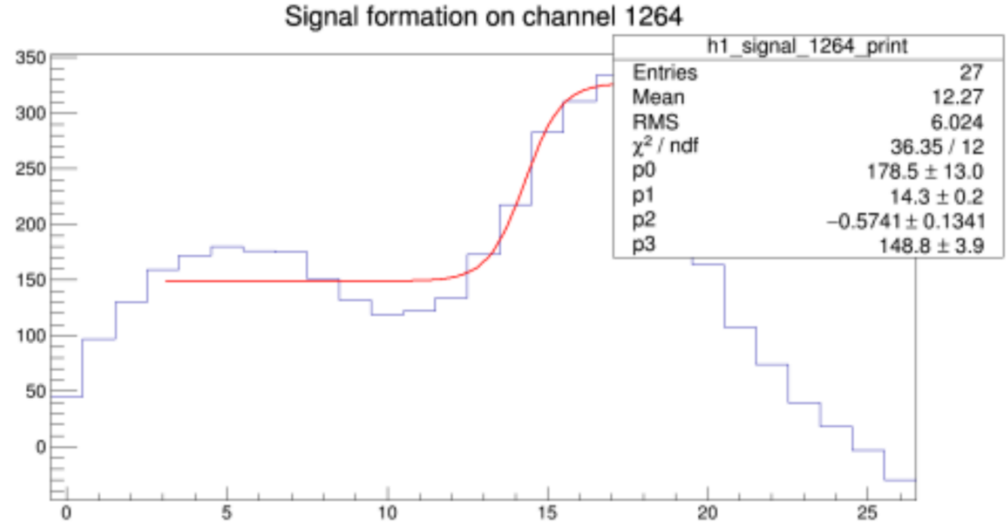

Figure 6. 6 Example of a rejected event due to a double maximum.

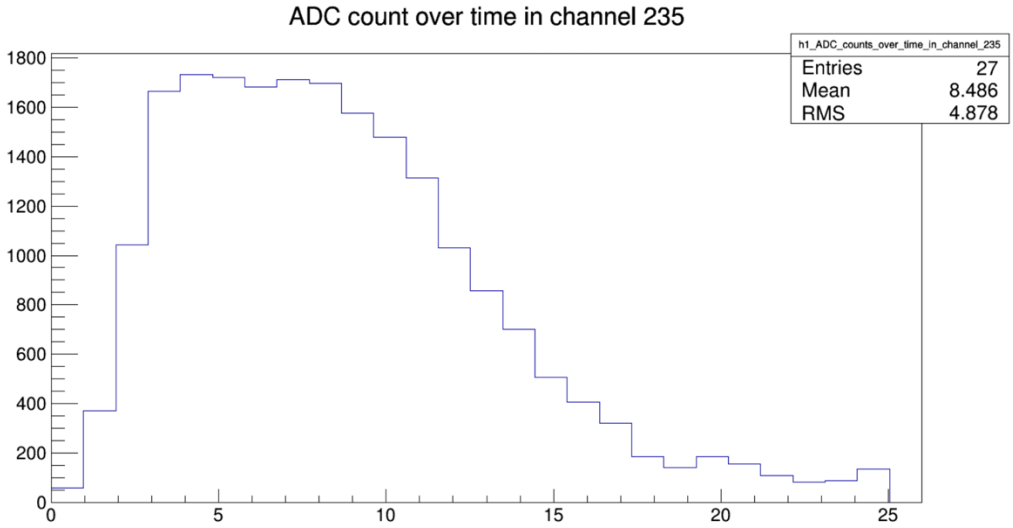

Figure 6. 7 Example of a rejected event due signal saturation.

6.4.2 Clusterization

Muons crossing the MUST^2 detector will create tens of electrons per cm travelled, which causes many hits on neighboring readout tracks. This effect can be used to implement a clustering algorithm in order to reduce the position incertitude.

The hit strips located next to each other are assembled in clusters. Nevertheless, it is possible that clusters present holes due to the presence of untouched readout tracks. This effect arises for several reasons: the strip might misfunction temporarily, or permanently (too noisy during the pedestal run or track cut), or due to transverse diffusion. Thus, a tolerance gap of two strips is allowed during the cluster formation.

On the other hand, even near-vertical muons cause several hits. Thus, a threshold number of hits is required to form a cluster. Figure 6.8 shows the number of hits per cluster on X and Y axis: the threshold value of hits is 2.

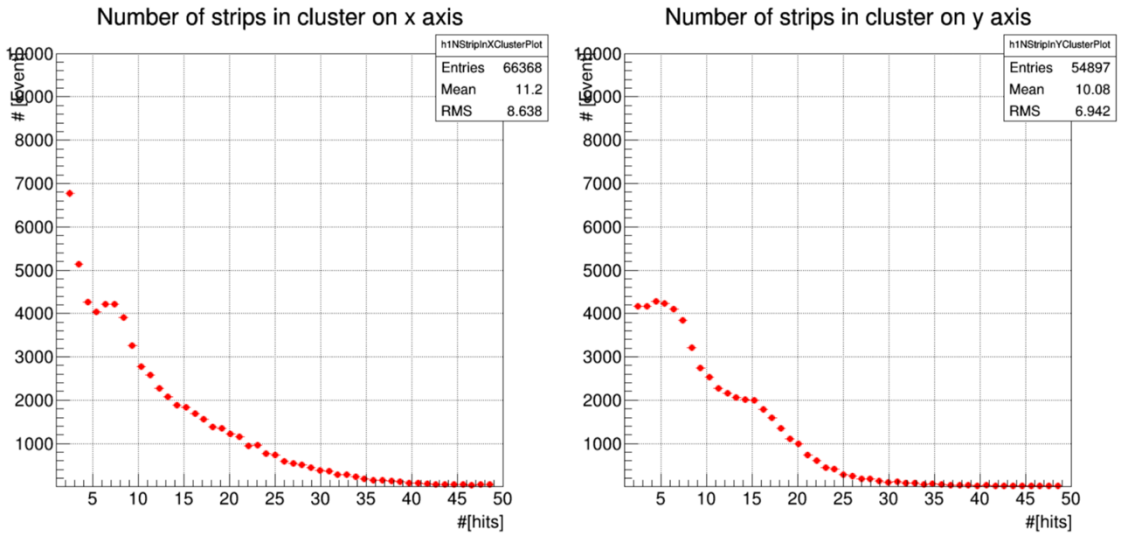

Figure 6. 8 Distribution of number of hits inside clusters per readout plane.

The number of hits per cluster decreases progressively, which is correlated with the zenith angle arrival distribution of muons seen in Figure 2.18. On the other hand, the anisotropy in the number of hits between X and Y readout planes is due to (i) the different number of total tracks per plane and (ii) to the ladder pattern layout of the resistive layer (detailed in Section 5.2.2), which creates an uneven charge spread along the X and Y axis.

6.4.3 Point determination

The clusters are generated in both axes. To retrieve the muon information, X and Y clusters must be associated. If there is only one cluster on each axis within the 675 ns, the association is trivial. However, in a multiple-cluster scenario, some criteria are required.

The total charge ratio between X and Y clusters for the MUST² Micromegas readout plane is distributed as shown in Figure 6.9. By comparing plane-to-plane the charge of each cluster, the clusters can be associated. Another useful parameter is the time of the signal formation. Time information can also be used to combine clusters.

Once X and Y clusters are associated, they form a 2D point in the readout plane. Each point corresponds to a muon. This permits constructing 2D histograms representing the position distribution of the muons traversing the detector.

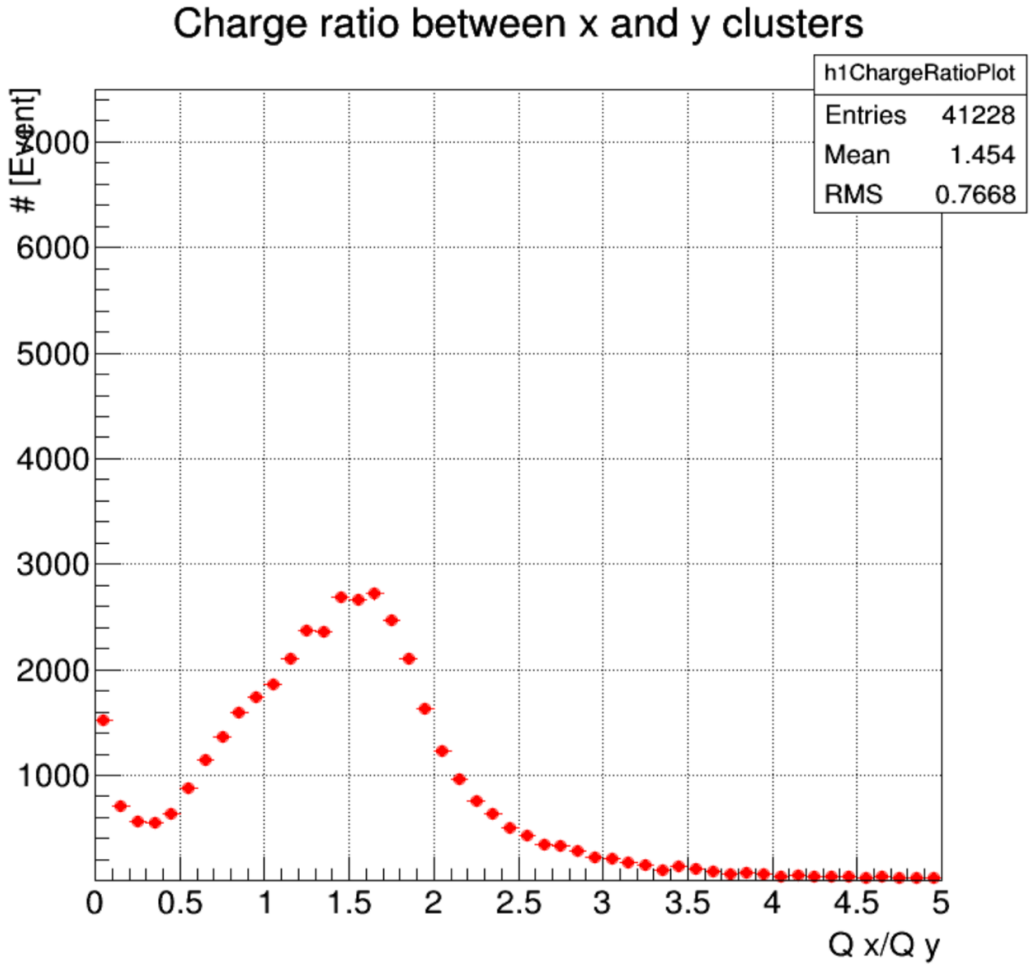

Figure 6. 9 Charge ratio between X and Y clusters. Charge is computed as the total sum of all ADC counts during 675 ns.

6.4.4 Trajectory reconstruction

Two different algorithms are used to determine the trajectory of the muon. The first is based on fitting the rising part of the signal. Different fitting models have been tested, with the one giving better results being the sigmoid fit following the logistic equation:

$$FD(t) = K \cdot \left(1 + e^{-(t-t_0)/\sigma_{FD}}\right)^{-1} + B \qquad (6.1)$$

where:

- K is a scale factor.

- t_0 corresponds to the time when the signal starts to rise.

- σ_{FD}: is the spread of the function.

- B corresponds to the zero level.

An example of the fit is shown in Figure 6.10. The time interval considered comprises from the first time bin with a significant signal rise to the maximum. The same analysis made on each hit from a cluster; the characteristic time, t_0, is calculated from each fit. By knowing the electron drift velocity, the height of the initial electron production (Z) can be retrieved.

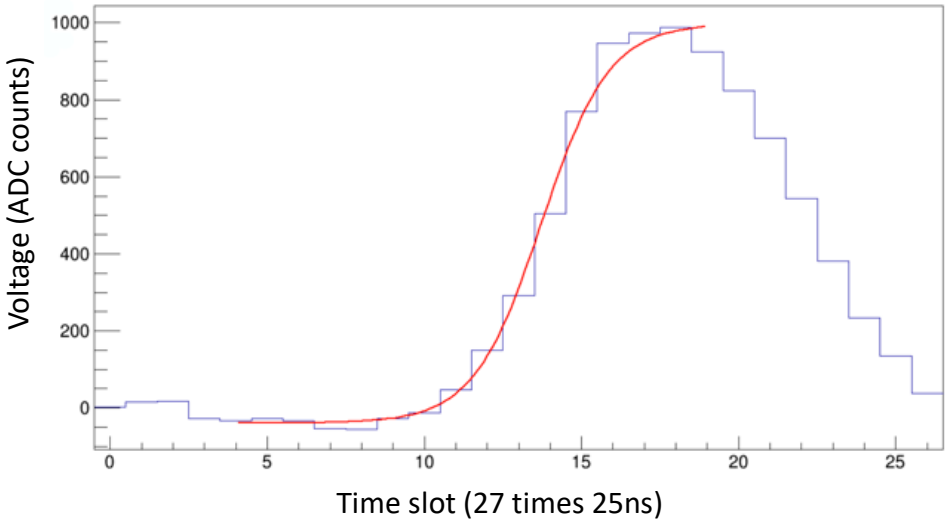

Figure 6. 10 Example of a signal fit with a logistic function for one channel.

For each X and Y cluster, there is a set of (X, Z) or (Y, Z) coordinates, respectively. Finally, a linear fit is performed to get angles in the (XOZ) and (YOZ) planes. An example of this linear fit is shown in Figure 6.11.

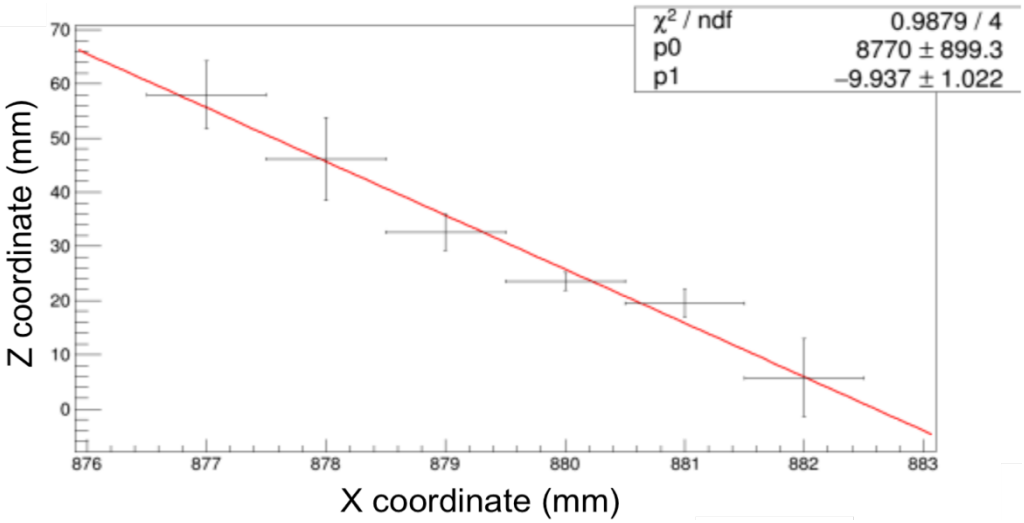

Figure 6. 11 Example of the linear fit of the coordinates in the (XOZ) plane.

It is possible to obtain a fit from at least two hits on each axis, but for a good precision at least three hits are required.

The reconstruction efficiency of this algorithm is thus very limited for near-vertical particles and trajectories parallel to the X and Y axes. This results in the creation of blind zones in the Zenith-Azimuth maps in trajectories with $|\theta_X|$ and $|\theta_Y|$[3] < 5º deg, or φ multiple of 90º± 5º.

In order to retrieve additional information, a second algorithm is used to establish the XY position of near-vertical events by fitting each cluster with a weighted mean of its hits, according to Equation (6.2).

$$(X,Y) = \sum_{i=1}^{hits} ADC(X_i,Y_i)\cdot(X_i,Y_i) \Big/ \sum_{i=1}^{hits} ADC(X_i,Y_i) \tag{6.2}$$

Hence, the evolution of the X and Y position over time obtained from the centroid fit provides information on the trajectory. Analogous to the rise fit algorithm, a linear fit is performed to retrieve the track angle. An example of this fit is shown in Figure 6.12.

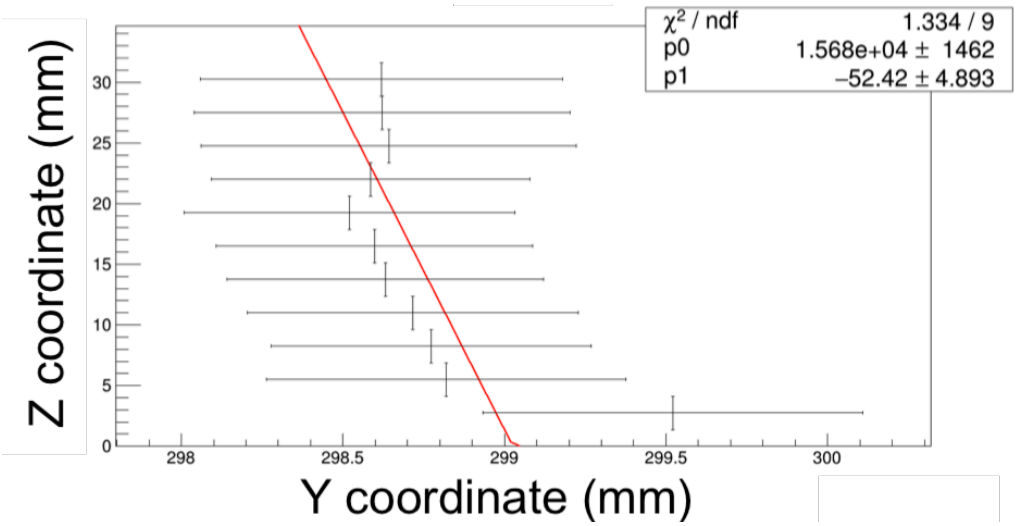

Figure 6. 12 Example of the linear fit of the coordinates in the (YOZ) plane with the centroid method.

The performance of the second technique has however proven not to be strong enough, and the reconstructed events via the centroid algorithm seems to be quite random. Therefore, the information derived from this source will not be considered for imaging purposes until a proper validation.

The data resulting from the MTRA is stored in a ROOT file with a TTree structure, designed for storing large numbers of same-class objects. The data is sorted in different “leaves” and contains the information relative to the passage of muons, as well as the results from intermediary calculations that has been

[3] θ_X and θ_Y are the reconstructed incident angles to the readout plane in X and Y axes respectively.

preserved for debugging purposes. An example of the output file organization is shown in Figure 6.13.

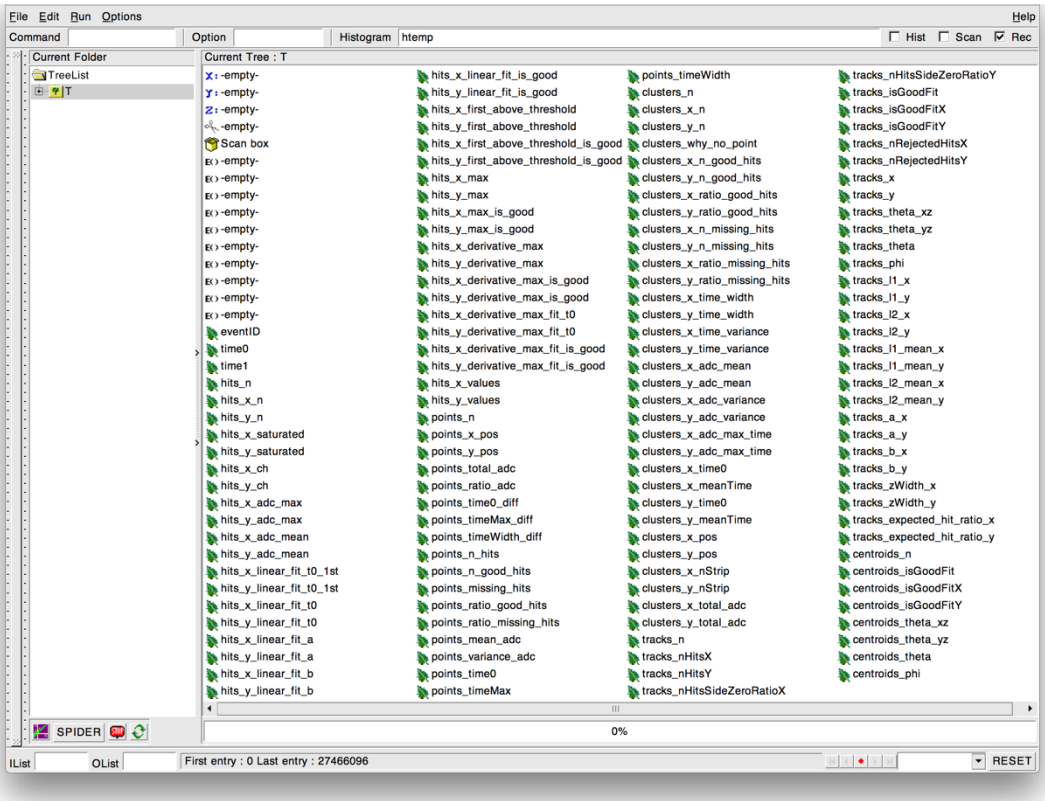

Figure 6. 13 View of all data included in ROOT file created by the MTRA.

6.5. Post analysis

The post analysis process covers the data visualization and filtering following completion of the track reconstruction.

The ROOT file created by the MTRA might prove a bit clumsy for managing the data relative to the muon passage. Instead, some variables of interest are extracted to a lighter text file. The Matlab® [MathWorks®, 2018][iv] based program called Muon Analysis Interface for Data files (MAID) has been specifically created perform this task.

The parameters exported to the text file are the following:

- Starting time of the event, divided into two components; UNIX time in seconds and microseconds.

- 2D position of the event, in X and Y coordinates.

- Zenith and azimuth coordinates of event.

- Number of readout tracks triggered during the passage of the muon.

This multiplatform software can be installed with the support of the freely available Matlab® runtime engine, and allows direct visualization of the file content, the comparison between .dat files, and some simple data filtering.

6.5.1 Data filtering

The analysis algorithm which reconstructs the muon trajectories has problems to reconstruct some tracks, and creates some points that are not associated with the passage of the particle. These points have no physical meaning and require filtering. Some recognizable characteristics of these points are:

- Reconstructed 2D coordinates outside of the detector boundaries.

- Several consecutive points reconstructed in the same 2D position within a short time interval and with different zenith and azimuth. The algorithm is not able to fully reconstruct the one track (for instance due to the excessive distance between its points), and creates a series of dummy consecutive points.

- Excessive number of tracks touched: On some occasions, the instrumental noise produces signals above the threshold level in all channels at the same time. As seen in Figure 5.12, the muons with zenith angles below 80º should not intersect more than ~500 channels. One way to avoid this kind of "false positives", is to establish a cutoff between 500 and 1.536 channels depending on the desired range of angle acceptance.

Figure 6.14 shows an example of the data filtering. It presents a 2D histogram with the reconstructed passage points above the surface detector before (Figure 6.14 (A)) and after the filtering (Figure 6.14 (B)).

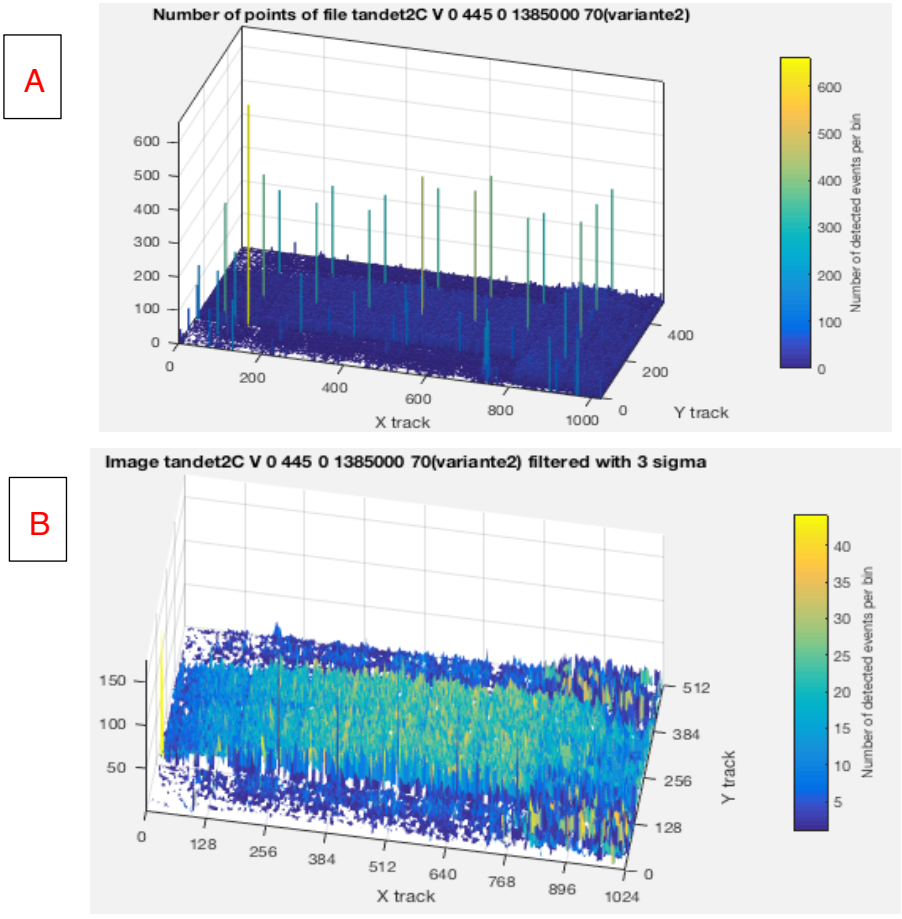

Figure 6. 14 Histogram of muon position distribution from an acquisition (A) before and (B) after filtering.

6.6. Other considerations

6.6.1 Data size

Data acquisition with the current configuration generates quickly large volumes of data. Figure 6.15 illustrates the size distribution of the files created during one acquisition (corresponding to the campaign of measurements at the dam of Saint-Saturnin-les-Apt presented in Chapter 8). It contains ~4 TB of information with 27.466.100 events recorded by 1.536 channels.

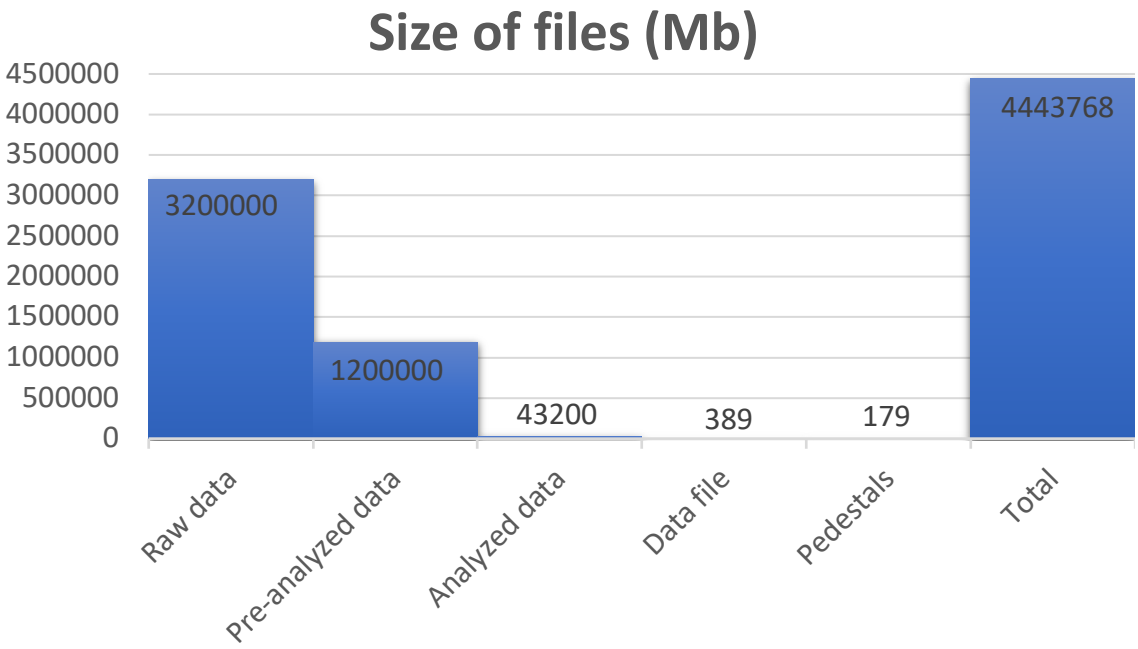

Figure 6. 15 Distribution of the different file sizes created during data analysis.

The smallest file contains the raw data acquired to calculate the pedestals, due to the low number of events considered (1.000). Once this data is analyzed to produce the pedestal file (containing only the pedestal values and its variances), its size drops to a few tens of kB.

The raw file generated during the data acquisition by DATE is by far the largest file, representing almost ¾ of the total size. Nevertheless, this file contains potentially useless information such as void events or instrumental noise. A good way to improve the efficiency of the data acquisition is to replace the FEC firmware, including the zero-suppression capability. This enables suppressing non-useful (empty) data locally in the FPGA, so the data to be transferred from the SRS to the Data Acquisition PC is optimized. The selection is based on comparing the integral of the pedestal-corrected signal from a given channel with the pedestal variation (σ) in each channel. This reduces the presence of false positive events associated with noise peaks. The data of the pedestal has been previously stored in the FPGA to compare the signal measured and the σ value.

The file generated by the preanalysis with AMORE SRS after comparison with the pedestal noise file, reduces the size of the file by 3 and includes all the relevant information for the muon flux trajectory reconstruction.

6.6.2 Computing time

Figure 6.16 presents the time elapsed during the different stages of the data acquisition and analysis. The required computing time with the current analysis chain is problematic for long data acquisitions. Since the zero-suppression of the data isn't implemented, the volume of data to reanalyze produces a bottleneck, and requires four times the acquisition time. On the other hand, the data analysis process requires only ¼ of the acquisition time: for example, more than 17 days were required to fully analyze the data acquired during less than 4 days of measurements.

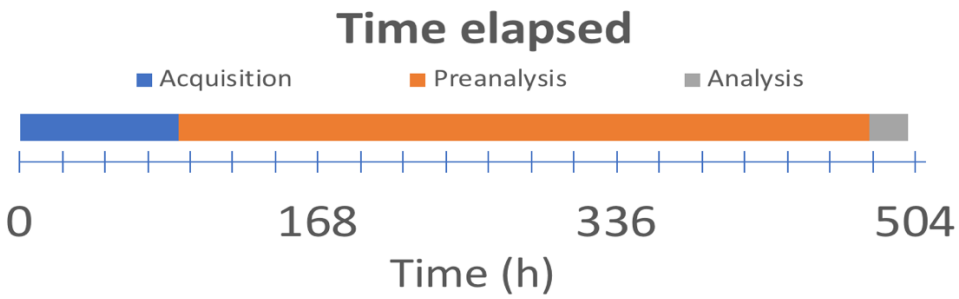

Figure 6. 16 Time elapsed during the different analysis stages.

A recently-released tool compatible with the current APV25 and FEC cards, named SCRIBE, includes on-line pedestal calculation and zero-suppression [Colafranceschi, 2016][v]. This software could be a great leap forward for the MUST[2] operation in terms of volume of data stored and especially in computing time, as it effects the preanalysis live in the FPGA.

6.7. References

[i] ALICE collaboration (2008). The ALICE experiment at the CERN LHC. JINST ,3.

[ii] Haller, B. V. et al. (2009). The ALICE data quality monitoring. Proc. 17th International Conference on Computing in High Energy and Nuclear Physics, J. Phys. Conf. Ser. 219:022023

[iii] ROOT 6.15. ROOT reference documentation. https://root.cern/doc/master/index.html

[iv] MathWorks, (2018). Matlab Primer (R2018a). Retrieved July 5, 2018 from https://fr.mathworks.com/help/pdf_doc/matlab/getstart.pdf

[v] Colafranceschi, S. (2016). A new Slow Control and Run Initialization Byte-wise Environment (SCRIBE) for the quality control of mass-produced CMS GEM detectors. arXiv:1612.04461v3

Chapter 7. Measurements towards detector characterization.

Chapter 7 abstract

Chapter 7 presents the results of the measurements made towards the detector's performance characterization in controlled environments.

Section 2 details the tests done in the test beam facilities at CERN that has led to the acquisition-chain latency optimization, detector's gain characterization, detection efficiency determination and the calculus of the ratio of charge between planes. The importance of having a proper trigger and its influence in the data reconstruction are discussed as well.

Section 3 is dedicated to the open sky measurements, where the measurements performed on the top of the mountain hosting the LSBB gave us information about the experimental angular acceptance of the detector when triggered by plastic scintillators. A comparison of the experimentally measured muon flux against the predicted value provided by the model is shown and commented.

Section 4, dedicated to underground measurements, covers the tests with a first comparison between apparent opacity and measured muon flux. It also assesses the effect of the detection plane tilt angle in the measurement, and the amount of gas necessary to operate properly the detector.

Section 5 explains the procedure to obtain a measurement of the muon flux attenuation at the entry of the LSBB by comparing the *in situ* and open sky measurements. The damage caused by a storm in the experiment during the acquisition is presented as well.

Lastly, Section 6 shows the comparison between two different instrumentation electronics in the MUST^2 detector: the CEA's IRFU CLAS12 and the CERN's SRS. The muon detection was successfully tested with both technologies and different trigger configurations. The different format of the data produced with the CEA electronics prevented however the data from being reconstructed with the MTRA.

7.1. Introduction

A series of experiments have been carried out with the MUST^2 in order to find the best operational parameters, characterize the detector performance and to validate the technology.

These experiments were conducted in different controlled environments according to the specific test needs:

-CERN SPS test beam facilities (Prévessin, France).

-LSBB underground galleries and surface facilities (Rustrel, France).

-IRIS Instruments headquarters (Orléans, France).

7.2. Test beam

The membership of T2DM2 in RD51 has allowed the project to carry out some characterization tests at CERN's Super Proton Synchrotron (SPS). This particle accelerator provides mono-energetic beams of muons or pions in their test-beam facilities.

The setup during the experiment is shown in Figure 7.1. The MUST^2 detector was located immediately following the SPS beam line; the detector, SRS electronics and scintillators to provide a trigger were located inside the beam zone. The gas bottle used during the experiment was stored in a designated area outside of the beam zone, and a new gas circuit was specifically created for the test. The rest of the equipment, high voltage power supply and data acquisition computer were operated remotely from the control room. The gas used during the experiment was Ar:CF_4:iC_4H_{10} (88:10:2), and the drift field was E_{drift}= 600 V/cm. Due to the narrow active surface affected by the beam (~100 cm^2), only the central part of the detector was active during the tests (X channels $\in [1,1024]$ and Y channels $\in [129,385]$) to minimize the instrumental noise.

Figure 7. 1 Latency scan setup within the SPS' beam test facilities.

7.2.1 Trigger

The trigger signal planned for the experiment was provided by the coincidence signal of two superimposed plastic scintillators of 100 x 20 cm (see Figure 7.2 (A)).

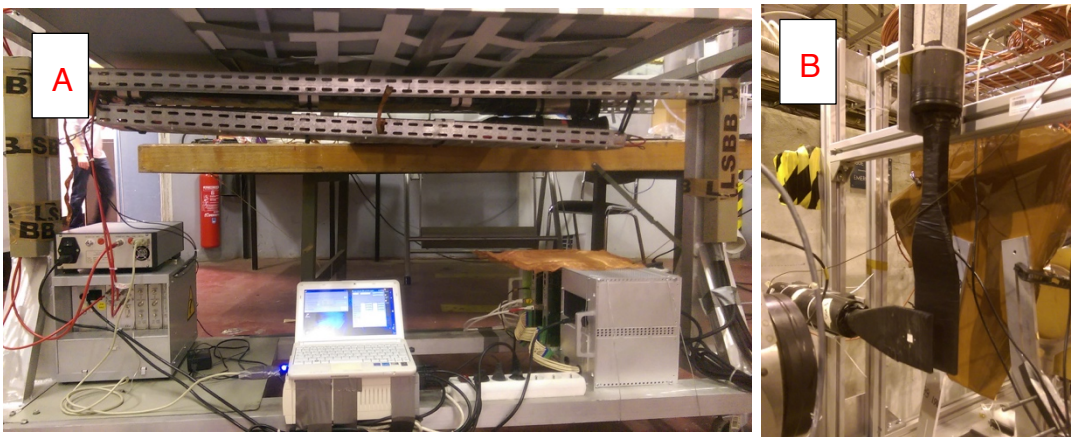

Figure 7. 2 (A) built-in MUST² scintillators and (B) tracker scintillators.

After the analysis of the data acquired in the first run however, the presence of instrumental noise was evident.

Figure 7.3 (A) represents a 2D histogram with the position distribution of the detected muons, in which the acquisition was triggered with the built-in scintillators and the test beam centered in the coordinates (X channel 256, Y channel 325). It is possible to see the instrumental noise induced by a faulty trigger, which randomly distributed and specially concentrated in the zone with channels $X \in [600,800]$ and $Y > 200$.

After verification of the SRS electronics noise levels, its contribution to the measured noise was considered negligible. Different configurations of scintillators (changing their relative position, orientation and emplacement) were tested in order to eliminate this noise - yet, the problem persisted.

At this point a decision was made to change the trigger chain from the built-in scintillators to the plastic scintillators integrated in the tracking device at the end of the beam line. The coincident surface of these two scintillators, seen in Figure 7.2. (B), is 7 x 10 cm^2. Their reduced dimension and vertical configuration reduced the number of trigger events associated to cosmic muons, which are statistically neglectable given the rate of the muon beam (~5 to 9 kHz).

On the other hand, Figure 7.3 (B) derivates from an acquisition triggered by the tracker scintillators, with the test beam centered at the position (X channel 850, Y channel 325).

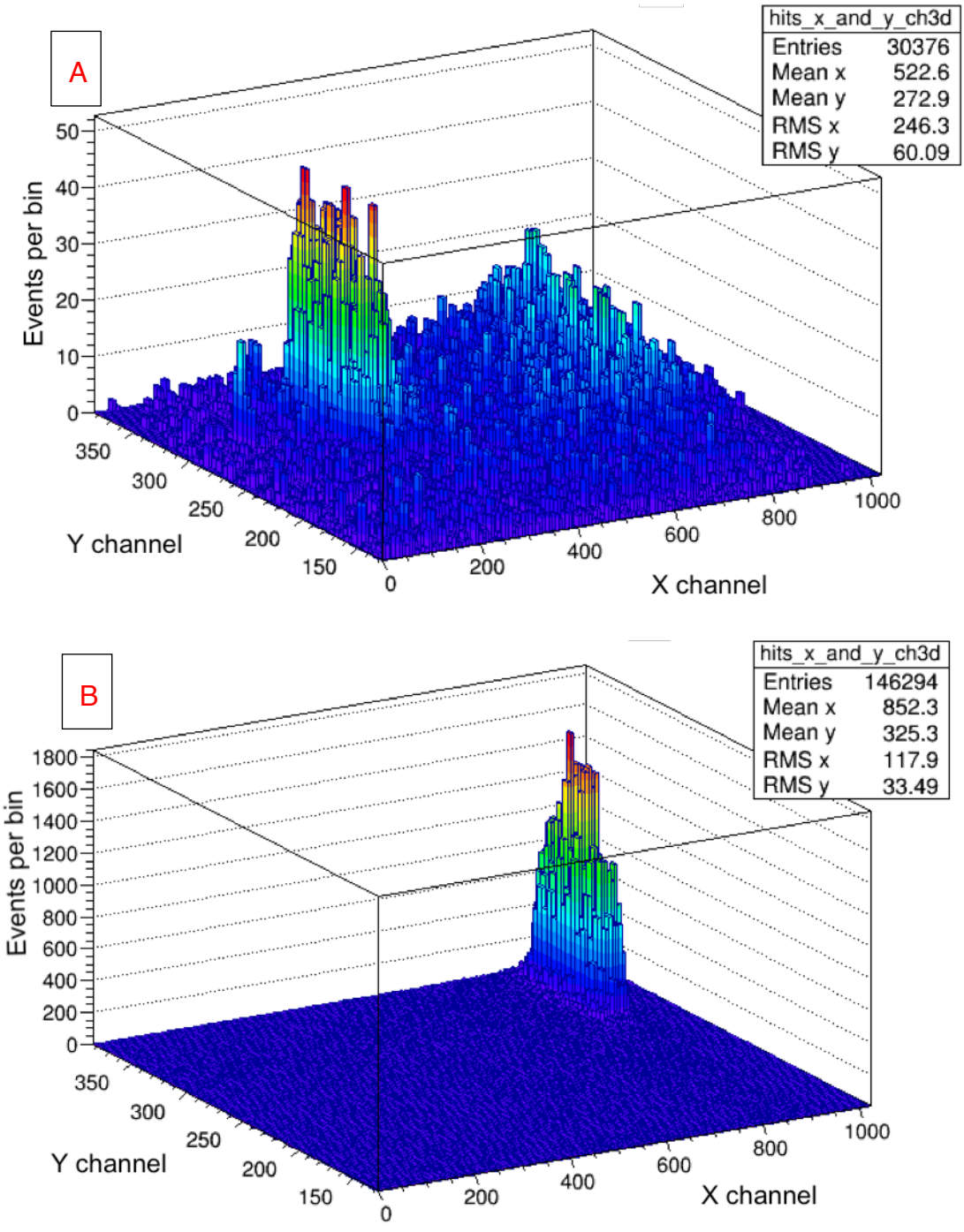

Figure 7. 3 2D histogram of the detected points with a trigger provided by (A) built-in MUST² scintillators, and (B) tracker scintillators.

The new acquisition chain reduced the instrumental noise. About 50% of the events detected in Figure 7.3 (A) were located outside the beam-triggered influence zone, whereas in in Figure 7.3 (B) the shape of the intersection between the beam and the trigger scintillators is clearly recognizable and well delimited.

7.2.2 Latency

The system's latency is the time interval between the passage of the muon (stimulation) and the signal detection by the electronics (response). This parameter depends on factors such as the physical processes described in Chapter 4, as well as on the delay inherent to the electronic components and the signal transmission through the wires. Therefore, the latency value is a function of the experimental setup.

The SRS APV25 front-end electronics has a time buffer of 4 μs, yet can record a maximum of 27 samples every 25 ns yielding a time window of 675 ns. It is important that the signal is centered in this time window, in order to enable a proper fit of the data in retrieving the correct time information for the trajectory reconstruction. The slow control of the electronics permits to customizing the offset of the data logging within the buffer time.

A scan of offsets is necessary to determine the acquisition chain latency with the best value for operation. A series of 8 measures with 5.000 events each was made by changing the offset in increments of 125 ns (5 time bins of 25 ns).

Figure 7.4 shows the bin position of the reconstructed time when the signal starts to rise, t_0. Negative time bins derive from the extrapolation of the sigmoid fit function, and are not reliable since the rise information of the signal is biased. On the other hand, reconstructed t_0 values greater than 20 bins also derive from biased signals. Nevertheless, the loss of information is produced in the signal end. Considering that the data fit interval ends at the signal maximum, the impact in the t_0 calculation is smaller.

The selected offset value is 112 time bins (2,8 μs), since the reconstructed t_0 is predominantly within the positive values (no extrapolation from incomplete data) in the first 8 time bins (signal bias minimized), which enables the reconstruction of a higher number of events.

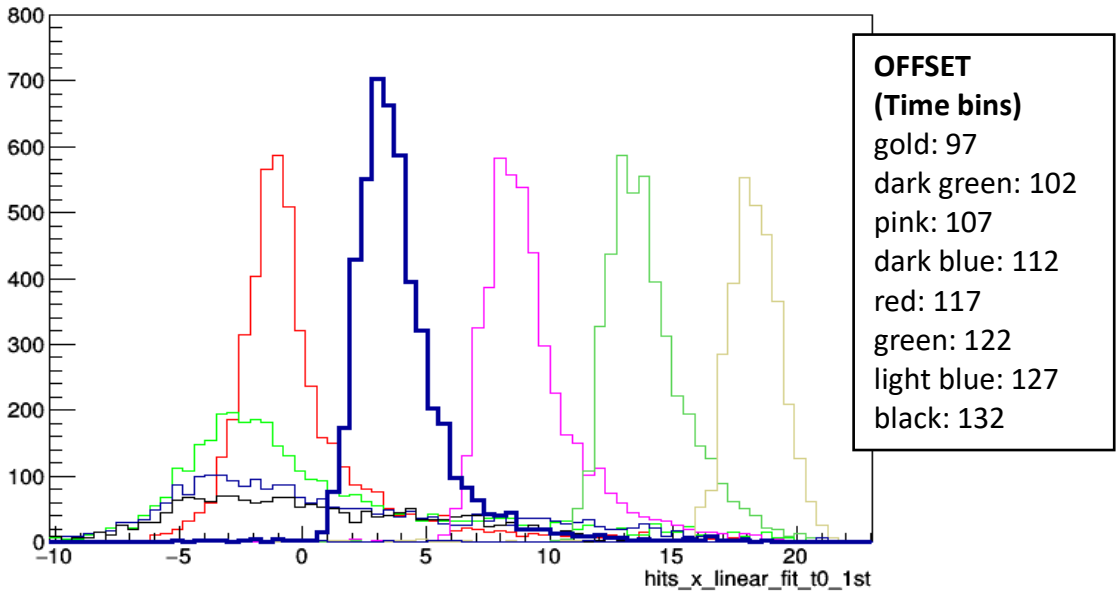

Figure 7. 4 Time bin containing the beginning of the signal for different offsets.

7.2.3 Gain

The gain of the detector is a key performance parameter as it plays a major role in the signal amplitude. As seen in Section 4.9.1, the gain for a given temperature and pressure depends mostly on the electric field of the amplification zone (E_{Amp}), which is controlled by the difference in voltage between the grounded micromesh and the polarized resistive layer.

The gain of the detector has been calculated as the ratio of (charge supplied to the amplification zone) to the (charge generated by the incoming muons) according to the following equation:

$$G = \frac{\Delta I}{N_T \cdot d \cdot {}^{\mu}/_{S} \cdot q_{e^-}} \tag{7.1}$$

where:

- G is the gain of the detector for a given temperature and resistive layer voltage, and q_{e^-} is the charge of the electron.

- ΔI is the average variation of the current consumption between spills[1] and breaks (nA). The voltage and intensity of the HV power supply that polarizes the resistive layer is monitored, as shown in Figure 7.5. It is possible to identify periodic current peaks associated with the injection of muons through the detector. ΔI has been calculated as the difference between the average peak current with a spill, and the average bottom current between spills for 10 samples once the current is stabilized after changing the voltage.

- N_T= 161,3 ± 12,7 is the number of electron-ion pairs per cm generated in the TPC by ionization of a traversing muon (detailed in Section 4.4).

- d is the distance travelled by the muon inside the TPC. Two tests have been conducted, one with the detector perpendicular to the beam (θ=0º, 5,00 cm of path within the TPC), and the other with the detector shifted from the orthogonal plane (θ=20º, 5,32 cm of path within the TPC).

- μ/s is the number of muons per second during the measurement (muons per spill/spill length). The number of muons emitted per spill and the spill length are known via the wire chamber placed in the beam line that characterizes the beam profile.

The environmental data of the beam zone was monitored. The thermic amplitude during the gain determination acquisitions was smaller than 1ºC, and any temperature effect was neglected.

The results of the calculated gain are shown in Figure 7.6. where the gain of the detector increases with E_{Amp} up to a peak in 465 V, then decreases slightly. The gain calculated with the two incidental angles shows a good consistency. The tests could not go beyond 485 V (for θ=0º) and 490 V (for θ=20º) because

[1] The SPS facility provides a discontinuous muon beam consisting of spills with a muon rate of $4{,}5 \cdot 10^3$-$9{,}5 \cdot 10^3$ μ/s of length ~5 s at intervals of 14-30s

of the detector instability and loss of amplification due to current leaks and the high event rate. This experimental breakdown voltage is in good agreement with its predicted value in Section 4.9.3.

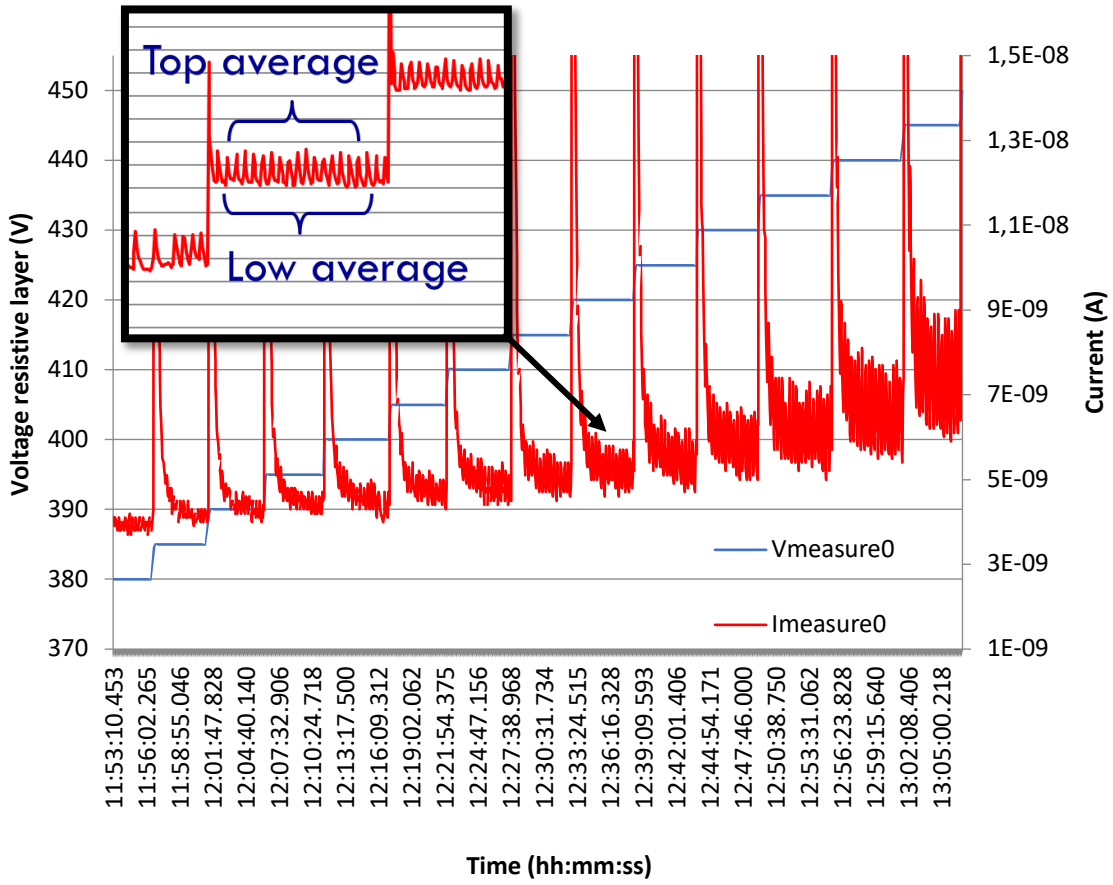

Figure 7. 5 Current and voltage of the resistive layer during the test beam.

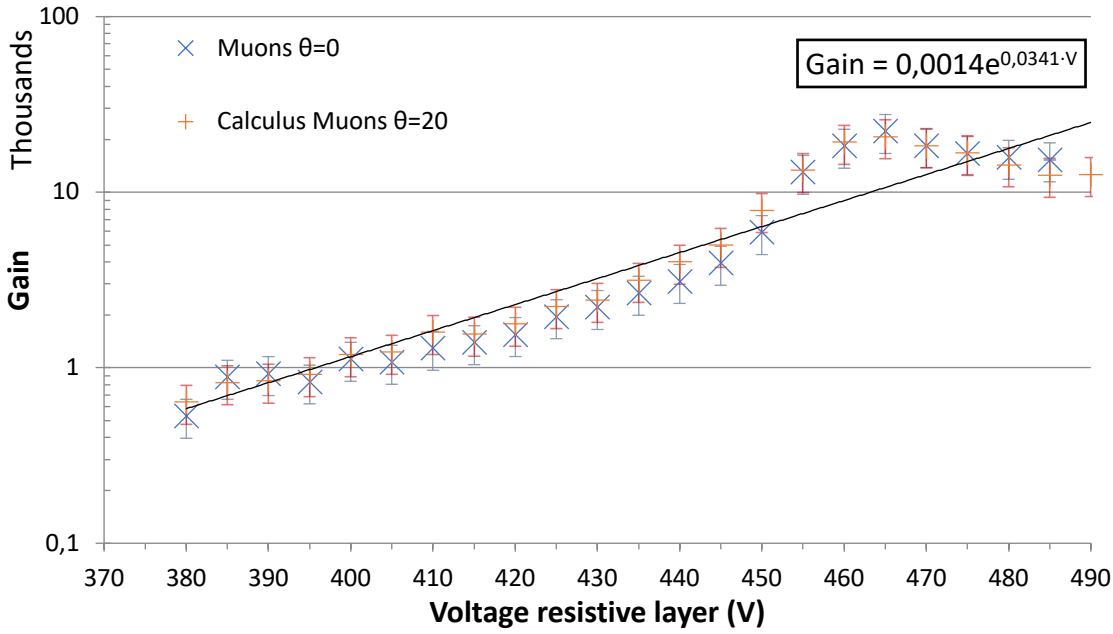

Figure 7. 6 Calculated gain of the MUST² detector as a function of the resistive layer voltage.

As mentioned above, the gain influences signal amplitude. Figure 7.7 shows the maximal measured voltage in ADC counts in the X and Y readout strips, (the Y results are shifted 1 V for better visualization). The figure shows a good correlation between the exponential regression slopes of the calculated detector gain and the amplitude of the signal measured in the readout tracks. Moreover, it is possible to see a difference of amplitude in the induced charge on the two readout planes illustrated in Figure 6.9. A good gain value should provide a compromise between a strong enough signal in the lower readout plane with less induced charge, and a signal without saturation on the X readout tracks.

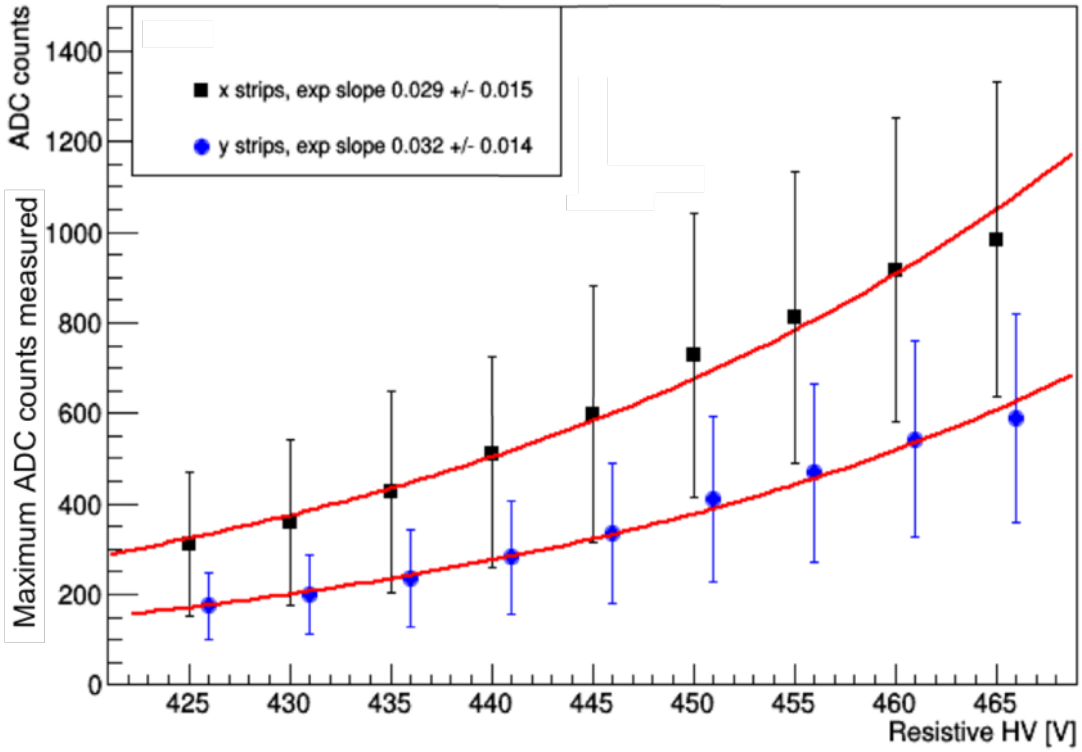

Figure 7. 7 Signal amplitude of the MUST² detector as a function of the resistive layer voltage.

The amplitude below 425 V is too low, and the signal fails to significantly doesn't surpass the threshold level. On the other hand, for voltages above 465 V, the APV25 reached saturation at 1.750 ADC counts, which the signal should not exceed to avoid the loss of information. The calculated gain values are in good agreement with other experiments using resistive Micromegas [Kuger, 2017] [i].

7.2.4 Detection efficiency

The detection efficiency is defined as the ratio between the events that contain X-Y correlated hits over threshold and the triggered events. Therefore, the efficiency of detection relies upon the choice of a cutoff value for the chosen pedestal noise.

As seen in Section 6.2.2., the pedestal noise determination provides the offset and RMS noise in ADC counts for every channel of the system. A hit is defined as a readout track that contains a signal with a mean ADC counts value larger than σ times the rms noise.

To improve the determination of the pedestal cut, a geometric factor was included. The S/N ratio represents the relation between the number of points reconstructed whithin the projection of the scintillator used for triggering (S) and the reconstructed points outside the expected zone times a normalisation factor, which compensates for the difference of surface (N).

Figure 7.8 shows the value of detection efficiency vs the S/N ratio for different σ values.

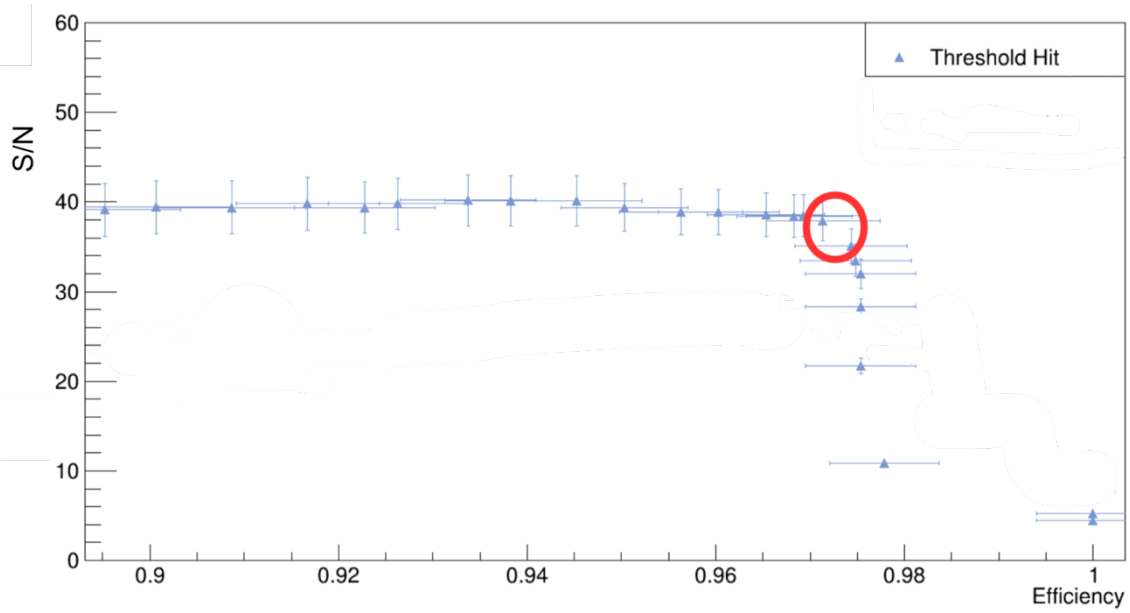

Figure 7. 8 Detection efficiency of the MUST² detector vs S/N ratio.

From the figure, it is seen that for σ = 20 (in the red circle) the S/N ratio is still in the plateau at around 39, and it has a detection efficiency of 97,2 ± 0,55%. This value is consistent with the loss of active detection surface due to the presence of pillars, 2,5%.

7.2.5 Ratio of charges between planes

As mentioned in Chapter 5, the superimposed readout layers of the Micromegas detection plane present a heterogeneity in terms of charge induced in the X and Y coordinates.

Figure 7.9 shows a histogram with the maximal ADC counts sorted by coordinate. It is possible to see how the layer closer to the resistive anode (X) presents a larger signal amplitude, despite its smaller section and shorter length, and due to the screening mentioned in Section 5.2.1.

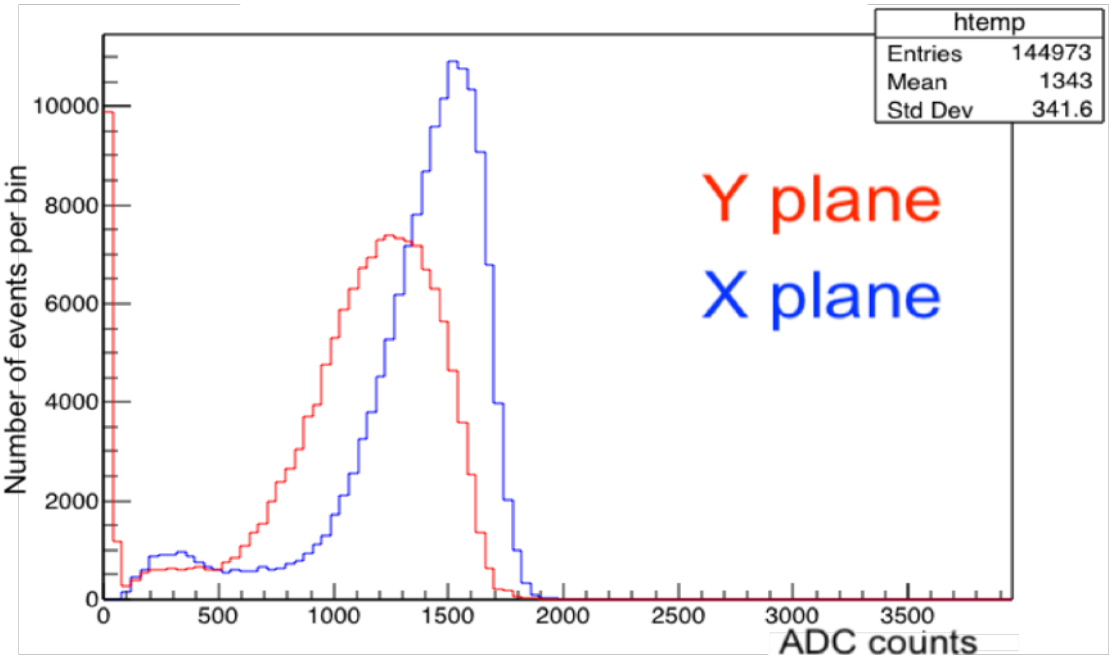

Figure 7. 9 Maximal signal amplitude in both planes.

To quantify the difference in charge induced between the two readout coordinates, the signal has been integrated over the 675 ns, and compared as shown in Figure 6.9. The charge induced on the X coordinate is 1,6 $\pm$ 0,28 times larger than that of the Y coordinate.

7.3. Open sky measurements

This campaign of measurements aimed at assessing the track reconstruction efficiency by comparing the experimental results of an acquisition in open-sky conditions (no massive obstacles within the angular acceptance field of view of the detector) to the number of muons predicted by the theoretical model. This campaign was carried out on the top of the mountain hosting the LSBB facilities, the Vestale site seen in Figure 7.10 (latitude 43,942122°N, longitude 5,48551°E, 1.017m above sea level).

Figure 7. 10(A) View of Vestale site (B) and detector setup.

7.3.1 Experimental acceptance angles

The experimental setup consists of two liquid scintillators, of 93 x 93 x 5 m^3 each, stacked with the MUST^2 on top of them. The angular acceptance of this setup is 80º ± 2º depending on the azimuth angle. Due to size constraints, the MUST^2 could not be perfectly centred over the scintillators, and the middle point of the scintillator was shifted 90 mm towards the high values of X channel (approximately over X channel 600).

Figure 7.11 (A) shows the distribution of the azimuth angle along the X axis. The zones near the perimeter present a selective screening of azimuth angles according to their position. For channels X < 200, angles between -90º and 90º (towards the center of the detector) are accepted with the rest appearing progressively as the distance to the border increases. The opposite effect is verified for channels X > 800. Figure 7.11 (B) shows the zenith angle distribution along the X axis. The progressive detection of near-perpendicular angles to the detection plane towards the center of the detector can be explained by the relative position of the MUST^2 detector and the scintillators. The same effect has been observed for the Y axis.

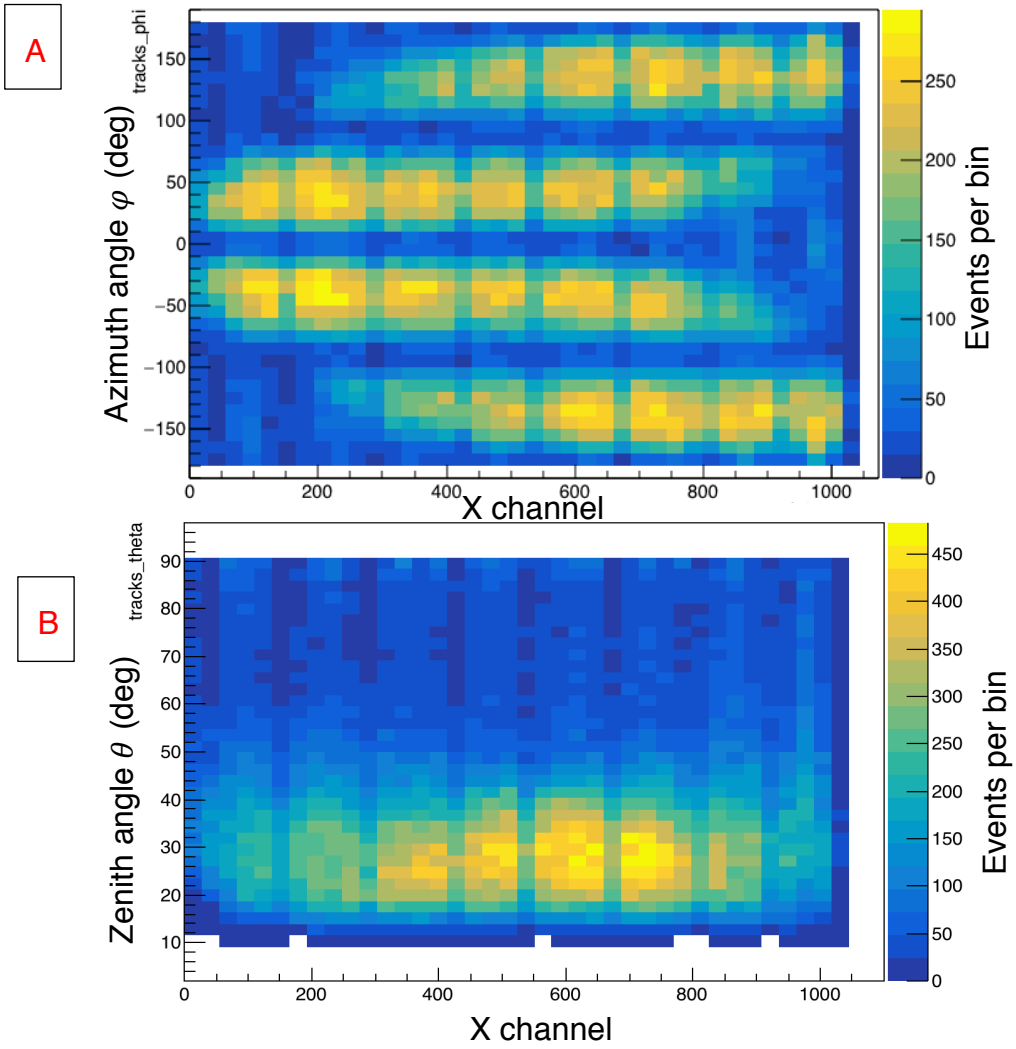

Figure 7. 11(A) Azimuth and (B) zenith arrival angles of muons as a function of the position along the X axis.

7.3.2 Theoretical muon flux vs measurement.

To quantify the flux drop for imaging purposes, it is necessary to obtain a precise muon flux characterization at ground level as a reference input for the tomography. The empirical model used in this work was explained in Section 2.4.1 and described by Equation (2.19). The four charts of Figure 7.12 illustrate the muon arrival distribution in a polar chart.

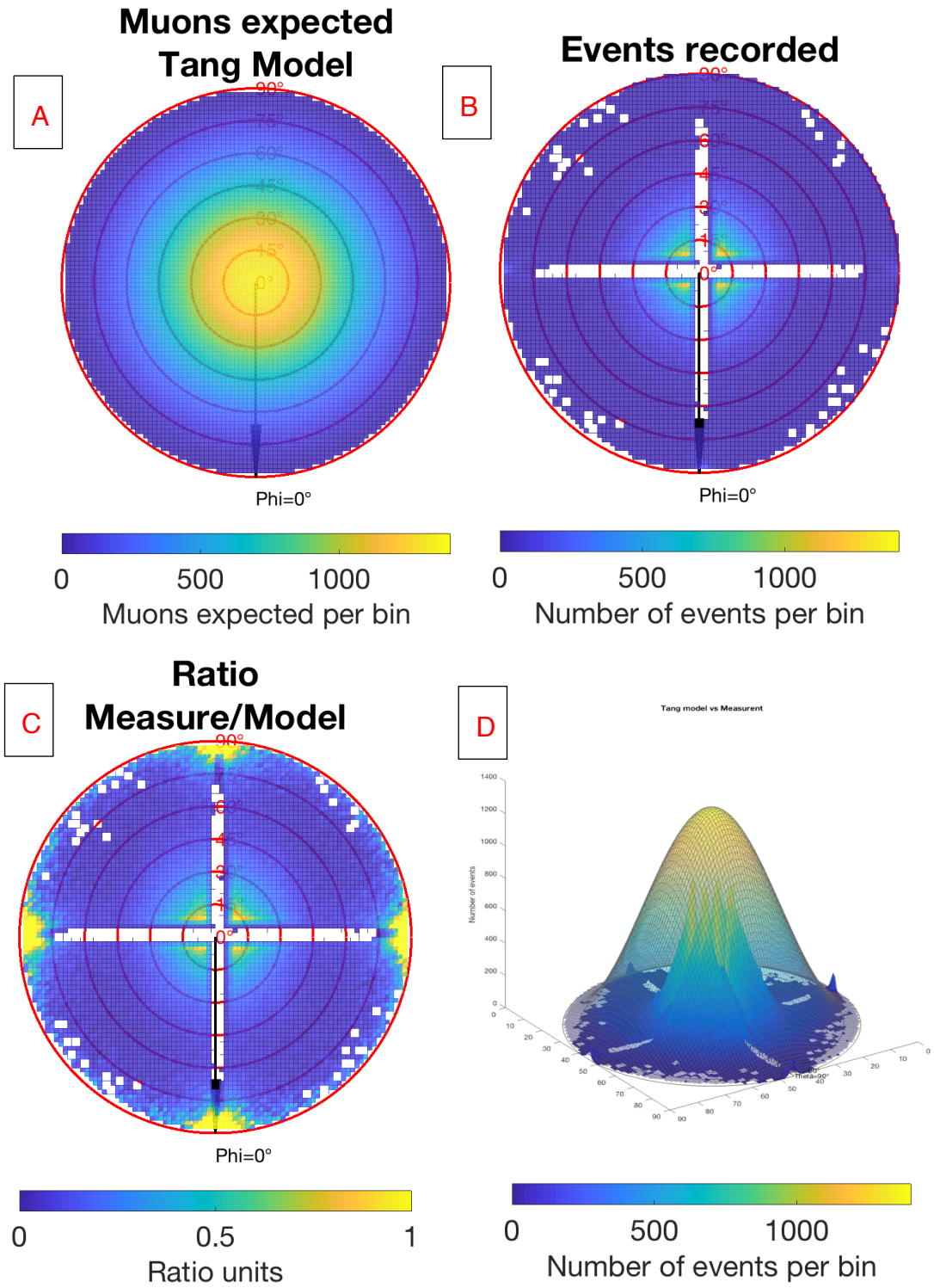

Figure 7. 12 Polar chart of the muon arrival distribution for the Tang model and experimental measurements.

The red concentric lines represent the zenith angle (θ, 0º=zenith, 90º=horizon), and the black arrow the azimuth (φ, Phi=0º stands for the reference azimuth of the detector, which during the acquisition was aligned to 63º of geographic north). Figure 7.12 (A) shows the theoretical muon arrival distribution for particles with energies over 105 MeV, integrated over 204 min (length of acquisition) to 0,52 m^2 (active surface of detection). Figure 7.12 (B), shows the successfully reconstructed events, which can be used as a reference for the detector's acceptance to correct the measured muon distribution for imaging purposes.

As seen in Chapter 6, the MTRA is today unable to track muons with trajectories aligned with the X and Y micromegas readout tracks. The reconstruction artefact in the zones with θ ∈ [80º,90º] and φ near 0º, 90º, 180º and 270º is a side effect of the reconstruction algorithm. This zone, recognisable in yellow in the Figure 7.12 (C), should have no effect on the inversion results if the detector is correctly positioned towards the target. Figure 7. 12 (C) might be interpreted as an efficiency distribution of the muon trajectory reconstruction, and as in Figure 7.12 (B) may help to correct the muon distribution. The drawback of this technique is that, in this case, the influence of the empirical muon arrival model is included.

Lastly, Figure 7. 12 (D) represent in the same figure the theoretical muon arrival distribution (translucent surface) and the experimental measurement (opaque surface underneath).

7.3.3 Hits vs zenith angle.

The total number of hit tracks (tracks on both X and Y coordinates) depends on the zenith and azimuth arrival angles of the particle. Figure 7.13 (A) shows the experimental distribution of zenith angle against the number of stripes hit. The figure is in good agreement with Figure 7.13 (B) in which the theoretical number of hits[2] was calculated.

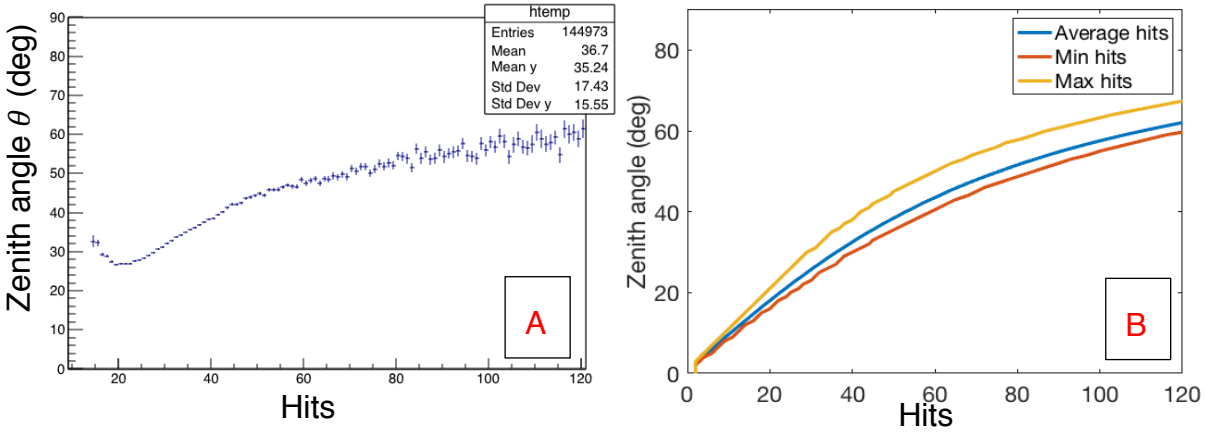

Figure 7. 13 Number of hit tracks as a function of the zenith angle measured (A) and calculated theoretically (B).

[2] The theoretical number of hits has been calculated as the number of tracks in X and Y coordinates that intersect the projection of the muon trajectory within the TPC for arrival angles θ ∈ [0º,90º] and φ ∈ [-180º,180º].

7.4. Underground measurements

Underground measurements at 62 m depth were performed in the LSBB's galleries. The experimental setup consists of the rack structure seen in Figure 7.14, where three liquid scintillators, analogues to the ones of the open sky experiment, have been stacked and placed in coincidence mode. The angular acceptance of this setup is ~54º. The temperature of the room has been monitored, and remained steady at ~15ºC during the entire experiment.

Figure 7. 14 Experimental setup with MUST² detectors and liquid scintillators.

Figure 7.15 shows the location of the detector relative to the LSBB galleries. The red square symbolizes the intersection of the acceptance angle of the detector and a horizonal plane distant of 62 m, the vertical distance from the detector to the surface.

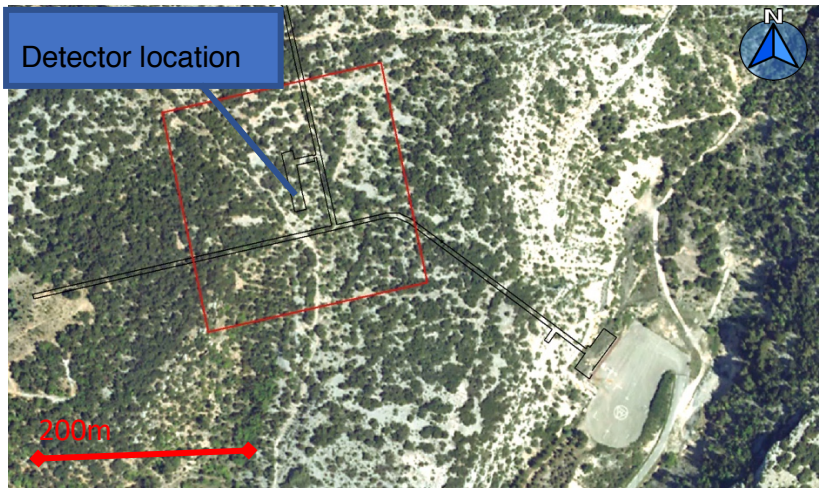

Figure 7. 15 Terrain over the detector. The red square indicates the approximate surface monitored within the acceptance angle.

7.4.1 Effect of the gas filling.

A data acquisition was launched while the detector still contained some air in the TPC volume (first acquisition). It permits to assess the performance of the detector during the gas filling process and to stablish the amount of gas introduced before steady operation. The data logging began ~24 h after starting flushing the gas with a 4 L/h flux. The gas flux remained constant during the acquisition. Figure 7.16 shows the temporal evolution of one detector's gain-dependent parameter, the average signal amplitude of the X readout plane in ADC counts.

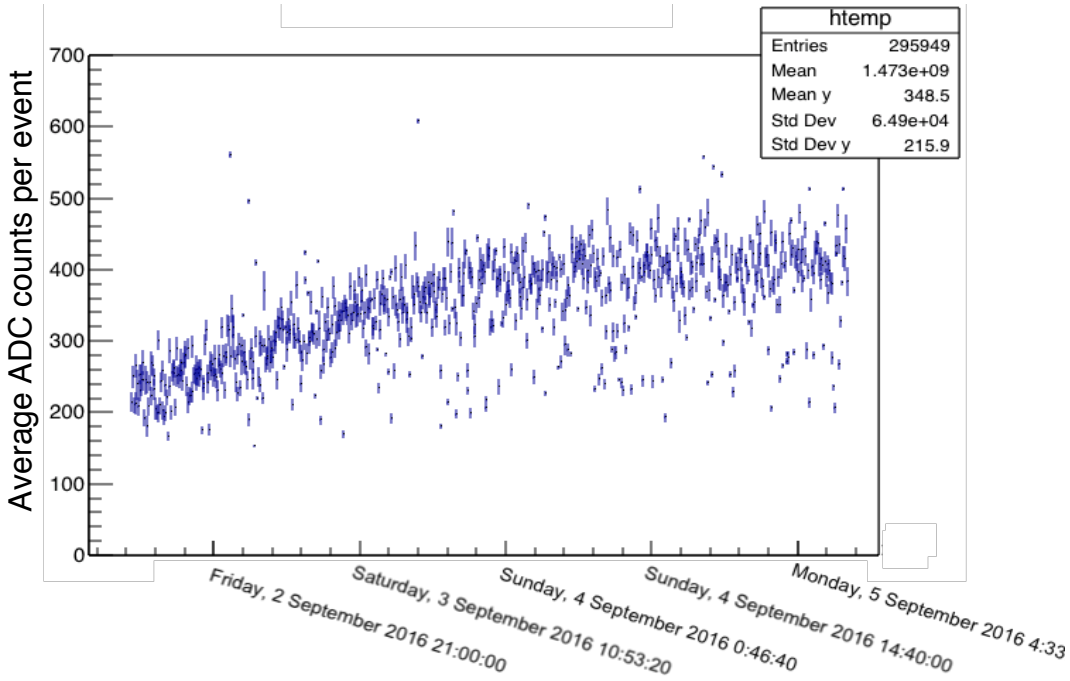

Figure 7. 16 Temporal evolution of the average signal amplitude of the X coordinates during the gas filling process.

One observes how at the beginning of the acquisition the gain of the detector increases until it reaches a plateau value. The steady gain value was achieved when the introduced gas blend was approximately ten times the volume of the TPC (~250 L of gas blend).

7.4.2 Tilted acquisition.

To verify the independence of the zenith angle reconstruction from the detector tilt, two measurements were made; one with the detector parallel to the ground, and another with the detector tilted 30º along the Y axis. The distribution of reconstructed zenith angles in the XZ and YZ planes is presented in Figure 7.17.

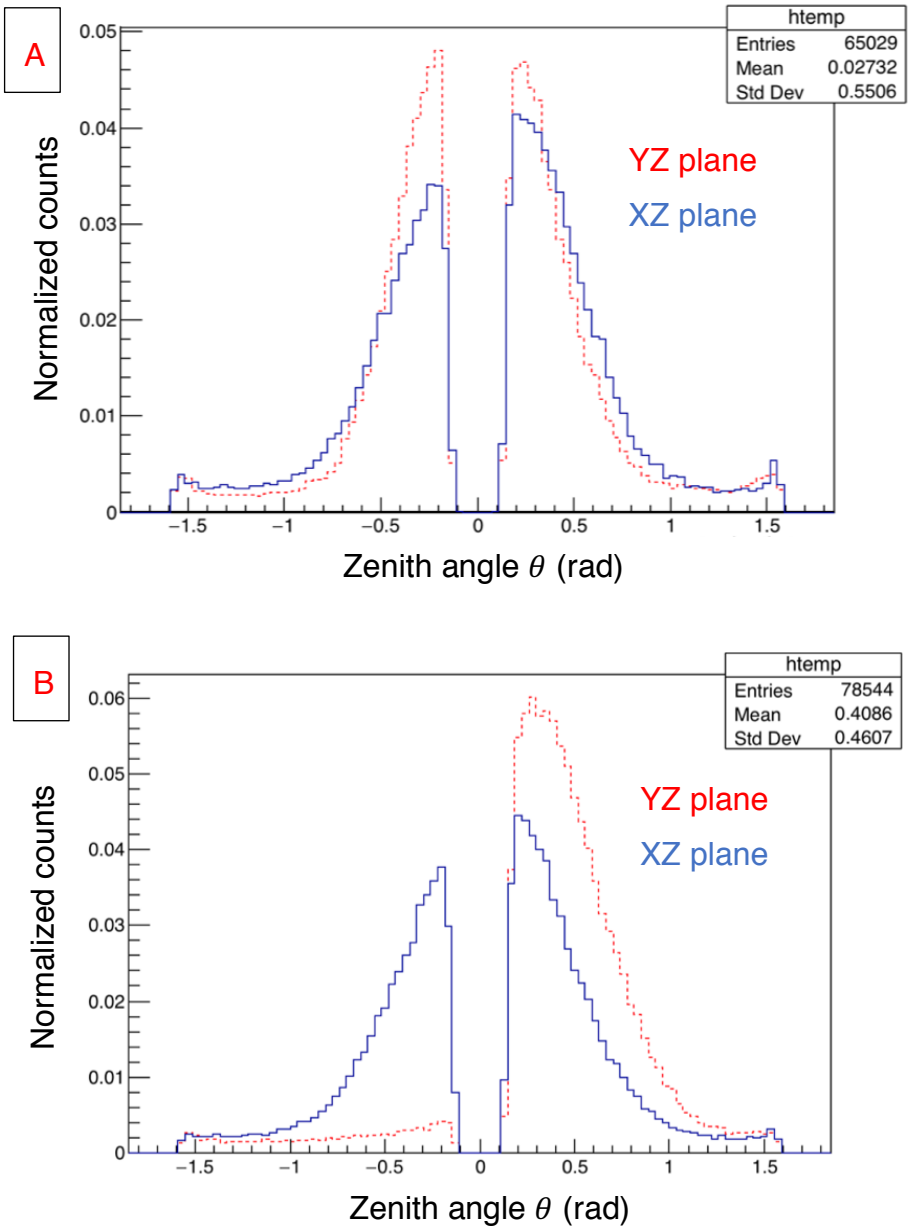

Figure 7. 17 Distribution of measured zenith angles on the XZ and YZ planes with (A) the detector parallel to the ground and (B) tilted 30° over the Y axis.

One sees that the data on the XZ plane has barely changed, whereas the center of gravity of the YZ data has shifted of 26,35° ± 9,4°. Which is consistent with the experimental setup modification.

7.4.3 Muon flux measured vs apparent opacity.

The elevation information of the terrain over the MUST² detector, seen in Figure 7.18 (A), was downloaded from the French National Institute of Geographic and Forest Information (IGN) with a 1 m resolution. Considering a rock density of 2.600 ±130 kg/m³ obtained from a direct measurement, the map of apparent opacity shown in Figure 7.18 (B) was calculated.

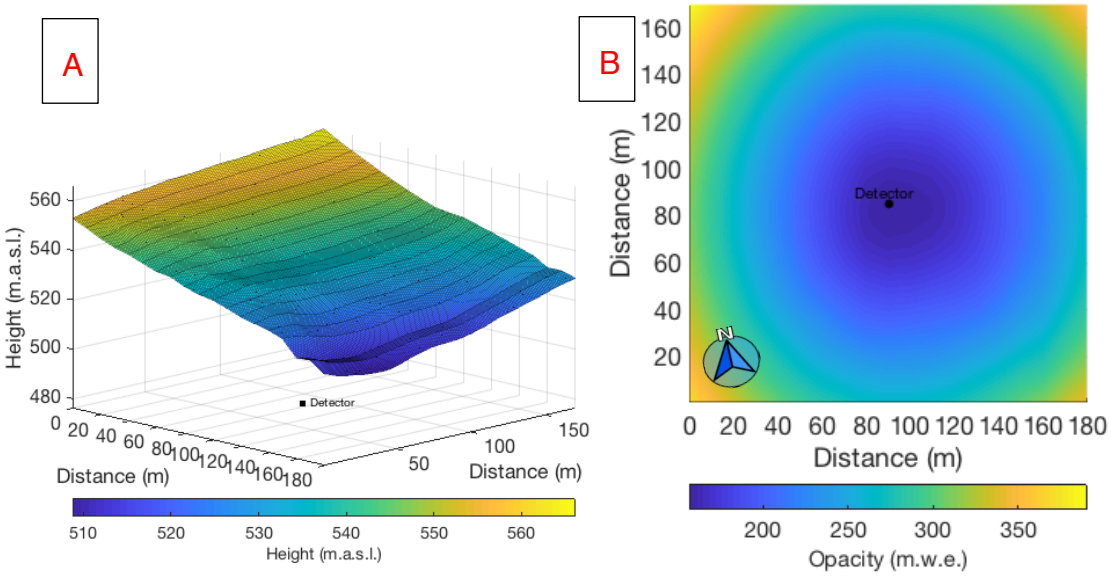

Figure 7. 18 (A) Topography of the terrain over the detector and (B) apparent opacity of the medium.

Figure 7.19 shows a polar representation of the angular distribution for all the muons reconstructed after ~3 days of acquisition (2.000.000 events). The acquisition length was conditioned to the availability of the experimental site. The closure of the site for maintenance works motivated the displacement of the experimental setup to the external entry of the laboratory.

Figure 7.19 (A) shows the normalizes raw angular distribution of reconstructed events, whereas in Figure 7.19 (B) the angular distribution is corrected via the open sky measurement to minimize the effect of the detector acceptance in the measurement. The values of Figure 7.19 (B) are calculated by dividing the normalized arrival probability of arrival from the underground measurement by one from the open sky. Hight ratio values indicate an opacity diminution in the monitored direction.

The reconstructed muon flux distribution presents in both cases an asymmetry, with the larger number of muons coming from the azimuth angle where the apparent opacity of the volume over the detector is smaller, as one should expect. Most of the reconstructed muons fall within the acceptance region established by the scintillators configuration. It is also possible to observe a reconstruction artifact (an unusual group of reconstructed events) created by the MTRA in the zones with zenith angles near 90º and azimuth 0º, 90º, 180º and 270º.

The high ratio values of Figure 7.19 (B) for zenith angles larger than 54º (experimental angular acceptance) lack of physical meaning and are a product of the instrumental noise.

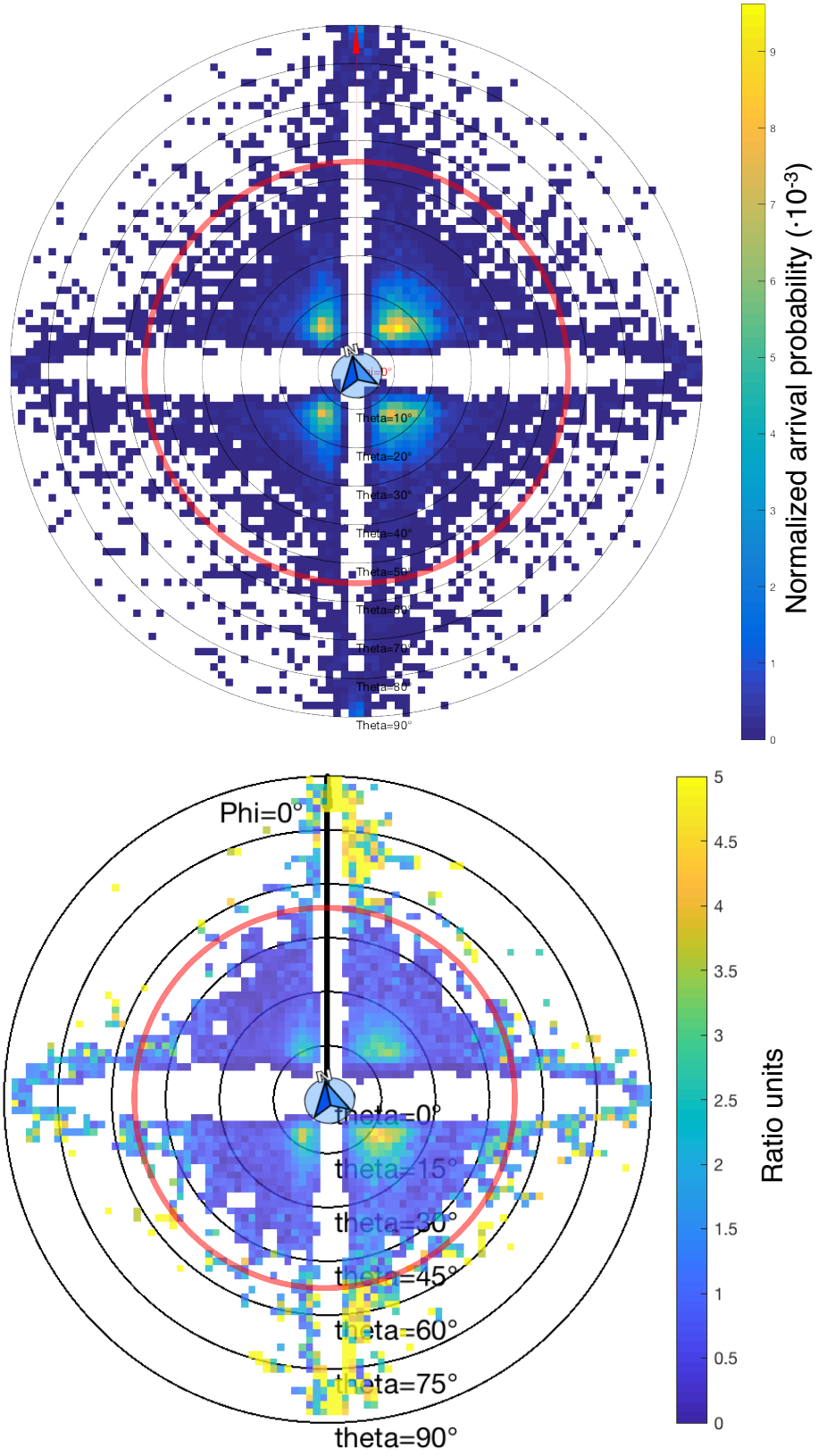

Figure 7. 19 Polar representation of the angular distribution of reconstructed muons: (A) direct measurement and (B) corrected with the open sky measurement. The red circle indicates the acceptance of the scintillators.

7.5. Valley measurements

The laboratory main entrance is located, as seen in Figure 7.15, at the lowest point of a narrow valley. Figure 7.20 (A) shows a 360º panoramic view with the location of the detector, inside the white modular building. An experimental measurement was carried out at the entry platform of the LSBB with the same experimental setup as for the open sky measurements. A dataset corresponding to 3h of acquisition was been compared by means of the ratio shown in Equation (7.2). The elements of the ratio are inversed compared to the previous section to highlight the zones with larger attenuations.

$$Ratio = \frac{Muons\ per\ azimuth\ degree_{Open\ sky\ measurement}}{Muons\ per\ azimuth\ degree_{Valley\ measurement}} \quad (7.2)$$

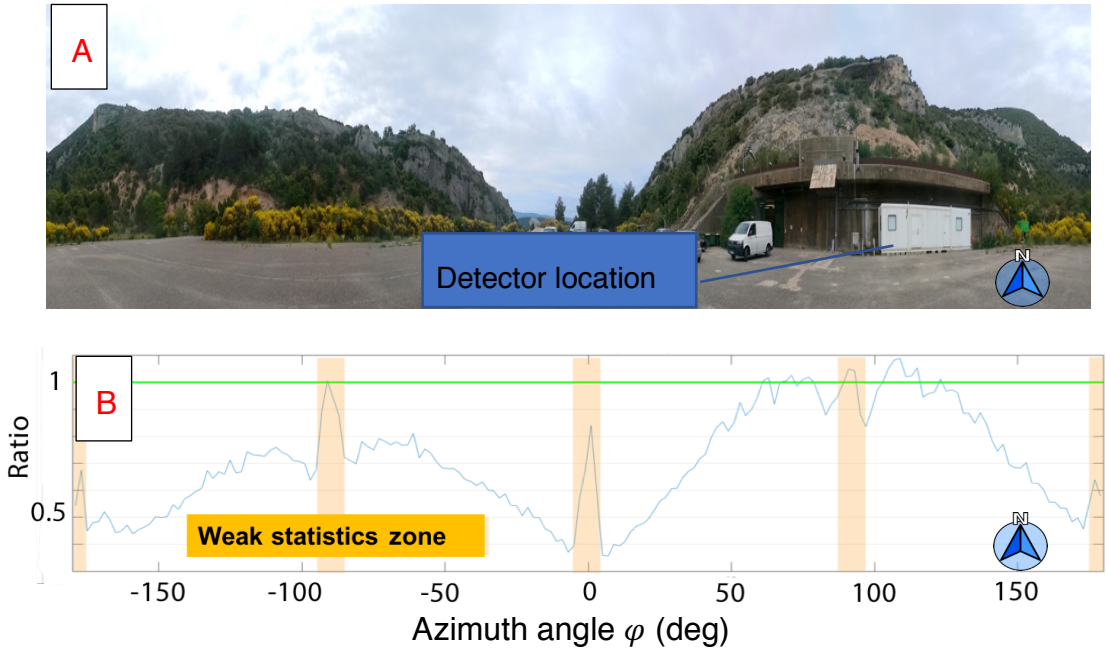

Figure 7. 20 (A) 360º panoramic view of the LSBB's entry for illustrative purposes, (B) the ratio between this and the open sky acquisitions as a function of azimuth angle.

Figures (A) and (B) present the same azimuth angle alignment. The high ratio values are due to the attenuation of the muon flux because of the medium's opacity. It is possible to see how the skyline of the valley is reflected in the Figure (B). The data in the orange is from the blind spots of the detector, and is caused by MTRA. Therefore, it has no physical meaning and should be ignored.

Another representation of the same ratio is shown in Figure 7.21 (A), this time considering the zenith and azimuth angles. The number of muons measured has been distributed into a 90 x 90 matrix, with the color scale indicating the ratio value in a given bin. It is possible to see that Figure 7.21 (A) presents two zones with high attenuation, corresponding well with the position of the two sides of the massif seen in Figure 7.21 (B).

The yellowish ring in the high zenith values represents a zone with low statistics due to the angular acceptance of the experimental setup (80º ±2º). The blank spots indicate zones where not enough muons were collected for the ratio comparison. The four zones marked with the blue boxes indicate the artifacts made by the MTRA and have no physical meaning.

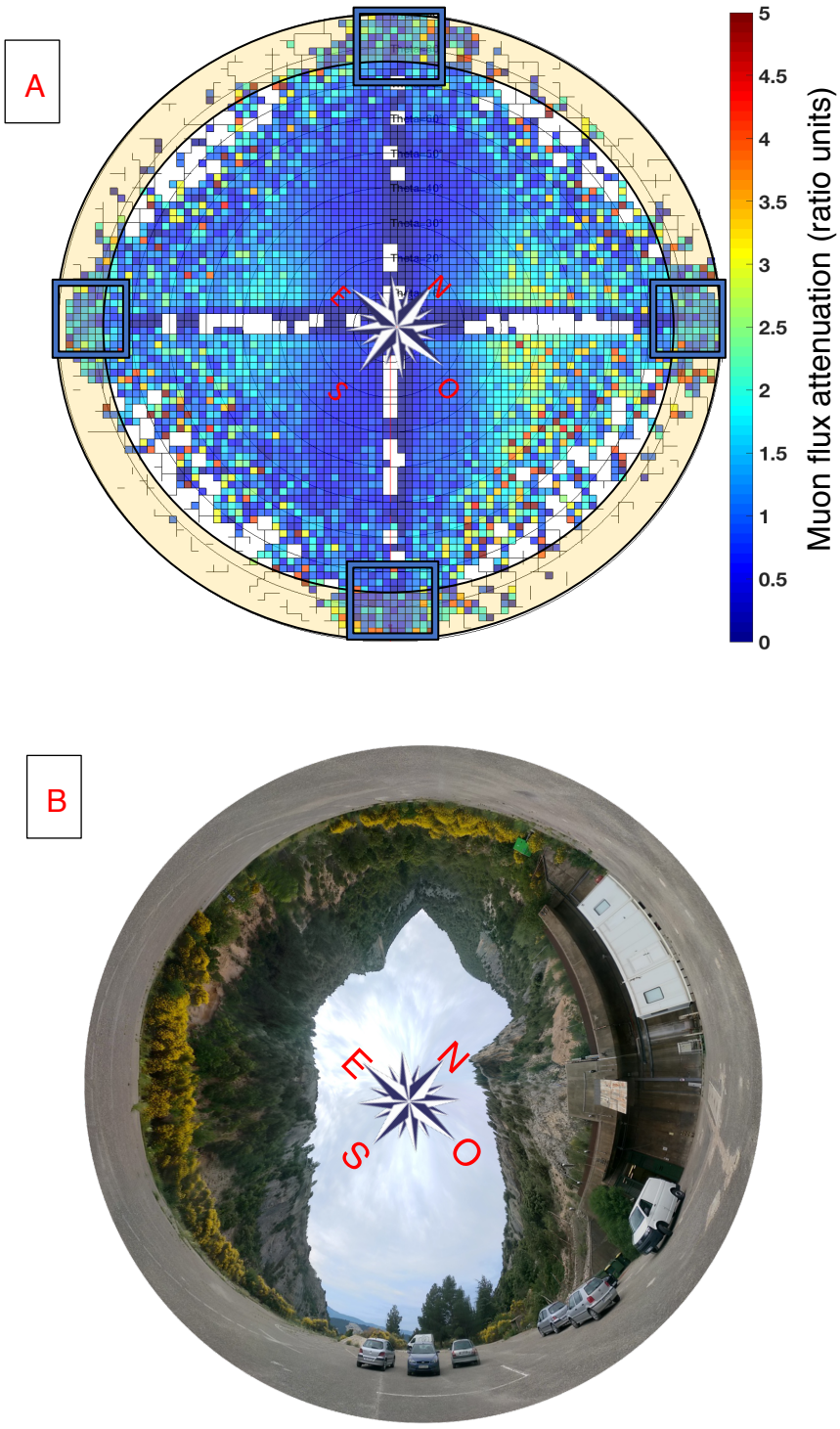

Figure 7. 21 (A) Representation of the ratio between the measurements at open sky and valley with the bins sorted by zenith and azimuth angles. (B) Spherical picture for illustrative purposes only.

The experimental data shown above comes from a preliminary run made for the fine tuning of the operational parameters prior to a longer acquisition. During this second acquisition, the experimental site was affected during the night by a storm with lightnings and severe precipitation. The amount of precipitation was approximately 25L per m^2 in few hours, but the exact values are unknown because the laboratory environmental station was temporarily out of service due to the blackout caused by the storm.

The ceiling of the modular building, where the detector was installed, presented important water leaks and the experimental setup was flooded. Figure 7.22 shows the aspect of the detector and the DAQ machine the morning after the storm.

Figure 7.22 (A) Presence of water in the experimental setup after the storm, (B) damaged acquisition computer, and (C) presence of water inside the protection box.

The computer used for the data acquisition was found off and soaked. After a complete disassemble and drying the machine was irrecoverable and the data stored in the hard drive couldn't be retrieved. On the other hand, the protection box of the detector allowed water entrance, and the detector and its electronics were in direct contact with water. The servicing tasks were successful in this case and the detector was recovered. Due to schedule constraints, the detector was installed into a new emplacement in the dam of Saint-Saturnin-les-Apt and the experiments in the entry of the LSBB postponed.

7.6. SRS vs DREAM electronics

A comparison of two different electronics was made at IRIS Instruments headquarters. The two families of technologies have been introduced in Section 5.7; the CERN's SRS and the CEA's FEU.

The experimental setup consisted of a stack of 4 detectors: from bottom to the top, two scintillators, one MUST^2 detector with the SRS electronics and a second MUST^2 detector with the CEA electronics. Figure 7.23 shows the two MUST^2 detectors with the cases open before being stacked.

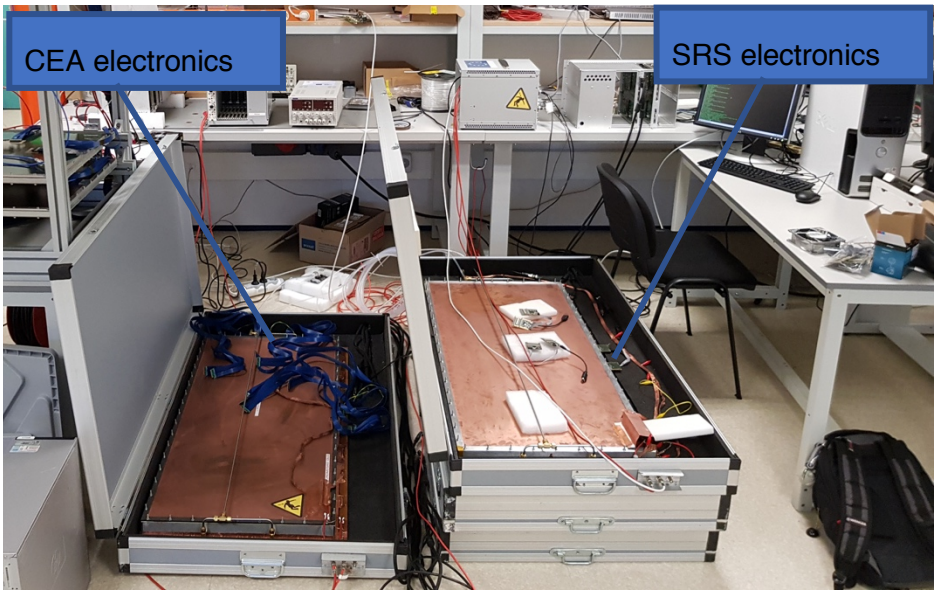

Figure 7. 23 Experimental setup overview for the electronics comparison.

The experiments were performed with a single trigger signal from the coincidence pulse of the two scintillators, then converted to NIM and TTL to trigger the SRS and DREAM electronics respectively. Both MUST^2 detectors have been operated under the same gas blend and similar voltage parameters.

Due to the limitation in the number of instrumented channels because of the available hardware, only the central section of 256 x 256 channels was monitored. This corresponds to 4X and 4Y DREAM chips and 2X and 2Y APV25 cards with CEA's and SRS systems respectively.

Figure 7.24 shows a typical signal recorded during the experiment by the two different systems. It is seen that both systems succeeded in identing the muon passage through the detector. The slight saturation in the CEA's electronics is a result of the operational parameters having been optimized for the SRS electronics, and that this configuration was applied directly without performing a fine tuning.

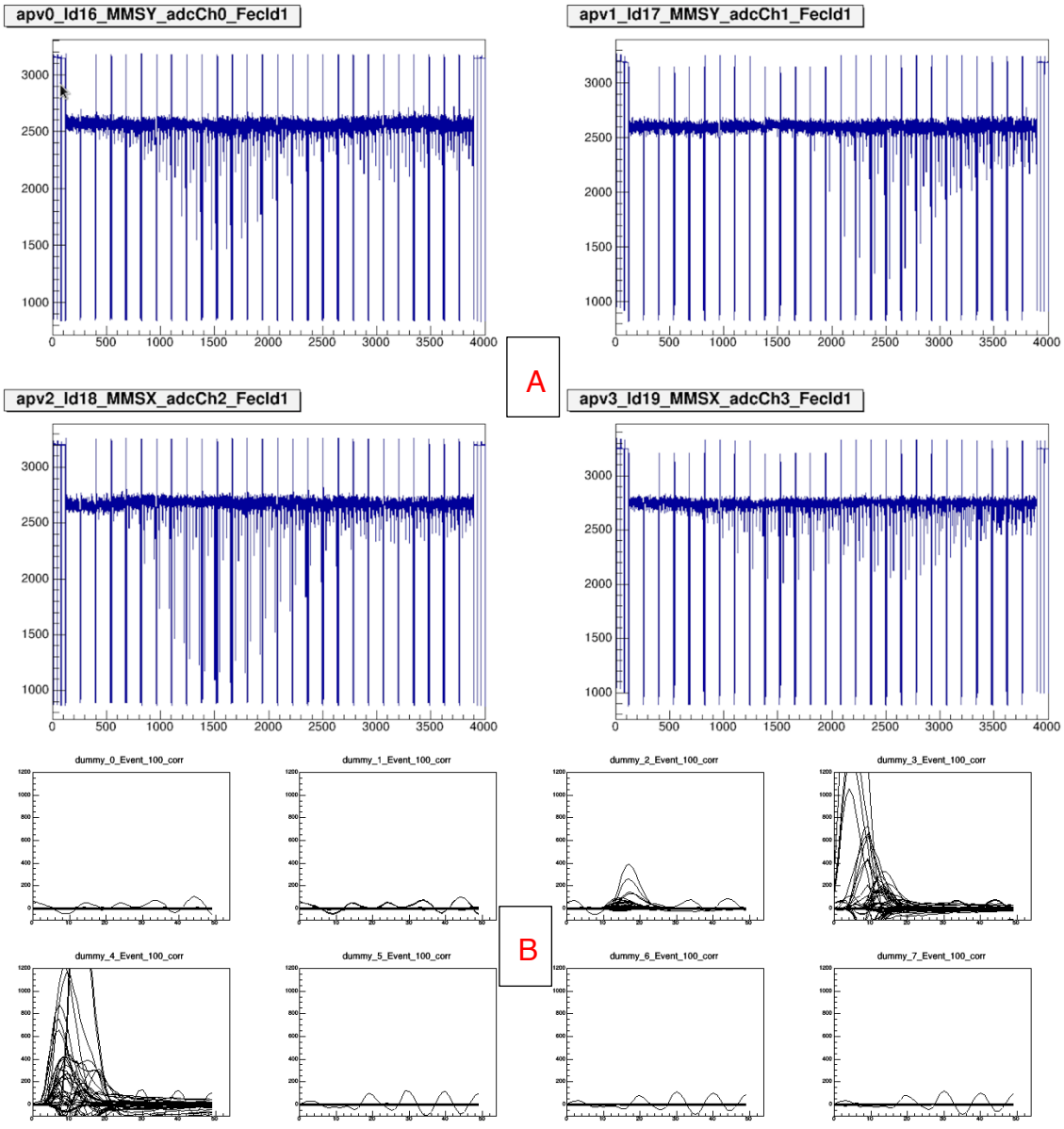

Figure 7. 24 Typical events of the MUST² detector measured with the (A) SRS system and (B) CEA electronics.

A second data acquisition was made done with the two systems triggered independently: the SRS with the signal from the scintillators, and the CEA with its self-trigger by track. In the second case, a topology condition has been set: only events with correspondence between X and Y planes were recorded.

A third trigger option was also tested, with the SRS electronics having successfully acquired data with a signal created by the FEU card self-trigger.

Unfortunately, a deep data analysis has not been possible due to the different structures of the acquired data by the two acquisition systems. A tool to convert the data format in order to use the MTRA with the data from the CEA electronics is being developed to continue with a proper performance comparison.

7.7. References

[i] Kuger, F. (2017). Signal Formation Processes in Micromegas Detectors and Quality Control for large size Detector Construction for the ATLAS New Small Wheel. Doctoral dissertation.

Chapter 8. Study site: dam.

Chapter 8 abstract

Chapter 8 describes the full field test of the MUST^2 detector. It begins with presenting in Section 1 the interest in the experimental location at Saint-Saturnin-les-Apt, as well as its characteristics. It also describes in Section 2 the actions taken to overcome the technical challenges found while adapting the experiment site at the foot of the dam to host the detector and to monitor the environmental conditions.

Section 3 explains the motivations of building a digital terrain model of the targeted volume, and presents the results of the simulations of apparent thickness and opacity of the medium from the point of view of the detector.

Section 4 describes the experimental results obtained during the campaign, and analyzes factors such as the detector intrinsic performance and muon reconstruction algorithm efficiency. The result of the muon reconstruction is compared with the simulated apparent opacity.

The influence of the temperature, on the gain, and subsequently in the efficiency of the track reconstruction algorithm, is also discussed. Temperature has an effect on the measurement of the water level as well.

Lastly, the effect of the Earth tide has been assessed in order to see its influence on the daily fluctuations measured water level.

8.1. Introduction

After the characterization of the detector in a controlled environment, the first acquisition test under actual field conditions aimed at imaging a water reservoir in the village of Saint-Saturnin-les-Apt, Southeast of France (see Figure 8.1). The interest in this site lay in its combination of different monitoring aspects:

- Geophysics: host rock body of the reservoir.

- Civil engineering: two aligned dams.

- Temporal monitoring: water level variations of the reservoir.

- Risk surveillance: The dam prevents the water reservoir from flooding the village downstream.

- Cultural heritage: the narrow rock strip that separates the eastern side of the water reservoir from the village hosts castle remains (with at least one known tunnel that crosses the rocky volume).

Nowadays the reservoir has a maximal capacity of ~11.500 m^3 of water, with depths ranging from 0 to 14 m.

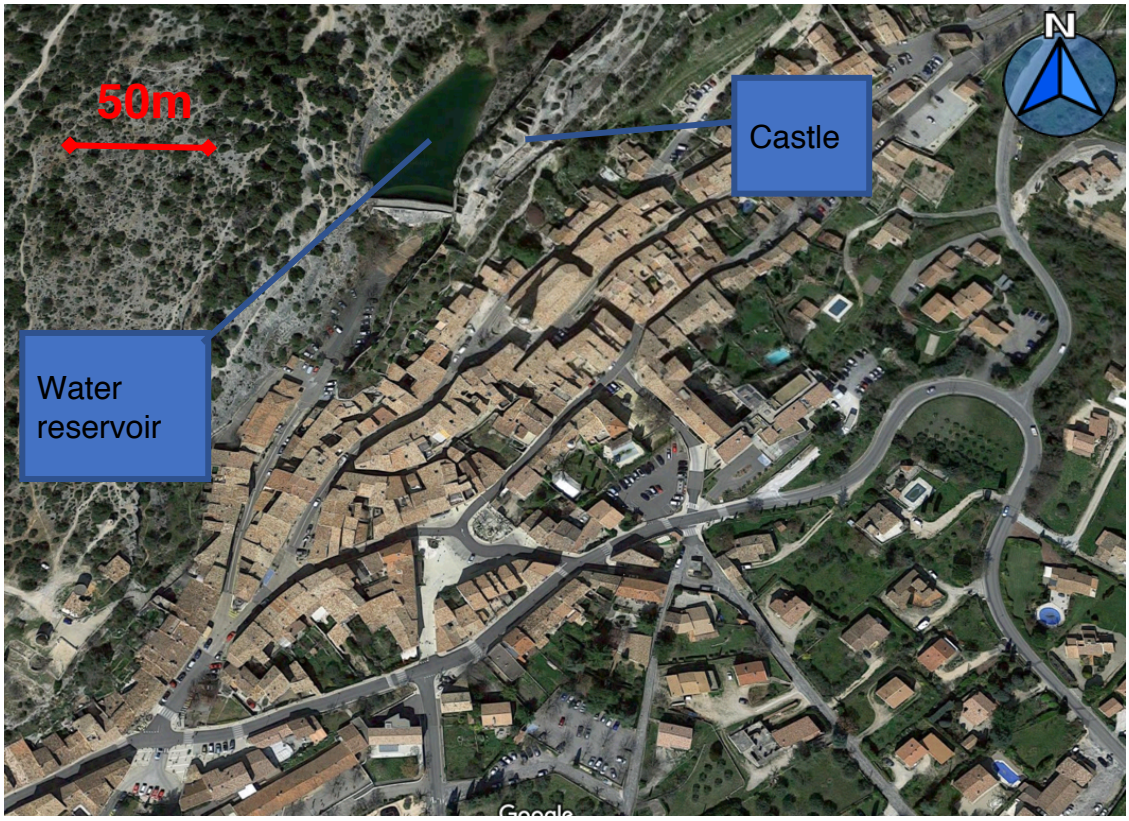

Figure 8. 1. Satellite view of the water reservoir with respect to the village. Source: Google maps.

8.1.1 Dams

The experimental site includes two dams made at different times, for different reasons.

The oldest structure dates back to 1763 and was located near the end of a narrow valley overlooking the village. This valley is the result of the erosion caused by the water from a larger drainage basin. The concentration of water during heavy rainfalls produced flash floods in the village. The city archive, as seen in Figure 8.2, still conserves all the documents related with its construction, including plans and materials

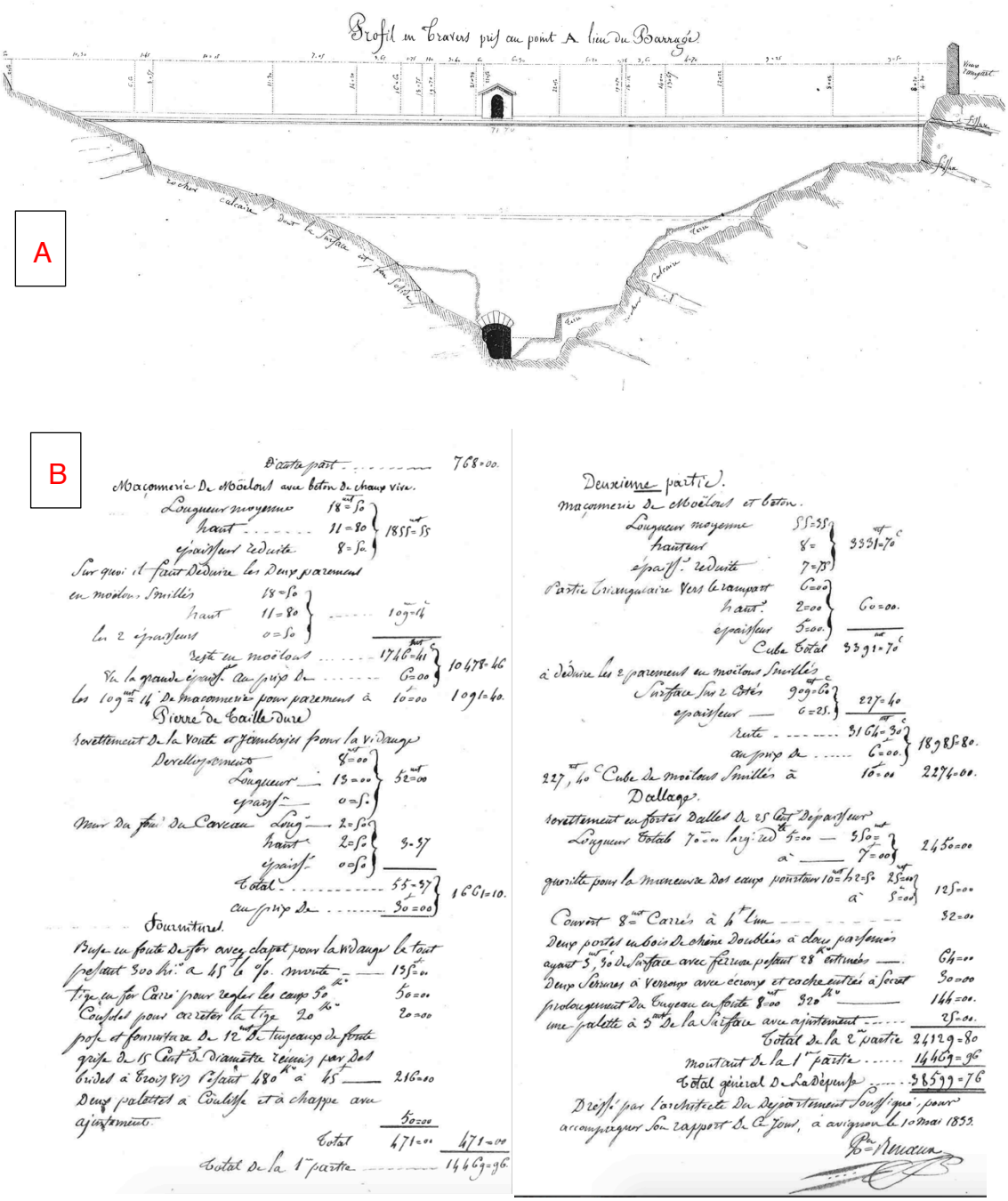

Figure 8. 2 (A) Plan of the old dam and (B) construction budget with details of the materials used. Source: City archive of Saint-Saturnin-les-Apt.

After its construction, the water (non-potable) was collected by the village's supply network to supply the parks and fountains. The hydraulic head was however not high enough to reach the entire village, and construction of a second higher structure a few meters downstream, as seen in Figure 8.3, was concluded in 1855.

Figure 8. 3 View of the two dams.

The reservoir is filled exclusively by water from precipitations and surface runoff, and today the village does not collect water from the reservoir. The reservoir is however emptied for servicing approximately once every ten years. To control the water level, a drain valve is located at the foot of the dam inside a valve house (seen in Figure 8.4).

The topography of the site, seen in Figure 8.5, is well known due to the periodic maintenance made by the company *Société du canal de Provence*.

Figure 8. 4 View of the main dam and the valve house.

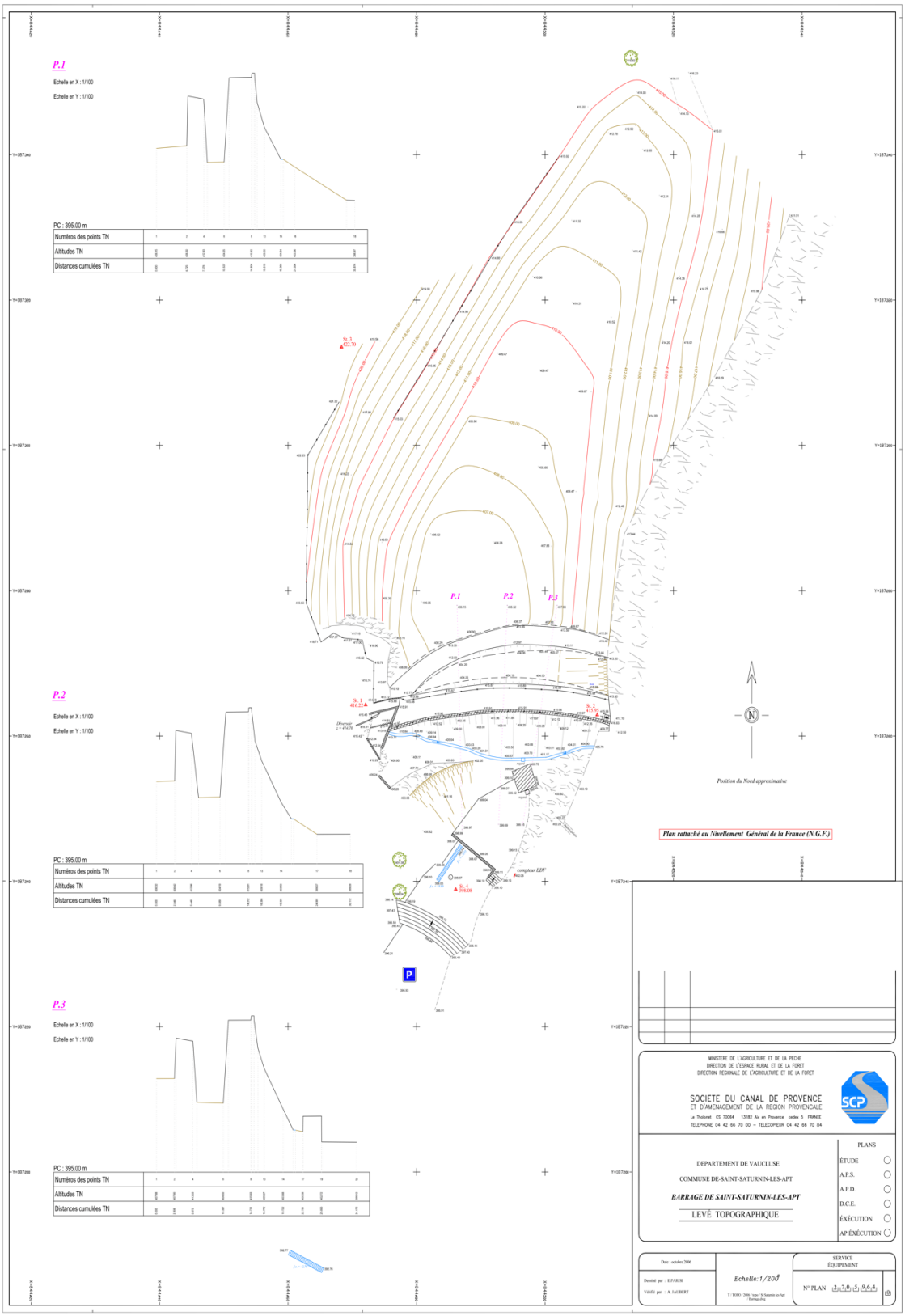

Figure 8. 5 Topographic map of the water reservoir and the dams' structures. Source: Société du canal de Provence.

8.2. Experimental setup

The valve house presents an excellent detector emplacement site due to its location at the foot of the dam, and dimensions (seen in Figure 8.6). Nevertheless, it presents some drawbacks:

-A lack of electricity.

-The wall contiguous to the dam present constant water leaks, due to the proximity to the dam, and the fact that the lower half of the room is underground.

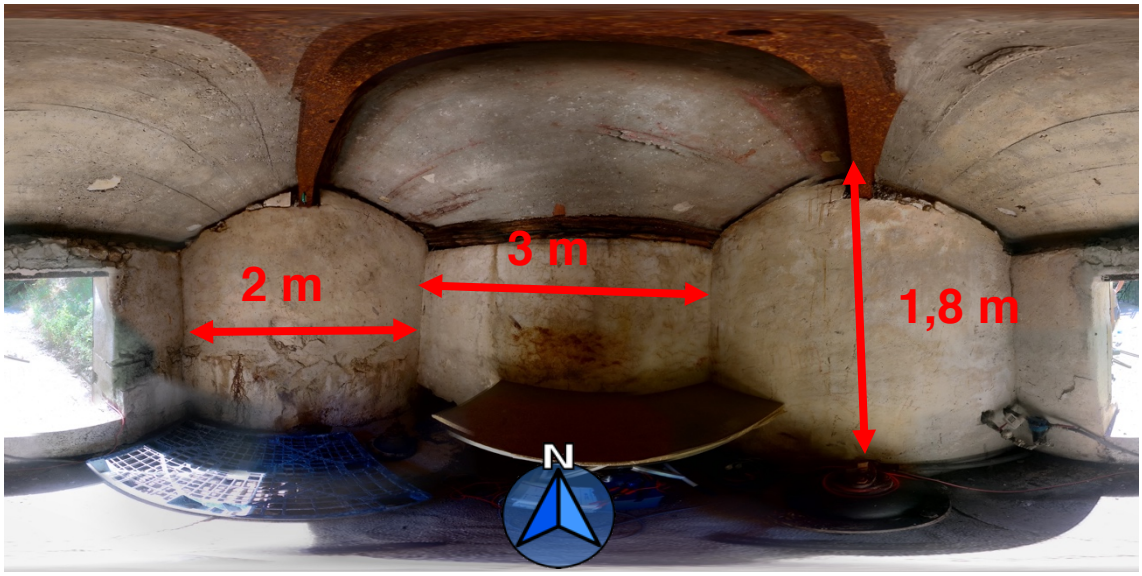

Figure 8. 6 360º panoramic view of the valve house.

8.2.1 Bringing electricity

To address the lack of electricity inside the valve house, a new electric line was created. The starting point was a previously-existent electrical cabinet installed by the city 20 m away.

The line is composed of a 30m R2V-3G2,5 cable that was partially buried and ends inside the valve house. At this point two protections were included:

-A 30 mA ground fault circuit interrupter, to quickly and automatically disconnect the circuit when it detects a current leakage

-A 16 A circuit breaker, to protect from excess current damage from an overload or short circuit.

These protections are particularly important due to the presence of water in the walls and ground.

To conclude, an uninterruptible power supply (UPS) protects the system from overcurrent and blackout events, and to power the instruments.

8.2.2 Humidity control

Different methods have been tested to minimize the presence of water inside the valve house and reduce the humidity, which could harm the electronics as the components are not protected against humidity.

The floor of the room is made of concrete, except for a central trench containing the drainage pipe of the dam and refilled with gravel. To avoid puddles in the concrete, a small 5 cm trench was dug along the wall contiguous to dam, where the water leaks are more important; this trench collects the water and conveys it into the central gravel trench.

Also, as the room floor is ~30 cm below ground level, a wood barrier was been installed next to the door and fixed with silicone cement to avoid the entry of rain water through the door gap.

The temperature and relative humidity inside the valve house were monitored, and are presented in Figure 8.7. When opening the door to access the valve house, a significant and fast increase of the temperature and relative humidity drop are recorded, which is seen several times in the figure.

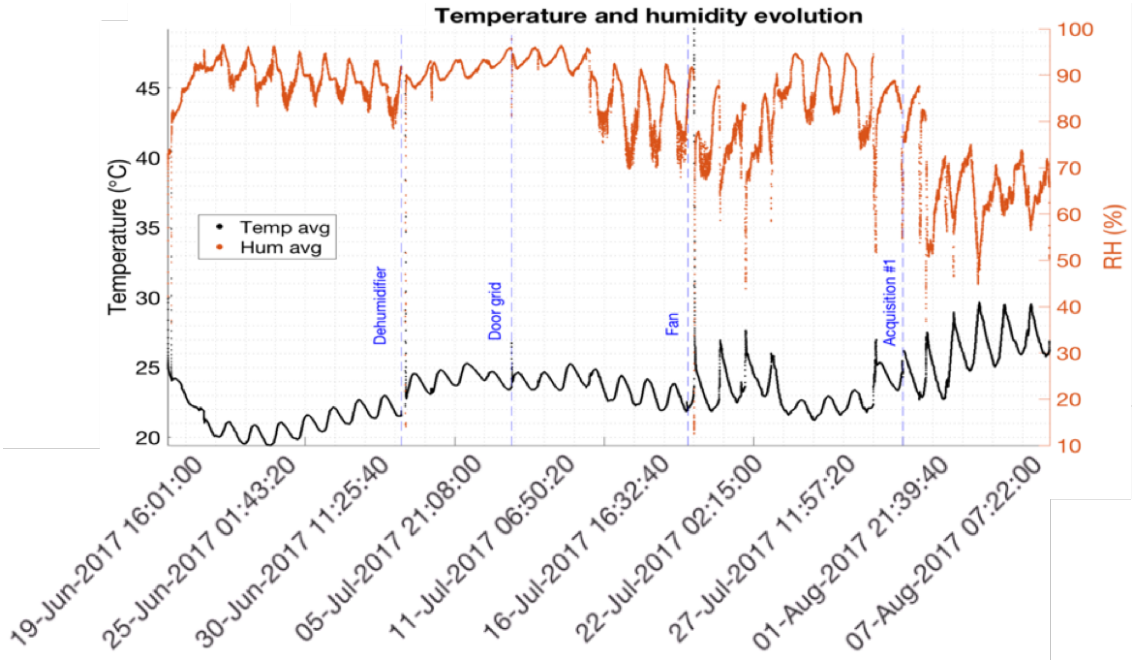

Figure 8. 7 Temperature and humidity inside the valve house.

Despite the elimination of the water puddles, the humidity remained over 90% and the water condenses on all metallic surfaces. The first approach to reduce this was to install a dehumidifier, but after 4 days it seemed ineffective. The next step was installation of a ventilation grill on the door; due to the poor natural convection of the room, the improvement was not as significant as anticipated. Finally, a fan was installed next to the door grid to force air convection and renewal. At this point the condensation finally disappeared and the MUST[2] detector was installed.

In the last stage of the experiment, the temperature rise associated with the working electronics in the room produced a temperature increase (with peaks at 30ºC) and reduction in the humidity. No humidity-related issue was detected during the data acquisition.

8.2.3 Environment monitoring

A series of sensors to monitor the environmental parameters during the experiment were installed at the points seen in Figure 8.8:

-A USB environmental sensor (Yocto-Meteo), located inside the valve house near the MUST^2 detector, which monitored atmospheric pressure, temperature and relative humidity each minute.

-A CTD-Diver DI 27 located at the Point A inside the water near the dam's wall, which monitored pressure, temperature and water conductivity each 2 minutes.

-A Micro-Diver DI 605 located at Point B inside the water on the opposite side of the reservoir, which monitored pressure and temperature each 2 minutes.

-A Baro-Diver located inside the valve house and hung from the ceiling, which monitored atmospheric pressure and temperature each 2 minutes. This detector is provided with the CTD-Diver and permits compensating directly for the effect of the atmospheric pressure on the water level calculation.

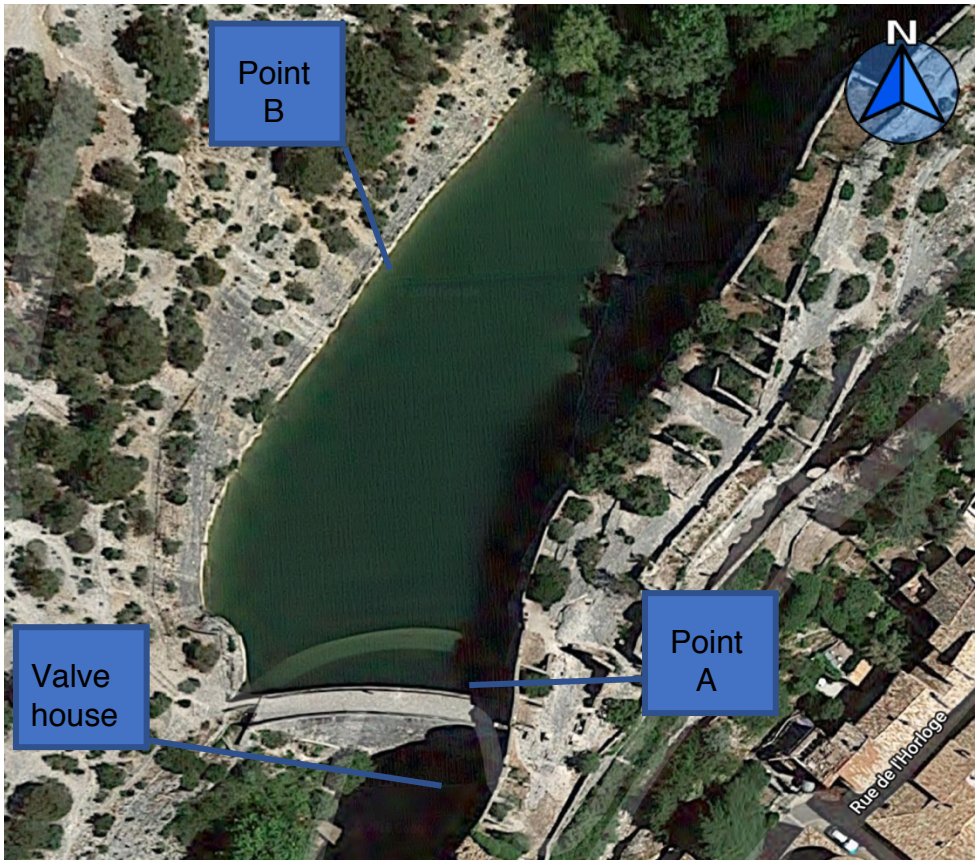

Figure 8. 8 Satellite view of the water reservoir and instrumented points. Source: Google maps.

The barometer used for pressure compensation should ideally be at same level as the water, but was kept inside the valve house to secure it. The deviation of pressure change due to the 10 m height difference between the water surface and the cabin was corrected thanks using the isothermal atmosphere model equation recommended by the detector provider:

$$P_H = P_0 \cdot e^{-M \cdot g \cdot H/(R \cdot T)} \tag{8.1}$$

where: P_H is the atmospheric pressure at elevation height H, P_0 is the atmospheric pressure at the reference height, M is the molecular mass of air, g is the standard gravity, R is the ideal gas constant and T the temperature in Kelvin. For reference, the difference at H=10 m and 20ºC is ~0.22%.

The two diver detectors located underwater were placed inside custom-made concrete blocks (such as the one seen in Figure 8.9), and deployed at the bottom of the reservoir. This block prevents the detector for moving in the bottom and screens the fast water pressure and temperature fluctuations due to currents.

The data was stored locally and recovered at the end of the experiment. The drift time of the inner clock was verified, and neglected (less than 1 s deviation).

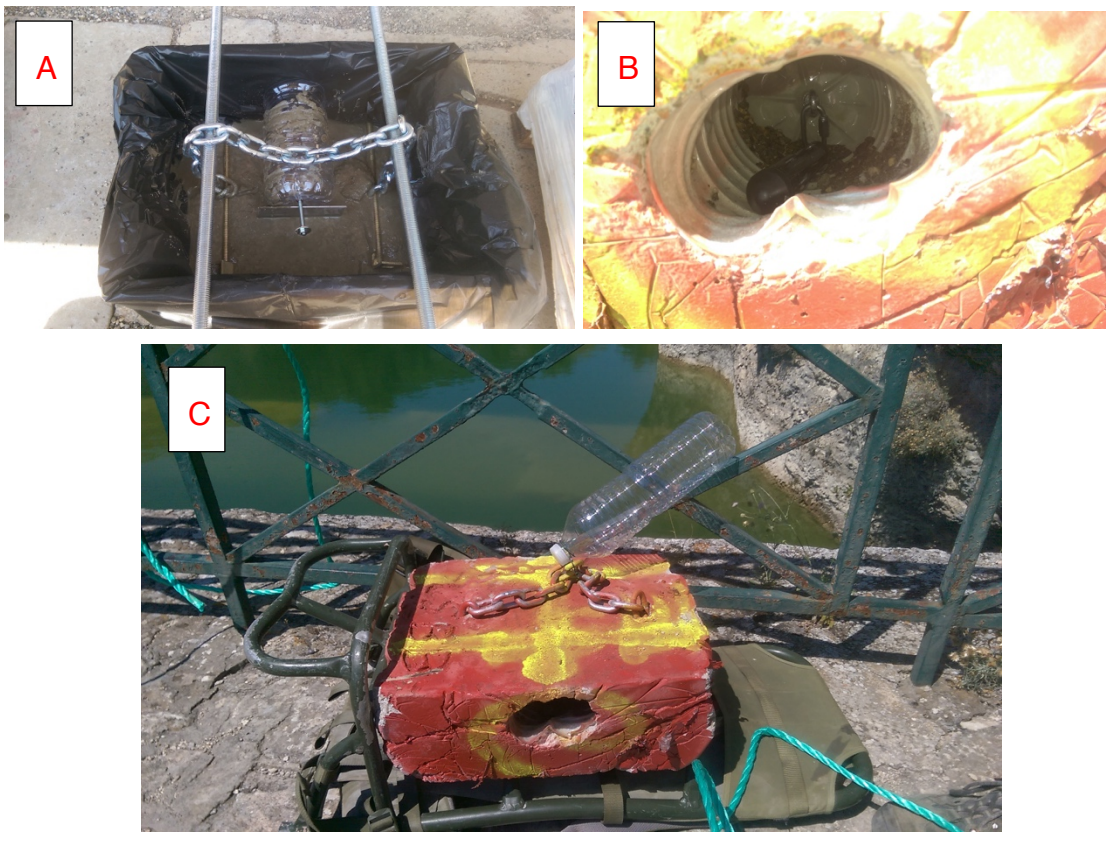

Figure 8. 9(C) Concrete block hosting the diver detector before its deployment. (A) During its fabrication. (B) Diver inside the block.

8.3. Digital model of terrain

A digital elevation model (DEM) of the terrain was made with the topographic information from Figure 8.5. and is shown in Figure 8.10 (A).

In parallel, a second DEM (see Figure 8.10 (B)) was made to include the water content of the reservoir at the beginning of the data acquisition, 414 meters above the sea level (m.a.s.l.). The second model is superimposed on the first, and covers the volume between the ground level inside the reservoir zone and a selectable height ranging from 404 m (minimum level) to 414,6 m (maximum level of water before overflow). The red dot locates the position of the detector. The north axis is parallel to the Y axis of the figure and corresponds to φ=0 in Figure 8.11 (A) and (B).

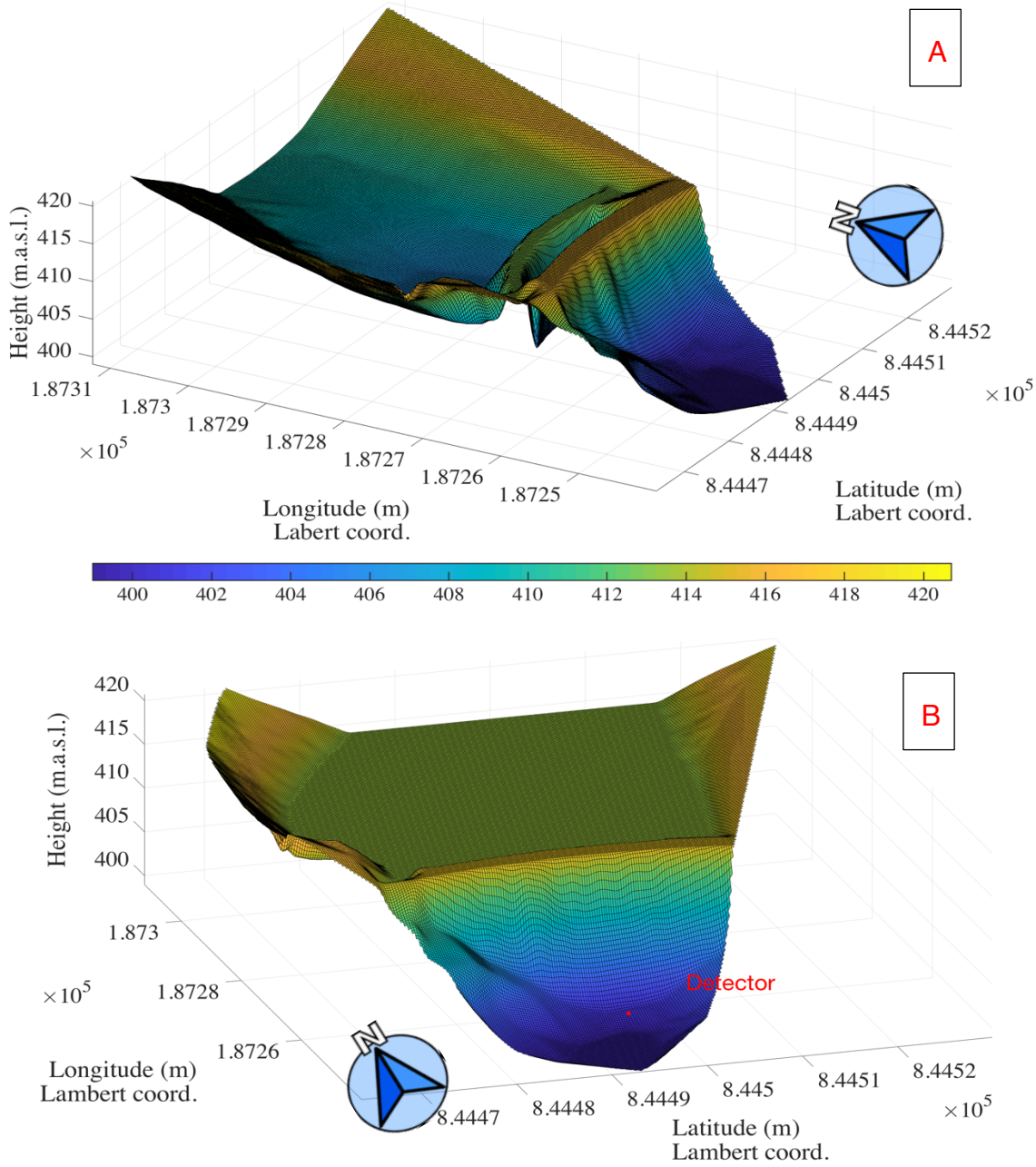

Figure 8. 10(A) DEM of the empty water reservoir and (B) with water at 414 m.a.s.l.

8.3.1 Apparent thickness

The usefulness of the DEM in muography is helping to estimating the muon flux attenuation due to the target topography. The first stage is to calculate the distance travelled by the muon through each medium.

A Matlab® code, originally developed by K. Jourde and subsequently adapted by the author, computes the apparent medium thickness. In other words, it calculates the underground distance between the detector location and the open sky without taking into consideration of the muon scattering.

Figure 8.11 was been calculated using this code, and shows the apparent thickness of the targeted volume from the point of view of the detector in two different scenarios: Figure 8.11 (A) assumes there is no water in the reservoir, while Figure 8.11 (B) assumes a water level of 414 m.

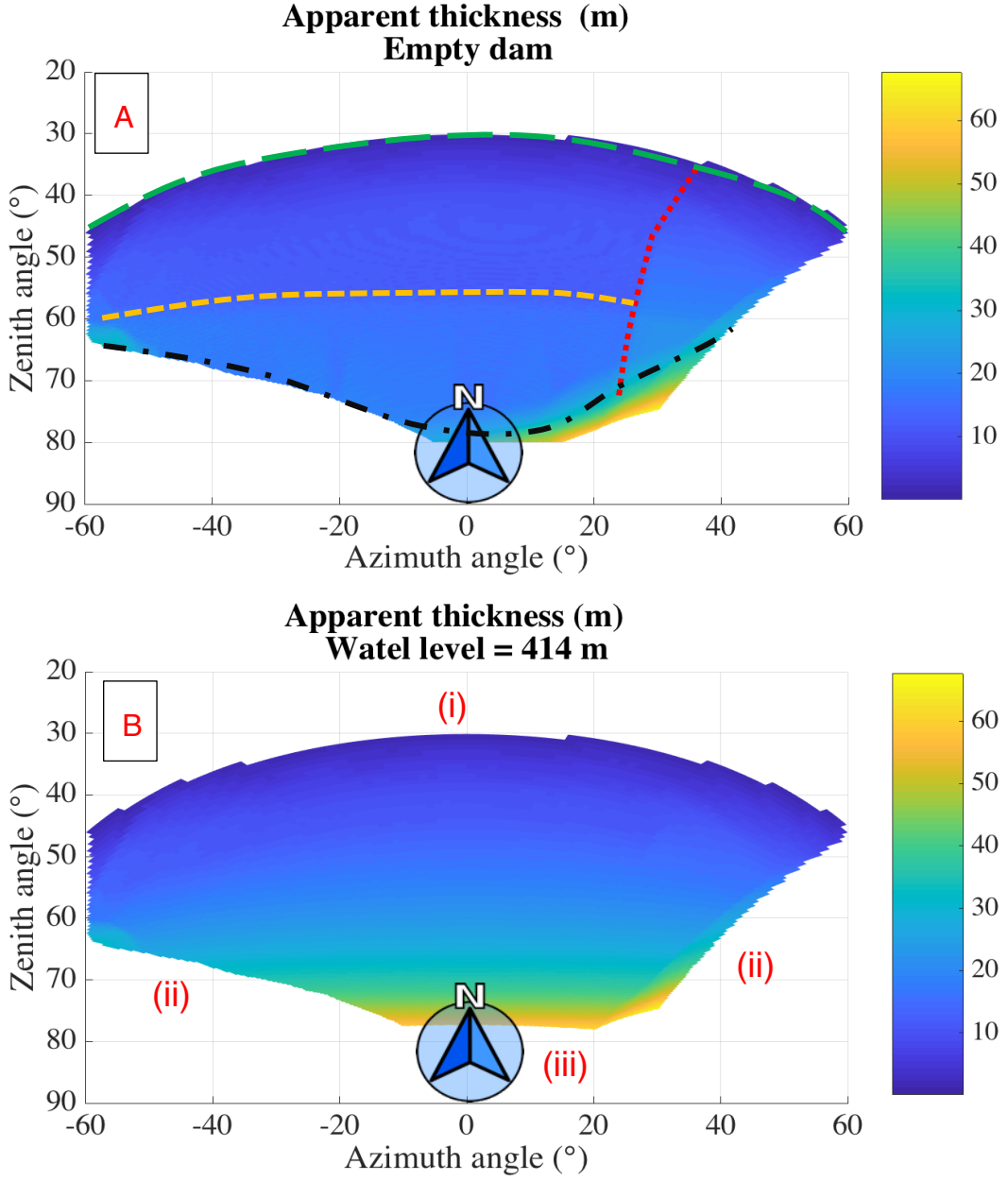

Figure 8. 11(A) Apparent thickness of the dam without water and (B) with a water level of 414 m.a.s.l.

It is possible to identify in Figure 8.11 (A) some structural elements, such as:

- Black dot-dashed line: limestone bed beneath the reservoir
- Red dotted line: near-vertical rock cliff of the castle's hill.
- Green long dashed line: summit of the main dam.
- Orange dashed line: summit of the ancient dam.

The blank parts of Figure 8.11 have three different explanations:

i. The muon does not interact with the target volume; its flux attenuation is due to the atmosphere, and can therefore be neglected at this level.
ii. The angular values exceed the limited reach of the DEM, and the apparent thickness cannot be calculated.
iii. The calculated value of apparent thickness exceeds the established calculus cut-off of 70 m. Beyond this distance, the apparent thickness calculated by the code cannot be considered representative of the real muon's path, as most of its trajectory takes place outside of the DEM's reach.

Figure 8.12 provides an approximated of the view of the targeted volume as seen by the detector.

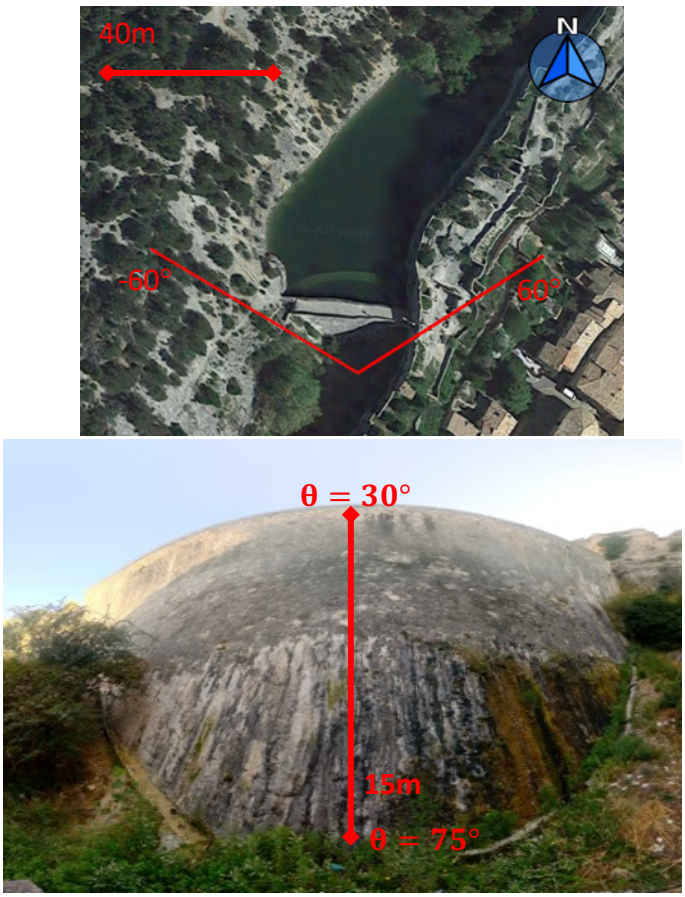

Figure 8. 12 Targeted volume as seen by the detector.

8.3.2 Apparent opacity

As seen in Chapter 3, the medium opacity better describes the muon flux attenuation though matter. The apparent opacity can be computed by integrating the density over the path length.

The terrain was described with two different, superimposed models corresponding to:

1) the water in the reservoir: its height was set to the water level at the moment of the beginning of the acquisition, 414 m.a.s.l.
2) the limestone of the valley and concrete/rock structure of the dam.

Each volume was characterized with a representative density of the medium. For (1) the density is set to $\rho=1\cdot10^3$ kg/m^3, which corresponds to fresh water. For (2) the density is set to $\rho=2{,}4\cdot10^3$ kg/m^3. This value represents a compromise between the densities of regular concrete ($\rho=2{,}4\cdot10^3$ kg/m^3) and limestone ($2{,}3\cdot10^3$ kg/m^3 – $2{,}7\cdot10^3$ kg/m^3).

Figure 8.13 shows the result of the computed apparent opacity in meters water equivalent[1] (mwe) of the targeted volume from the point of view of the detector.

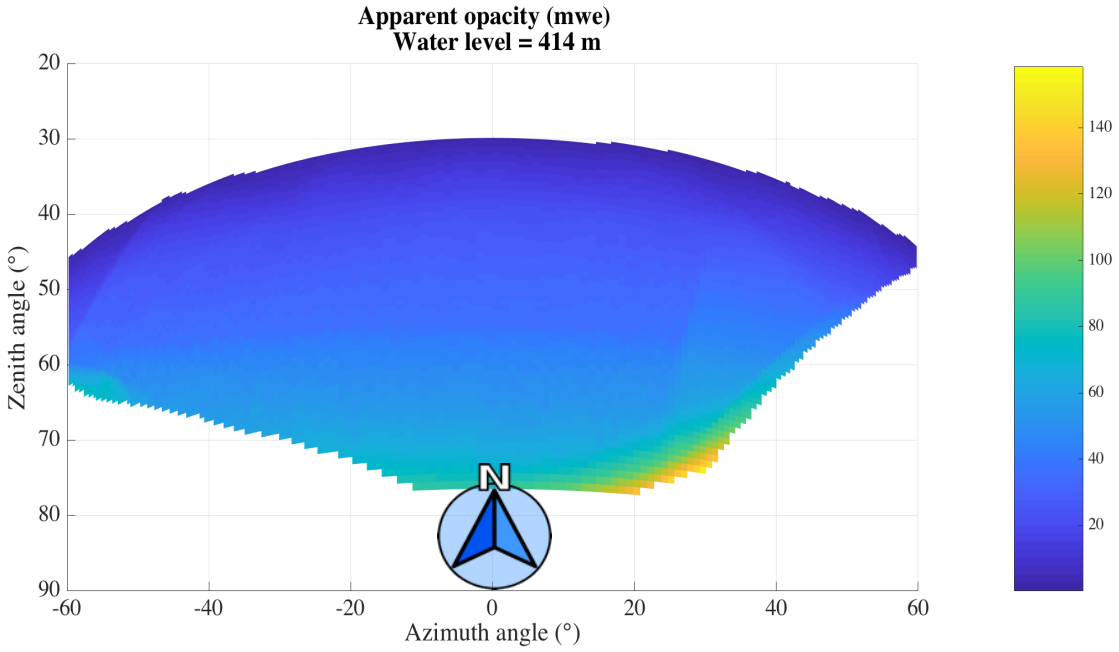

Figure 8. 13 Apparent opacity of the targeted volume with a water level of 414 m.a.s.l.

[1] 1 mwe = 100 g/cm^2

8.4. Experimental results

8.4.1 Data acquisition

The detector setup during the acquisition is shown in Figure 8.14. Three protection boxes containing two plastic scintillators and the MUST^2 detector respectively were stacked at the nearest wall to the dam. The stack was placed over a pallet to avoid direct contact with the wet floor. Due to the narrow space and ground heterogeneities the detectors couldn't be leveled perfectly. The angular deviations from horizontal in X and Y coordinates are shown in Figure 8.14 (A).

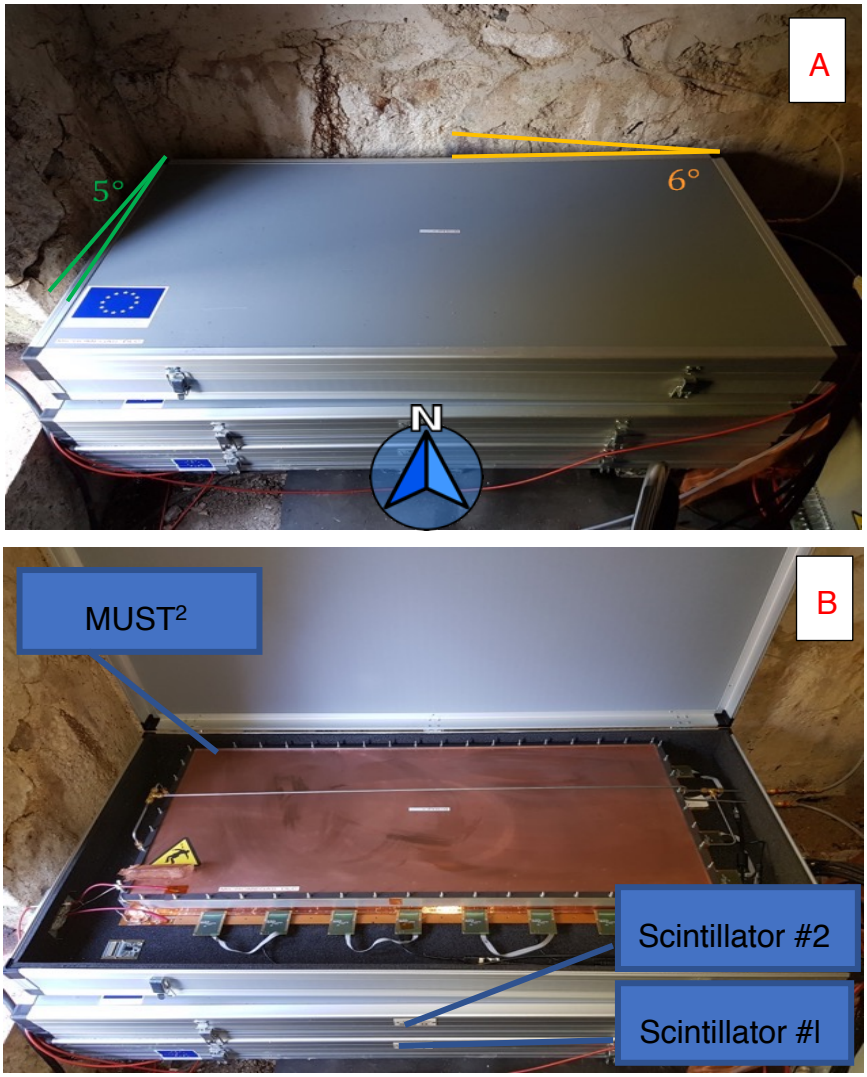

Figure 8. 14 Detector setup during the data acquisition at the valve house.

Prior to the data acquisition, a pedestal run and a reconstruction efficiency scan were performed to tune the operational parameters. A series of 12 short acquisitions were made by varying the resistive voltage in 10 V intervals from 300 V to 420 V. Figure 8.15 shows the number of recorded events in blue and the number of tracks reconstructed in orange. When examining the signal, some saturation was seen in acquisitions beyond 415 V, and the V_{amp} for the long run hence chosen was 410 V.

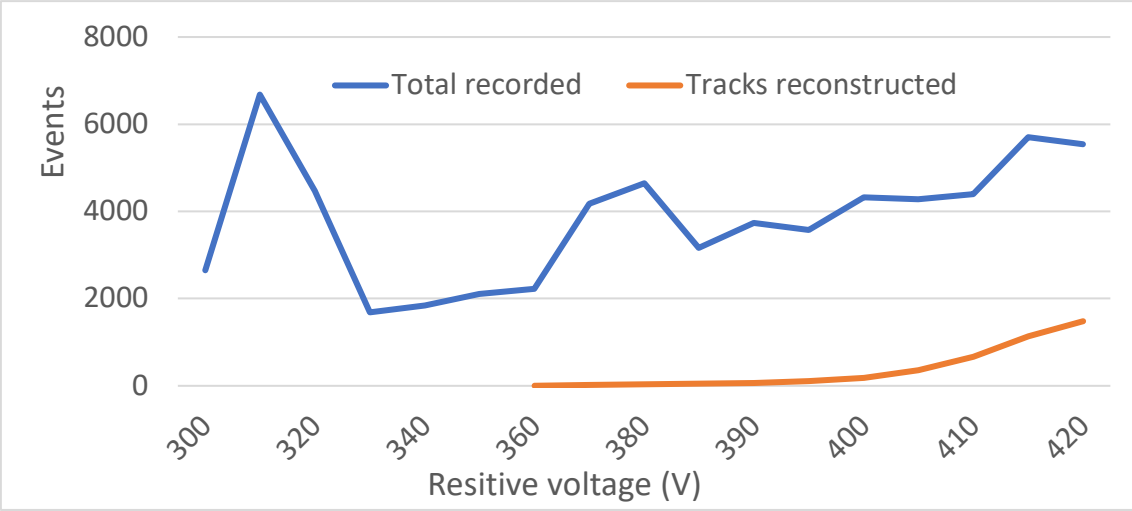

Figure 8. 15 Reconstruction efficiency scan prior to data acquisition.

The instrumental parameters during the acquisition were as follows: gas mixture Ar:CF_4:iC_4H_{10} (88:10:2), gas flow 4 L/h, V_{drift}= -3.000 V/cm, V_{amp}= 420 V.

The trigger signal was provided by two plastic scintillators in coincidence mode and aligned with the MUST[2] detector, as seen in Figure 8.14.

The data acquisition was continuously active from of 27th of July at 17h15 to the 31th of July at 10h24. The end of the acquisition was conditioned by the size of the 4 TB external hard drive used to locally store the raw data. During the more than 89 hours acquisition, the detector recorded 27.466.111 events with an average trigger rate of 85,6 Hz.

After the data analysis, the distribution of events according to the trajectory reconstruction is shown in Figure 8.16.

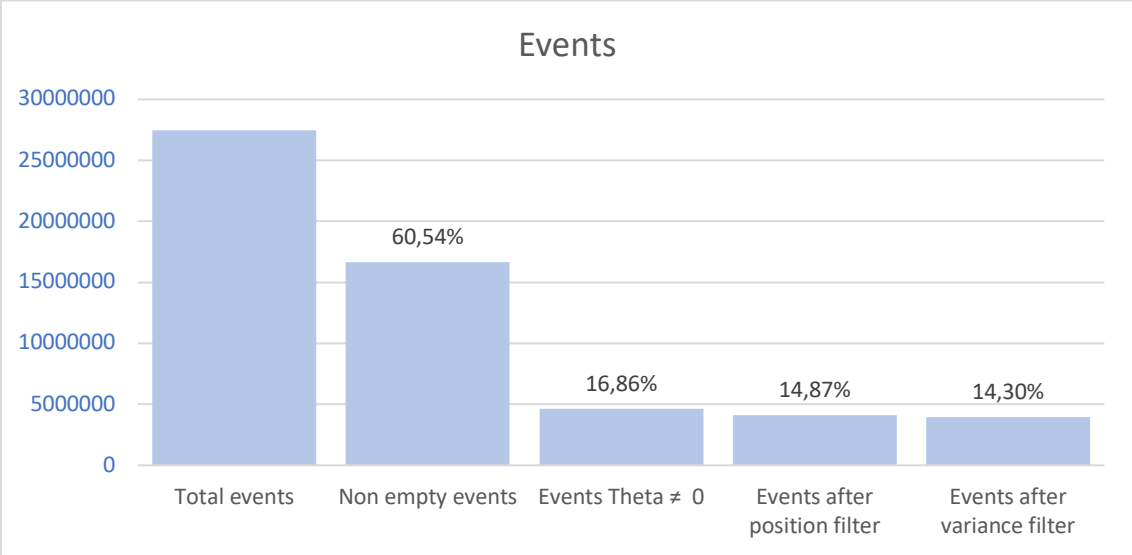

Figure 8. 16 Distribution of recorded events according to track reconstruction.

Figure 8.16 reveals two issues: the low efficiency of the trigger and efficiency of reconstruction. The first issue may be explained by different factors; such as (i) a bad alignment of the detectors with the scintillators during the experience, (ii) a threshold excessively low of the scintillators, which leads to an increase of random coincidences, and mostly due to (iii) the lack of recorded signal in almost 1/4th of the detector, as seen in Figure 8.17. On the other hand, only ~28% of non-void events have been reconstructed. Besides the electronics misfunction aforementioned; the position of the detector, inside the valve house and surrounded by massive bodies, has increased the relative arrival of near-vertical muons (harder to reconstruct), penalizing the efficiency of the algorithm.

Figure 8.17 shows a 2D histogram of the position of the reconstructed events for trajectories with a zenithal angle different from 0º. The bin size is 2 x 2 mm^2.

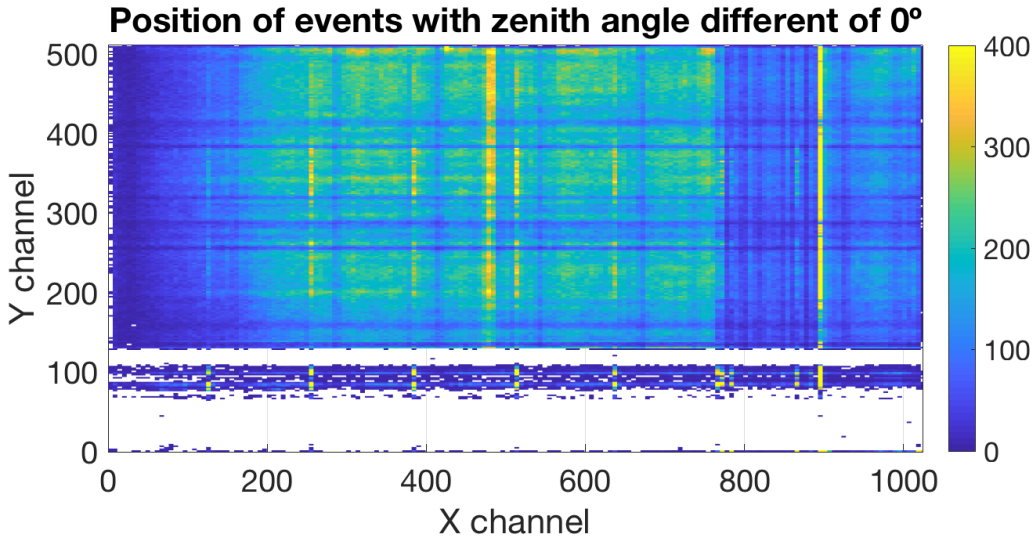

Figure 8. 17 Position of the detected events with zenith angle different of 0º.

The figure reflects a malfunction of one fourth of the detection surface., i.e. zone with Y channel ∈ [0 127]. It seems that the resistive layer underwent current leaks which made the signal amplification insufficient for track reconstruction (possibly as a consequence of the water intrusion a few weeks before, as seen in Section 7.5). The zone with events near Y channel 100 is certainly associated with instrumental noise. It also seems that the APV25 card instrumenting the X channels 769 - 896 had problems after the pedestal run. The same behavior was noticed in previous testing and appeared with a random frequency. The main disadvantage of this malfunction is that it cannot be easily identified during data acquisition, but in the data analysis after the acquisition. To overcome this problem, it is necessary to perform a cold restart of the FEC card and reboot the APV25 cards.

A progressive increase in the number of detected events is also noticeable in the zone of X channel < 150. This effect is due to the combination of geometric acceptancy loss near the perimeter of the detector, and a slight misaligning of the trigger scintillators with the MUST^2 detector as a result of the size constraints inside the valve house.

The effect is more visible in Figure 8.18, which shows the reconstructed zenith angle as a function of the position in the detector along the X axis. The same geometric effect is seen in Figure 8.19.

The X channels close to the perimeter (near 0 and 1.024) indicate a distribution of muon arrivals of influenced by the shape of the detector.

Figure 8.20 shows the angular distribution of all reconstructed events. The data has been filtered with a zenith angle cut-off of 80º due to the lack of physical meaning beyond this point.

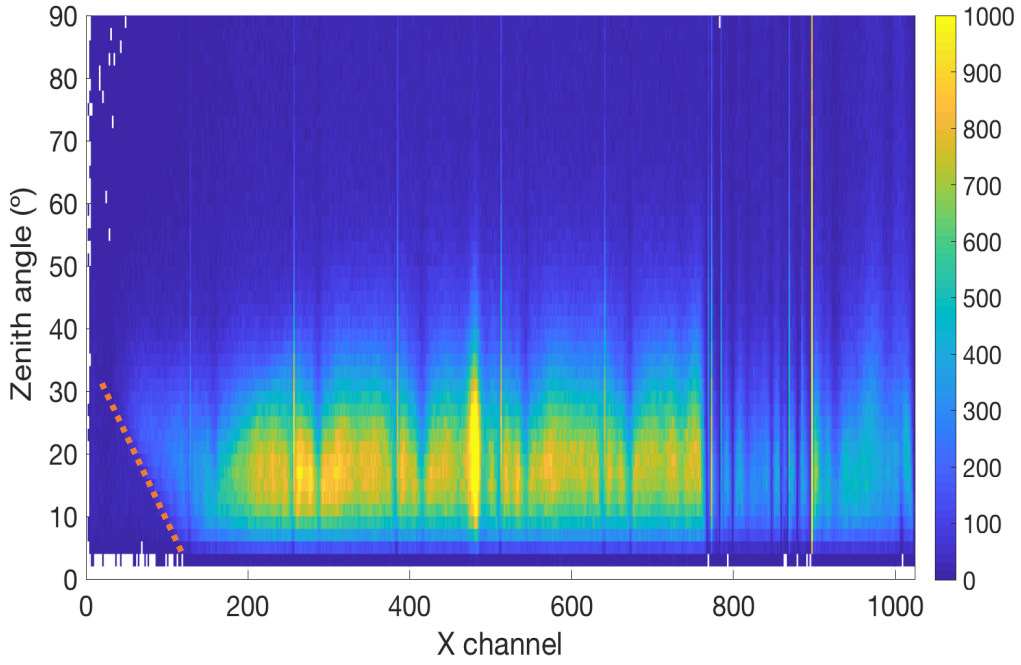

Figure 8. 18 Distribution of reconstructed zenith angle along the X position.

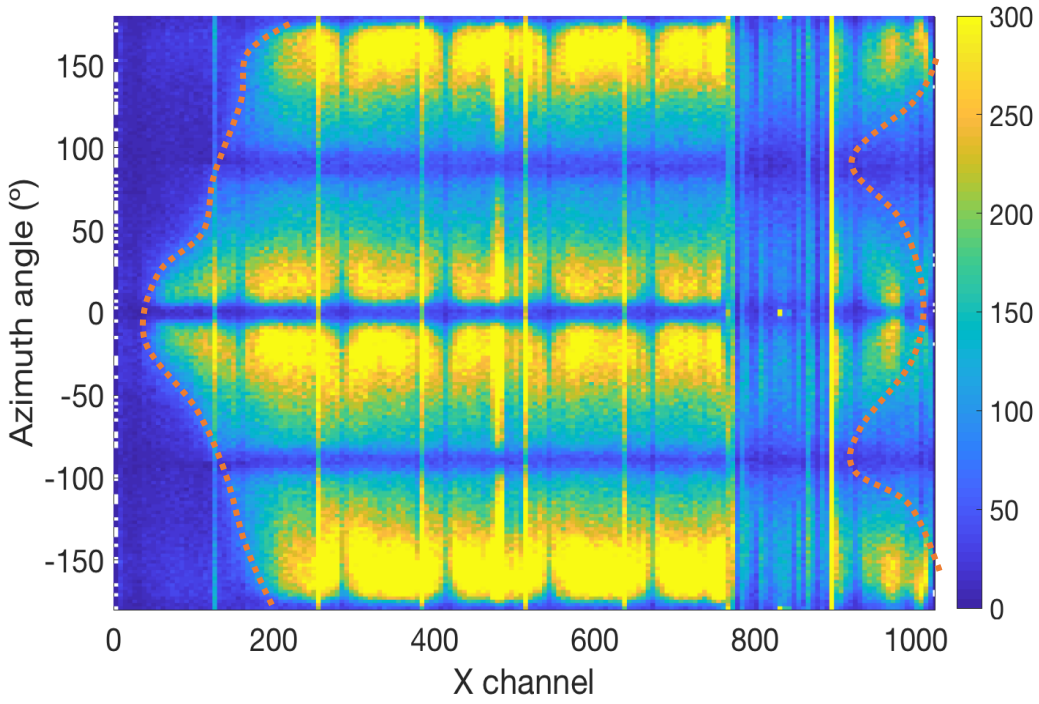

Figure 8. 19 Distribution of reconstructed azimuth angle along the X position.

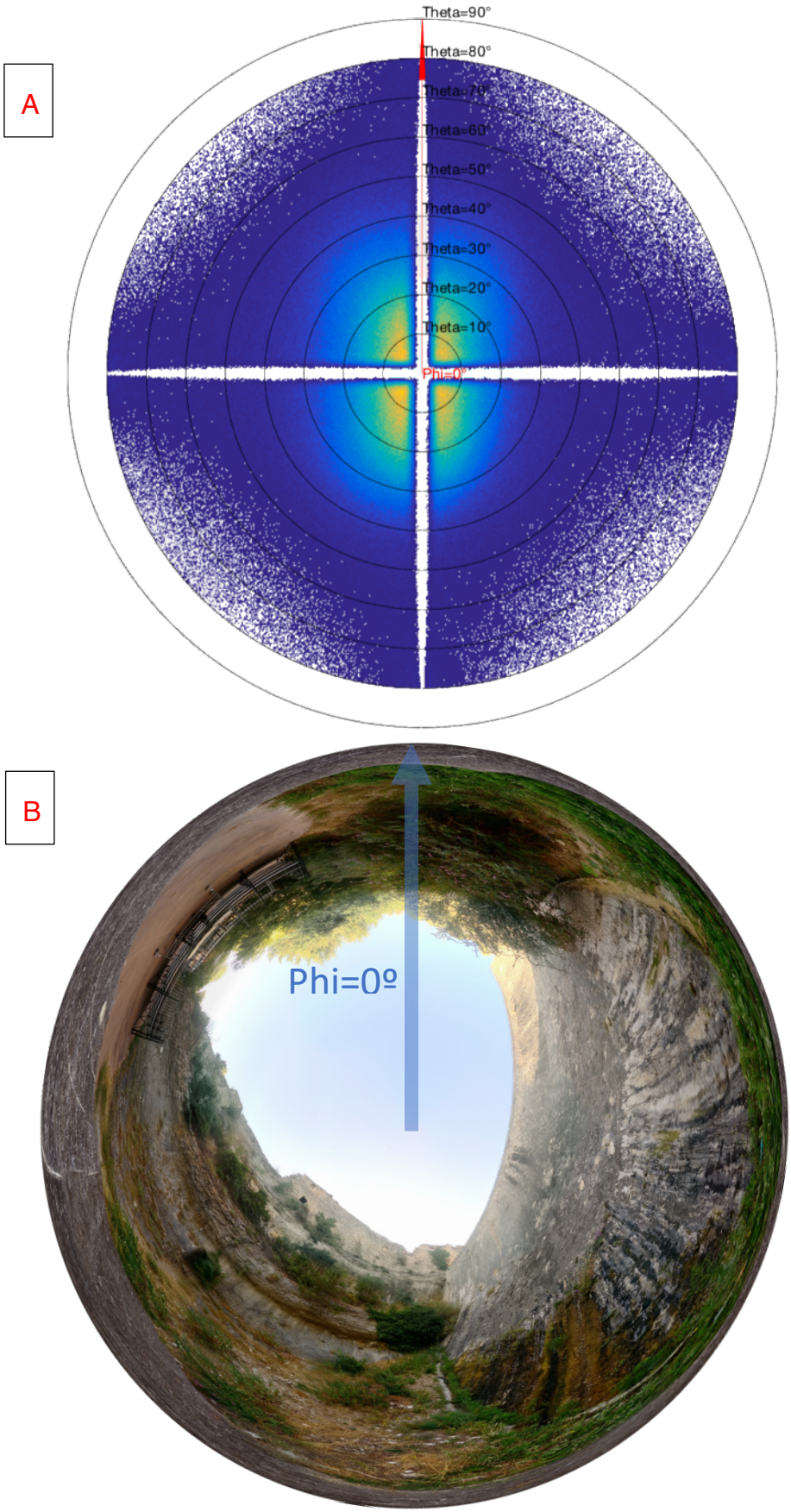

Figure 8. 20(A) Polar chart of the angular distribution of the reconstructed events. (B) Spherical picture for illustrative purposes only.

8.4.2 Muon flux vs opacity

Figure 8.21 shows the experimental muon flux measurement integrated over ~90h. The azimuth angle has been corrected with an offset of 96º to align the axis φ=0º of the detector with the geographic North, easing the comparison of the data with the model, the corrected zenith values are renamed to φ*. In the same spirit, the azimuth limits of the image are set from -60º to 60º.

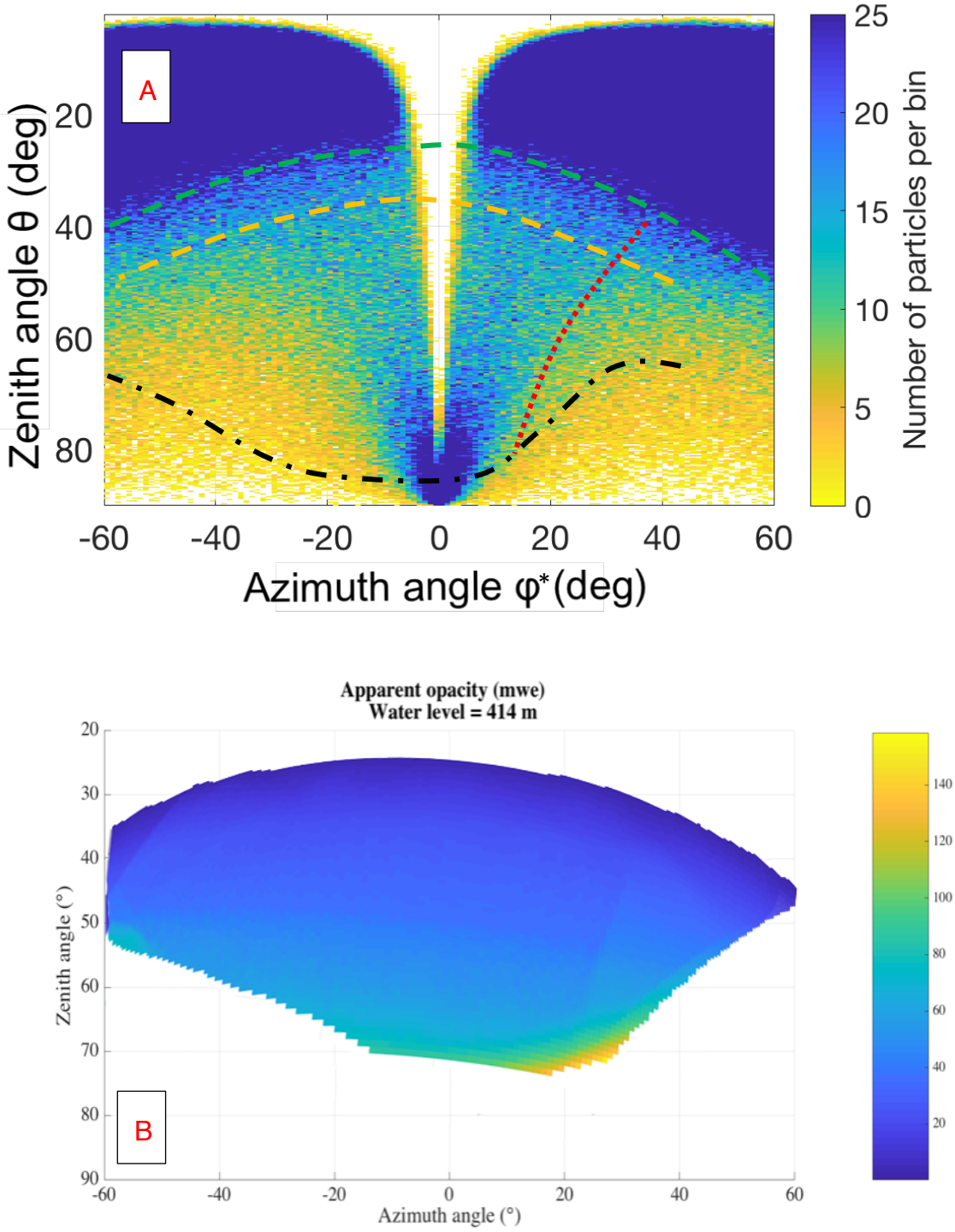

Figure 8. 21 (A) Muons measured coming from the direction of the target volume and (B) apparent opacity of the targeted volume with a water level of 414 m.a.s.l. with the deviation from the horizontal corrected.

The high values of attenuation for muons with near horizonal trajectories create data blanks at some points of Figure 8.21 (A). As explained in Chapter 6, the blank near φ=0º and θ<10°, and the artefact near φ=0º and θ=80°, and are due to the reconstruction algorithm failures.

The following structural elements, detailed in Section 8.3.1, are superimposed to Figure 8.21 (A) as a reference:

- Black dot-dashed line: bed of limestone beneath the reservoir
- Red dotted line: near-vertical rock cliff in the castle's hill.
- Green long dashed line: summit of the main dam.
- Orange dashed line: summit of the ancient dam.

A good correlation between the image of measured muon flux and the apparent opacity simulation of the target volume is observed.

8.4.3 Temporal monitoring and temperature influence

The rate of recorded and reconstructed events per minute is shown in Figure 8.22. This figure represents a frequency density plot, with the flux values grouped in 60 min bins. While the recorded rate is exclusively dependent on the scintillator coincidence, the reconstructed rate depends on the performance of the MUST^2 detector and the reconstruction algorithm.

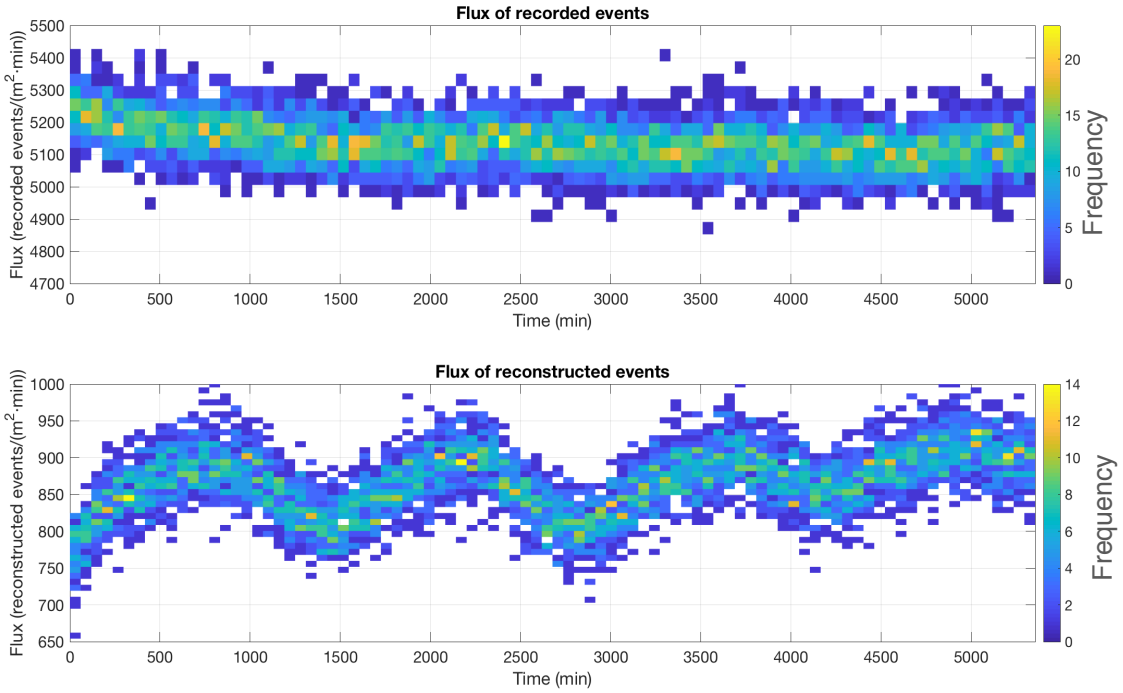

Figure 8. 22 Rates of recorded events and reconstructed events.

The sine-wave form of the reconstructed data is caused by the influence of the detector temperature, which has a direct effect on the detector's gain as explained in Chapter 4. The voltage of the resistive layer was chosen in a test

with a temperature of 25ºC. Nevertheless, the thermal amplitude of ~6ºC during the acquisition has caused noticeable affects in the detector gain that have modified the trajectory reconstruction performance. Figure 8.23 (A) shows the evolution of the measured amplification current (current used to polarize the resistive layers) and the environmental temperature, without a significant correlation.

Figure 8.23 (B) shows the effect of the temperature on the trajectory reconstruction performance. The Pearson correlation coefficient is -0,49, indicating a moderate inverse lineal correlation between the two variables. On the one hand, the gain decrease associated with a rise of temperature reduces the signal amplitude to a value below the detection threshold level. On the other, the gain increase leads to signal saturation and hence a drop of efficiency in trajectory reconstruction.

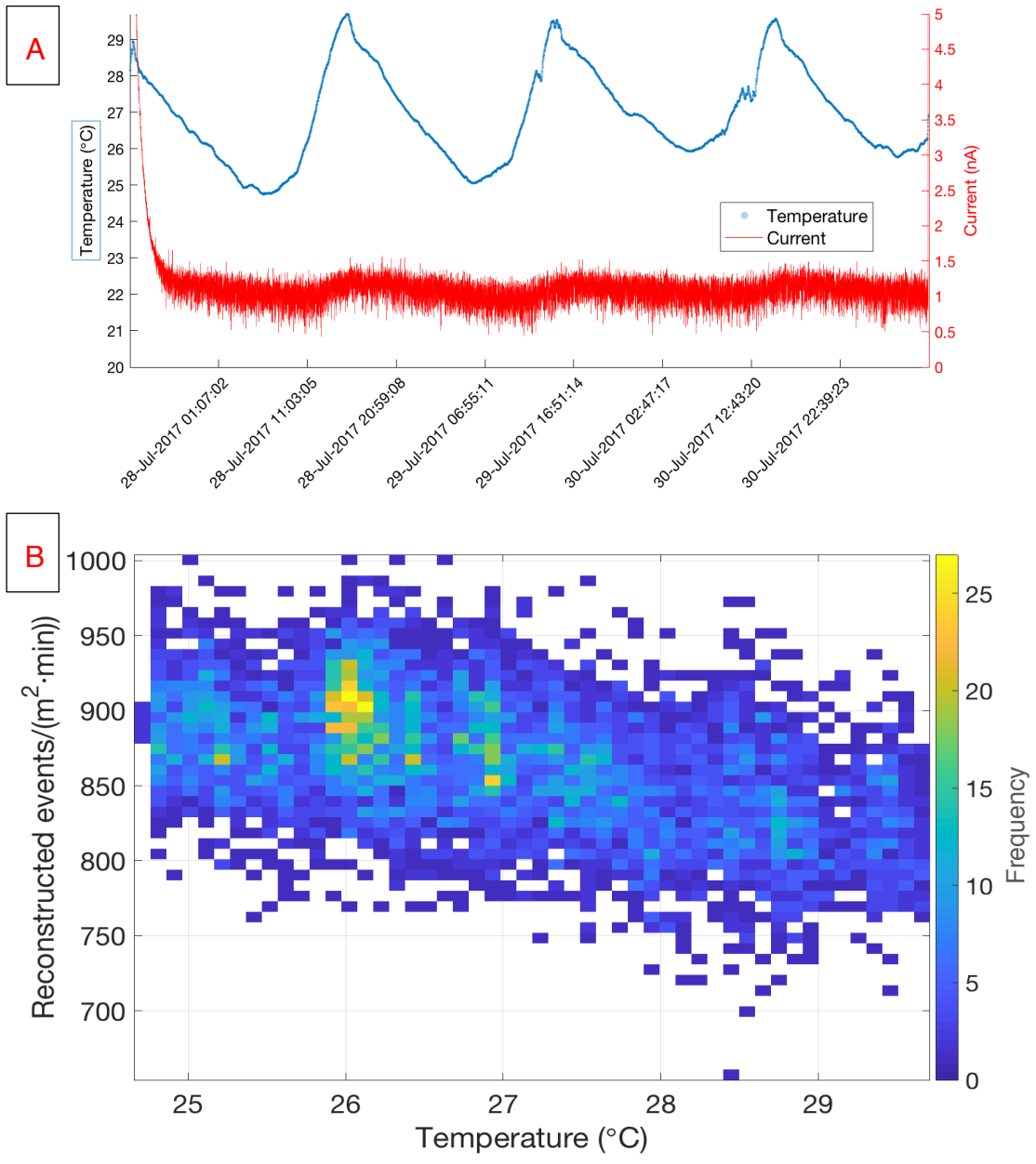

Figure 8. 23 (A) Amplification current and (B) rate of reconstructed events as a function of the temperature.

The effect of temperature was also noticed in the measurement of the water level (see Figure 8.24). The barometer, used for pressure compensation, was in the valve house near the detector with daily fluctuations of temperature of ~10º, while the diver detector was underwater at a nearly constant temperature.

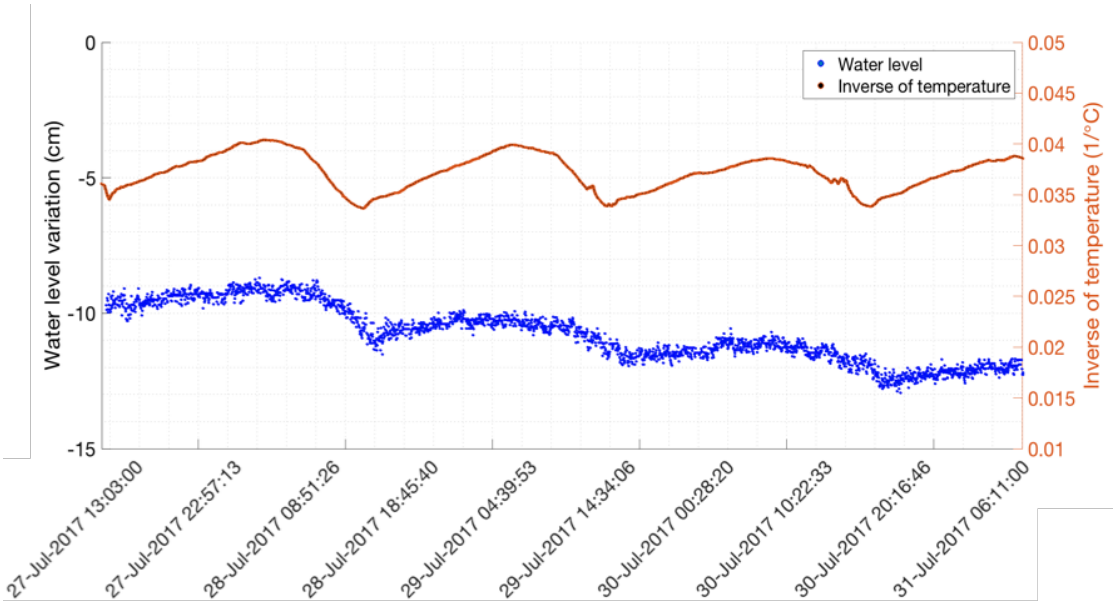

Figure 8. 24 Graphic of measured water level of the dam and inverse of temperature.

The water level was measured manually at the beginning and at end of the experiment. The level drop was 33±1 mm during the data acquisition, and is in good agreement with the value calculated with a linear fit of the data seen in Figure 8.25, which presents the temporal evolution of the water level of the dam and the recorded muon flux. The origin value of water level stands for the reference height of the water at the beginning of the experiment, 16 days before the data acquisition. The slow emptying trend of the water reservoir is clearly indicated. The calculated value of the Pearson correlation coefficient between the de-trended water level and temperature is -0,62, confirming the inverse relation between the variables.

The effect of the temperature, in both the barometer used to determine the water level and the MUST^2 detector, explains why when the measured water level increases locally, the measured muon flux increases as well contrary to what's expected: in normal conditions, a water level rise should result in a flux drop and vice versa. Nevertheless, when performing a linear regression of the entire data, the emptying trend of the dam is clearly translated into a rise of the muon flux. A Welch's t-test was performed between the initial and final halves of the muon flux data series (corresponding to 45h of data for each subseries): the p-value=$1{,}77 \cdot 10^{-43}$ allows rejection of the null hypothesis, and quantifies the rise of the reconstructed muon flux in 46,8±6,6 particles per square meter and per minute (95% confidence level). This implies an average increase of the muon flux of 1,88±0,2%, which is in consistent with the 0,94% of the simulated apparent opacity decrease in the targeted volume, seen in Figure 8.26.

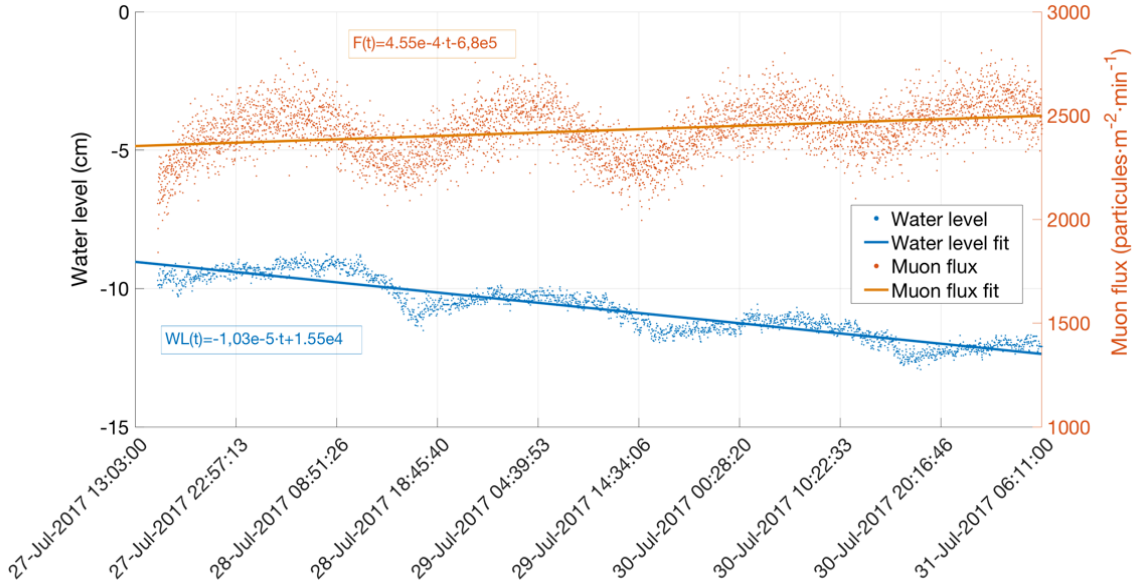

Figure 8. 25 Temporal evolution of (blue) water level of the dam and (orange) recorded muon flux.

Figure 8.26 presents the difference of apparent opacity of the targeted volume during a 3,3 cm water drop between the beginning and end of the data acquisition.

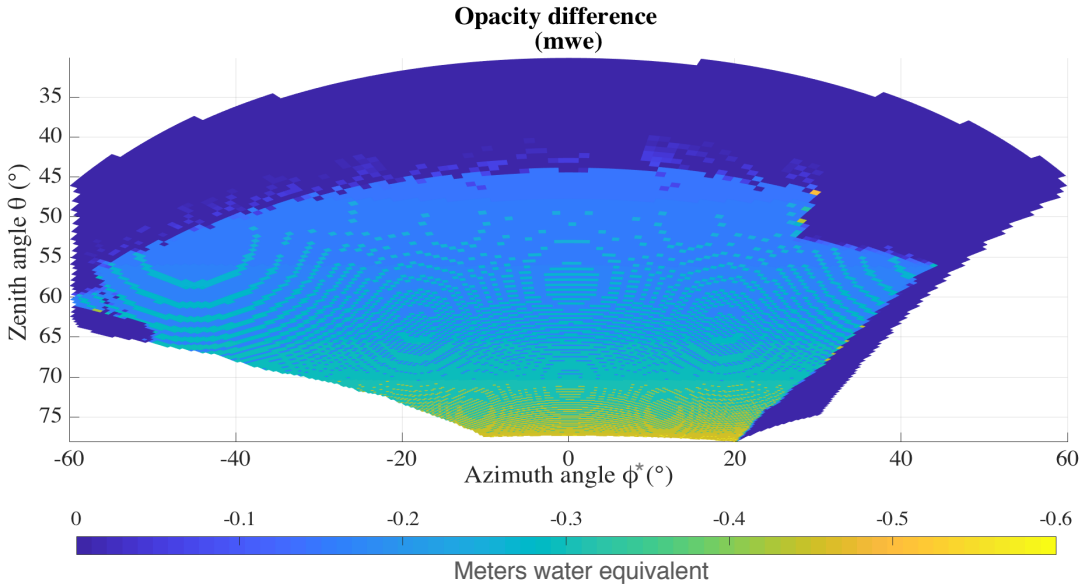

Figure 8. 26 Difference of apparent opacity between the beginning and the end of the data acquisition.

With the aim of performing a directional analysis of the reconstructed muon flux fluctuation, the hemisphere above the detector is divided into 2 zones: the zone with $\theta<25^{o}$ (aiming to the sky), and the zone with $\theta>25^{o}$ (aiming to the target volume). Figure 8.27 shows the normalized reconstructed muon flux for the two zones as a function of time.

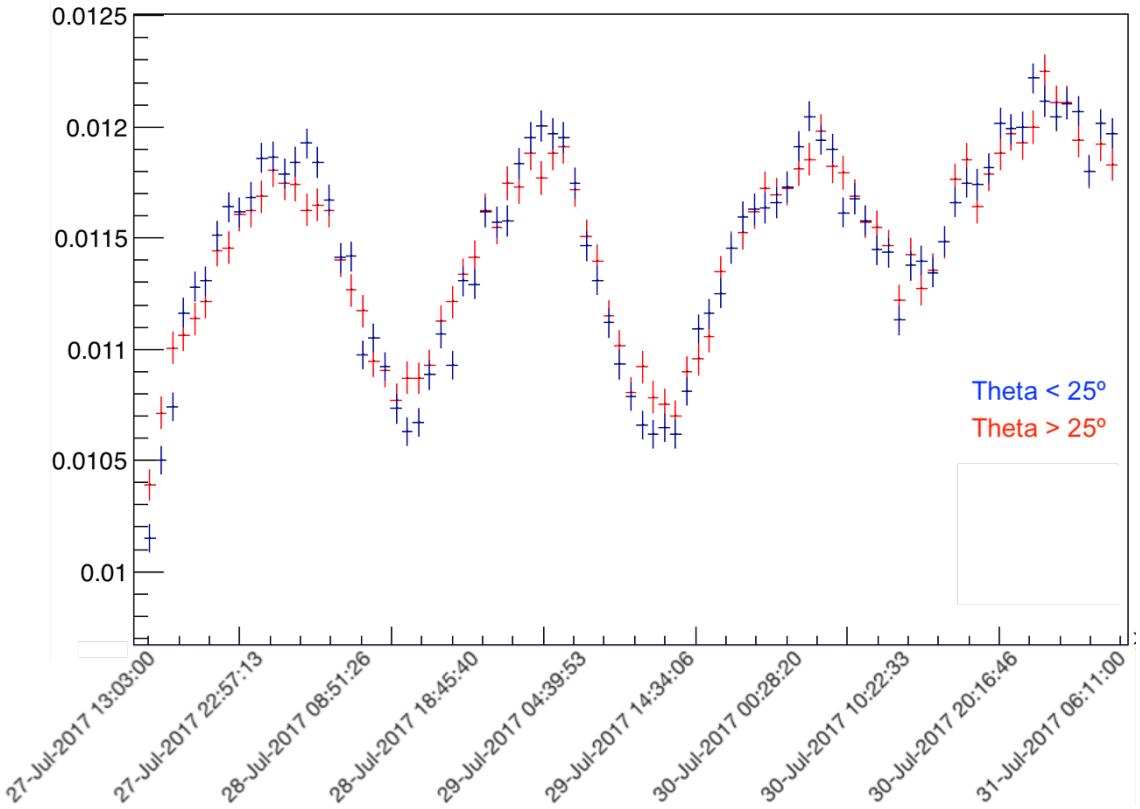

Figure 8. 27. Normalized reconstructed muon flux for muons with θ<25º and θ>25º as a function of time.

The fluctuations in the rate of reconstructed events are in the same order of magnitude in the two cases, with a slightly bigger amplitude in the case of the muons coming from the open sky.

Despite that all the aforementioned measured values are in good agreement with the simulated values, it is not possible to directly validate the sensitivity of the detector because of the following factors:

- The gain of the detector was not constant during the experiment

- The variation of the water level during the experiment was too small to be statistically significant against the natural variations of over 3% in the muon flux [Jourde, 2016][i].

Additional data should be collected with constant gain and a larger opacity contrast to fully validate the temporal sensitivity of the detector.

8.4.4 Effect of the Earth tides in the water level

At first moment, when looking at the periodic fluctuations of the water level variation, it was thought that the water level could be somehow affected by a thermal effect of dilatation of the water. Nevertheless, this effect was discarded because of the small daily variation of the water temperature (on the order of few tenths of ºC).

A second, longer campaign of measurements was made to verify possible the influence of tides in the measurement. The data recorded in this second campaign is shown in Figure 8.28.

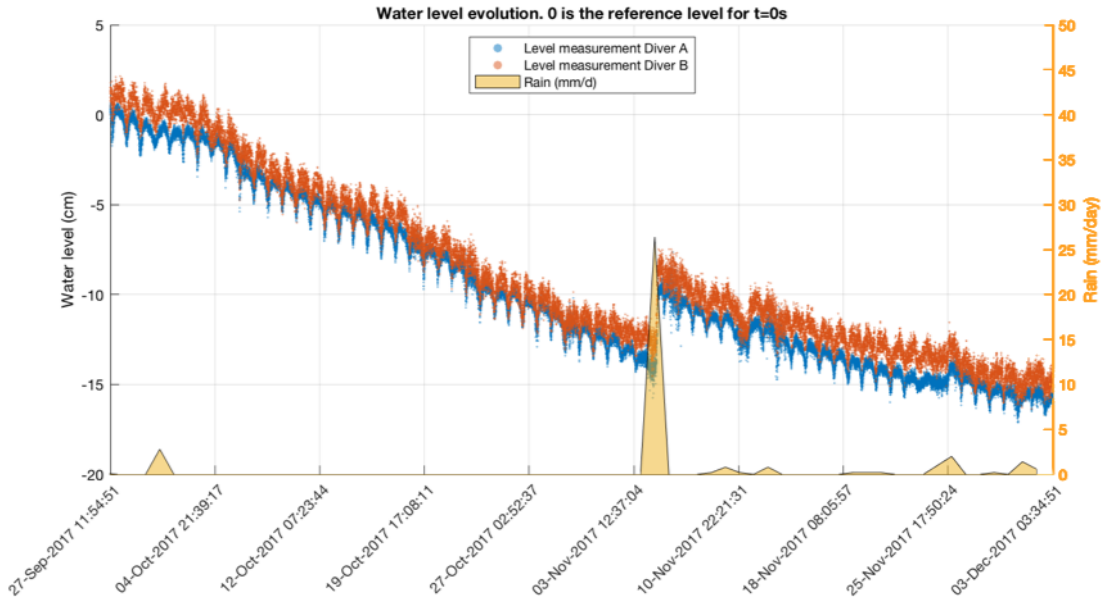

Figure 8. 28 Water level in the reservoir measured in two points and precipitations.

One again observes emptying trend of the dam with a constant slope of ~0.3 cm/day and a daily fluctuation of ~2,5 cm in amplitude per day.

Due to the small size of the reservoir and the signal synchronisation between the two detectors at two opposite locations, the presence of classic tides (caused by gravitational forces) was rejected. The effect of the wind was also discarded due to the accurate periodicity of the phenomena.

A Fast Fourier Transform (FFT) analysis with a of the water level data revealed two peaks of periods of 23,96h and 11,98h. These values, quite similar to the values of some Earth tidal constituents, motivated a data comparison.

The software ETERNA34 [Wenzel, 1997][ii] was used to simulate the Earth tide behaviour, providing values of strain in μm/m at the desired location and during the data acquisition.

Figure 8.29 shows the FFTs of the Earth tide simulated signal and the water level at two different points of the dam. One observes that the two measurements of water level present peaks at the same frequency, but with slightly different amplitudes. This might be caused by the difference of depth between the two divers: diver A was located at about 3 meters depth, while diver B was under about 1,5 meters of water.

On the other hand, the comparison between the Earth tide and the water level results indicates that despite some of the constituents being shared between datasets, not all appear in the two series.

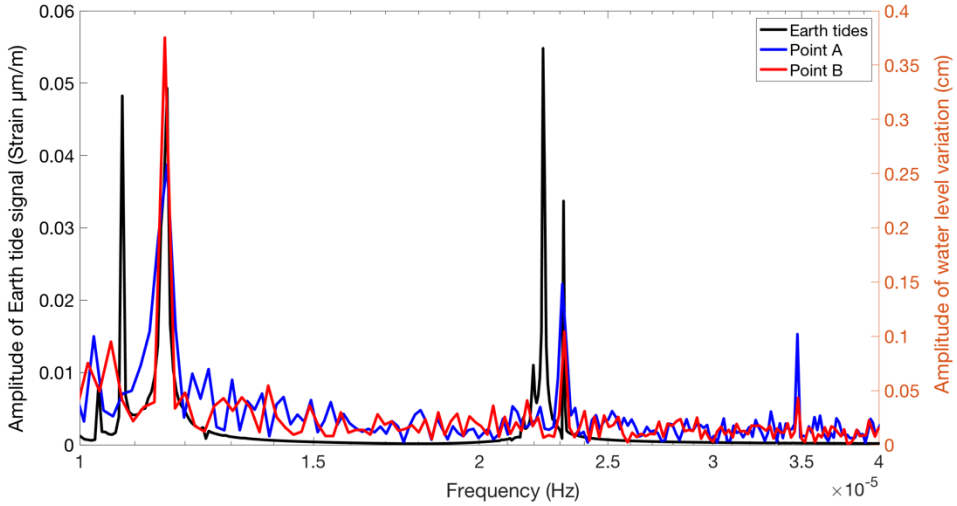

Figure 8. 29 FFT of the Earth tide simulated signal and water level at two different points of the dam.

This reinforces the hypothesis that the daily fluctuations are caused by the temperature of the barometer use for compensating both divers' pressure data.

8.5. References

[i] Jourde, K. et al. (2016). Monitoring temporal opacity fluctuations of large structures with muon radiography: a calibration experiment using a water tower. Sci. Rep. 6. 23054

[ii] Wenzel, H.G. (1997). ETERNA34 Manual of versión 3.40. http://www.eas.slu.edu/GGP/ETERNA34/MANUAL/ETERNA34.pdf

Chapter 9. Conclusions

Transmission muography is an expanding technique based on the attenuation of the natural-occurring cosmic-muon flux due to the opacity of the material they traverse. With a reach up to a few hundreds of meters, it allows estimating density distribution around the detector. This non-destructive, passive technique provides original information to ease the resolution of the inverse problem.

The usefulness of muography is proven in applications that include the characterization and monitoring of volcanoes or cultural heritage study or the analysis of hydrodynamics in natural or man-made bodies.

This thesis was dedicated towards the creation of a new direction-sensitive tool for muon flux measurement based on a thin time projection chamber with a Micromegas readout, to achieve a compact detector with an angular resolution compatible with civil engineering and geophysics applications. The main motivation was to conceive a detector capable to fill the technological gap for applications with compactness and transportability constraints.

The principal phases of design of the detector were: (i) the design of a Micromegas readout layout with good spatial resolution and a balanced charge distribution in the two coordinates, (ii) the choice of a gas with low diffusion for better resolution and an electron drift speed compatible with the time projection chamber operation, (iii) the conception of a field homogenizer to minimize the deflection of the electron trajectories in the drift zone towards the readout plane, (iv) the choice of the electronics instrumentation and its trigger signal to be able to reconstruct the muon flux and trajectories, and (v) the creation of an auxiliary system to manage the gas flow and prevent impurities and contaminants from entering into the detection volume.

The data acquisition and preanalysis were made with software developed for the CERN Scalable Readout System electronics (i.e. DATE and AMORE SRS respectively). Nevertheless, the muon trajectory reconstruction was made via the algorithm created by T. Serre. This algorithm retrieves the time, 2D position, zenith (θ) and azimuth (φ) angles of the muons traversing the detector.

The downside of this algorithm, as it currently stands, is the impossibility to correctly reconstruct trajectories with less than 3 activated readout tracks per coordinate. This leads to a blind zone of detection near the φ multiples of $90^{o}\pm5^{o}$ and the creation of a few dummy events without physical meaning concentrated in the zone $\theta=85^{o}\pm5^{o}$ in these azimuth angles. The influence of the two effects aforementioned on the inversion results can be minimized if the detector is correctly positioned towards the target.

The track reconstruction algorithm still has room for improvement, such as the development of the centroid technique to reduce the blind zone. The analysis of further data will help in order to enhance the robustness of the results.

The presented characterization tests represent a mandatory stage for the fine tuning of the operational parameters of detector and assessing its performance. The access to the CERN beam facilities allowed the fine tuning of the latency of the acquisition chain, estimate the gain of the detector at different voltages (a key parameter for signal formation), and detection efficiency. The obtained values are found to be in good agreement with other Micromegas-based detectors. The tests highlighted also the importance of a reliable trigger source.

The second campaign was dedicated to the open sky measurements, which permits comparison between the theoretical model described in Chapter 2 and experimental data. This test allows to estimate the acceptance of the experimental setup (useful to correct the tomographic images) and enhance their fidelity, and to assess the efficiency of the muon trajectory reconstruction algorithm.

The tests made both in underground and at the entry of the LSBB served as preliminary measures of muon flux attenuation in a controlled environment. In both cases, and despite the weak statistics, the images have shown a good correlation with the target volume.

The collaboration with the CEA's IRFU made possible a series of comparative tests between their CLAS12 electronics and the CERN's SRS electronics. Both systems have succeeded to log data from the MUST^2 with an external trigger provided by plastic scintillators in coincidence mode. Moreover, CEA electronics was compatible with the self-trigger operation mode and capable to propagate the signal to the SRS electronics. Nevertheless, a thorough performance comparison was not possible due to the different data format from both systems, which prevent from doing a muon trajectory reconstruction of the data acquired with the FEU card.

The implementation of digital models of allows simulating the apparent thickness of the target volume. This is helpful in order to adapt and dimension the experiment before the data acquisition, and to analyze the outcome of the measurements.

During the campaign of measurements in the Saint-Saturnin-les-Apt dam, the field transportability and the capability to perform long-term out-of-lab measurements have been demonstrated. In view of the promising results presented, the successful proof-of-concept trial allows to validate the MUST^2 camera for transmission muography purposes. On the other hand, temperature had a non-neglectable influence during the data acquisition in the MUST^2 detector, inducing variations of the reconstructed muon flux of the same order as the natural variations of the muon flux. A system for adapting the amplification voltage as a function of the environmental temperature, to keep the detector gain constant, could and must be envisaged for experimental sites with variable temperatures.

Further data analysis development and experimental data is required to improve the reconstruction efficiency, especially in the blind zones, and to validate the sensitivity of the detector to small opacity variations.